Technical University of Munich
TUM School of Natural Sciences

Iodine-Passivated Au(111): A Substrate for Molecular Self-Assembly and On-Surface Synthesis

Arash Badami Behjat

Complete reprint of the dissertation approved by the TUM School of Natural Sciences of the Technical University of Munich for the award of the

Doktor der Naturwissenschaften (Dr. rer. nat.).

Chair: Prof. Dr. Martin Zacharias

Examiners:

1. Prof. Dr. Markus Lackinger
2. Prof. Dr. Johannes Barth

The dissertation was submitted to the Technical University of Munich on 22 May 2024 and accepted by the TUM School of Natural Sciences on 25 June 2024.

Table of Contents

List of Figures

List of Abbreviations

AFM	Atomic Force Microscopy
BE	Binding Energy
DFT	Density Functional Theory
DOS	Density of States
FFT	Fast Fourier Transform
IR	Infrared
LDOS	Local Density of States
RT	Room Temperature
SPM	Scanning Probe Microscopy
STM	Scanning Tunneling Microscopy
LT	Low Temperature
UHV-LT-STM	Ultra-High Vacuum Low Temperature Scanning Tunneling Microscopy
STS	Scanning Tunneling Spectroscopy
UHV	Ultra-High Vacuum
1D	One Dimensional
2D	Two-Dimensional
3D	Three dimensional
OFHC	Oxygen-Free High Thermal Conductive Copper
TPD	Temperature-Programmed Desorption
I-STM	Immersion Scanning Tunnelling Microscope
LEEM	Low-Energy Electron Microscopy
LEED	Low Energy Electron Diffraction
LUMO	Lowest unoccupied molecular orbital
HOMO	Highest occupied molecular orbital
6A	Hexanoic acid
7A	Heptanoic acid
9A	Nonanoic acid
SA	Stearic acid
BTB	1,3,5-benzenetribenzoic acid
HOPG	Highly oriented pyrolytic graphite
PEEK	Polyether ether ketone
PZT	Lead zirconate titanate
TMA	Benzene-1,3,5-tricarboxylic acid (trimesic acid)
TPA	Benzene-1,4-dicarboxylic acid (terephthalic)
XPS	X-ray-induced photoelectron spectroscopy
BF	Bright field

Abstract

The Physics Nobel Prize "for fundamental experiments with the two-dimensional material graphene" (a single atomic layer of graphite) in 2010 was a milestone for the highly topical and prosperous research field of two-dimensional (2D) materials. The so-called 2D polymers (2DP) play a unique role as organic representatives of this new class of materials.[1] These materials are principally synthesized via the covalent linking of functionalized molecules to form stable and resilient 2D networks. The significant advantage of the organic 2DP is the capability to tailor the optical, chemical, electronic, and magnetic properties for various applications. For instance, the existence of the intrinsic electron band gap in 2DP is a requirement for use as electrically active materials in transistors. Polymerization of functionalized molecules on a solid surface also gains a unique understanding and better insight.[2] A significant benefit of this approach is the ability to image starting materials, intermediates, and end products with high resolution using Scanning Probe Microscopy (SPM).[3]

Through this perspective, the primary focus of this thesis lies in the improvement of an existing STM to establish a highly stable cryogenic system based on a flow cryostat operated with liquid nitrogen. Moreover, the enhancement of the Ultra-High Vacuum Low Temperature Scanning Tunneling Microscopy (UHV-LT-STM) optimized both lateral and vertical drift properties, thereby enabling Scanning Tunneling Spectroscopy (STS) for localized measurements of electronic properties with high spatial resolution. This enhancement also allows for the examination of intricate molecular systems using very low imaging currents in the pA range. Subsequently, utilizing the improved microscope, we explore two-dimensional conjugated organogold networks. As a result, the networks were synthesized by debromination of a tetra-brominated thiophene rich precorsor on iodine-passivated Au (111) surfaces promoted the formation of highly regular 2D structures. Additionally, Density Functional Theory (DFT) calculations, supported by STS, reveal a relatively small electronic band gap of approximately 1.0 eV in the organogold networks, attributed to their high p-conjugation.

The customary solvents employed to study the self-assembly of supramolecular monolayers at liquid-solid interfaces play a crucial role in understanding kinetics and thermodynamics. Variable temperature experiments conducted by STM serve as the experimental cornerstone for acquiring such knowledge, specifically monitoring the reversibility and irreversibility of monolayer structures. Therefore, during the initial investigation, it was observed that upon heating to

temperatures where the supramolecular monolayers were desorbed and subsequent cooling to room temperature, the monolayers failed to fully restore as anticipated. Consequently, the comprehensive use of multiple techniques consistently indicated that solvent intercalation was the origin of the changes in graphite's ability to serve as a substrate for monolayer self-assembly.

Later, iodine-passivated Au (111) surfaces constituted a viable alternative for fundamental studies of monolayer self-assembly at liquid-solid interfaces as explored by variable temperature STM experiments. Here, an immersion STM (I-STM), which was utilized to prolong the experiment duration by operating within the solution and addressing challenges such as solvent evaporation and ensuring temperature stability, was employed to study molecular self-assembly at a liquid-solid interface. The study indicated that different polymorphs appear on two substrates, graphite and I−Au(111), with lower molecular packing densities but stronger hydrogen bonding on I−Au(111), which demonstrated noticeable substrate effects.

Chapter 1

Introduction

Supramolecular self-assembly is a fascinating and complex phenomenon in chemistry, where molecules and molecular entities come together through interactions to form larger, organized structures.[4,5,6] This fascinating study area has received significant attention in recent decades due to its critical role in various scientific disciplines, including chemistry, biology[7,8], materials science, and nanotechnology.[9,10]

Unlike traditional chemical reactions that involve the breaking and formation of covalent bonds, supramolecular self-assembly relies on non-covalent interactions such as hydrogen or halogen bonding, van der Waals forces, and electrostatic interactions. These interactions allow for the spontaneous organization of molecules into well-defined, functional architectures, resembling nature's ability to build complex structures from simple building blocks. The relative weakness of the interactions would also facilitate bond reversibility, hence error correction, which yields more ordered structures.

The on-surface synthesis also represents a contemporary approach that advances the fabrication of atomically precise organic nanostructures directly on solid surfaces. This innovative technique harnesses the distinctive characteristics of surfaces to facilitate precise chemical reactions and assembly at the atomic and molecular scales, marking a departure from conventional liquid-based chemistry practices. The formation of nanostructures through the covalent bonding of monomers on solid surfaces, which is also hailed as a significant milestone in the field[11,12,13,14,] demonstrates exceptional mechanical, thermal, chemical, and electronic properties. Besides, more extended structures in 1D and 2D can be fabricated on surfaces that are intricate, if not impossible to make in solution. These remarkable attributes position covalent nanostructures as exceptionally promising candidates for a diverse array of nanotechnological applications, including electronics, sensors, and energy storage devices.[15]

The effective characterization of on-surface synthesized nanostructures necessitates the imperative employment of surface-sensitive and chemically sensitive methods. The predominant methods for such characterization are Atomic Force Microscopy (AFM), Scanning Tunneling Microscopy (STM), and X-ray-induced photoelectron spectroscopy (XPS) as a chemically more sensitive approach to verifying chemical changes, which are capable of resolving nanostructures. Furthermore, a combined Scanning Tunneling Spectroscopy (STS) measures the local electronic

properties with high spatial resolution. In this thesis, STM and STS are the primary techniques used for measurements and analysis, and the underlying theoretical principles are discussed in Chapter 2.

The initial endeavor to comprehend surface-supported nanostructures involves the identification of key parameters that contribute to the development of molecular nanoarchitecture. Accordingly, Chapter 3 offers a concise summary of molecule-surface and intermolecular interactions. This section also provides insight into supramolecular self-assembly, encompassing a discussion on-surface synthesis.

Previously, our research group developed an STM, which was integrated with a flow cryostat and embedded in a double-walled radiation shield housing inside an Ultra-High-Vacuum (UHV) condition, enabling the investigation of nanostructures on solid surfaces with high-resolution imaging at liquid nitrogen temperatures. For STM characterization, achieving submolecular precision in intricate molecular systems requires very low imaging currents and optimized drift properties of the microscope. Consequently, the earlier version of the instrument, due to the lack of temperature stability, led to a thermal gradient across the STM and caused thermal drift. Therefore, the primary goal in meeting the strict temperature stability requirements for performing high-quality tunnel spectroscopy was optimizing the heat flow to and within the core of the STM.

Chapter 4 includes details on the optimization of a high-stability cryogenic STM using a flow cryostat. Critical improvements have been implemented to achieve temperature stability requirements, especially for tunneling spectroscopy measurements, which involve a systematic approach to minimize thermal drift through material substitutions, mechanical modifications, and the establishment of docking stations for thermally anchoring wires.

The formation of strong bonds leads to irreversibility, and the resulting lack of dynamic error correction on-surface synthesis of regular 2D polymers by dehalogenative couplings still remains challenging.[16] On the other hand, the covalent bonds are desirable because they endow the molecular networks with much sought-after properties such as robustness and electronic conjugation. Moreover, regular structures, i.e., crystalline materials, are advantageous because of their well-defined structure-property relationship, which is expressed in the emergence of an electronic band structure. In Chapter 5, by utilizing the optimized STM, the dehalogenative coupling of a tetra-bromine-substituted thiophene-rich monomer on an iodine-passivated Au(111) surface is presented, which yields highly regular 2D networks. While on pristine Au(111), only irregular structures were obtained. The main aspect of synthesizing the highly 2D network was utilizing a partially passivated Au(111) surface with an adsorbed monolayer of iodine (I-Au(111)). This demonstrated the role of the iodine monolayer by allowing debromination activation through

direct contact with the Au(111) metal surface, besides inducing the reversibility of carbon-Au-carbon bonds, thus facilitating dynamic error corrections. Remarkably, organogold networks with carbon-Au-carbon bonds emerged instead of the expected carbon-carbon-bonded networks. However, the organogold networks are highly stable and π-conjugated, as shown by DFT calculations and confirmed by STS.

In addition to the two-dimensional on-surface synthesis of covalent and organometallic networks, our research has also employed the STM-based exploration of molecular self-assembly at liquid-solid interfaces. Traditionally, these experiments rely on substrates that are atomically flat, chemically inert, and electrically conductive. The consequence is that almost all experiments are carried out using graphite. Besides, previous studies have meticulously examined the role of solvent properties, solute concentration, and temperature in shaping the kinetics and thermodynamics of monolayer formation, underscoring their pivotal role in determining structural outcomes. Nevertheless, a predominant concentration of experiments on highly inert graphite surfaces has neglected the profound influence of the underlying surface.

However, chapter 6 explains particular challenges and pitfalls that are associated with such approaches. In this chapter, customary solvents employed to study the self-assembly of supramolecular monolayers at liquid-solid interfaces induce degradation in graphite substrates at higher temperatures. The degradation effect was reversible through high-temperature annealing in a vacuum. In addition, strongly adsorbing hydrogen-bonded monolayers of trimesic acid (TMA) have been effectively determined as kinetically hindering solvent intercalation and thus protecting the graphite substrate. Subsequently, in the heptanoic acid solvent (7A) and terephthalic acid (TPA) on graphite substrate (HOPG), the anticipated reduction in molecular coverage with increasing temperature has been observed. However, intriguingly, the full restoration of the TPA monolayer after cooling to room temperature was not achieved, as evidenced by STM imaging, which revealed only an empty surface.

Moreover, in Chapter 7, Au(111) passivated with a monolayer of chemisorbed iodine (I-Au(111)) has also been introduced as a promising alternative for fundamental studies in liquid-solid STM experiments. Employing aromatic homologues of tricarboxylic acids as a versatile model system, a direct comparison between graphite and I-Au(111) has been conducted, shedding light on the decisive impact of molecule-surface interactions. As a result, three instances of a novel substrate-mediated polymorphism on I-Au(111) have been unveiled, which indicated clearly diminished molecule-surface interactions with lower packing density and optimized intermolecular binding. Further, to validate this hypothesis, we delved into the monolayer's thermodynamic stability through variable temperature STM experiments, utilizing a home-built STM specifically

designed for prolonged studies in liquid environments at elevated temperatures has been employed.[17]

Chapter 2

Theory and Experimental Methods

2.1 Scanning Tunneling Microscopy

2.1.1 Introduction

In science and technology, there is a noticeable shift toward exploring the nanoscale and even down to the atomic level. A prime example is the ongoing transformation in the field of electronics, where we are witnessing a transition from conventional microelectronics to nanoelectronics. Furthermore, this move to the atomic scale is motivated by a fundamental understanding of material properties, which are inherently defined by atomic structures.

In this context, Scanning Probe Microscopy (SPM) stands out as an outstanding tool for nanoscale research that, unlike other techniques, not only records atomically resolved real space images but also has the unique capability to manipulate atoms.[18] In SPMs, localized interactions with the apex atoms of a probe are employed to precisely detect local characteristics at a surface or interface. By systematically scanning across the surface, these detected properties can be mapped and typically interpreted as an image.

This chapter provides an overview of the principles underlying both microscopic and spectroscopic techniques, accompanied by their respective theoretical foundations.

2.2 Scanning Tunneling Microscopy (STM) Principle

In 1981-1982, Binnig and Rohrer developed the Scanning Tunneling Microscope (STM), who received the Physics Nobel Prize in 1986 for their groundbreaking work.[19] The STM, as a subcategory of SPMs, emerges as a remarkable tool that is operated in real space and visualizes surface topographies.[20,21] Within the domain of surface science, the STM proves to be a potent instrument for investigating molecular structures and detecting local properties with atomic-level precision.[22,23,24]

Besides, its exceptional resolution and sensitivity to the electronic structure of the adsorbate-surface system further enhance its analytical capability.

STM can be employed in diverse settings, including but not limited to ambient conditions[25], vacuum[26], high-pressure environments[27,28], and even liquids[29], providing details of the intricate molecular structures on the surface. Additionally, STM is versatile in terms of temperature, capable of functioning at temperatures ranging from millikelvin (mK)[30] to extremely high temperatures exceeding 1000 K.[31]

Figure 2.1 illustrates a schematic principle of an STM employing a sharp metal tip as a probe. In this setup, a voltage is applied between the tip and an electrically conductive sample. The tip is brought extremely close, i.e., < 1 nm, to the sample surface until an electric current begins to flow. Just before the tip and sample make direct contact, a current, known as the tunneling current, becomes detectable. This occurs at distances between the tip and sample of approximately 0.5–1 nanometer. Notably, the tunneling current increases exponentially as the tip-sample distance decreases. Due to the extraordinary sensitivity of the tunneling current and the tip-sample distance, this characteristic can be utilized to achieve an excellent vertical resolution that also translates into the capability for atomic lateral resolution.

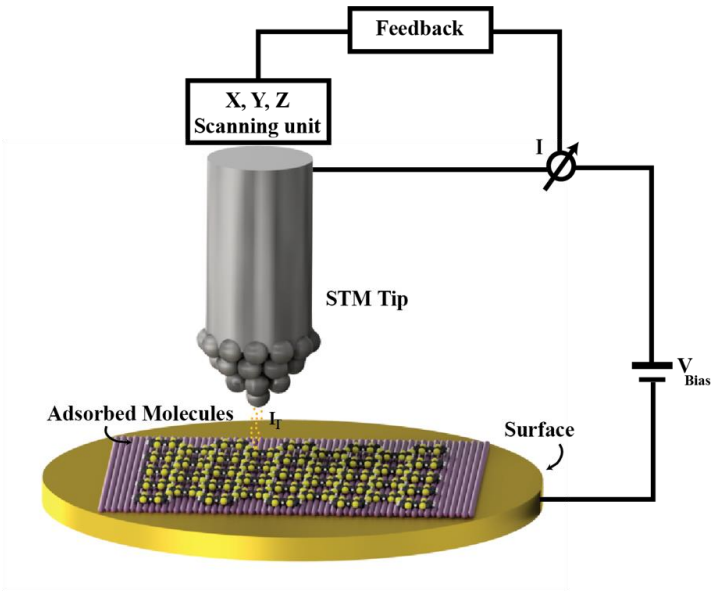

Figure 2.1 A schematic principle of a scanning tunneling microscope (STM). Molecules adsorbed on a surface are probed by the STM tip. V_{Bias} is applied between the sample and STM tip and gives rise to a tunneling current that is kept constant by Feedback while scanning the sample.

As the tip scans across the surface along the x-y directions, a feedback system continually adjusts the tip's height, either moving the tip closer or farther away, such that a constant tunneling current is maintained. Consequently, when the tip approaches an elevated area during the scan, the tunneling current increases due to the reduced distance between the tip and the sample. In response, the feedback circuit retracts the tip to sustain a steady tunneling current. By recording the feedback signal, which represents the tip's height, as a function of its lateral position, a map or image of the tip's height is generated. This often corresponds to the surface topography of the studied sample.

2.3 Theoretical Background

2.3.1 One Dimensional Tunneling Junction

This section introduces fundamental concepts of tunneling through a one-dimensional potential barrier, which provides insights into the STM's fundamental theoretical principles. In classical mechanics, an electron subjected to a potential U(z) is defined by:

$$\frac{p^2}{2m} + U(z) = E \tag{2.1}$$

"m" represents the electron's mass, and E stands for energy. When the energy E > U(z), the electron has a nonzero momentum of $\mathrm{p} = [2\mathrm{m}(\mathrm{E} - \mathrm{U})]^{1/2}$. Conversely, the electron cannot enter any area where E<U(z), which indicates the presence of a potential barrier. (Figure 2.2a)
In quantum mechanics, probabilities of finding an electron are expressed by the absolute square of the wavefunction, which can be calculated by the Schrödinger equation:

$$-\frac{\hbar^2}{2m}\frac{d^2}{dz^2}\psi(z) + U(z)\psi(z) = E\psi(z) \tag{2.2}$$

And $\hbar$ is the reduced Planck constant.
In the classically allowed region where E > U, Equation 2.2 will have a solution of:

$$\psi(z) = \psi(0)e^{\pm ikz} \tag{2.3}$$

where k is the wave vector.

$$k = \frac{\sqrt{2m(E-U)}}{\hbar} \tag{2.4}$$

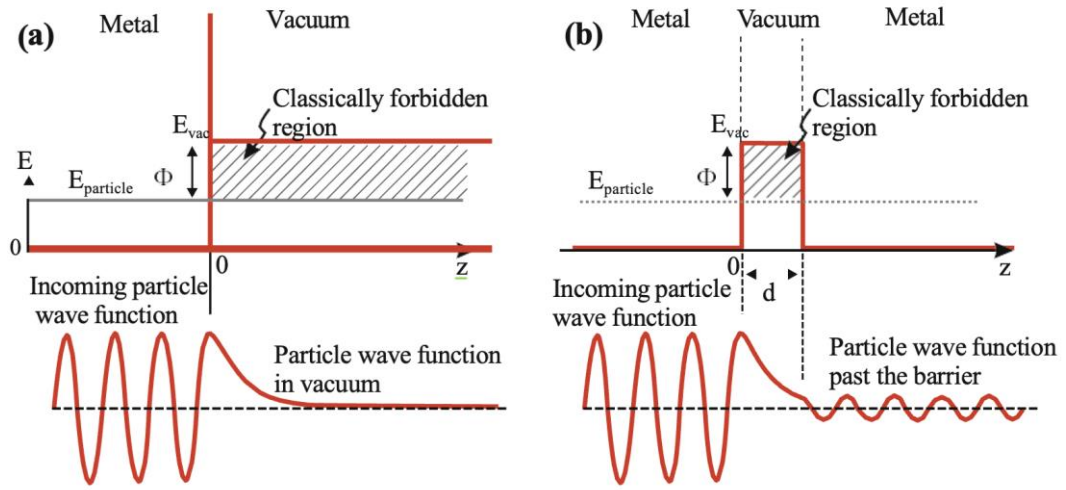

Figure 2.2 Metal-Vacuum-Metal model of classical vs. quantum mechanics regarding the behavior of particles when encountering a potential barrier. The top graph in (a) shows a one-dimensional potential diagram with a potential step between a solid and a vacuum. The step height is the metal's work function. The exponentially decaying wave function in the classically forbidden vacuum region is illustrated in the lower graph. In section (b), The upper graph displays a finite potential barrier as the model for a metal-vacuum-metal configuration with the vacuum gap width d forming a potential barrier. The lower graph shows the electron wave function, which is a harmonic plane wave on both metal sides and an exponential decay inside the barrier. Adapted and modified after ref. 34

Here, according to the classical case, electrons move with a constant momentum $\mathrm{p} = \hbar k$ or $\mathrm{v} = \mathrm{p}/\mathrm{m}$ (a constant velocity).

While in the non-classical region, Eq. 2.2 has a solution of:

$$\psi(z) = \psi(0)e^{-\mathcal{K}z} \tag{2.5}$$

And represents the exponentially decaying wave function inside the barrier, where $\mathcal{K}$ (*Koppa*) is the decay constant.

$$\mathcal{K} = \frac{\sqrt{2m(U-E)}}{\hbar} \tag{2.6}$$

The probability density of detecting an electron near a point z is proportional to:

$$|\psi(0)|^2 e^{-2\mathcal{K}z} \tag{2.7}$$

which maintains a nonzero value within the barrier area. As a result, there is a nonzero probability of the electron passing through a thin barrier and not too high. (Figure 2.2b)

Figure 2.2 illustrates the basic diagram of the difference between classical and quantum mechanics regarding the behavior of particles when encountering potential barriers. In classical mechanics (Figure 2.2 a), particles cannot pass through these barriers and leave the metal to vacuum level Evac. In contrast, quantum mechanics (Figure 2.2b) introduces the concept of a finite

probability for particles, where the particles can penetrate and tunnel into the region with a potential barrier that is higher than the particle's energy.

The metal surface work function, $\emptyset$ (eV), is the minimum required energy to displace an electron from the metal bulk to the vacuum level. In general, the work function depends on the material as well as the surface crystallographic orientation. The Fermi level (E_F) also represents the upper boundary of occupied states within a metal (at zero Kelvin). By considering the vacuum level as the reference energy point, $E_F = -\emptyset$, and assuming both the tip and sample have the same work function, electrons within the sample can tunnel into the tip and vice versa.

Applying a bias voltage V will initiate a tunneling current. Accordingly, a sample state ψ_n with an energy level of E_n, between E_F - eV and E_F, has the possibility to tunnel into the tip. When the bias voltage remains considerably smaller than the work function, $eV << \emptyset$, all relevant sample states are close to the Fermi level $E_n \approx -\emptyset$. Here, a transmission coefficient, T, can be described as a ratio between the tunneling current at the tip's surface z and the current at z = 0.

$$T \equiv \frac{I(z)}{I(0)} = e^{-2\mathcal{K}z} \tag{2.8}$$

$$\mathcal{K} = \frac{\sqrt{2m\emptyset}}{\hbar} \tag{2.9}$$

$\mathcal{K}$ (1/nm) is the decay constant of a sample state near the Fermi level within the barrier region and $U-E=\emptyset$. (The transmission coefficient T is an approximation and does not represent the exact solution)

In summary, the one-dimensional barrier model is a straightforward explanation to describe the exponential dependency of tunneling current to the distance of the tip-sample by highlighting the vertical sensitivity of the STM. However, importantly, this simple model is an approximation and not an exact model to define the STM characterization and actual electronic structures.

2.3.2 The Density of States:

The distribution function ρ(E), known as the density of states (DOS), characterizes the number of electronic states within a system found in the interval from E to E + dE. The DOS plays a crucial role in understanding the electronic properties of materials and influencing phenomena such as electrical conductivity and thermal behavior. The number of states within a specific energy range, from E_1 to E_2, can be expressed as:

$$N(E_1, E_2) = \int_{E_1}^{E_2} \rho\,(E)dE \tag{2.10}$$

The local density of states (LDOS) is also determined by measuring the probability of a particle at a specific position, r.

$$LDOS = \rho(E,r) = \sum_{n} |\psi_n(r)|^2 \delta(E - E_n) \quad (2.11)$$

Where δ denotes the Dirac delta function.

2.4 Bardeen Metal-Insulator-Metal Model

As a simple interpretation, the STM image indicates the surface topography of the sample. However, the meaning of the term "topography" in the atomic scale becomes unclear. One plausible model implies that a topographic image is a depiction of the STM tip tracking the *LDOS* at the Fermi level under small bias voltages.

Bardeen's first-order perturbation theory is the prevalent theory that is employed to explain tunneling in both solid materials and STM.[32,33] Bardeen formulated a model for tunneling in solids before the invention of the STM, with a focus on tunneling in metal-insulator-metal tunneling junctions. His approach involved treating the tip and the sample as two distinct systems that are weakly interacting through a barrier. The electronic states of these subsystems can be determined by solving the stationary Schrödinger equation for each. In the simplified one-dimensional case, the solutions are harmonic wave functions with different energies and an exponentially decaying tail inside the barrier.

Consequently, the transition (scattering) from the initial (tip) states to the final (sample) states is evaluated using time-dependent perturbation theory, and an electron initially in a tip state can scatter (or be transferred) into a sample state.

When a positive voltage is applied to an electrode, it reduces the energy of that electrode. Conversely, in the opposite scenario, a negative voltage applied to an electrode causes an upward shift in the energy levels (it is unfavorable for electrons to hop onto a negatively biased electrode). Additionally, the analysis considers the zero-temperature limit, where all electronic states are occupied up to the Fermi level of either the tip or the sample and remain unoccupied for higher energies. This implies that tunneling or scattering from one electrode can only occur within the bias window delineated by $E_{F,sample}$ and $E_{F,tip}$.[34]

In Bardeen's methodology, the calculation of the transition rate from one electrode to the other involves employing an assumption of weak coupling between the two electrodes. This calculation relies on specifically considering a variant of Fermi's golden rule, which outlines the particle transition probability in a perturbed system over time. In the tunneling case, Fermi's golden rule indicates that the scattering from a specific initial tip state (i) at energy level $E_{tip,i}$ to a particular final

sample state (f) at energy level $E_{sample,f}$ given by : (expressed as the number of electrons per unit of time) [34,35]

$$w_{tip,i\rightarrow sample,f} = \frac{2\pi}{\hbar}\left|M_{fi}\right|^2 \delta(E_{sample,f} - E_{tip,i}) \quad (2.12)$$

Where the matrix element M_{fi} is:

$$M_{fi} = \frac{\hbar^2}{2m} \int_{S_{tip/sample}} \left[\psi_{tip,i}(r)\,\nabla\psi^*_{sample,f}(r) - \psi^*_{sample,f}(r)\,\nabla\psi_{tip,i}(r)\right].dS \quad (2.13)$$

The presence of the Dirac delta function in Eq 2.12 indicates that the energy of the final state should be the same as the energy of the initial state, which is consistent with the principle of energy conservation.

To determine the overall rate of transfer from any initial state to any final state, a summation across all pairs of initial and final states is required.

$$w_{tip\rightarrow sample} = \frac{2\pi}{\hbar}\sum_{i,f}\left|M_{fi}\right|^2 \delta(E_{sample,f} - E_{tip,i}) \quad (2.14)$$

As a result, the current would be the multiplication of the transition rate $w_{tip\rightarrow sample}$ with the electron charge considering factor two for the spin degeneracy.

$$I = \frac{4\pi e}{\hbar}\sum_{i,f}\left|M_{fi}\right|^2 \delta(E_{sample,f} - E_{tip,i}) \quad (2.15)$$

The tunneling current variation with tunneling voltage depends on the summation over energy states that needs to be approximated by an integral across the density of states for both the sample (ρ_{sample}) and the tip (ρ_{tip}). (Figure 2.3) Furthermore, a general term is considered as individual work functions for both the sample (Φ_{sample}) as well as the tip (Φ_{tip}). Therefore, in a one-dimensional approximation, the matrix element can be substituted with a transmission factor $|M_{fi}|^2 = T(\Phi, d)$. It's important to note that this approximation is valid only for rectangular potential barriers, whereas more real STM junctions typically have a trapezoidal shape. Nevertheless, this approximation is commonly employed, given the relatively small thicknesses of barriers encountered in practice. [3,34]

As a result, the tunneling current would be:

$$I = \frac{4\pi e}{\hbar}\int_0^{eV} \rho_{tip}(\varepsilon - eV)\rho_{sample}(\varepsilon)\,T(\varepsilon, V, d)\,d\varepsilon \quad (2.16)$$

And,
$$T(\varepsilon, V, d) \propto \exp\left[-2d\sqrt{\frac{2m}{\hbar^2}\left(\frac{\Phi_{tip}+\Phi_{sample}}{2} + \frac{eV}{2} - \varepsilon\right)}\right] \quad (2.17)$$

Where T is the transmission factor, and ε is the energy of the tunneling electron.

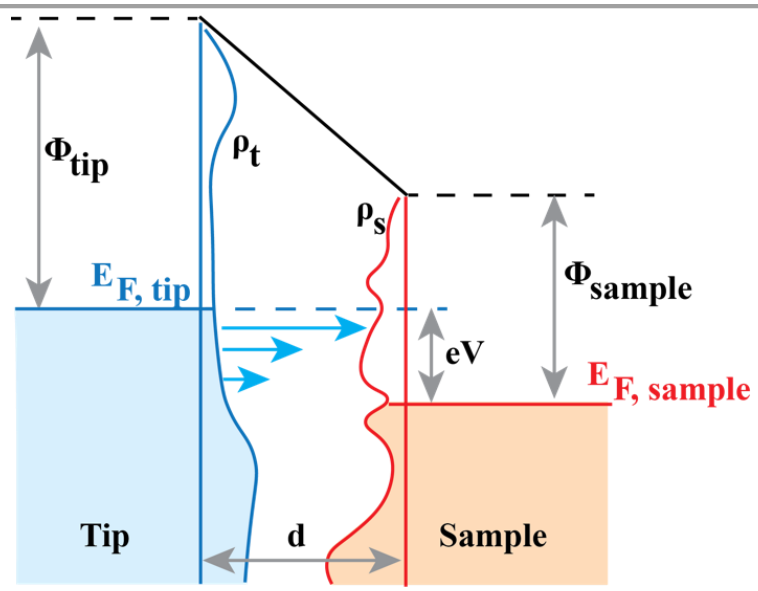

Figure 2.3 Bardeen tunneling model. The energy level diagram illustrates the tunneling junction, where the applied bias causes a shift in the Fermi level by eV. The density of states is depicted by ρ_{tip} and ρ_{sample}, with colored regions representing filled states. Adapted from Scanning probe microscopy (Springer, 2015) [34]

Applying a positive bias voltage results in a tunneling current moving from the occupied states of the tip to the unoccupied states of the sample. The unoccupied states in the sample are shifted downward by eV relative to the Fermi level of the tip. It is reasonable to assume that the contribution to the tunneling current at a specific energy is proportionate to the density of occupied states in the tip and the density of unoccupied states in the sample.

The general Bardeen equation for tunneling current is subjected to specific approximations for further evaluation. The Tersoff-Hamann approximation, which is commonly used, assumes a negligible tunneling voltage, allowing the simplification of the matrix element's energy dependence and the densities of states' energy dependence. This approach prioritizes a realistic consideration of the spatial variations in surface wave functions. Additionally, the Tersoff-Hamann model assumes a simple spherical s-wave for the tip wave function. This approximation results in a straightforward relationship between surface wave functions and tunneling current, making it helpful in simulating STM images based on specific surface structure models.[36,37]

2.5 STM Operation Modes

The movement of the tip in STMs is precisely achieved by piezoelectric systems. Initially, a piezo actuator facilitates accurate vertical positioning by approaching the tip towards the sample in the z-axis within tiny steps, which is controlled by feedback control. Additionally, a tube piezo, commonly utilized in the majority of STMs, is employed to raster scan the sample surface.

STM offers different operational modes. It can operate in the Constant Current Mode (CCM), where an electronic feedback system ensures a stable tunneling current while the tip scans across the x-y plane of the sample's surface. Variations in height are also measured with respect to the z-axis, generating an image that is determined by a combination of geometric and electronic factors. (Figure 2.4a)

Conversely, the STM can also operate in the Constant Height Mode (CHM). In this mode, the feedback loop maintains a constant height relative to the sample's surface on average. At the same time, the tunneling current's variations are recorded for the different positions within the x-y plane. (Figure 2.4b)

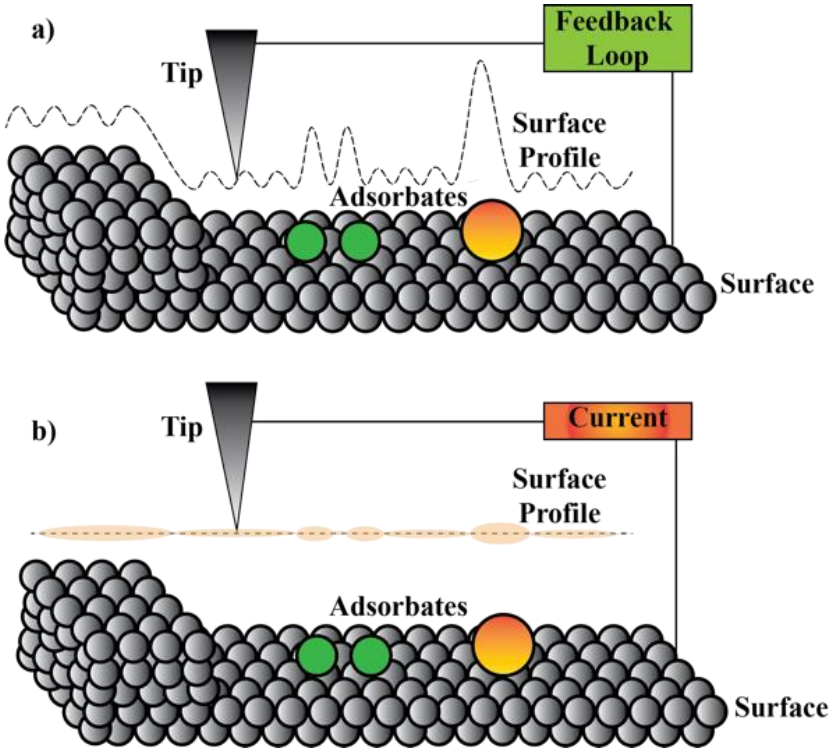

Figure 2.4 Schematics explanation of two STM operation modes: (a) constant current and (b) constant height

2.6 Scanning Tunneling Spectroscopy

2.6.1 Principal of Scanning Tunneling Spectroscopy

Often, the STM contrast in high-resolution images exhibits a strong dependency on the applied bias voltage polarity. [3, 34] Adjusting the voltage, whether positively or negatively, significantly impacts the quality and resolution of the resulting image, whether recorded from occupied or unoccupied electronic states of the sample.

While this bias-dependent tunneling current can pose challenges in terms of STM image interpretation, it holds interesting information on the electronic properties of the sample that can be

measured by tunneling spectroscopy. In combination with STM, STS investigates the electronic structure of the sample.

2.6.2 STS Measurement Techniques

The STS measures the density states of the sample by examining the current-to-voltage characteristics, specifically on how the tunneling current changes with variations in bias voltage across the tunneling junction.

There are various spectroscopic techniques that can be employed in the STM. One of those involves the measurement of dI/dV while maintaining either constant height or constant (average) tunneling current. In practical terms, an STS spectrum, which represents the differential conductance, is obtained by positioning the tip over a specific lateral location on the surface as chosen in a previously recorded STM image while applying certain tunneling parameters I and V to define the tunneling gap. Subsequently, the feedback loop is deactivated, ensuring that the tip-sample distance remains constant during spectrum acquisition, and the dI/dV signal is required as a function of bias voltage, which is ramped across the range of interest.

STM is typically characterized as a non-AC (direct current) technique. Therefore, for the STS measurements, an alternating current (AC) modulation voltage ($V_M \cos \omega t$) is generated by an oscillator and added to slowly sweep the primary bias voltage, and the resulting total bias voltage is applied to the sample. By adding the oscillator reference frequency for first derivative measurements and introducing a phase shift for compensation, the reference signal is multiplied by the tunneling current's voltage. Additionally, the band-pass-filtered output corresponds to control of the derivative of the I-V curve. (Figure 2.5)

$$I(t) = f(V + V_M) \cos \omega t \tag{2.18}$$

In principle, increasing a small voltage increment by superimposing a harmonic modulation on the bias voltage with amplitude dV causes a downward shift in all sample states and results in modulation of the tunneling current with dI.

The additional current, dI, for a voltage increase dV = dε/e, can be calculated by the integrand in Eq 2.16 at the upper limit of the integral, ε = eV as:

$$\frac{dI}{dV} \approx \frac{4\pi e^2}{\hbar} \rho_{tip}(0) \rho_{sample}(eV)\, T(eV, V, d) \tag{2.19}$$

In the simplest approximation, the density of states of the tip and the transmission factor are presumed to be voltage-independent. Consequently, the differential conductance is directly proportional to the energy-dependent local density of sample states.

$$\frac{dI}{dV} \propto \rho_{sample}(eV) \tag{2.20}$$

Accordingly, the differential conductance, dI/dV, quantifies the DOS of the sample at an energy level of eV relative to the sample Fermi energy.

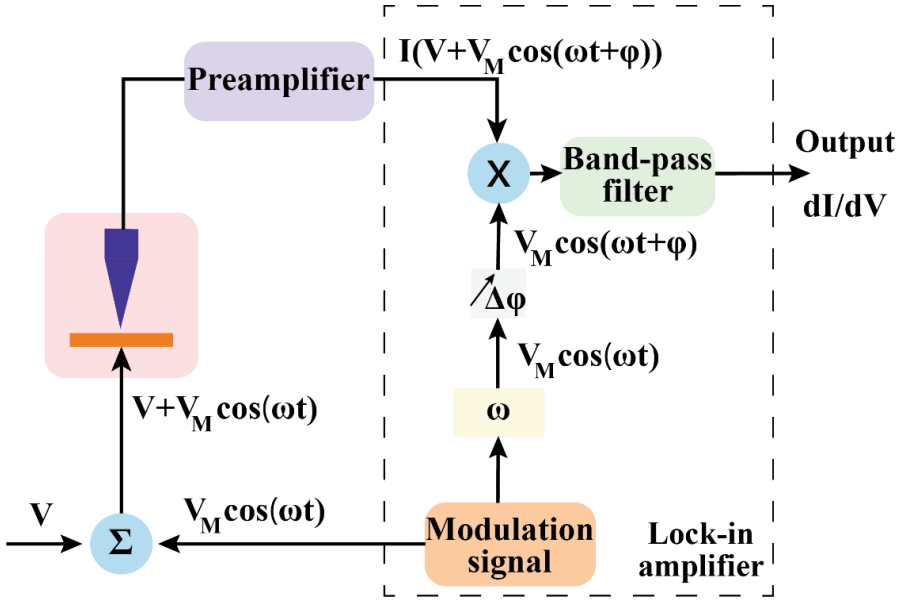

Figure 2.5 Experimental setup for the first derivative of the I-V curve utilizing the lock-in technique. Adapted from Scanning probe microscopy (Springer, 2015) [34]

A slow scan of voltage allows measuring the first derivative dI/dV using a lock-in amplifier as a function of voltage. Lock-in detection with long averaging times provides a good signal-to-noise ratio. However, long-time measurements increase the drift properties since the influence of drift becomes larger as the measurement time increases and changes the tip-sample distance, which affects the current measurement. While the lock-in technique requires substantially more time for measuring a signal as compared to simply measuring current vs. voltage curves (for instance, lock-in measurement might require on the order of tens of seconds to complete, while I(V) curves can be recorded in seconds), the numerically calculating the derivative is generally associated with a lot of noise, and therefore, heavy averaging is required. Consequently, the lock-in technique offers superior noise reduction and signal recovery.

2.7 STM Operation Mechanism

2.7.1 Piezoelectric Effect

The piezoelectric effect is the property of certain ceramic materials to yield an electric surface charge when mechanical stress is applied. These materials are used in various technical applications, such as sensor technology. Conversely, when an electric voltage is applied to a piezoelectric material, it induces deformation in the crystal, known as the inverse piezoelectric

effect. This effect allows for miniature deformation movements on a continuous scale, even smaller than the diameter of an atom.

Quartz is an instance of a piezoelectric material. Another example commonly used for piezoelectric actuators is lead zirconate titanate (Pb[ZrxTi1−x]O3) (PZT) ceramics, which exhibit both piezoelectric and ferroelectric properties.

In SPMs, the precise tip positioning and scanning of the sample surface are achieved by utilizing piezoelectric elements that extend or retract in direct response to the applied voltage applied to electrodes. This enables fine movement of the tip's position with sub-ångström precision in three dimensions along the x, y, and z axes.

2.7.2 Piezoelectric Actuators Extensions

When an electric voltage ΔV is introduced to a cubic shape piezoelectric material (Figure 2.6a) with dimensions x, y, and z and poled along the z-direction, the external electric field due to the plate capacitor is: (The voltage is applied to metallic electrodes that are added to piezo ceramics, and since the piezo ceramic is a dielectric, it basically becomes a plate capacitor.)

$$\varepsilon_3 = {}^{\Delta V}/_{z} \tag{2.21}$$

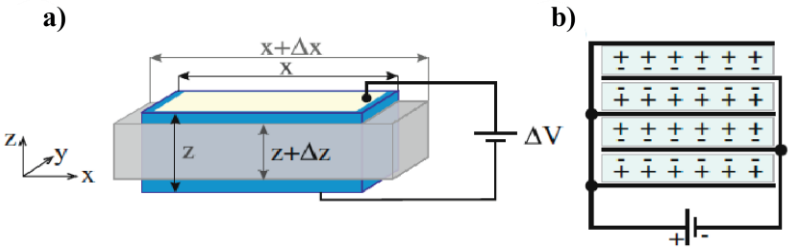

Figure 2.6 a) A schematic of a piezoelectric plate with dimensions x, y, and z, poled along the z-axis. It shows the longitudinal piezoelectric effect. Applying a voltage V in the z-direction generates an electric field in the same direction, resulting in a strain denoted as Δz along the z-axis. Applying a voltage in the z-direction, due to the transverse piezoelectric effect, also induces strains both in the x-direction and the y-direction. In this case, the piezo constant (The piezo constant represents the measure of the piezoelectric effect in a material and describes the relationship between applied mechanical stress and the resulting electric polarization within the material. When mechanical stress is applied to a piezoelectric material, it generates an electric charge, and the piezoelectric constant quantifies this relationship.) is directly proportional to the length "x" of the plate. b) In the longitudinal piezoelectric effect, the piezo coefficient remains unaffected by the thickness "z" of the plate. Therefore, to enhance the piezo constant, multiple plates on top of each other should be stacked. Adapted from Scanning probe microscopy (Springer, 2015) [34]

The spatial coordinates x, y, and z are often labeled as 1, 2, and 3, respectively. When a piezoelectric plate undergoes deformation in the z-direction with a thickness of z, the strain in that direction is represented as:

$$S_3 = \Delta z / z \tag{2.22}$$

The relationship between mechanical strain in a piezoelectric material and the applied electric field is governed by the piezoelectric coefficients, acting as constant factors at the constant temperature. Piezoelectric coefficients, which are intrinsic material properties, describe the mechanical strain or deformation to the resulting electric field or voltage, or vice versa, and are a tensorial quantity, meaning that they vary depending on both the direction of the applied electric field and the direction in which the strain is considered. Specifically, they are expressed as the ratios of strain components in a particular direction to the corresponding component of the applied electric field.

For example, the longitudinal piezo effect would be:

$$d_{33} = {}^{S_3}/_{\varepsilon_3}, and\ d_{31} = {}^{S_1}/_{E_3} \tag{2.23}$$

Where the orientations of strain components in x, y, and z are often labeled as 1, 2, and 3, respectively, and E is the applied electric field.

2.7.3 Stack Piezo Actuator

The practical approach to enhance the extension length per voltage is to stack multiple piezo plates atop each other. This way, applying a moderate voltage to thin layers results in an amplified electric field, and consequently, the total accumulating of parallel extension leads to a desired travel, i.e., micrometer (µm) range. (Figure 2.6b).

In this configuration, adjacent plates must be poled in opposite directions such that the extension is in the same direction. This configuration is commonly referred to as a "piezoelectric stack actuator." The total displacement achieved is the cumulative sum of the displacements exhibited by the individual piezo plates.

The piezo constant for motion along the x-axis is as follows:

$$\frac{\Delta x}{\Delta V} = d_{31}\frac{x}{z} \tag{2.24}$$

d_{31} is the piezoelectric coefficient, which is defined as a ratio of strain components S_1 over the applied electric field component E_3.

2.7.4 Tube Scanner

The tube piezo, commonly referred to as a tube scanner, is the by far most prevalent actuator type for fine scanning motion in SPMs. Scanner tube piezo achieves precise positioning of the probe tip on the sample with an accuracy of less than an ångström in all three dimensions. The tube scanner is made of inner and outer covered metal electrodes, which are poled radially. The outer electrode is partitioned into four quadrants, as depicted inFigure 2.7. To achieve motion along the

longitudinal axis (z-direction), a voltage is applied between the inner and all outer electrodes. Conversely, deflection in the xy-direction occurs by applying voltages of opposite polarity to the two opposing outer electrodes. Due to the transverse piezoelectric effect, one segment of the tube elongates along the tube axis and the opposite segment contracts. This results in a bending of the upper part of the tube. For SPM scanning, the probe is also mounted axially on top of the tube scanner.

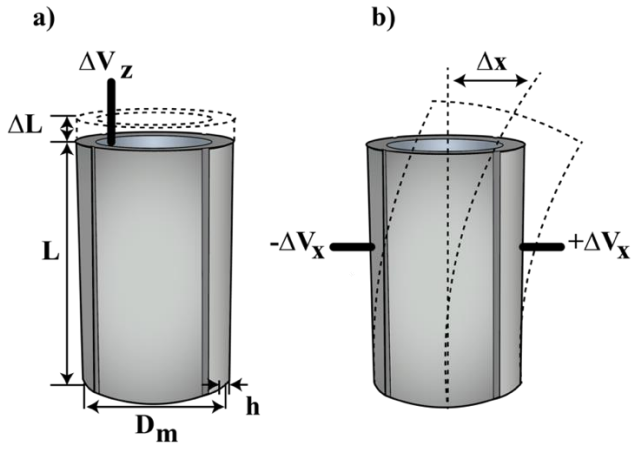

Figure 2.7 Schematic representation of the scanner tube. a) side view with extension in the vertical direction of z, b) movement in x direction. Adapted and modified from Scanning probe microscopy (Springer, 2015)[34]

The vertical displacement on top of the tube piezo is given by:

$$\Delta L = \Delta z, \quad and \quad \frac{\Delta z}{\Delta V} = d_{31}\frac{L}{h} \tag{2.25}$$

Further, to calculate the lateral displacement, the bending angle should be assumed as the tube bends on a circular arc:

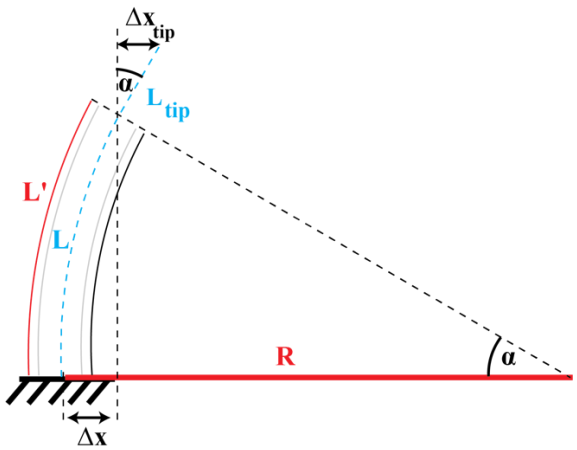

Figure 2.8 Schematic geometry of the bent scanner tube. Adapted from Scanning probe microscopy (Springer, 2015)[34]

The bending angle is:

$$\alpha = \frac{L}{R} \tag{2.26}$$

More sophisticated calculations consider non-uniform stress on the tube due to the bending result in:

$$\frac{\Delta x}{\Delta V} = \frac{2\sqrt{2} d_{31} L^2}{\pi D_m h} \tag{2.27}$$

Where D_m is the tube diameter, and $L' = L + \Delta L$.

If we consider the tip on top of the piezo tube, the total piezo constant for the lateral deflection would be:

$$\frac{\Delta x_{total}}{\Delta V} = \frac{2\sqrt{2}\, d_{31} L_{piezo}}{\pi\, D_m\, h} (L_{piezo} + 2L_{tip}) \tag{2.28}$$

2.7.5 Approach and Retract Mechanism

To establish a quantum mechanical tunneling current from the tip to the sample surface or vice versa, the tip must be positioned in remarkably close proximity to the surface of the sample with a gap < 1 nm, i.e., just a few atom diameters. This requirement necessitates the implementation of a very precise nano-positioning system. One of the most commonly used nano-positioning mechanisms is the slip-stick nano-positioner, which is employed for both the approach and retraction movements of the probe to the sample, as depicted in Figure 2.9.[38]

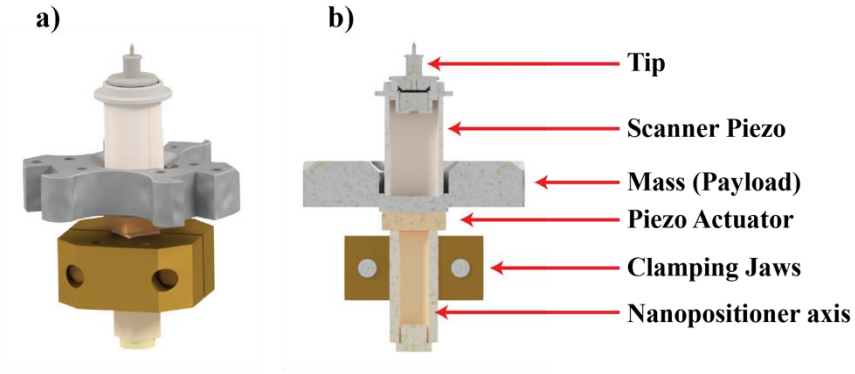

Figure 2.9 Scheme representation of the stick-slip nano positioner mechanism a) a full unit, b) a sectional view

The slip-stick nano-positioner relies on the principle of utilizing friction to achieve precise movements. It employs a multi-layered piezoelectric actuator that is firmly attached (glued) between a mass, known as the payload, and an axis securely clamped in place by two spring-loaded jaws with a defined force as adjusted by springs.

When an electrical signal is applied to the piezoelectric actuator, it generates a force that induces controlled deformations (elongation) in the actuator material. These deformations result in a displacement of the payload. Importantly, two spring-loaded clamping jaws apply a defined clamping force on the axis, creating frictional resistance between the axis and the payload.

As the piezo actuator deforms under the applied voltage and overcomes the static frictional force (albite, depending on the voltage slew rate); eventually, fast applied voltage changes lead to a "slip" motion. This is simply due to large acceleration, which is caused by the high inertial mass of the payload.

When the drive voltage of the stack actuator is altered or reversed, the spring-loaded clamps re-engage and re-establish static friction, resulting in a "stick" motion.

This slip-stick cycle enables precise and incremental movements of the nano-positioner in both the approach and retract directions with a defined step width (dependent on clamping force and voltage amplitude) on the order of 100 nm. (Figure 2.10)

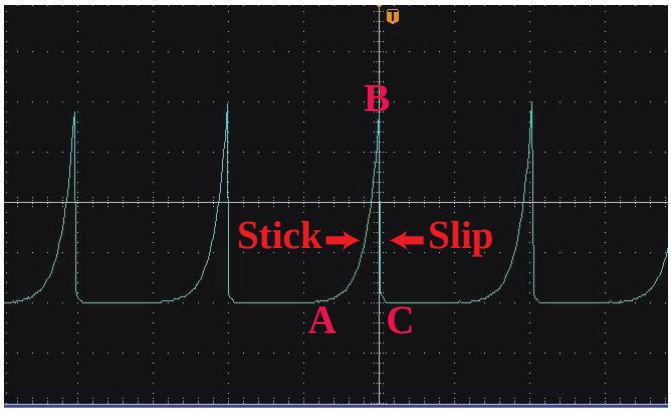

Figure 2.10 Exponential applied pulse voltage for a stick-slip nanopositioner.[39]

For a safe and especially efficient approach of the tip to the surface, an automated approach is used. This approach cycle evolves through several stages, which initially start with complete compression of the tube piezo actuator. Subsequently, the nano-positioner is activated to execute a predetermined number of steps toward the sample surface. It is critical to ensure that the total displacement directed by the nano-positioner remains within the bounds of the maximum Z-range of the tube piezo actuator.

Considering a large safety margin also reduces any potential collision risks between the tip and the sample. After the movement of the nano-positioner, the tube piezo actuator extends up to its maximum length. During this extension phase, the STM controller upholds a constant tunneling bias (V_{Bias}) between the tip and the sample, with the system continually monitoring the measured tunneling current (I_T).

If the tube scanner reaches its full extension during the expansion and the measured tunneling current remains below the desired setpoint current ($I_{T, set}$), it signifies that the tip is still too distantly from the sample and tunneling conditions are not achieved. In this case, it is essential to initiate a new approach cycle to bring the tip into closer proximity. This iterative process continues throughout the automated coarse approach until a tunneling current is detected and the measured tunneling current aligns with the setpoint current.

Chapter 3

On Surface Synthesis

3.1 Introduction

On-surface synthesis is a dynamic and versatile nanofabrication technique that has gained prominence in materials science and nanotechnology.[40] It involves the precise coupling of monomers into molecular structures directly on a substrate's surface, utilizing a range of chemical reactions, including covalent bonding.[41] This controlled fabrication method produces well-defined nanostructures with unique properties and functionalities, enabled by strong and irreversible covalent bonds, and essential for applications like molecular electronics, which require long-term stability.[23,42]

In on-surface synthesis, the initial stage often involves unreacted adsorbed molecules forming supramolecular self-assemblies held together by weak bonds like hydrogen or van-der-Waals interactions. While these structures are highly ordered, they show weak stability, which limits their practical applications. The primary goal of on-surface synthesis is to connect these molecules with strong covalent bonds while maintaining structural order; however, covalent bonds present challenges in creating defect-free structures.

Furthermore, on-surface synthesis enables efficient charge transport within the architected nanostructures. The direct connection between the molecules facilitates electron transfer and can lead to enhanced electrical conductivity. This feature is particularly advantageous in the development of electronic devices. [23,43]

Various interfaces have been established for surface-mediated synthesis, including solid-liquid[44] and solid-vapor[45] methods. The most popular approach involves depositing precursor molecules in a monolayer under ultra-high-vacuum (UHV) conditions, allowing reactions at the solid-vacuum interface. The choice of surface for these reactions is crucial. Therefore, the substrate's reactivity, symmetry, and electronic structure significantly influence the synthesis outcome.[46,47,48,49,50,51,52,53,54]

The field of on-surface synthesis continues to evolve rapidly, with ongoing research efforts focused on refining techniques, expanding the range of possible reactions, and exploring novel applications.

It holds great promise for advancements in various technological sectors, including molecular electronics, catalysis, and sensor development.

3.2 Supramolecular Self-assembly

Self-assembly is a fundamental process in which a supramolecular entity spontaneously bonds with similar or distinct entities, often resembling a straightforward convergence toward the desired assembled structure.[55,56] To comprehend self-assembly, one can assume individual molecules as building blocks, possessing the ability to locate and unite with their suitable counterparts in the final assembly.[55] Self-assembly phenomena are encountered across a broad spectrum of chemical systems, including crystal growth[57], the formation of liquid crystals[58,59], the synthesis of metal-coordinated complexes[60,61], and the arrangement of molecules on surfaces.[62]

The exploration of supramolecular self-assembly on surfaces involves the transformation of initially random molecular distributions into well-defined patterns, which manifest as ordered structures or otherwise are often characterized as irregular arrangements. This process is driven by non-covalent interactions, including metal-coordination bonds, π–π interactions, hydrogen bonds, and van der Waals forces.

The inherent reversibility of these bonds drives the self-assembled system towards its thermodynamic equilibrium, a state that can only be attained through numerous molecular rearrangements and reorientations. Achieving these dynamic processes depends on the capability of intermolecular bonds to undergo repeated cycles of breaking and formation, making surface self-assembly a complex interplay of molecular interactions and dynamic equilibria in a surface-confined environment, which holds significant implications in nanoscience and surface chemistry. However, the research and fundamental understanding of these reactions on surfaces often face challenges; for instance, metal surfaces that are commonly employed for catalytic purposes have difficulty preparing pristine atomically flat surfaces, which is a notable obstacle and necessitates meticulous preparation using Ultra-High Vacuum (UHV) equipment.

Thermodynamic equilibrium within a self-assembled system means they are simultaneously in thermal, mechanical, and chemical equilibrium. Additionally, when experimental systems are in UHV environments, it is reasonable to consider them operating under constant pressure (isobaric) and constant temperature (isothermal) conditions. Consequently, such systems naturally achieve mechanical and thermal equilibrium. However, it is crucial to emphasize that true thermodynamic equilibrium is attained only when there is an additional achievement of chemical equilibrium within the system. In this state of complete thermodynamic equilibrium, all three facets – thermal, mechanical, and chemical equilibria – harmoniously coexist.

With constant pressure and temperature, the chemical equilibrium occurs when Gibbs' free energy is minimized. In this context, for a thermodynamically stable final structure to form during the self-assembly process, the change in Gibbs free energy for the system must be negative.

$$\Delta G = \Delta H - T\Delta S \quad (3.1)$$

Here ΔH is the enthalpy change, ΔS is the entropy change, and T is the temperature of the respective system.

The ΔS for a self-assembled structure of molecules on a surface tends to be negative. This is a consequence of the confinement of molecular motion and orientations, leading to reduced degrees of freedom. As a result, reaching a negative ΔG, which drives the stability of self-assembled structures, depends upon having a sufficiently large negative ΔH with a magnitude surpassing TΔS. This scenario is applicable to stable self-assembled structures where the enthalpy is effectively minimized through the optimization of interactions between molecules and the substrate during the self-assembly process.

In addition to the formation of monolayers under the vacuum-solid interface in a UHV environment, where molecular diffusion and reorientation are controlled by interactions among molecules and between molecules and the substrate, self-assembly at liquid-solid interfaces has additional complexity due to interactions between molecules and the solvent, as well as between the solvent and the substrate. In general, self-assembly here is stabilized through adsorption and desorption at a dynamic equilibrium[63] between the interface and within the solution.

Sometimes, the formation of self-assembled structures occurs under kinetic rather than thermodynamic control. This could occur as a result of hindering the forward or backward reactions, which potentially steer the system toward alternate states. These kinetically trapped states represent a start of higher Gibbs free energy enthalpy compared to the thermodynamic minimum, and even though ΔG is negative, the system is situated in a local minimum rather than reaching an absolute minimum. In general, the direction in which the system evolves, whether towards thermodynamic equilibrium or a kinetically trapped state, hinges upon the available thermal energy in relation to activation barriers that need to be overcome.

This tendency is more prevalent when dealing with larger molecules characterized by numerous intermolecular interactions, particularly when employing more flexible building blocks. Additionally, it is often observed when incorporating metal ions into the supramolecular structure[56] particularly those known for their kinetic inertness.

3.3 Molecule-Substrate Interactions

Interactions between molecules and surfaces play a pivotal role in the self-assembly of organic adsorbates on surfaces, exerting several notable effects.[64] Firstly, when molecules adhere to a surface, they become constrained to a two-dimensional plane, which imposes restrictions on their translational, rotational, and vibrational motions.[63] Furthermore, the characteristics of the surface, including its symmetry, reactivity, and electronic properties, can significantly impact the mobility and structural arrangement of the molecules.[24] In this manner, surfaces have a direct and influential role in shaping the outcomes of self-assembly processes. Surfaces offer unique properties, rendering them highly attractive for molecular investigations. These distinctive characteristics often arise from the disruption of crystal periodicity, which leaves the surface with unsaturated chemical bonds.

The interactions between adsorbed molecules and surfaces are broadly categorized into two types: physisorption and chemisorption. Physisorption represents a weak adsorption phenomenon where forces such as van der Waals interactions serve to bind the adsorbates to the surface. This type of interaction typically occurs on less reactive surfaces like graphite and has minimal impact on the geometrical and electronic structures of both the adsorbent and adsorbates. In contrast, chemisorption involves a strong adsorption interaction characterized by orbital overlap, charge transfer, and electron sharing, leading to the formation of chemical bonds. Unlike covalent bond formation between atoms or molecules, which generates bonding and antibonding orbitals derived from two atomic orbitals, the bond formation mechanism in chemisorption is usually more complex.[65]

The electronic structure of transition metals influences the strength of bonds formed with adsorbates on surfaces and explains the observed variations in reactivity patterns.[65] Understanding the interplay between molecular orbitals and the s and d bands of transition metals is fundamental in deciphering the dynamics of chemisorption. This process, involving the binding of atoms onto transition metal surfaces, can be deconstructed into two sequential steps. In the initial step, the frontier orbitals of molecules experience broadening and shifting due to their interaction with the s band of transition metals. This interaction results in the formation of a bonding state situated notably below the Fermi level. This bonding state exhibits relatively weak chemisorption characteristics, a phenomenon observed across a range of transition metals.

In the subsequent phase, the bonding state engages with the d band of the metal, leading to the formation of both bonding and antibonding states. Notably, the bonding state occupies a lower energy level compared to its original state, while the antibonding state is positioned slightly higher in energy relative to the unperturbed metal d band. The collective energy outcomes in these states depend upon the strength of the coupling between the hybrid formed by the interaction of

adsorbates with the s band and the d band. Furthermore, the extent to which the antibonding state is filled depends on the relative positioning of the antibonding state concerning the Fermi energy. Differences in this second step arise from variations in the coupling strength and Fermi energy, both being properties unique to each metal. These distinctions account for the varying strengths of chemisorption bonds observed across different transition metals. It is noteworthy that the energy of the antibonding state is influenced by the metal-specific positioning of the d bands. As one progresses from left to right across a row of transition metals in the periodic table, the center of the d band progressively shifts further below the Fermi energy. For metals on the right side of the table, such as Cu, Ag, and Au, the d band, and correspondingly, the antibonding state, is positioned below the Fermi energy. Consequently, the antibonding orbitals are filled, generating repulsive forces that may offset the attractive forces arising from the initial bonding state. Conversely, for transition metals situated on the far-left side of the table, the antibonding state is situated above the Fermi level and remains unoccupied, resulting in overall attractive forces and highly exothermic chemisorption processes.

3.4 Molecule-Molecule Interactions

Intermolecular forces can be broadly categorized into two distinct classes: short-range and long-range interactions.[66,67,68] Short-range interactions are primarily characterized by the sharing of electrons and the overlap of molecular orbitals, similar to the principles underlying covalent bond formation. These interactions are renowned for their remarkable strength, representing some of the most robust bonds within molecular systems. In contrast, long-range interactions contain a diverse array of forces, including hydrogen bonds, halogen-halogen bonds, metal-coordination bonds, $\pi - \pi$ interactions, van der Waals forces, and electrostatic interactions. These forces play key roles in the intricate formation of supramolecular assemblies. A common feature that unifies these forces is their mathematical proportionality to the inverse of the internuclear distance raised to a positive integer power, r^{-m}; within the context of these interactions, the individual molecular constituents involved in the assembly of supramolecular structures typically undergo minimal chemical transformation. Unlike covalent bonds, where the wave functions of the molecules are altered, long-range interactions are characterized by their relatively modest impact, which contributes to their inherently weaker bonding attributes.

3.5 Van der Waals Interactions

Van der Waals interactions belong to a broader category of electrostatic forces. Electrostatic interactions can be categorized into three principal groups: permanent-permanent dipole

interactions, known as Keesom forces; permanent-induced dipole interactions, commonly referred to as Debye forces; and van der Waals interactions. These electrostatic forces exhibit a characteristic long-range interaction, capable of extending their influence over regions that generally exceed the collective spatial extent of the electron clouds surrounding the participating molecules. The first two groups, namely permanent-permanent and permanent-induced dipole interactions, fall within the group of classical inductive forces and are commonly referred to as polar interactions. In the absence of permanent dipoles, electrostatic forces display as van der Waals interactions. These interactions arise due to the presence of non-zero instantaneous dipole moments within all atoms and molecules. The random fluctuations in electron density within the electron cloud surrounding these molecules lead to the emergence of fluctuating dipoles. These fluctuating dipoles, when positioned near neighboring molecules, have the capacity to induce the formation of additional dipoles, resulting in the phenomenon known as fluctuating dipole-induced dipole interactions, more commonly recognized as London dispersion forces. Furthermore, it is essential to acknowledge that London dispersion forces apply universally, including interactions involving non-polar molecules or atom-atom associations. Notably, the strength of London dispersion forces is directly proportional to the polarizability of atoms and molecules, a characteristic reliant on the total number of electrons they have and the spatial distribution of these electrons. Consequently, an atom with a greater electron count will exhibit a more pronounced associated London force than an atom with a smaller electron population.

3.6 π − π Interactions

π-π interactions are a class of non-covalent interactions that occur between aromatic systems in organic molecules.[69] These interactions encompass various subtypes, including aromatic-aromatic (commonly known as π-stacking) interactions, π donor-acceptor interactions, anion/cation-π interactions, etc.[70]

They are named for the involvement of the π-electrons in the aromatic rings, which are part of the molecular orbitals responsible for the distinctive electronic properties of aromatic compounds. In π-π interactions, the π electrons from one aromatic ring interact with the π electrons of another aromatic ring, creating attractive forces between the two systems. These interactions play a crucial role in various fields of chemistry, including molecular recognition, supramolecular chemistry, crystal engineering, and the formation of complex molecular assemblies.

The strength and direction of π-π interactions are influenced by several factors, including the distance between the aromatic rings, the orientation of the rings relative to each other, and the electron density in the π orbitals. Aromatic-aromatic interactions, commonly referred to as π-

stacking, are a prevalent type of π-π interaction. In π-stacking, two or more aromatic rings align in parallel, with the π electron clouds of one ring interacting with those of the other. These interactions are essential in stabilizing the three-dimensional structure of molecules, such as DNA base pairs and protein structures, and are crucial for understanding molecular recognition and binding events in biochemistry and pharmaceutical research. Overall, π-π interactions are fundamental in chemistry and biology, which contribute to the structural stability and function of a wide range of organic compounds.

3.7 Metal-Coordination Bonds

The presence of free adatoms on metal surfaces can also significantly influence interactions between molecules and the substrate in the formation of self-assembled structures. Metal-coordination bonds involve the interaction between metal atoms[71] and organic ligands, except in cases involving carbon-metal bonds, which are known as organometallic bonds. The establishment of metal-coordination bonds necessitates the presence of electron-rich ligands. These bonds can be established using either anionic ligands like carboxylates and thiolates[72,73] or neutral ligands such as nitriles and pyridines.[74,75] In the case of neutral ligands, the electron lone pairs on nitrogen atoms create attractive coordination bonds with the positively charged metal adatoms.

Based on orbital theory, the creation of a metal-coordination bond involves a four-step process.[76] First, electrons are removed from the metal center, resulting in the formation of a cation. In the second step, hybridization of the metal's atomic orbitals occurs, generating a series of equivalent hybrid orbitals that extend toward the ligands. Subsequently, the metal's electrons undergo reorganization to ensure that these hybrid orbitals remain unoccupied. Finally, the bond between the metal center and the ligand is established through the overlap of the metal's hybrid orbitals with the ligand's orbitals, which contain lone-pair electrons. It's important to note that the metal atoms participating in these metal-coordination bonds do not necessarily have to originate from the surface but can also be co-deposited onto the surface.

3.8 Hydrogen Bonds

A so-called hydrogen bond is formed when a hydrogen atom is attracted by two other atoms and effectively makes bridges between them. Technically, both atoms are highly electronegative; the first atom attracts the hydrogen atom electron closer and forms a polar covalent bond; consequently, the hydrogen bond becomes a donor due to the hydrogen-positive partial charge within this interaction. On the other hand, the high electronegativity of the second atom within its own intermolecular configuration leads to a negative potential, which makes it a hydrogen bond

acceptor. Accordingly, the electrostatic attraction between the negatively charged atom and the positively charged hydrogen provides an attractive interaction.[77] N-H, O-H, S-H, P-H, F-H, Cl-H, Br-H, and I-H are hydrogen bond donors, whereas N, O, P, S, F, Cl, Br, and I, as well as alkenes, serve as hydrogen bond acceptors. The broad energy range of hydrogen bonds arises from the diverse contributions of various interaction types to the overall strength of the H-bond. The binding energy range of hydrogen bonds can differ from very weak to very strong (2-40 kJ/mol). Depending on bond strength based on the electronegativity of the interacted atoms, hydrogen bonds possess van der Waals, electrostatic, and even covalent characteristics.[77,78] For instance, bonds like P-H···O, C-H···O, and C-H···N are weak hydrogen bonds (2-20 kJ/mol) with an electronegativity of moderate to low, which shows a weak donor and strong acceptor bonds. In contrast, O-H···S orN-H···π indicate a strong donor to weak acceptor bonds.[79,80,81] On the other hand, O-H···O orN-H···O bonds are strong hydrogen bonds (20-40 kJ/mol) and are characterized by the strong donor-to-strong acceptor interaction.[77] The interaction energy between the hydrogen and the second involved molecules usually influences the hydrogen bond distance; consequently, increasing the bond energy decreases the bond distance. For weak hydrogen bonds, the distance typically ranges from 0.3 to 0.15 nm, while stronger bonds have a reduced distance close to covalent bonds, with distances of 0.15 to 0.12 nm.[82] This is also evident in the geometry of the bond. Stronger bonds tend to have an angle closer to 180°, while weaker bonds typically exhibit smaller angles (160°±20°).[80,83]

Hydrogen bonds, due to defined directionality and selectivity, play a crucial role in supramolecular systems.[84] In this context, molecules with carboxylic acid groups are interesting and usually display reliable intermolecular hydrogen bonds in the aggregated state. Their dual character allows consistent intermolecular cross-linking where the oxygen atom in the carboxy group could act as an acceptor for hydrogen bonds and the hydroxyl group as a donor, which results in enhancing the formation of well-organized structures in molecular self-assembly.[85]

Figure 3.1 illustrates the common carboxylic acid hydrogen bonding motifs, which are observed on surfaces as well as molecular crystals and consist of cyclic dimers, trimers, and catemeric motifs.[86,87]

In Chapter 7, we explore the self-assembly of aromatic homologues of benzene tricarboxylic acids supramolecular monolayers at liquid−solid interfaces on iodine-passivated Au(111) (I-Au(111)). This study unveils that molecule−surface interactions can cause substrate-induced polymorphism, and for different tricarboxylic acids (TMA, BTB), chicken wire polymorphs exclusively feature an ideal two-fold cyclic H-bonds on I−Au(111). Moreover, experiments carried out on graphite express the carboxylic acid groups show a formed 3-fold cyclic or mixed catemeric

H-bond and C−H···O bond motifs that are energetically inferior in addition to ideal hydrogen bonds.

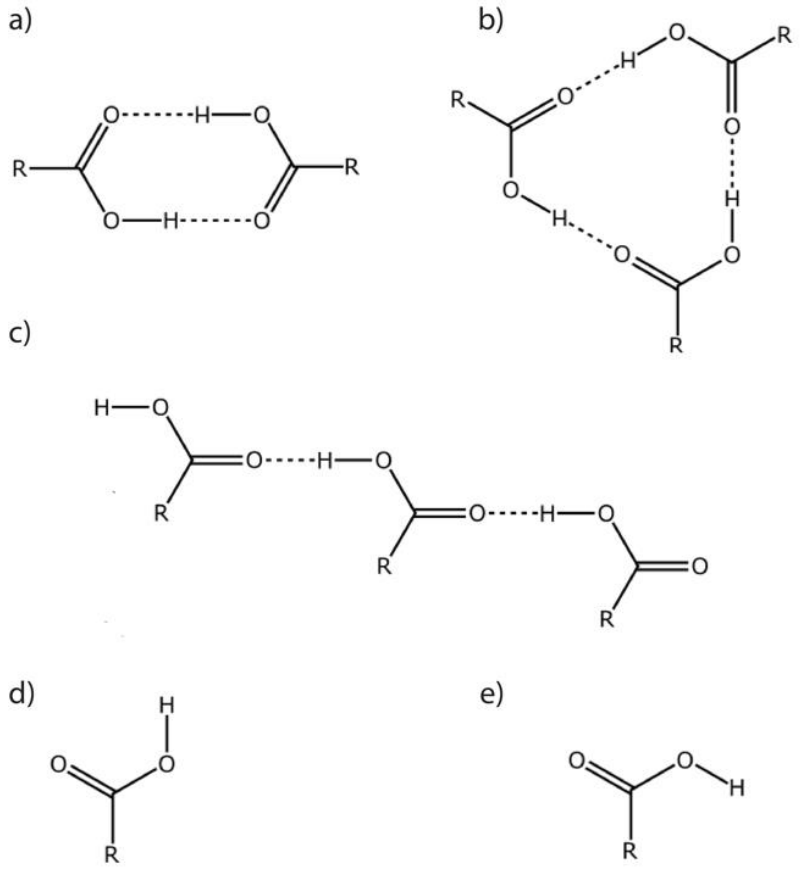

Figure 3.1 Hydrogen bonds binding motifs in between carboxylic acid group. (a) cyclic dimer, (b) catemeric, and (c) cyclic trimer motifs. For the catemeric motifs, carboxylic groups can either be in the (d) syn planar or (e) antiplanar configuration. Adapted and reprinted with permission from Lackinger and Heckl. Copyright (2009) American Chemical Society.[88]

3.9 Covalent Bond

Covalent bonds are the fundamental type of chemical bonds that are formed between atoms by sharing one or more pairs of electrons. In fact, these bonds are formed according to the electrostatic attraction between the positively charged nuclei of the participating atoms and the negatively charged shared electrons between them. Covalent bonds commonly occur between non-metallic elements or compounds, where atoms have a strong tendency to share electrons to achieve a stable electron configuration.

In a covalent bond, the shared electrons are usually located in the outermost electron shells of the atoms, known as valence shells. The atoms share these electrons to fill their valence shells and achieve a full complement of electrons. This sharing of electrons allows both atoms to attain a more stable, lower-energy state. Covalent bonds can vary in strength, from very strong, as in the case of double or triple covalent bonds where multiple electron pairs are shared, to weaker single covalent

bonds, which involve the sharing of only one electron pair. These bonds are vital for the formation of molecules and play a central role in the structure and function of a wide range of chemical compounds, including organic molecules, which are the building blocks of life.

The interaction of atomic orbitals leads to the creation of molecular orbitals, which are solutions of the Schrödinger equation governing electrons in an atom. This interaction can result in two outcomes: constructive overlaps, where wave functions are in phase, forming bonding molecular orbitals, or destructive overlaps, where wave functions are out of phase, giving rise to antibonding molecular orbitals. In the case of bonding orbitals, the electron density is concentrated more between the nuclei, leading to lower energy compared to the original atomic orbitals. Conversely, antibonding orbitals have higher energy, and their occupation weakens the bond as electron density between the nuclei is reduced compared to non-bonded (isolated) atoms.

3.10 Organometallic Bonds

Organometallic bonds, a special case of covalent bonds, serve as a key bridge between organic and inorganic chemistry. They also indicate interactions between carbon-containing organic molecules and metal by sharing electron density between an organic ligand carbon atom and a metal atom.[89] Organometallic compounds involve a wide range of metals, including alkali, alkaline earth, and transition metals, in addition to metalloids such as boron and silicon.[89,90]

Ullmann-type dehalogenative couplings are a prominent example of utilizing the on-surface synthesis in order to generate stable surface radicals via dissociation of the carbon-halogen bond. However, in this type of synthesis on metal surfaces, organometallic intermediates through Carbon-Metal-Carbon linkages are almost always formed on copper and silver and often on gold surfaces.[91,92]

Sometimes, mild annealing also enables structural improvements and reveals the reversibility of the organometallic bonds.[46,93] In addition to thermally activated organometallic networks, organometallic self-assembly is also a promising approach and has significant potential for constructing one or two-dimensional molecular nanostructures with enhanced stability.[90]

The synthesis of organometallic and covalent nanostructures has been investigated in Chapter 5 through the dehalogenative coupling of 2,5,9,12-tetrabromoanthra[1,2-b:4,3-b′:5,6-b″:8,7-b‴]tetrathiophene (TBATT) precursor on Au(111) and I-Au(111) substrates. These experiments demonstrate both organometallic self-assembly as well as thermally induced debromination, which results in regular and irregular organogold and covalent networks. This work demonstrates iodine's capacity to induce reversibility in robust organometallic C-Au-C bonds, facilitating error correction, healing, and ultimately enhancing network quality.

3.11 On-Surface Synthesis

Supramolecular self-assembly on surfaces affords complex 2D nanostructures stabilized by weak and reversible bonds like Van der Waals interactions, hydrogen bonds, and metal complexation.[5,6,94] However, the stability of these structures is limited by these weak interactions and charge transport. Overcoming these limitations necessitates the formation of robust covalent bonds among the molecules to undergo on-surface chemical reactions and have the stability to withstand mechanical and thermal stresses in practical applications. Moreover, reversible covalent reactions are well-suited for building regular molecular networks due to their intrinsic self-healing properties as exploited in dynamic covalent chemistry. On the contrary, irreversible reactions form more robust bonds but lack the ability to heal the structure after bond formation. Here, a two-step reaction can be considered as a solution, where high structural quality is obtained in the first non-covalent step, while only the second step is irreversible and results in the formation of robust covalent bonds.[95,96] One reaction that possibly exhibits these characteristics is on-surface Ullmann coupling. It is worth mentioning that the reversible step can also involve the formation of organometallic intermediates, which can subsequently be equilibrated into better-ordered structures.

Covalent intermolecular bonds are typically formed during chemical reactions that are carried out on surfaces, most often under UHV conditions. Additionally, UHV offers the advantage of enabling the use of mildly reactive coinage metal surfaces that, under the atmospheric constituents, are prone to oxidation and contamination. Besides, UHV conditions allow the application of various characterization complementary techniques, for example LEED, and X-ray photoelectron spectroscopy (XPS), to monitor and analyze the reaction process.

3.11.1 On-Surface Ullmann Reaction

On-surface Ullmann coupling is a highly favored reaction for synthesizing conjugated polymers on metal surfaces due to several key advantages. Notably, it excels in selectivity when it comes to choosing specific coupling sites, as well as offering a high degree of control over the coupling process. Additionally, the possibility for hierarchical growth, facilitated by the presence of different halogen substituents, allows for the arrangement of precise and tailored nanostructures.[16,97]

In the Ullmann reaction, the produced polymer structure is closely related to the monomer precursor. Therefore, this method has enabled the realization of a diverse array of structures, ranging from linear and two-dimensional polymers to macrocycles, for instance, one-dimensional polymer chains, which are formed by monomer precursors with two halogen substituents.[16] The possible path to initiate this reaction is initially forming an organometallic intermediate, which is

then followed by demetalation (i.e., reductive elimination of the organometallic metal atom), resulting in the formation of the final covalent C-C bond.

Figure 3.2 illustrates the on-surface Ullmann reaction and describes the reaction of iodobenzene precursors on a Cu(111) surface.[98,99] The reaction mechanism demonstrates the insertion of a copper atom into the Cu-I bond to form an organometallic intermediate. These intermediates subsequently react to produce the final biphenyl product. In fact, two reaction mechanisms can be explained, each depending on the state of the copper atom, which can be either a lattice atom or a surface adatom.

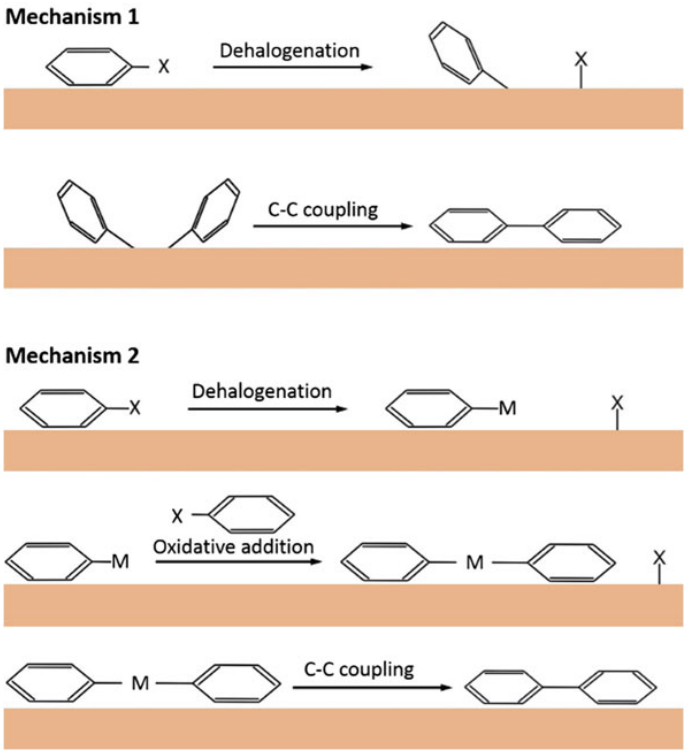

Figure 3.2 Scheme of On-surface Ullmann coupling exhibits whether the metallic atoms involved from the surface lattice: Mechanism 1 or involved with adatoms: Mechanism 2. Adapted and reprinted with permission from Springer.[91]

Chapter 4

Improving the Existing High-Stability Cryogenic Scanning Tunneling Microscope Based on a Flow Cryostat

4.1 Introduction

In Chapter 2, we have broadly discussed scanning tunneling microscopy (STM) and Scanning Tunneling Spectroscopy (STS) [3] as crucial techniques in surface science. These methods provide unparalleled insights into the atomic structures of various nanoscale systems and their electronic properties.

Conducting STM experiments by aiming to explore the spatially dependent spectroscopic characteristics necessitates essential operation under the demanding conditions of UHV and cryogenic temperatures. Operating within a UHV environment facilitates the preparation of clean and atomically defined surfaces. Additionally, maintaining stable low temperatures enhances the stability of the STM junction, which freezes the motion of weakly bound adsorbates and boosts the STS spectroscopic resolution by minimizing thermal broadening effects.

Most high-performance STM systems designed for advanced STS experiments have been integrated with various cryostats, including continuous flow[100,101,102] or bath cryostats.[103,104,105] These cryostats have traditionally relied on the use of cryogenic substances. Although the most optimal performance is achieved through the utilization of liquid helium, liquid nitrogen also offers several distinct advantages. Liquid nitrogen has a substantially lower cost than liquid helium, which makes nitrogen cryostats an attractive option for researchers and institutions operating within constrained budgets. Additionally, the availability of nitrogen facilitates more accessible procurement and distribution. Furthermore, the operational simplicity of nitrogen cryostats contributes to more straightforward engineering solutions, potentially lowering maintenance requirements and increasing overall system reliability.

In a prior endeavor, our research group developed an advanced STM tailored for the exploration of self-assembled nanostructures on solid surfaces. The primary focus of this project was the design of a highly stable instrument with a highly reliable coarse approach mechanism.[106] The success in realizing this vision hinged on the integration of a piezo-based nanopositioner from attocube Systems AG into the STM framework. This novel microscope configuration was further integrated with a flow cryostat and designed to facilitate low-temperature experiments conducted within a UHV environment.

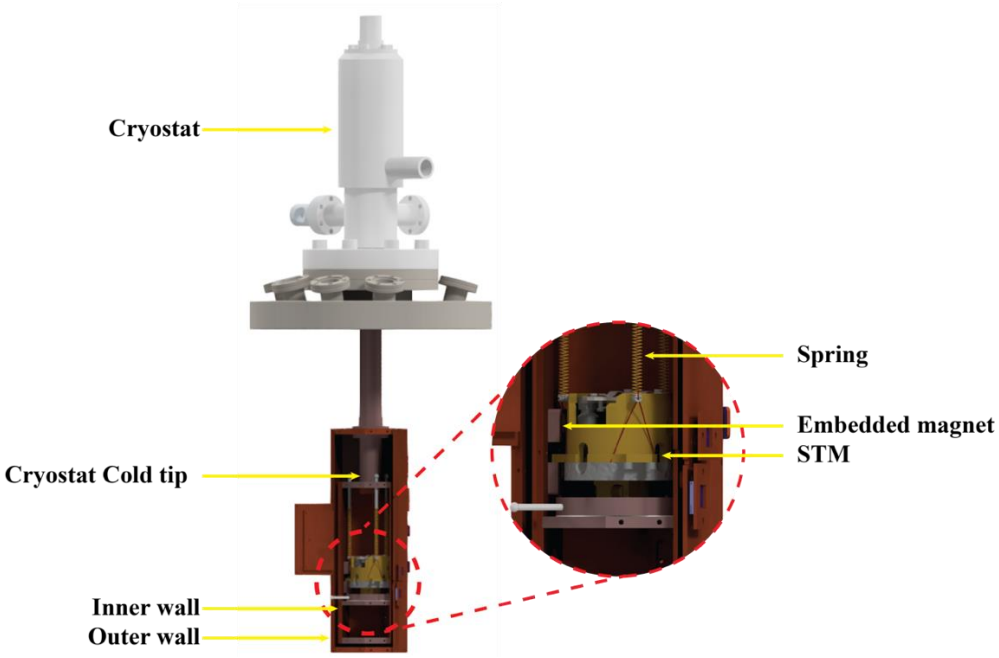

Figure 4.1 The schematic illustration of the STM, including an integrated flow cryostat and the double-walled radiation shield, with the magnified view of the spring-suspended STM.

The Low-Temperature Ultra-High-Vacuum Scanning Tunneling Microscope (LT-UHV-STM) was housed in a double-walled radiation shield for improved thermal insulation (Figure 4.1) and equipped with three springs, which were utilized for the free suspension of the STM, in addition to an integrated eddy current damping mechanism, achieved through the placement of three magnets on the side walls. The inner housing is firmly fastened to the cryostat's cold tip. Simultaneously, the outer housing is connected to the upper section of the cold tip.

In Scanning Probe Microscopes (SPM), particularly for high resolution at atomic scales, thermal drift is a critical challenge. This issue arises from the thermal expansion of various components due to temperature variations within the microscope. Although our previously home-built LT-UHV-STM setup showed promise in reduced drift, achieving high-resolution imaging at liquid nitrogen temperature was accompanied by a noticeable increase in thermal drift. Consequently, the instrument needed critical improvements to meet the strict temperature stability requirements.

4.2 Concept and Requirements

In our endeavor to enhance the existing STM for STS measurements at liquid nitrogen (LN_2) temperatures while preserving imaging at low tunneling currents of a few pA, we aimed at the pivotal significance of thermal drift. To address this challenge systematically, we undertook an optimization focused on minimizing temperature gradients across the microscope.

Our multifaceted approach to thermal drift reduction encompassed three primary categories. These include optimization by material substitution of some mechanical parts inside the STM, mechanical modifications, and the implementation of newly constructed parts to the system, and then the establishment of docking stations for thermally anchoring control and signal wires. (Figure 4.2) This comprehensive strategy aims to enhance the STM's thermal stability, thereby reducing thermal drift.

After specific components of the STM have been redesigned, modified, or newly machined and integrated into either the STM or the housing, the entire selection process with underlying principles was tested and examined by experiments. Hence, a direct comparison was made between the different configurations based on the behavior upon cooling with LN_2. To this end, the UHV system was not baked, but the pressure was consistently below 10^{-9} mbar, which gave a realistic impression of the cooling. The temperature was measured directly on the scan unit using a Si diode temperature sensor. (Figure 4.11a) Further temperature vs. time traces were recorded and analyzed during the cooling time.

The following sections provide a detailed discussion of specific measures undertaken for thermal equilibration, enhancing temperature stability, and reducing thermal drift within the system.

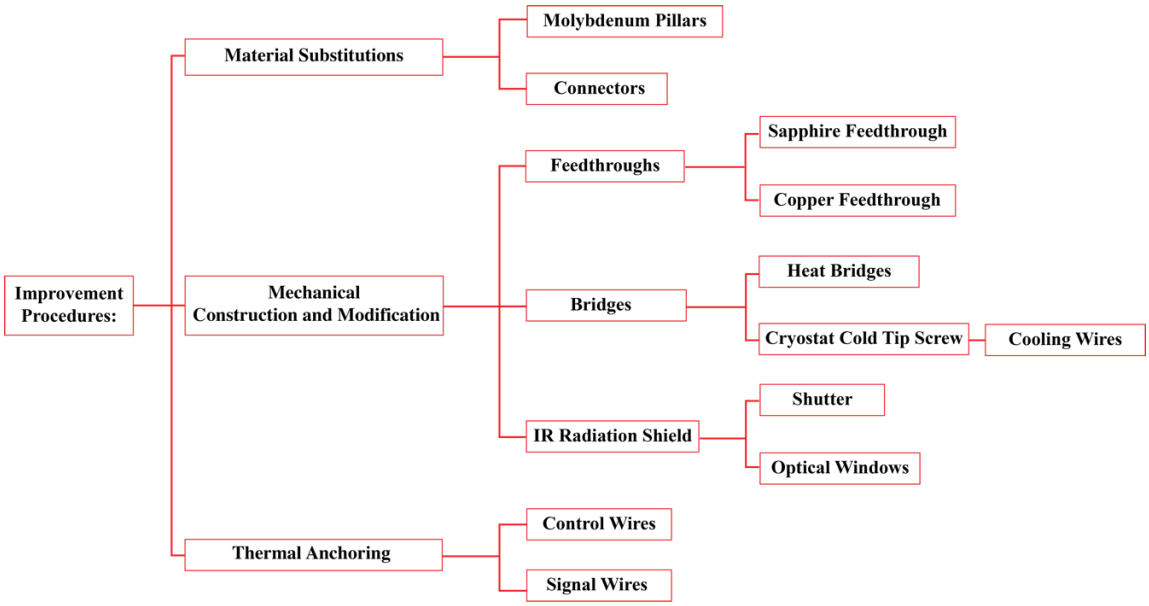

Figure 4.2 Schematic illustration of the improvement steps for STM thermal stability.

4.3 Material Substitutions

The fundamental idea for improving the STM's thermal equilibrium with optimized heat distribution within the microscope is substituting materials with low heat conductivity with alternative, better thermally conductive materials. For instance, some STM designs still utilized machinable ceramics like Macor (with thermal conductivity of ~1 W/m-K at 100K)[107], which, in this context, could be effectively replaced by alternative machinable ceramics like Shapal (with extraordinarily high thermal conductivity of ~210 W/m-K at 100 K)[108] or Sapphire which is renowned for its high thermal conductivity, and has a key role in heat dissipation at LT (with thermal conductivity of ~ 400 W/m-K at 100 K)[109], known for their significantly superior heat conductivity.

4.3.1 Molybdenum Pillars

The sample for the STM measurement is mounted on three stands which are firmly screwed on top of the molybdenum base plate. (Figure 4.3) These stands were initially fabricated by ceramic pillars and composed of piezoelectric ceramic material (PZT). PZT, known for its relatively low heat conductivity (with thermal conductivity of ~ 0.01 W/m-K at 15 K)[110] , has undergone a substitution with molybdenum pillars (with thermal conductivity of ~200 W/m-K at 15 K).[111]
While both molybdenum and PZT also exhibit thermal expansion, which influences drift properties, it was essential to prioritize materials with high heat conductivity and select the materials with similar or closely matched thermal conductivity. Therefore, as the STM base plate was also made from molybdenum, the choice of pillar material guaranteed a uniform and quick cooling procedure between the sample and the STM body.

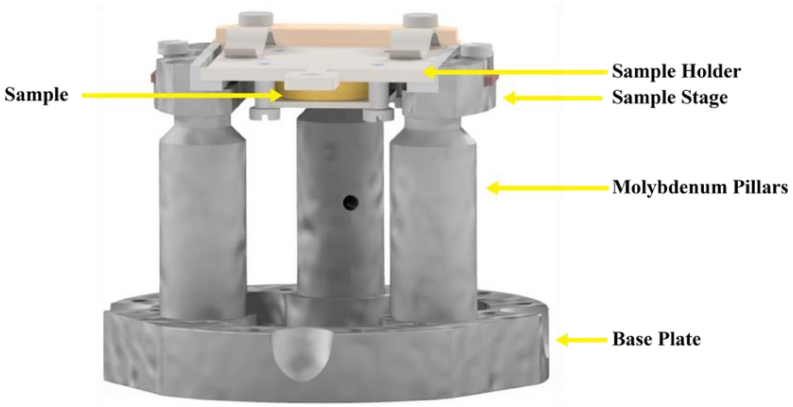

Figure 4.3 Schematic design of Molybdenum Pillars.

4.3.2 Connectors

Within the central core of the STM, three connectors are used for wiring: one to the scanner piezo, another to the stack piezo of the nanopositioner, and the third to the Si diode used for temperature measurement. The purpose of using these connectors is to safeguard the fragile wiring, which is soldered to piezos and the diode, by firmly placing and gluing connectors on the scanner piezo base plate. (Figure 4.10)

Among these connectors, the scanner piezo connector has an important role. The heat from the control wires can be directly transferred to the scanner unit, which results in drift. Therefore, it is necessary to choose a suitable material for the connector to provide efficient thermalization with the base plate.

In the previous design, the connectors were made from polyether–ether–ketone (PEEK) material. (Figure 4.4a) While this material is advantageous for its ease of machining and compatibility with UHV environments, it presents a notable disadvantage of low thermal conductivity (with thermal conductivity of ~ 0.25 W/m/K at room temperature).

Utilizing the PEEK connector for the scanner piezo connection wires hinders the effective dissipation of heat inside the STM core and acts as a heat resistor. As a result, this connector was redesigned and machined from Shapal. Besides, Oxygen-Free, High Thermal Conductive Copper (OFHC) pins were used to ensure wires were at the same temperature as the Shapal connector and STM base plate. (Figure 4.4b)

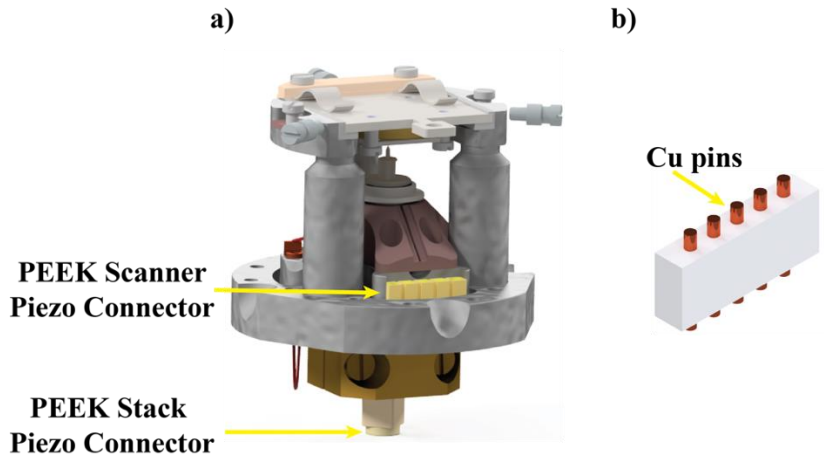

Figure 4.4 The Schematic design depicts a) the STM core featuring the PEEK connectors and b) the Shapal connector with the Oxygen-Free High Conductivity (OFHC) pins for the Scanner Piezo.

4.4 Mechanical Constructions and Modifications

In addition to material substitution for certain parts in the STM, various modifications, redesigns, and additional components have been implemented in the system. Key components that

have undergone significant changes include feedthroughs, heat bridges, and infrared radiation shields.

4.4.1 Feedthroughs

The operation of the STM involves eleven wires, each serving a distinct role with controlling capabilities and measuring values. Among these, seven wires are dedicated to the control of the STM for functions such as the movement of the piezo components, two for temperature monitoring, and the other two wires are the bias voltage and tunneling current as signal wires.

Notably, these wires act as the primary sources for heat transfer from the outside due to their connections to ambient feedthroughs, and hence, they could result in temperature gradients at the instrument.

To address this issue and minimize the temperature effect, new feedthroughs were designed and replaced with the originally used feedthrough and implemented within the inner housing wall. The inner housing wall was specially modified to accommodate two feedthroughs and intentionally separate control and temperature measurement wires from signal wires. (Figure 4.9) This design effectively impacts the reduction of external heat from the outside atmospheric feedthroughs by interrupting control and temperature monitoring wires and spontaneously cooling them. (See the result in Figure 4.12) The following sections will provide a detailed explanation.

4.4.1.1 Sapphire Feedthrough

The separate signal wire feedthrough (Figure 4.5) and control wires feedthrough were both made from a thin sapphire plate with a 1.6 mm thickness. This feedthrough featured ten holes to insert pins, each with a diameter of 0.5 mm and positioned 1.8 mm apart.

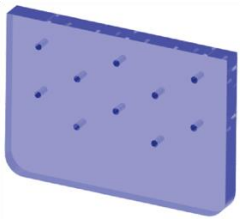

Figure 4.5 Schematic drawings of sapphire feedthrough

Ten stainless steel pins (Figure 4.6a), each with a diameter of Ø 0.55 mm, were securely glued with silver-filled epoxy (Panacol, Elecolit 3655, with thermal conductivity of 11W/m-K [112]) into

individual holes. Stainless steel pins, chosen for their low thermal conductivity, served as an optimal material for the feedthrough, which can effectively minimize heat transfer by thermally interrupting the wires between the outer feedthrough and STM. Using larger diameter pins also addressed holes' tolerances from machining and provided maximum contact between the pins and the Sapphire.

A standard electronic socket (Miniature Spring Sockets, AMP incorporated Harrisburg, pa 17105-3608) was used as the pins' connectors on both sides of the Sapphire feedthrough, with minimal contact area, which additionally helped to reduce heat transfer. (Figure 4.6 b)

While the front side of the feedthrough sockets with a smaller contact area helped to reduce the heat transferred between pin and wire, on the feedthrough side that faces the STM side, pins were shortened, the sockets were fully inserted into the pins, and socket head had direct contact with the cooled sapphire surface. Additionally, Kapton-insulated OFHC Copper wires (Ø 0.15 mm) were used for the connection between the sapphire feedthrough and the STM. (Figure 4.6c) Although utilizing comparatively thicker copper wires poses a higher susceptibility to transmitting mechanical noise, this mechanism provided an additional cooling source for the STM through the control wires and further enhanced the cooling process.

Since the heat flow in our STM setup is from the outer atmospheric feedthroughs towards the STM, the selection of optimal control wire dimensions and material is a critical consideration in design. To efficiently minimize heat transfer to the microscope, all control wires have been replaced between the atmospheric feedthrough and the sapphire feedthrough with thin stainless steel wires (Ø 0.127 mm, ss-5T1A from Science Products).

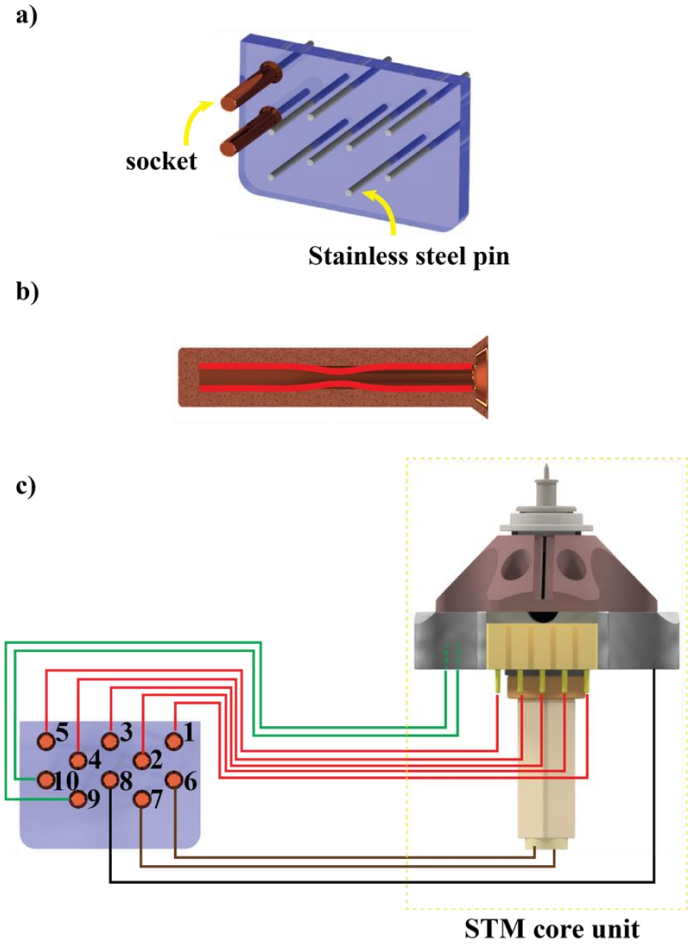

Figure 4.6 Schematic illustrations of the designs of (a) sapphire, pins, and connector sockets and (b) a sectional view of the socket. Notably, the red lines in the diagram signify the minimized contact points of the pins inside the socket. This reduction in the contact area is pivotal in lowering heat transfer originating from the wires connecting to the outside environment. (c) The schematic configurations of the signal wire connections on the sapphire inside and the core of the STM. The scanner piezo electrodes were connected to the pins as follows: #1 for +Y, #2 for +X, #3 for Z, #4 for -X, and #5 for -Y. Connections #6 and #7 were connected to the stack piezo of the nanopositioner, #8 was for STM grounding, and #9 and #10 were for the diode connections used for measuring the STM temperature.

4.4.1.2 Copper Feedthrough

The main idea behind using two separate sapphire feedthrough was dividing the signal wires and control wires into distinct groups. This approach aims to prevent cross-talk of control wires with applied high and changing voltages for piezo movements, especially on the tunneling current. In the initial design, Sapphire feedthrough was also used for the signal wire feedthrough, and the pins, which were made from stainless steel, were secured with low-temperature epoxy (Epoxy Technology, H74) within the designated holes with the same socket connectors design. (Figure 4.6 a) In the subsequent configuration, these pins were horizontally arranged on the Sapphire to maximize contact area with the cold surface and affixed using silver-filled epoxy (Panacol, Elecolit

3655). (Figure 4.7b) The signal wires were intentionally interrupted and soldered to the endpoints of the pins by aiming to cool the wires.

For both configurations, significant noise and offset of the pA range were observed (~100 pA). This noise was primarily attributed to thermoelectric voltage. Thermoelectric voltage, also referred to as the Seebeck voltage, arises when two distinct conductive materials experience a temperature difference and consequently result in generating a voltage. Conversely, applying a voltage induces the transfer of heat from one side to another, generating a temperature difference. On the atomic scale, the induced temperature gradient prompts charge carriers within the material to move from the hotter side to the colder side, which causes interference with the tunneling current signal and results in substantial noise and offset generation. Subsequently, the yielded noise renders imaging impossible to conduct at a few pA.

As an alternative approach to avoid the thermovoltage effect, OFHC pins were used instead of stainless steel as the same material for the co-axial signal wire core (AWG 38; Ernst and Engbring Gmbh). These pins were similarly laid on the Sapphire, glued with silver-filled epoxy, and signal wires were soldered at pins on both ends. Despite these adjustments, this configuration also exhibited unwanted induced noise.

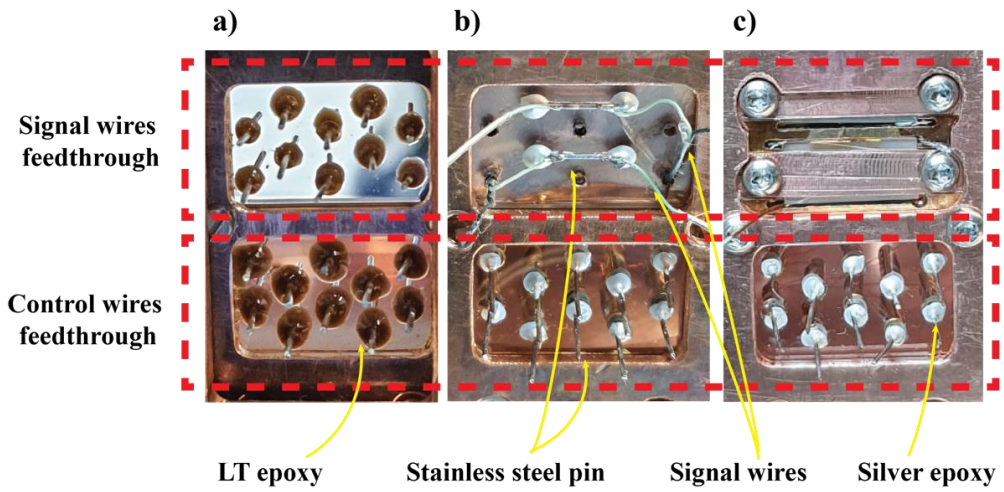

Figure 4.7 Photographs of sapphire feedthroughs display the pins fixed to the sapphire holes using two different epoxies. (a) low-temperature epoxy (H74) and (b,c) silver-filled epoxy. a,b,c, (upper windows) illustrates three distinct configurations of the signal wire feedthrough. In (a), identical sapphire feedthrough to the control and signal wires are depicted, with pins glued into the sapphire holes with H74 epoxy. In (b), the pins are arranged horizontally on the sapphire to enhance cooling efficiency and thermally anchor on the wires, with signal wires soldered at the start and end points of the pins. In (c), the signal wires window was replaced with a different copper feedthrough to provide uninterrupted connections, driven by the need to eliminate noise caused by the thermoelectric effect.

To achieve lower tunneling currents below ten pA, particularly beneficial when imaging molecules with low electrical conductivity or substantial resistance to the surface, such as 2D

polymer of fluorinated anthracene-triptycene (Figure 4.22) on iodine-passivated Au(111) (I-Au(111)), it is necessary to either introduce a preamplifier stage in the UHV close to the tunneling junction or design a feedthrough to maintain an uninterrupted co-axial wire while still minimizing heat transfer. Therefore, the co-axial signal wires should directly connect the sample from which the tunneling current is measured to the atmospheric feedthrough without any interruption.

Consequently, a feedthrough was designed to thermally anchor the signal wires from OFHC copper. (Figure 4.7c upper window, and Figure 4.8) Inside the copper feedthrough, signal wires were carefully positioned between two sapphire plates, which were then gently pressed together using small leaf springs to prevent excessive forces that could induce a shortcut between the inner wire core and the shield of the co-axial cable. This design preserves the signal integrity and the reduction of thermoelectric noise.

To further optimize the contact area, hence cooling efficiency of the co-axial wire, after removing the wires' outer Teflon insulation and placing it between two sapphire plates, the wires were positioned with an additional loop turn among sapphire plates. This arrangement is depicted in Figure 4.8. In addition, Figure 4.7 illustrates the improvement steps of the copper feedthrough.

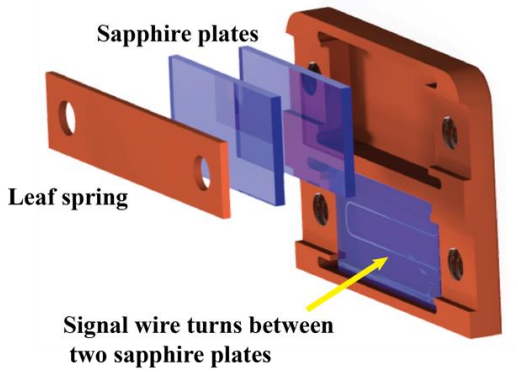

Figure 4.8 Schematic illustrations of the copper feedthrough: The design features sapphire plates, leaf springs, and the thermal anchoring of signal wires.

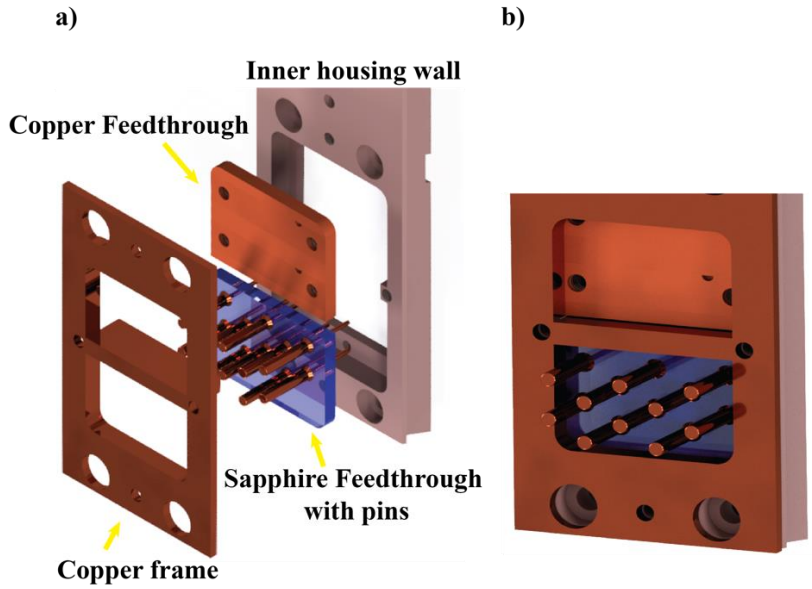

Figure 4.9 a) Exploded drawings of the sapphire and copper feedthrough, copper frame, and inner housing wall assembly; and b) Completely assembled unit.

Furthermore, both the sapphire and copper feedthroughs were positioned within the inner housing wall and fastened with a copper frame, as depicted in Figure 4.9b. Additionally, to minimize thermal resistance, a layer of gold leaf as a soft and thermally conductive material was placed in the contact areas of the feedthroughs, the inner housing wall, and the copper frame. Figure 4.9a provides a schematic representation of the assembly process, including the connection pins and sockets for the control wires.

4.4.2 Heat Bridges

The bridges, which are technically referred to as a "thermal short circuit," are pathways connected at various points on the STM. They enhance thermal equilibration by facilitating heat dissipation, thereby resulting in minimized temperature gradients. These thermal bridges were implemented both inside the STM and between the STM and the cold tip of the cryostat

The STM design comprises two distinct parts: the main scanner unit (as a core unit) responsible for the microscope's operation and a base plate that holds the scanner unit (see Figure 4.10). The scanner unit is mounted on a stick-slip nanopositioner, where a piezo actuator moves a ceramic axis clamped by two jaws mounted on the STM base plate. This arrangement with the ceramic axis introduces a considerable thermal resistance between the STM base plate and the core unit.

To address this thermal challenge, the design was modified by adding four copper heat bridges, as illustrated in Figure 4.11.

Highly flexible braided wire made of fine copper wire was employed in parallel for larger ceramic components that could not be substituted in principle. Initially, two parallel heat bridges were

affixed to the STM base plate and the scanner piezo base plate. (Figure 4.11b) Besides, to maintain the tip holder and the tip itself, which were positioned on top of the scanner piezo at the same temperature as the scanner base plate, two more heat bridges were added. (Figure 4.11a) One side was soldered to the tip holder, and the other side was screwed to the piezo base plate.

These heat bridges served a dual purpose: not only did they expedite the cooling process on the STM, but they also significantly contributed to maintaining a uniform temperature throughout the STM core and minimizing temperature gradients.

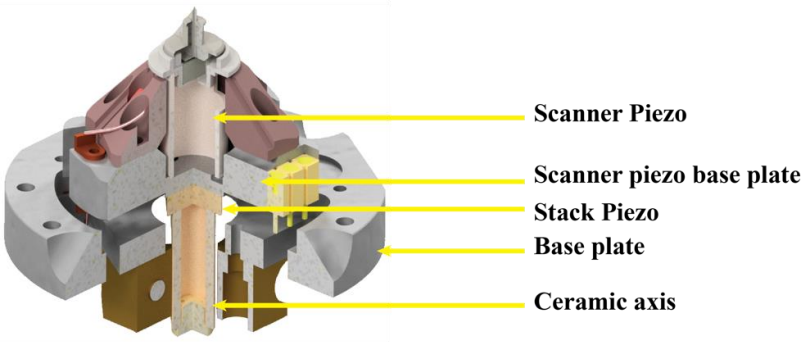

Figure 4.10 Schematic drawing of the STM (sectional view).

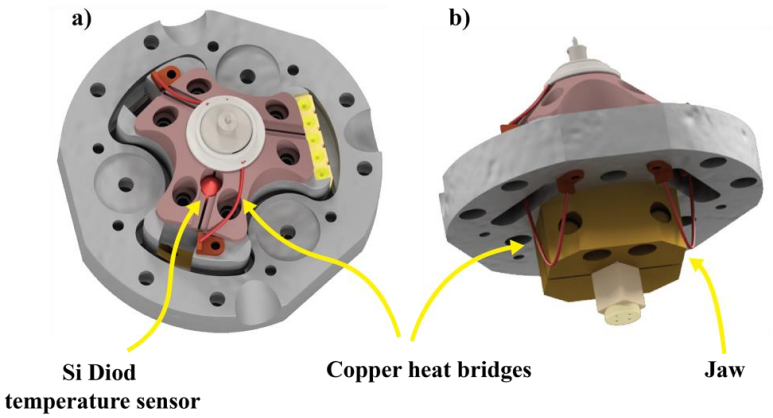

Figure 4.11 Copper heat bridges (Red wires). a) STM head top view, b) bottom view.

4.5 Combined Result of the Optimization

After integrating the mechanical components, which involved incorporating molybdenum pillars and installing the bridges into the STM, as well as feedthroughs on the inner housing wall, the temperature stability was evaluated by comparing temperature traces during cooling before and after these modifications.

The integrated flow cryostat, operating with liquid nitrogen (LN_2), establishes a base temperature of 77 K at its cold tip. During the cooling procedure, the STM was clamped, whereby it was

pushed against the inner housing for efficient heat transfer. As the cryostat reached its stable equilibrium temperature with a temperature drift smaller than 10 mK/h, the STM was unclamped. This served as a criterion to start the actual measurement by allowing it to hang freely on its spring for suspension. Subsequently, temperature vs. time traces were recorded. Comparing the temperature traces before and after the mentioned modifications, a significant change was observed. Although the temperature increased slightly after unclamping, there was a notable temperature decrease of approximately 10 K after modifications. However, it became evident that the temperature lacked sufficient stability over time, with approximately 5 mK / h changes, making it unsuitable for STS measurements. (Figure 4.12) As a result, although the combined measures succeeded in reducing the final temperature with a steady state, the temperature drift remains unacceptably large.

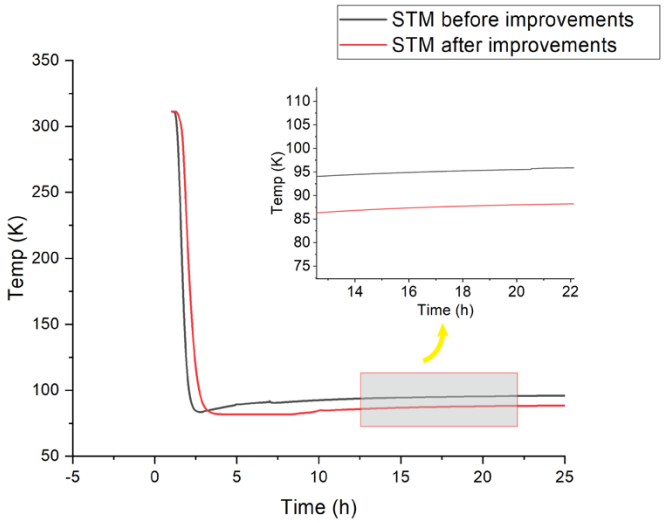

Figure 4.12 The plot of temperature changes over time for 1) before and 2) after implementation of the molybdenum pillars, feedthroughs, and heat bridges. The inset shows a magnification of the area marked with the gray rectangle. The plot offers a closer examination of a section of the temperature curve, highlighting the temperature difference in greater detail.

Following the implementation of all the aforementioned modifications, we aimed to gain a more comprehensive understanding of heat transfer, specifically the individual contributions of the signal versus control wires. To achieve this, a series of tests were conducted to evaluate the impact. Initially, a temperature trace with both signal and control wires connected was recorded (Figure 4.13, Plot 1). Subsequently, the measurement was repeated after disconnecting the signal wires (Figure 4.13, Plot 2) between the atmospheric feedthrough and copper feedthrough. (Section 4.4.1) Surprisingly, the temperature change without signal wires was comparable to the temperature change with both signal and control wires, which indicated that the main heat transfer occurred through the control wires and pins.

To prove the heat transfer effects through control wires, another test has been done by disconnecting control wires in addition to signal wires between the atmospheric feedthrough and sapphire feedthrough. As depicted in Plot 3 (Figure 4.13), the STM temperature became highly stable, affirming that the predominant heat transfer occurred through control wires.

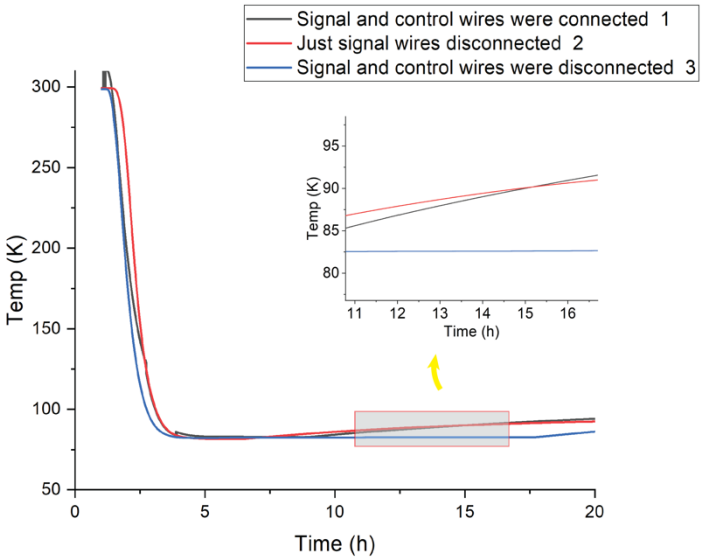

Figure 4.13 Illustration of the temperature traces for connected and disconnected wires. Plot 1 shows the temperature records with signal and control wires both connected to the outside feedthrough. Plot 2 displays the temperature records with just signal wires disconnected and control wires connected. Plot 1 and Plot 2 are comparable, indicating a minor effect of the signal wires. Indicating that there was no significant heat transfer with this setup. Plot 3 was acquired after disconnecting control wires as well as signal wires. The inset provides a magnified view of the area delineated by the gray rectangle in greater detail.

4.6 STM Mounting to Cryostat and Cooling Wires

In the initial design, the cooling mechanism of the microscope relied on establishing efficient heat contact with the inner housing through the STM base plate positioned on the three clamping stages. (Figure 4.14) These clamping stages served as the primary means of cooling, and the microscope remained clamped and in contact during the cooling process. However, once the final temperature was achieved, unclamping the microscope led to a temperature increase. (see Figure 4.12, the temperature changes over time for the STM after improvements) This rise was attributed to unavoidable heat uptake stemming from the uninterrupted signal wire and infrared radiation (IR) from the UHV chamber, which is at 300 K, through holes in the housing utilized for direct sublimation of molecules and optical accesses.

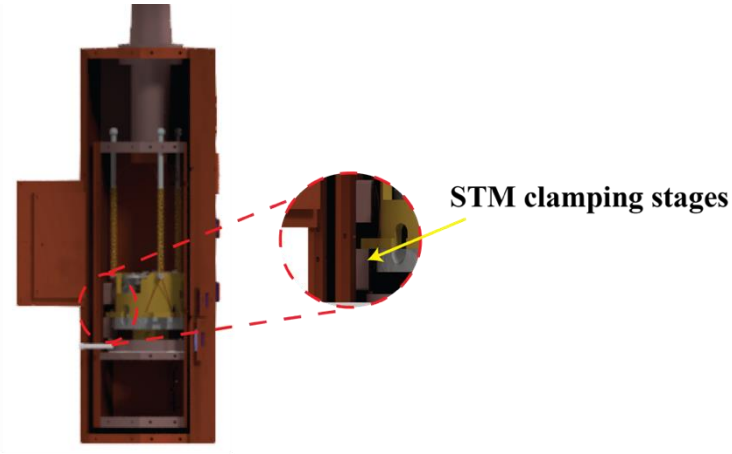

Figure 4.14 Drawing of the clamping stages embedded on the inner housing walls. During the cooling process, the STM is pushed against these stages by means of a spring, establishing direct contact and reaching lower temperatures.

4.6.1 Cryostat Cold Tip Screw

A fundamental modification was made to solve the above-mentioned issue by substituting the original 1/4" nominal diameter stainless steel screw responsible for securing the inner housing to the cryostat cold tip. The replacement involved designing a copper screw with an enlarged head (with thermal conductivity of ~ 395 W/m-K at room temperature)[113], as illustrated in Figure 4.15. The new design featured a head dimension 2.5 times larger than the previous screw. Subsequently, replacing the stainless steel screw with copper improves the thermal conductivity, which leads to more efficient heat transfer. Additionally, the screw's larger head dimension provides a greater contact area with the cold tip, which enhances the engagement between the screw and the cold tip and facilitates more effective cooling.

Furthermore, this copper screw included six symmetrically arranged tapped holes intended to accommodate M2 aluminum (Al) screws, served as a connection point for additional cooling wires, and were chosen for their notable high thermal conductivity (280 W/m.K at 100K).[114]

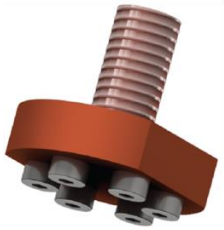

Figure 4.15 Schematic design of new copper screw used to mount the inner housing to the cold tip of the cryostat; in addition, it features six M2 Aluminum screws fastened on top.

4.6.2 Cooling Wires

These tapped holes on cryostat cold tip screw were used to fix an additional 12 OFHC cooling wires, each with a diameter of Ø 0.125 mm. These wires were fastened beneath the aluminum screw head and clamped at multiple points on the STM's base plate at the other end, as depicted in Figure 4.16. Additionally, to prevent any contact with these wires during sample positioning on the STM, they were routed through springs.

Selecting the clamping points for the cooling wires was also important to ensure there was no interference with the STM functionality. Specifically, the cooling wires should not come into contact with the inner core of the STM and hinder the approach mechanism. Besides, it was also essential to cool the base plate, as all STM parts were in contact with it.

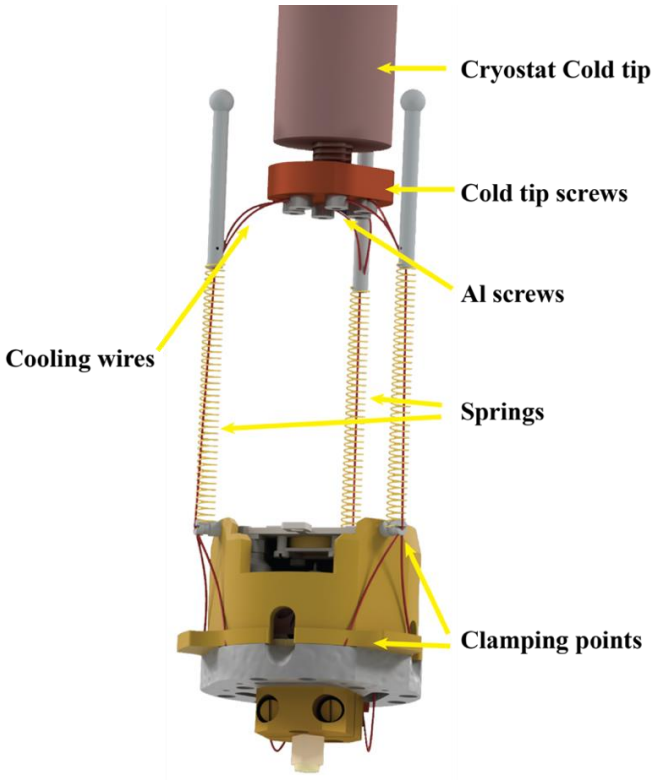

Figure 4.16 This schematic design showcases the arrangement of additional cooling wires that originate from the cryostat cold tip and are affixed at multiple points along the STM body to enhance the thermal equilibrium process by providing additional cooling power to lower the final equilibrium temperature and reducing temperature drift in equilibrium.

4.6.3 IR Radiation Shields

In LT-UHV-STM systems, the infrared (IR) radiation emitted from the walls of the UHV chamber is one of the primary causes of temperature rise. The heat absorption through IR radiation is susceptible to changes over time, influenced by variations in the ambient room temperature

within the laboratory. These fluctuations in IR radiation affect STM temperature, consequently introducing temperature gradients across the microscope and leading to subsequent drift.
Therefore, to minimize the influence of IR radiation, mechanical shutters and optical windows were implemented on the STM outer housing wall.

4.6.3.1 Shutter

On both the inner and outer housing of the STM, there are a few placed holes designed for optical access and direct deposition of molecules onto the sample while it is mounted in the STM. Therefore, although preventing direct exposure of the STM to IR radiation is crucial, it is equally essential to preserve the capability of depositing adsorbates onto the sample, especially at low temperatures.
Considering these requirements, a shutter was designed and installed on the outer housing wall (Figure 4.17). It was equipped with two magnets to fix the shutter in its two end positions of opening and closing and holding in the desired positions.
However, while the shutter effectively shields against external IR stray radiation, it may inadvertently become a source of IR radiation. Although magnets kept the shutter in position, this might not reduce thermal resistance when the shutter was not in good contact with the wall and resulted in maintaining different temperatures between the shutter and wall.
Therefore, the shutter was connected to the outer housing using a braided copper wire. This wire bridge was soldered to the wall and the shutter's surface to maintain the same temperature across the shutter as the housing walls.

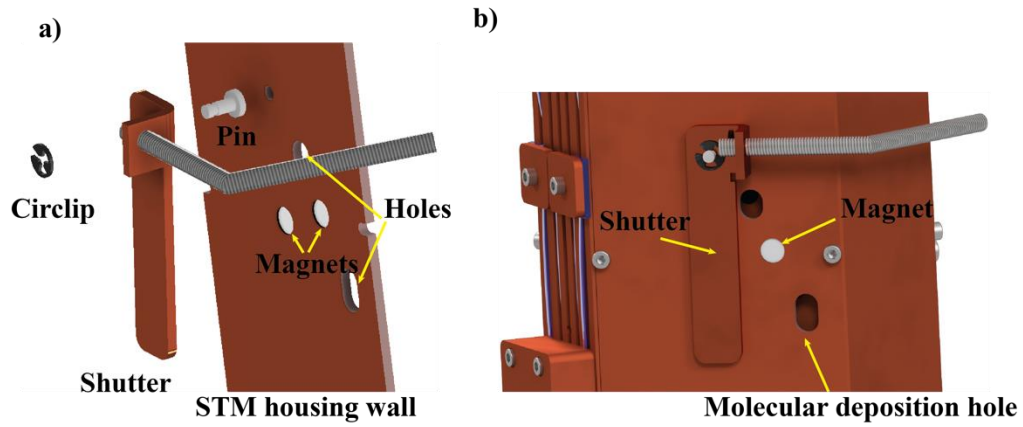

Figure 4.17 Schematic design of the mechanical shutter, with exploded parts view (a) and an assembled view.

4.6.3.2 Optical Windows

While the mechanical shutter for the deposition of adsorbates is just transiently opened during the deposition process, it would be advantageous to maintain permanent optical access to the STM. This is useful to approach the tip, but some photochemical experiments also require illumination at low temperatures as well, and opening a mechanical shutter can be disruptive to the experiment. For this purpose, optical windows were designed, consisting of square polished quartz glass and a copper frame that securely fastened with two M2 Aluminum screws to the outer wall. (Figure 4.18) Although quartz glass exhibits comparatively low thermal conductivity (around 2.52 W/m·K at room temperature[115]), it offers excellent transmittance, achieving 80% or higher across the entire wavelength spectrum. (From ultraviolet to near-infrared wavelength spectrum) Subsequently, quartz glasses became nearly intransparent in the infrared wavelength region and block the infrared radiation emitted from the UHV chamber at 300 K.

Additionally, quartz glass is more readily available at a lower cost compared to sapphire. Besides, to maintain the glass window at the same temperature as the outer wall, thick quartz glasses with a relatively large contact area (10x10x2 mm) were employed.

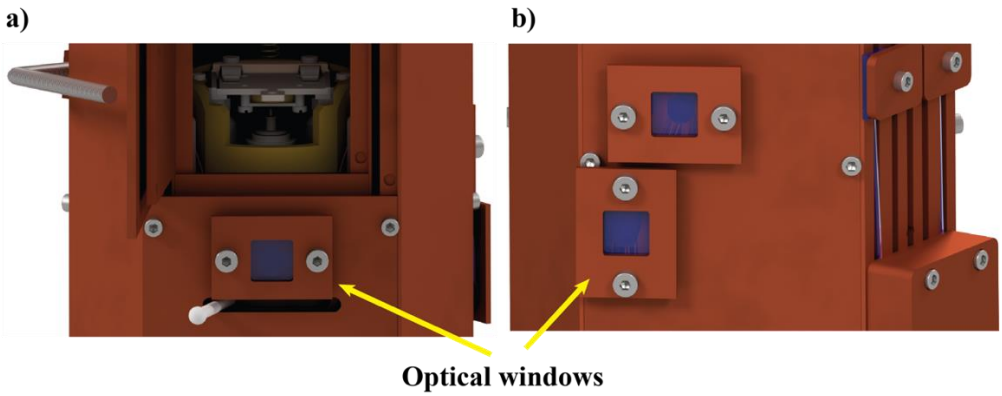

Figure 4.18 Schematic design of optical windows on the outer housing walls: a) is the STM housing front window designed to facilitate the use of an optical camera, ensuring secure tip coarse approach monitoring, and b) is the side windows positioned to support various surface illumination requirements for experimental purposes as well as illumination for tip approach.

4.7 Minimizing Heat Flow to STM through Thermal Anchoring of Wires on Outer Housing

As previously motioned, signal and control wires are connected to atmospheric feedthroughs that necessarily remain at room temperature, which poses a potential for inadvertent heat transfer through these wires. In our STM setup, the outer housing undergoes precooling (approximately 85 K) with cryogenic gas after evaporation in the cryostat. This presents an opportunity for some additional modifications and improvements aimed at thermally anchoring the wires to the outer

housing wall before clamping or connecting on the sapphire or copper feedthroughs in the inner housing wall.

4.7.1 Thermal Anchoring of Control Wires

For the thermal anchoring of the control wires, four separate docking stations were integrated into the back wall of the outer housing. Each station consisted of two small sapphire plates; one was glued to the outer housing wall using silver-filled epoxy, and the other was adhered to a square copper plate. Silver-filled epoxy was selected for its superior thermal conductivity of 11 W/m-K at room temperature compared to H74 epoxy, which typically has a thermal conductivity of 1.3 W/m-K under the same temperature. In addition, to allow sapphire direct contact with the wall surface, the epoxy was applied to its edges.

Two control wires were sandwiched and clamped between the two sapphire plates, and the copper plate was tightened to the wall using screws (Figure 4.19). Sapphire plates were chosen for two primary reasons, to provide electrical insulation and their intrinsic property of high thermal conductivity at low temperatures, which enhances cooling efficiency.
Therefore, this configuration facilitated the partial removal of the Polytetrafluoroethylene (PTFE) insulator from the stainless steel control wires at the clamping points and enabled direct contact with the sapphire surface.

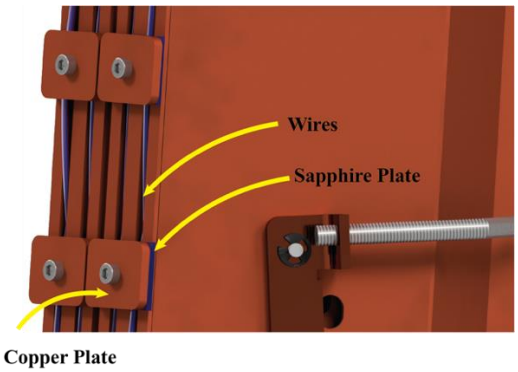

Figure 4.19 Schematic drawing of control wires clamped between two sapphire plates on the cooled cold STM outer housing wall.

4.7.2 Thermal Anchoring of Signal Wires

The coaxial signal wires were also directly clamped to the outer housing wall using copper plates at various locations, as depicted in Figure 4.21 (Dock Station 3), and along the top edge of the housing wall with additional clamps (Figure 4.20). To enhance thermal contact, the outer Teflon insulation was removed to provide contact between the metal braid and the wall. The signal wire could be directly clamped by a metal plate because of the additional Teflon insulation between the

coaxial wire core and the braid shielding, which prevents any shortcut. While the shield also served as grounding and reduced surrounding noise effects, thermal clamping could contribute to cooling the entire signal wire. Besides, this modification improved minimizing the potential for inadvertent wire movements that could introduce mechanical noise into the system.

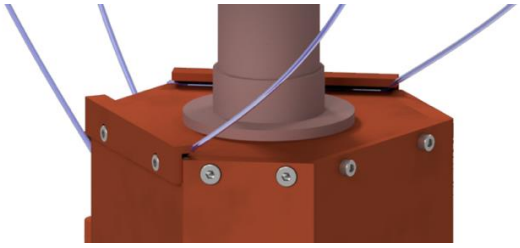

Figure 4.20 The schematic drawings depict the arrangement of signal wire clamping at the top edge of the outer housing.

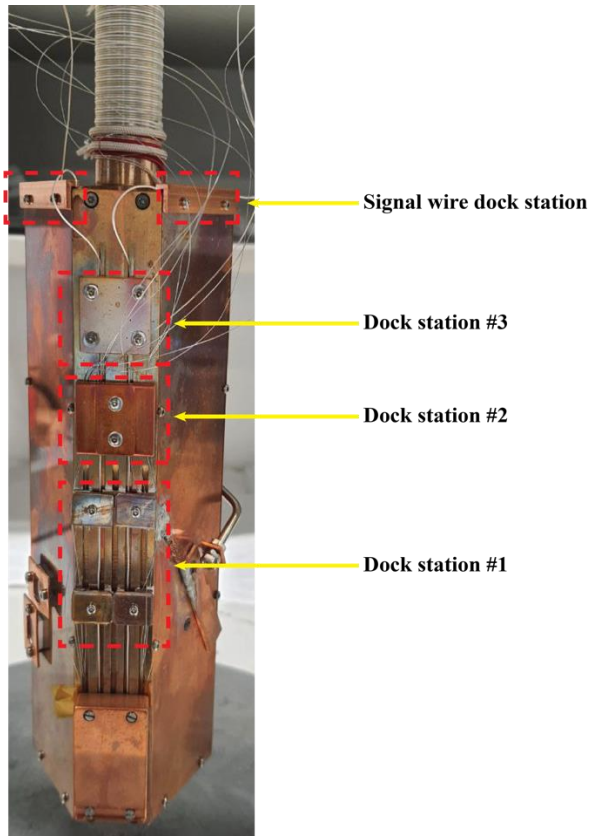

Figure 4.21 Photograph of the backside of the outer housing depicting the thermal anchoring locations.

4.8 Results and Conclusion

The implementation of cooling wires directly through the cryostat cold tip provided the necessary cooling power to the STM and thereby kept temperature stability throughout the experiment, even when the STM was unclamped for measurements. Besides, coupling with additional shields against infrared (IR) radiation to prevent heat uptake has provided the STM with

high-temperature stability and minimized thermal drift. Figure 4.23 illustrates that the STM reaches a base temperature of 82K within two hours of initiating the cooling procedure. This improved configuration allows the STM to rapidly reach low temperatures (previously, before improvements, a minimum of 4 to 5 hours was required to reach the base temperature of 95K) and start the measurement immediately after unclamping. Figure 4.22 also represents the STM image of the fluorinated anthracene-triptycene on I-Au (111) surface, which is recorded directly after unclamping at 82K and with no observable drift. This STM image was recorded using a tunneling current of 10 pA, which highlights the system's remarkable capability to operate effectively at low tunneling currents.

Consequently, the STM system achieves temperature stability at LN_2 temperatures within 10 hours with temperature variations measured less than 10 mK per hour, ensuring a sustained and stable temperature over extended durations and also showcasing a suitable instrument for STS measurements.

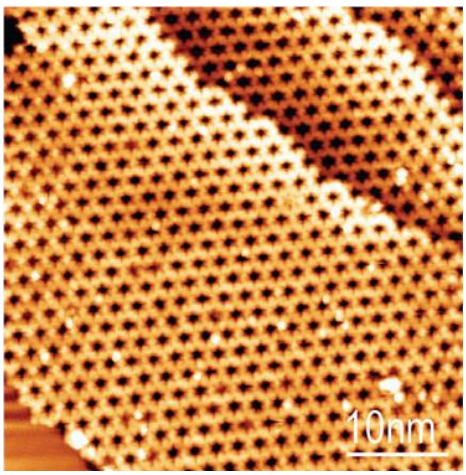

Figure 4.22 STM image of fluorinated anthracene-triptycene on I-Au (111) surface recorded immediately after the STM unclamping at~82K (tunneling parameters: 1.2 V, 10 pA)

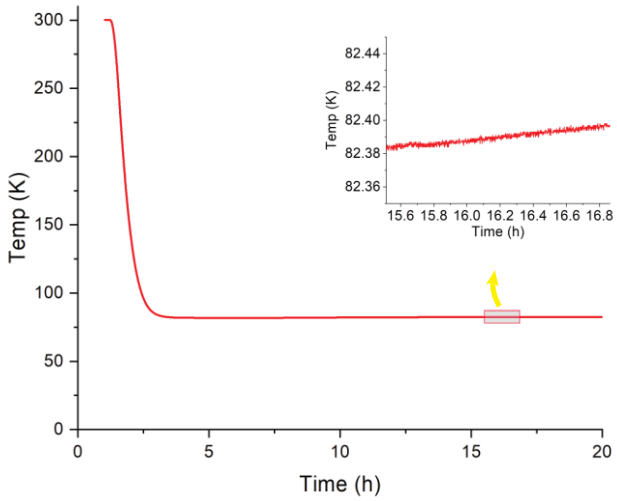

Figure 4.23 Temperature stability of the STM after the incorporation of cooling wires, cryostat cold tip screw, IR radiation shields, and thermal anchoring of the control and signal wires on the back side of the outer housing wall. The inset provides a magnified view of the area delineated by the gray rectangle for better detail.

Furthermore, the STM exhibits remarkable vertical drift stability even at approximately 82 K, as evidenced by the stability of the tunneling current and tunneling gap after deactivating the feedback. During a minimum period of 5 minutes, the current changes remained below 5%. However as depicted in Figure 4.24, during this time, the measured current was affected by noise. This sudden emergence of noise upon deactivating the feedback could be attributed to various sources, including mechanical vibrations or disturbances from the surrounding environment or the operation of turbomolecular pumps.

In conclusion, our existing home-built LT-STM setup has experienced significant enhancements that enabled cooling at LN_2 temperatures and minimized drift. These improvements have effectively reduced thermal drift by optimizing heat flow within the microscope. This optimization involved placing STM control and signal wires on a cold surface by means of interrupting heat transfer, substituting low heat-conductive parts with high-conductive materials, introducing thermal bridges, and directly supporting cooling wires from the cold tip to enhance cooling power

These implementations have resulted in enhanced temperature stability of 82K for prolonged operation in both STM and STS modes, with minimized thermal drift and reduced cooling time and liquid nitrogen consumption.

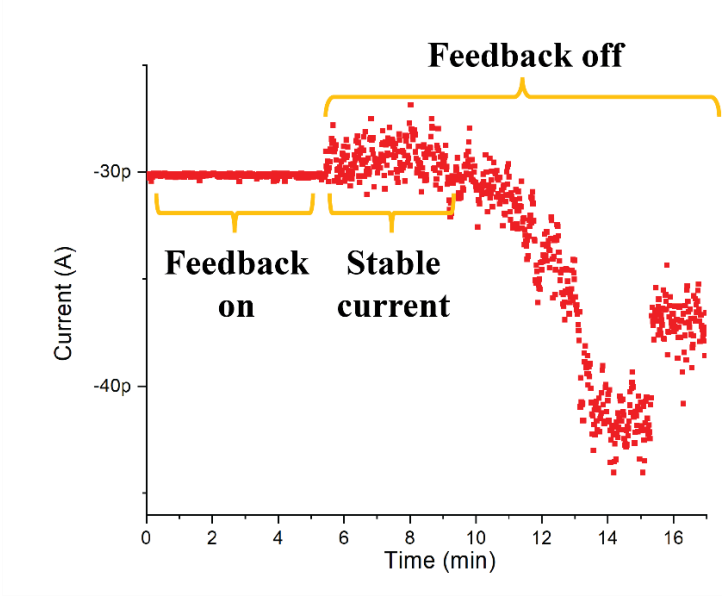

Figure 4.24 Graph showing the current stability over time. The plot is divided into two sections: one with the STM feedback control on (the left-hand side) and the other while it is off. When the feedback control is off, the STM exhibits drift stability, and the current remains unchanged for a minimum of 5 minutes.

Chapter 5

Iodine Passivation Facilitates On-Surface Synthesis of Robust Regular Conjugated Two-Dimensional Organogold Networks on Au (111)

This chapter delves into the On-Surface Synthesis of two-dimensional organometallic and covalent nanostructures. It indicates the presence of a partially passivated Au(111) surface with an adsorbed monolayer of iodine (I-Au(111)) yields a highly regular organogold 2D network. The foundation for this exploration lies in the published paper titled " Iodine Passivation Facilitates On-Surface Synthesis of Robust Regular Conjugated Two-Dimensional Organogold Networks on Au(111)" which is authored by Arash Badami-Behjat, Gianluca Galeotti, Rico Gutzler, Dominik L. Pastoetter, Wolfgang M. Heckl, Xinliang Feng, and Markus Lackinger, and was originally published in Nanoscale Horiz., 2024, Advance Article. This chapter is reprinted and partially adapted with permission from the Royal Society of Chemistry.

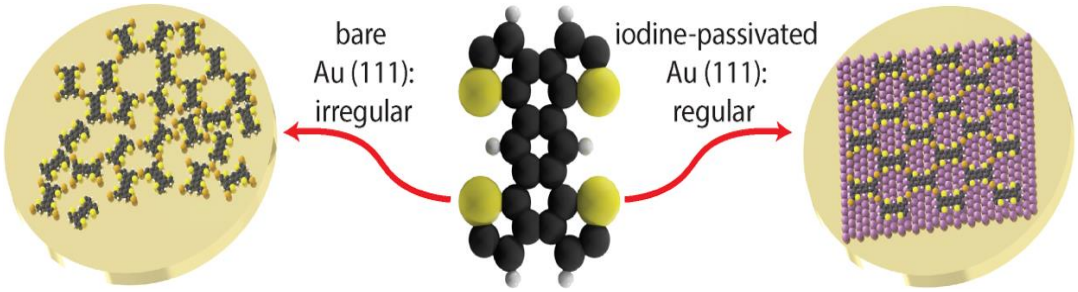

Two-dimensional conjugated organogold networks with anthra-tetrathiophene repeat units are synthesized by thermally activated debrominative coupling of 2,5,9,12-tetrabromoanthra[1,2-b:4,3-b′:5,6-b″:8,7-b‴] tetrathiophene (TBATT) precursor molecules on Au(111) surfaces under ultra-high vacuum (UHV) conditions. Performing the reaction on iodine-passivated Au(111) surfaces promotes the formation of highly regular structures, as revealed by Scanning Tunneling Microscopy (STM). In contrast, coupling on bare Au(111) surfaces results in less regular networks due to the simultaneous expression of competing intermolecular binding motifs in the absence of error correction. The carbon-Au-carbon bonds confer remarkable robustness to the organogold networks, as evidenced by their high thermal stability. In addition, as suggested by Density Functional Theory (DFT) calculations and underscored by Scanning Tunneling Spectroscopy (STS), the organogold networks exhibit a small electronic band gap in the order of 1.0 eV due to their high π-conjugation.

My contribution to this work involved performing UHV-LT-STM experiments, based on initial experiments performed by Gianluca Galeotti, substrate and sample preparation, and room-temperature STM experiments. Additionally, I was responsible for analyzing and interpreting the corresponding STM data for the manuscript preparation under the supervision of Prof. Dr. M. Lackinger who conceived and designed the study. Dominik L. Pastoetter and Xinliang Feng synthesized and purified the compound. Rico Gutzler performed the DFT calculations and analyzed the results.

5.1 Introduction

Dehalogenative couplings are arguably the most widely used and important reactions for the on-surface synthesis of extended covalent and organometallic nanostructures on coinage metal surfaces.[16,90,116,117] Topologically one-dimensional (1D) structures, with graphene nanoribbons being the most prominent example,[118,119] are obtained from ditopic precursor molecules. Two-dimensional (2D) organometallic networks and polymers, on the other hand, can be synthesized from precursors with more than two halogen substituents. But the structural quality obtained in 2D is typically relatively low. Linking monomers in two dimensions is more challenging, for example, because long-range order is often compromised by structural defects such as topological errors or missing repeat units, which are inherently absent in topologically linear structures. On the one hand, strong covalent, metal-organic, or organometallic bonds are the foundation for high robustness. On the other hand, high bond strength causes irreversibility, hence precludes error correction during growth.

Nevertheless, several strategies have proven viable to achieve the synthesis of highly regular 2D polymers on solid surfaces, including dynamic covalent chemistry,[120,121,122,123,124] organometallic templating,[125,126] lateral fusion of preformed entities,[127,128,129,130] the use of small rigid building blocks to kinetically suppress defect formation,[131] and topochemical photopolymerization.[132] Each approach to synthesis on solid surfaces has its specific pros and cons; for example, carbon-carbon bonded structures remain elusive for dynamic covalent chemistry, while π-conjugated structures present a challenge for photopolymerization by cycloaddition reactions.[133,134]

The goal here is to explore coupling on iodine-passivated metal surfaces as a possible complementary new synthesis route to regular and robust two-dimensional nanostructures. The conceptual idea of synthesis on passivated surfaces in general is that the substrate is still chemically active enough to initiate the reaction, while detrimental substrate effects such as limited monomer mobility or side reactions are shielded. The latter is particularly important for the thiophene-containing monomer studied here: while thiophenes are highly relevant for organic electronics,[135] their widespread use in on-surface synthesis on metals is limited by their susceptibility to decomposition.[136,137] Previous work on metal surfaces has used inorganic 2D materials such as graphene or hexagonal boron nitride as ultimately thin passivation layers.[138,139] While it has been shown that either the attenuated reactivity of the underlying metal or co-deposited metal atoms can promote dehalogenative couplings, the quality of the resulting structures has not been significantly improved compared to synthesis directly on metals.

In the present work, we have chosen passivation of Au(111) by a monolayer of chemisorbed iodine (I-Au(111) in the following) for several reason: Previously, my group has developed a method for post-synthetic decoupling of covalent nanostructures from the metal surfaces on which they were grown by intercalation of an iodine monolayer.[140,141] From X-ray Standing Wave experiments my research group inferred a relatively large adsorption height in the order of 6 Å with respect to the topmost metal atoms, which indicates efficient decoupling.[142] Moreover, in our recent studies of supramolecular self-assembly on I-Au(111) (see Chapter.7), I found that the molecule-surface interactions can be even weaker than on graphite.[143,144] Iodine adopts a variety of superstructures on Au(111) where the area density of the chemisorbed iodine atoms ranges from 4.63 nm^{-2} for the common $\sqrt{3}\times\sqrt{3}R\pm30°$ superstructure up to 5.55 nm^{-2} for the uniaxially compressed $p(5\times\sqrt{3})$ superstructure.[145,146] Accordingly, even a closed $\sqrt{3}\times\sqrt{3}R\pm30°$ iodine monolayer still has the capacity to additionally incorporate a fair amount of dissociated halogens as the byproduct of the coupling reaction. Finally, the I-Au(111) surface can dynamically and advantageously change its reactivity during heating due to iodine desorption.

In the present work, we demonstrate that iodine-passivated Au(111) surfaces can indeed remain reactive for dehalogenation reactions (cf. Appendix A for preparation parameters). Debrominative coupling of the tetra-bromine substituted TBATT precursor leads to highly robust and π-conjugated 2D organogold networks. More importantly, the synthesis on I-Au(111) also offers a crucial advantage over bare Au(111), namely the high regularity of the obtained 2D organogold networks.

5.2 Results and Discussion

5.2.1 Bare Au(111)

On-surface polymerization of the TBATT precursor (Figure 5.1a for structure) by debrominative coupling has previously been studied on Ag und Cu surfaces,[136,147] where organometallic networks formed with surface supplied metal atoms. These organometallic networks are considered metastable because reductive elimination of the organometallic metal atom results in the conversion to the thermodynamically more stable carbon-carbon bonds. However, the TBATT-derived organometallic networks were mostly irregular with only smaller regular patches due to the kinetic competition between syn- and anti-binding motifs in the irreversible regime, Apart from rare exceptions,[148] dehalogenation on Ag und Cu surfaces results in organometallic intermediates.[116, 125,126] This was also observed for TBATT on Cu(111), where the conversion from organometallic to covalent was averted by the decomposition of the thiophene

moieties at the required temperatures.[136] By contrast, decomposition was mitigated on Ag(111), where covalent networks could be obtained via the organometallic intermediate by annealing at 300 °C.[147]

For further reference, we first explore the debrominative coupling of TBATT directly on bare Au(111). Figure 5.1b and c show STM images of the self-assembled structures obtained directly after room temperature deposition of TBATT on Au(111), also confirming the purity of the reactant by the complete absence of impurities. The lattice parameters of the oblique unit cell are a=1.1 ± 0.1 nm, b=1.4 ± 0.1 nm and 76° ± 1°, and the arrangement of the intact TBATT molecules is controlled by intermolecular Br···S, Br···H and Br···Br halogen bonds,[149,150] as illustrated by the tentative model of the self-assembly in Figure 5.1d.

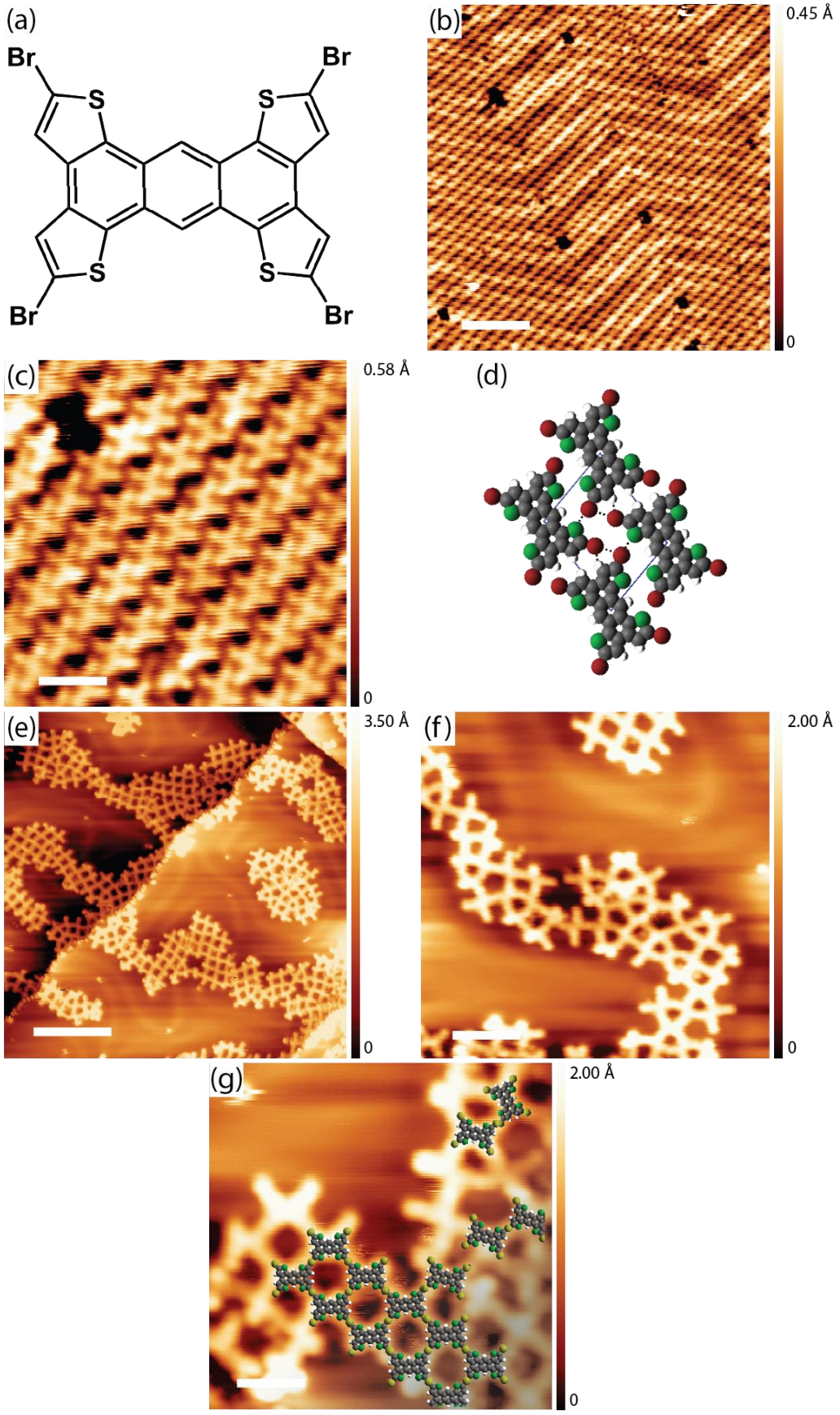

Figure 5.1 (a) Chemical structure of TBATT; (b) / (c) STM images of the TBATT self-assembly on bare Au(111) as observed after room temperature deposition; (d) tentative model of the self-assembly derived

from the experimental structure (C: gray; Br: red; S: green; H: white); intermolecular halogen bonds are indicated by dashed lines. (e) - (g) STM images of the irregular organogold networks as obtained after annealing to 200 °C - 220 °C; The image in (g) is overlaid with DFT-calculated organogold dimers and tetramers in which debrominated monomers are linked by carbon-Au-carbon bonds. The scaled overlays confirm the size match and thus the chemical identity of the intermolecular bonds. Covalent carbon-carbon bonds are about 0.26 nm shorter than organometallic carbon-Au-carbon bonds (cf. Appendix A, Figure A. 1) and would result in an obvious mismatch. (tunneling parameters and scale bars: (b) +1.1 V, 120 pA, 10 nm; (c) +1.1 V, 120 pA, 2 nm; (e) +900 mV, 120 pA, 10 nm; (f) +900 mV, 120 pA, 4 nm; (g) +900 mV, 120 pA, 2 nm, all STM images were acquired at low temperature)

Annealing at 200 °C - 220 °C activates the debromination, resulting in the mostly irregular networks shown in Figure 5.1e - g. The measured center-to-center distance of 1.5 ± 0.1 nm between adjacent molecules is incompatible with DFT-calculated values for direct carbon-carbon bonding of the monomers, but is consistent with corresponding calculations for organometallic carbon-Au-carbon bonds (see overlay in Figure 5.1g) and the organometallic structures obtained for TBATT on Cu(111) and Ag(111).[147] Similarly, organogold networks were observed for tri-bromo-terthieno-benzene on Au(111),[137] that is the three-fold symmetric analogue of TBATT. In summary, in view of our calculations and previously reported work,[137, 147] our experiments consistently indicate the formation of organogold networks after debromination of TBATT. To quantify the quality of the structure, we performed a statistical analysis of the pore shapes, resulting in a proportion of 28% rhombic pores (cf. Appendix A Figure A.2, 624 closed pores were counted in total) formed by four molecules with similar azimuthal orientations (see Figure 5.1f for structure.) Extension of the rhombic pore with the ideal homotactic bonding of all molecules would result in a fully regular network. All other shapes of closed pores suffer from bond deformation, hence are energetically not ideal. However, we were not able to obtain better ordered networks directly on bare Au(111). It is worth noting that although metastable organogold intermediates on Au(111) have been reported previously,[151,152,153,154,155,156,157] they are still the exception rather than the rule.

5.2.2 Iodine-passivated Au(111)

In the next step, TBATT was deposited on I-Au(111) (see Appendix A, Materials and Methods section for preparation procedures and parameters), where we observed intact molecules in ordered supramolecular structures (Figure 5.2a) that co-existed with dispersed single TBATT molecules (Figure 5.2b). Although the principal arrangement of the TBATT molecules in the self-assembly is comparable to that on bare Au(111) (Figure 5.2c), the rectangular unit cell is substantially larger with a=1.5 ± 0.1 nm, b=1.7 ± 0.1 nm. This marked change in lattice parameters compared to bare Au(111) underscores the adsorption of the TBATT molecules onto a closed iodine monolayer. As further illustrated by the tentative model in Figure 5.2c, the intermolecular distances have increased

significantly, resulting in a pronounced weakening of the intermolecular interactions. The model is based on a commensurate $\begin{pmatrix} 3 & 1 \\ 1 & 4 \end{pmatrix}$ superstructure (with respect to the iodine monolayer) that agrees with the experimental lattice parameters and reproduces the orientation of both the unit cell and the TBATT molecules with respect to the iodine lattice. It also suggests equivalent adsorption sites for all four bromine substituents of each TBATT molecule. Accordingly, we hypothesize that the self-assembly of fully brominated TBATT on I-Au(111) is governed by registry effects imposed by the highly corrugated iodine monolayer.

Annealing these samples at 200 °C - 220 °C induced a profound structural change from densely packed to the porous grid-like network depicted in Figure 5.2d - f with a centered rectangular unit cell measuring a=1.8 ± 0.1 nm and b=2.1 ± 0.1 nm. These experimental dimensions differ substantially from the DFT-calculated values of a=1.40 nm and b=1.96 nm for the putative covalent network (cf. Appendix A, Figure A. 1a). However, there is a good agreement with the DFT-optimized lattice parameters of a=1.81 nm and b=2.30 nm of the organogold networks, in which the anthra-tetrathiophene moieties are linked by carbon-Au-carbon bonds (cf. Appendix A, Figure A. 1b). This structural assignment is also corroborated by the scaled overlay in Figure 5.2f. Moreover, the center-to-center distance between adjacent molecules in the ordered network of 1.4 ± 0.1 nm matches perfectly with the organogold structures obtained on bare Au(111). More importantly, the organogold networks obtained on I-Au(111) are highly regular with 92% of the ideal rhombic pores (cf. Appendix A, Figure A.3, 1174 closed pores were counted in total).

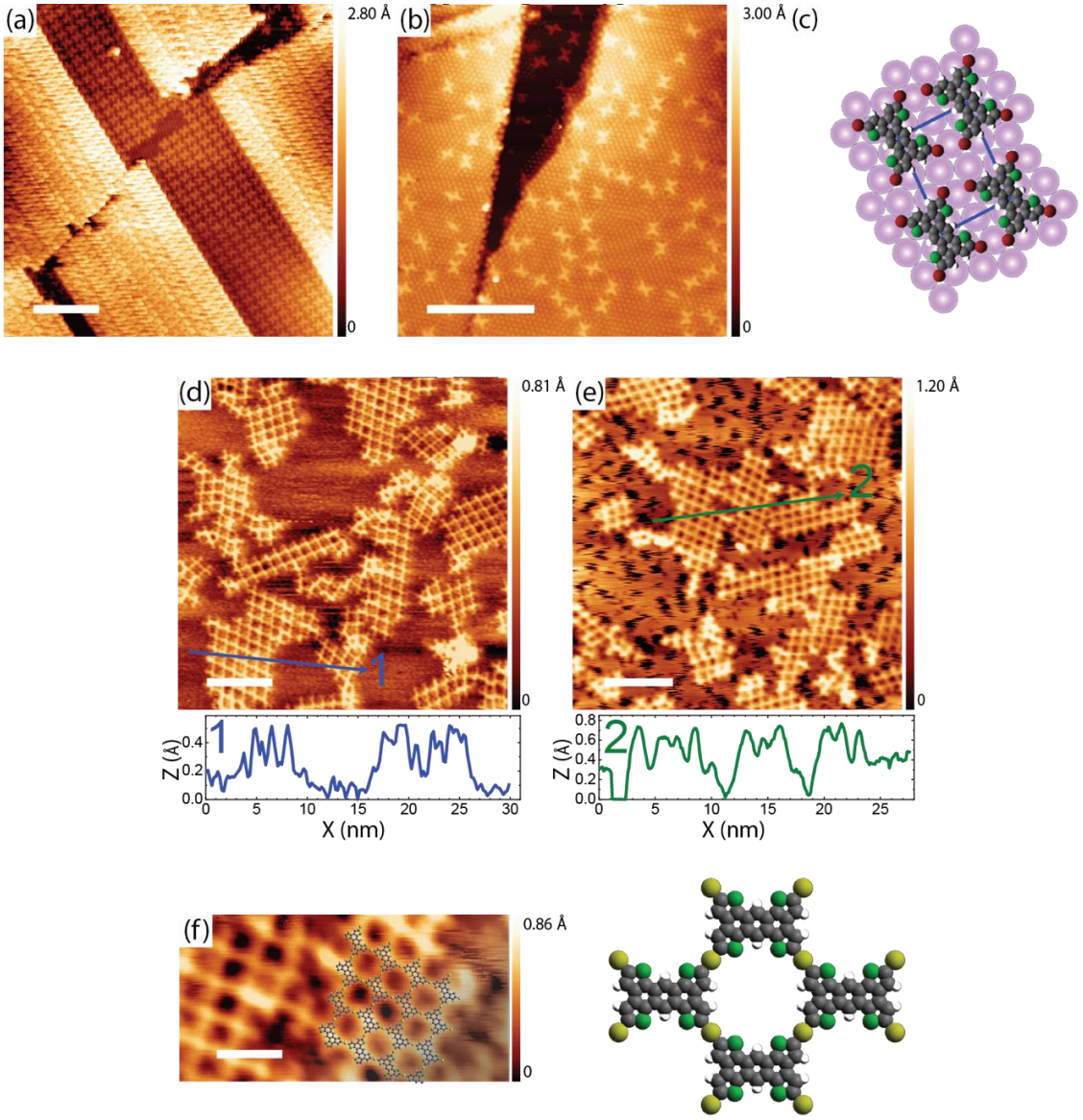

Figure 5.2 STM images of TBATT structures on iodine-passivated Au(111). (a) self-assembly of intact molecules and (b) dispersed single molecules as similarly observed after room temperature deposition; The brighter appearing areas in (a) correspond to a TBATT bilayer. (c) tentative model of the self-assembled TBATT structure on I-Au(111); Pink circles indicate iodine atoms of the monolayer. (d) - (f) STM images of highly regular organogold networks as obtained after annealing at 200 °C - 220 °C; The image in (d) was acquired at room temperature and shows an apparently closed iodine layer. However, the corresponding low-temperature STM image in (e) reveals the fuzzy black areas where iodine was desorbed during the annealing. (f) Close-up STM image with scaled overlay of the organogold network; besides a model of the organogold structure is shown (Au: yellow). (tunneling parameters and scale bars: (a) +1.8 V, 120 pA, 10 nm; (b) +1.8 V, 120 pA, 10 nm; (d) +1.0 V, 120 pA, 10 nm; (e) +1.0 V, 120 pA, 10 nm; (f) +1.0 V, 120 pA, 3 nm, all STM images were acquired at low temperatures except for (d))

Interestingly, while the iodine layer appears completely closed when imaged at room temperature (Figure 5.2d), corresponding STM images taken at low temperatures (Figure 5.2e) reveal darker appearing, fuzzy patches of missing iodine. We argue that iodine partially desorbs during the thermal treatment used to form the networks. This is supported by STM images of a similarly prepared I-Au(111) surface acquired at low temperatures before the annealing step, which

clearly show that the seemingly closed iodine monolayer does not completely cover and passivate the Au(111) surface (see Figure 5.3). Accordingly, a gradually decreasing iodine coverage during heating provides access to the bare Au(111) surface for activation of the debromination. This is also the most plausible pathway by which the Au atoms are made available for organometallic bond formation. While it is plausible that the iodine monolayer is mostly intact at the onset of debromination, we assume that the progressive iodine desorption will eventually result in iodine vacancy islands that can become large enough to accommodate monomers or even smaller domains of the organogold networks. Indeed, the resulting ruggedness of the iodine passivation layer may also hamper the growth of larger domains of the organogold networks. It also remains presently unclear whether the organogold networks are adsorbed on the remaining patches of the iodine layer or on the bare Au(111). The networks prepared directly on Au(111) (cf. Figure 5.1) exhibit apparent STM heights between 0.1 and 0.2 nm. On the iodinated surfaces the apparent height of the networks with respect to the underlying Au(111) can be estimated by line-profiles extending through the iodine vacancy islands as shown in Figure 5.2. There we find apparent STM heights either in the order of 0.15 nm but also occasionally > 0.2 nm. This may indicate a heterogeneous sample state with most organogold domains already adsorbed on bare Au(111) and few remaining on iodine islands. However, we note that apparent STM heights are generally bias- and tip-dependent and thus unreliable. For an accurate assessment of adsorption heights, X-ray Standing Wave experiments are the gold standard.[142]

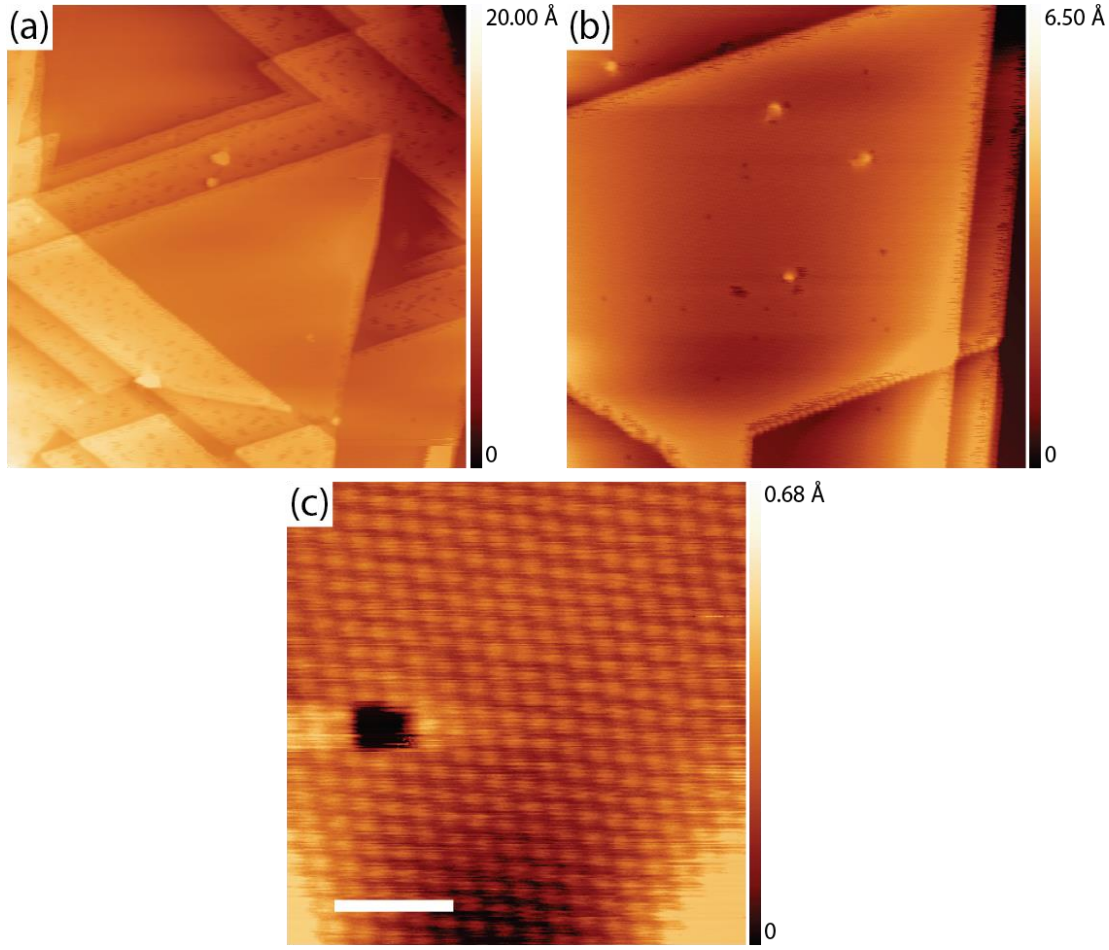

Figure 5.3 STM images of a still reactive iodine passivation layer on Au(111) prepared by mild iodine exposure (5×10^{-7} mbar of I_2 for 10 min) acquired at low temperature. (a) / (b) Overview and (c) close-up. These STM images reflect the stage of the I-Au(111) samples before they were annealed to form the networks. They confirm that the iodine monolayer is not fully closed prior to the thermal treatment to form the networks but exhibits a fair amount of vacancy islands. As shown in (b), the passivation of Au(111) is incomplete, especially at the substrate step-edges. (tunneling parameters and scale bars: (a) +1.0 V, 100 pA, 20 nm; (b) +1.0 V, 100 pA, 10 nm; (c) +1.0 V, 100 pA, 2 nm, all STM images were acquired at low temperature)

To confirm that a certain permeability of the iodine monolayer is crucial for debromination, we performed a control with a highly iodinated sample prepared with a 20-fold increased iodine exposure (see Appendix A, Materials and Methods section). After deposition of TBATT and subsequent annealing at 250 °C, which is 30 °C to 50 °C higher than normally used to initiate debromination, a mostly empty I-Au(111) surface was imaged by STM (see Figure 5.4a and b). Only upon further heating to 350 °C were small remnants of reacted molecules observed at the substrate step-edges, while the iodine was completely desorbed (see Figure 5.4c and d). This clearly indicates that the initial iodine exposure used to prepare the monolayer must not be too high to obtain reactive I-Au(111) surfaces that facilitate thermally activated debromination. In addition, we also observed that the reactive I-Au(111) surfaces prepared with lower iodine exposure show both areas where the iodine packing is less dense and residual single iodine atom vacancies (see

Figure 5.3 and Figure 5.5), as similarly observed for electrochemically deposited iodine adlayers.[146] Furthermore, we hypothesize that iodine desorption is enhanced in the less densely packed areas, ultimately promoting progressive desorption and the formation of larger vacancy islands.

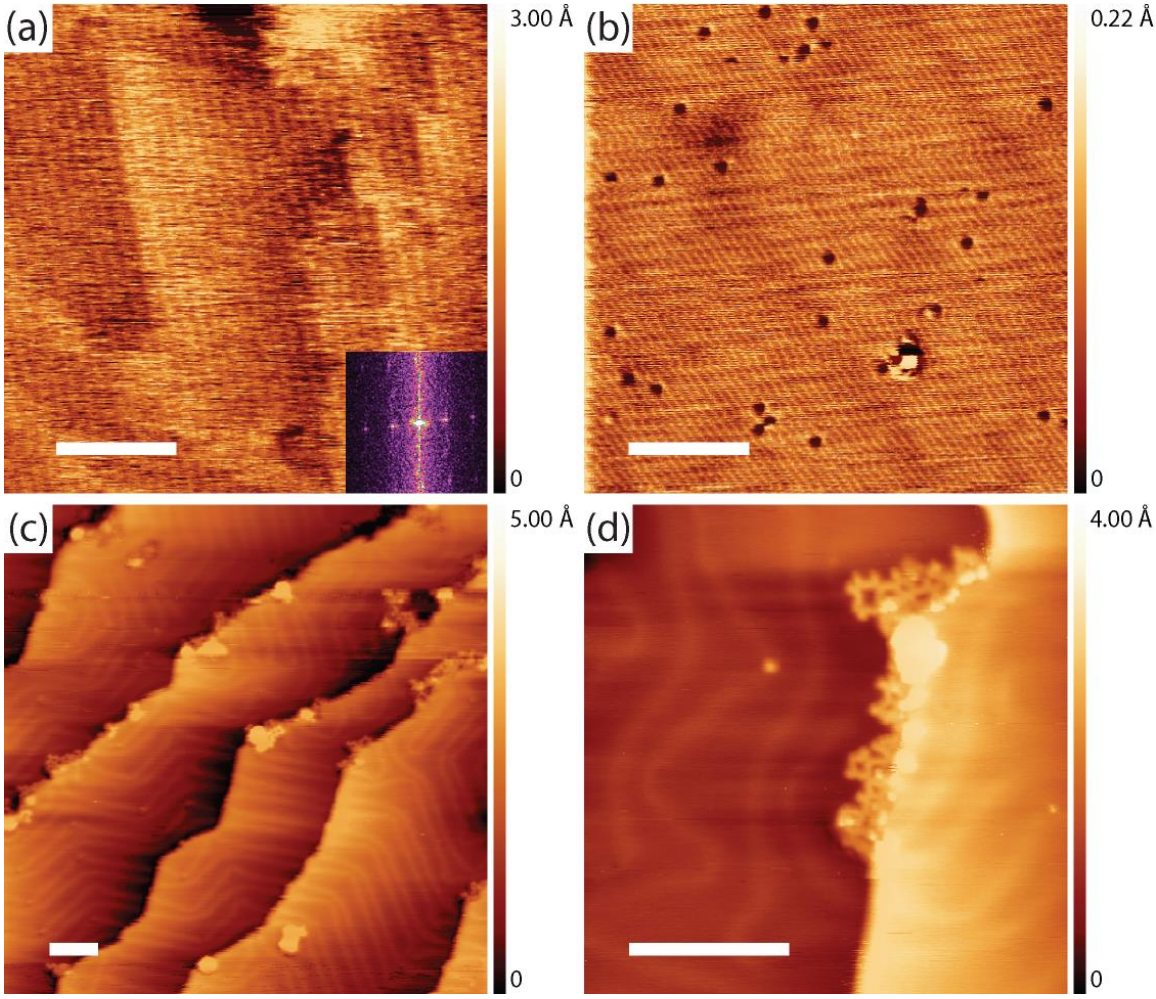

Figure 5.4 STM images of TBATT molecules deposited on a highly (5×10^{-6} mbar I_2 for 20 min) iodinated Au(111) sample acquired (a) directly after deposition, (b) after annealing this sample at 250 °C for 15 min and (c) / (d) after further annealing at 350 °C for 15 min. The stripes in (a) have a spacing of 1.2 ± 0.1 nm (2D Fast-Fourier-Transform shown as inset in (a)), which is in agreement with the lattice parameter of the self-assembled structure. We conclude that these stripes correspond to a self-assembly of intact TBATT molecules as expected. In contrast, after annealing at 250 °C, stripes were again observed, but with a significantly smaller stripe spacing of 0.6 ± 0.2 nm. This spacing is consistent with the densely packed iodine monolayer, indicating the desorption of most of the TBATT molecules and also the onset of iodine desorption, resulting in the clearly visible black holes. Upon heating to a higher temperature of 350 °C, the STM images in (c) and (d) show the reappearance of the Au(111) herringbone reconstruction, indicating the desorption of the iodine passivation layer. Smaller patches of molecular networks are observed, but only at the step-edges. We hypothesize that these form when the Au(111) surface becomes accessible by iodine desorption. However, the relatively low coverage suggests that most of the TBATT precursor molecules have already desorbed. (tunneling parameters: (a) +1.1 V, 120 pA; (b) +600 mV, 110 pA; (c) +600 mV, 110 pA; (d) +600 mV, 110 pA; all scale bars are 10 nm, all STM images were acquired at room temperature)

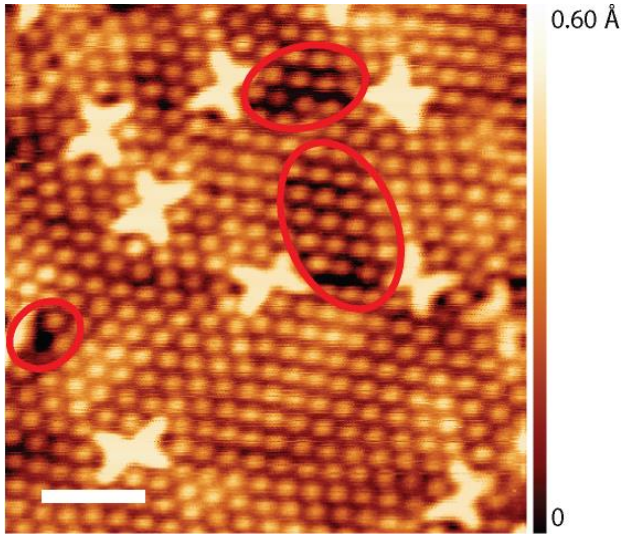

Figure 5.5 Low temperature STM image of a reactive iodine monolayer prepared with the lower iodine exposure. (see Appendix A for sample preparation). The image was acquired at low temperature after deposition of the TBATT molecules, but before the networks were formed by sample annealing. The bright butterfly-shaped features correspond to individual unreacted TBATT molecules. Although the iodine monolayer appears densely packed and completely closed at room temperature (see Figure 5.2), low temperature imaging reveals areas where the iodine layer is not densely packed (an example is highlighted by the larger oval). In addition, iodine vacancies can be observed (an example is highlighted by the smaller oval). In contrast, completely densely packed iodine monolayers prepared by a 20-fold increased iodine exposure are no longer reactive (see Figure 5.4). We conclude that the less densely packed regions are the active sites for the initial debromination and also provide the Au-atoms for the formation of the organogold networks. (tunneling parameters and scale bar: +900 mV, 120 pA, 2 nm, STM image acquired at low temperatures)

5.3 Robustness of the Organogold Networks

To explore the robustness of the organogold anthra-tetrathiophene networks, the samples were annealed to successively higher temperatures. After annealing at 300 °C, remnants of the iodine monolayer were still present (see Figure 5.6), which were completely desorbed after annealing at 320 °C. The corresponding STM images in Figure 5.7a and b confirm the persistence of the networks. Yet, the line profiles in Figure 5.7d and e reveal different pore sizes, where the smaller pores clearly indicate the onset of conversion of organometallic carbon-Au-carbon bonds into covalent carbon-carbon bonds as similarly observed on Ag(111).[147] However, this conversion is also accompanied by a loss of regularity. When heated to markedly higher temperatures of 400 °C, the degradation becomes apparent in the STM images (Figure 5.7c).[141] Although the stability is not directly tested at high temperatures, subsequent STM imaging allows conclusions to be drawn about the integrity of the networks. Disintegration of the organogold networks at high temperatures and reformation when cooling back to room temperature can be excluded, since individual monomers would desorb at temperatures above 300 °C (vide infra).

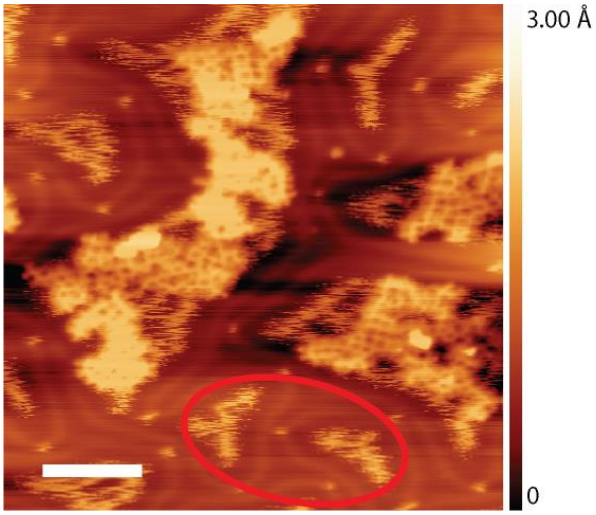

Figure 5.6 STM images of TBATT-derived organogold networks prepared on a reactive I-Au(111) surface obtained after additional annealing at 300 °C. This image was acquired at room temperature. While the organogold networks could be imaged, the image additionally shows fuzzy appearing features (an example is highlighted by the oval) corresponding to remnants of the mostly desorbed iodine layer. These features disappear completely when the sample is heated to a slightly higher temperature of 320 °C (see Figure 5.7). The characteristic soliton lines of the reappearing Au(111) herringbone reconstruction can also be seen. (tunneling parameters and scale bar: +1.2 V, 120 pA, 10 nm, STM image acquired at 300 ºC temperature)

Despite the onset of conversion to covalent at around 320 °C, the organogold networks exhibit a remarkable thermal stability, which may seem surprising at first glance: Metastable organometallic intermediates upon dehalogenative coupling on metal surfaces are routinely observed on Ag and Cu surfaces,[116, 125, 126, 158] but less commonly on Au surfaces. When observed on Au, the organometallic intermediates are usually not very stable: Heating to 200 °C - 250 °C already breaks the organogold bonds, resulting in defined [153,155,156] or undefined[159] covalent products by reductive elimination of the Au-atom. On the contrary, organogold nanostructures with high temperature stability of around 300 °C have been reported previously.[160,161] Most closely related are the organogold networks prepared from tri-bromo-terthieno-benzene precursors on Au(111),[137] which already allude to the special role of highly conjugated thiophene-rich monomers. Based on our observations and the experimental results published in Ref. 137, we formulate the working hypothesis that the high degree of electronic conjugation in the thiophene-containing scaffold as expressed by the relatively small electronic band gap (vide infra) gives rise to remarkably strong organogold bonds. This view is supported by the increase in DFT-calculated binding energies (BE) of organogold aggregates with increasing size (see Appendix A, Figure A.5). While the BE of a single carbon-Au bond of -1.8 eV derived for the thiophene dimer with a total of 12 π electrons shows only a moderate bond strength, the BE increases sharply to -2.7 eV already for 52 π electrons in the anthra-tetrathiophene dimer. Doubling the aggregate size to the 2×2 tetramer with 104 π electrons results in a modest further increase in BE to -2.8 eV, indicating that

a plateau has been reached. In summary, the high BE of the carbon-Au bonds found for larger aggregates can be associated with a high degree of π-conjugation, and is consistent with the experimentally observed high temperature stability of the organogold networks. Moreover, the resulting lack of bond reversibility also explains the limited regularity of the organogold networks obtained on bare Au(111) (Figure 5.1e - g).

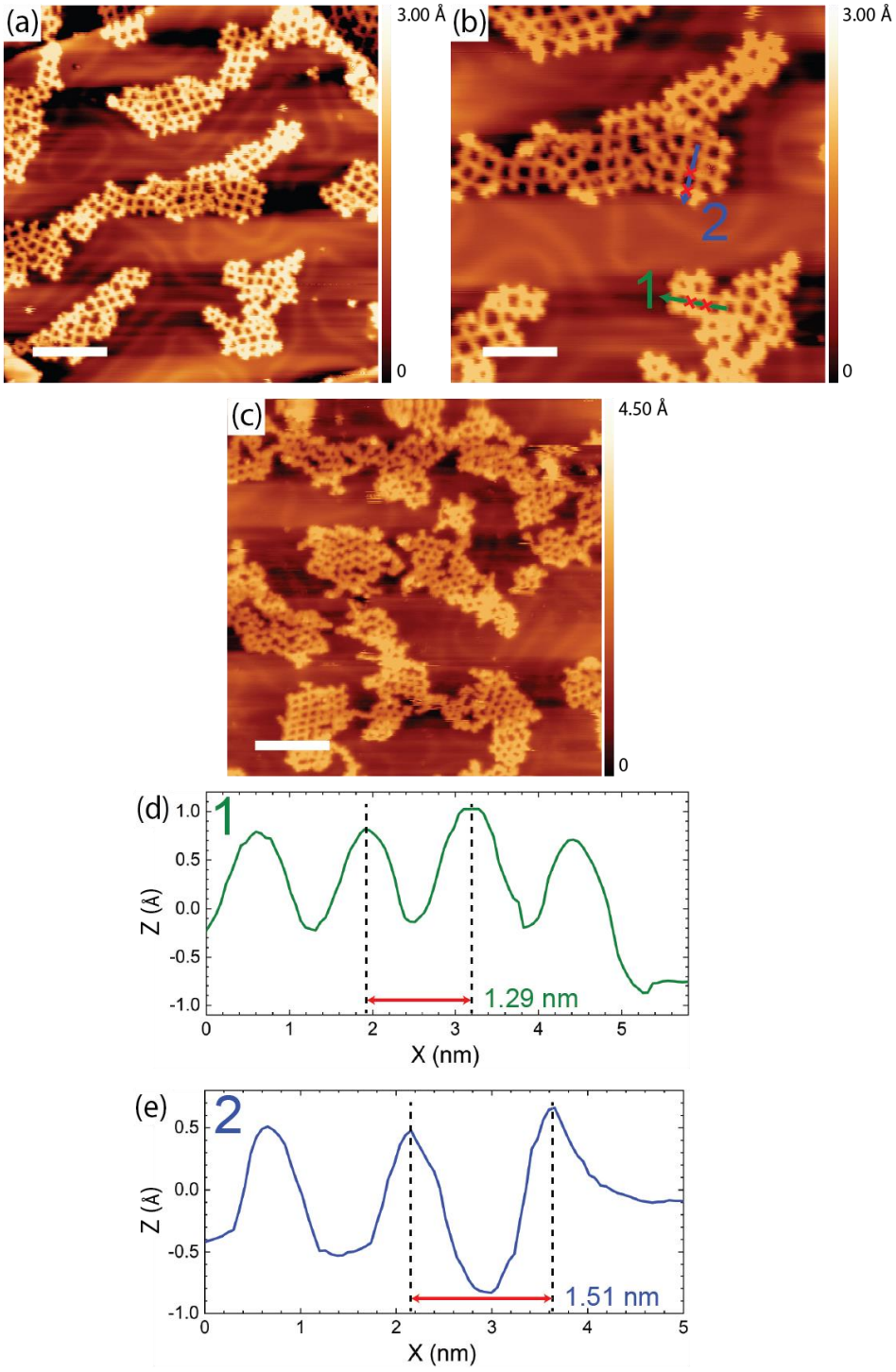

Figure 5.7 STM images of TBATT-derived organogold networks synthesized on I-Au(111) acquired after additional heating to (a) / (b) 320 °C and (c) 400 °C. (d) / (e) corresponding line-profiles as marked in (b). The iodine is completely desorbed at 320 °C, while the networks persist. The line-profiles reveal two

different pore sizes, indicating that annealing at 320 °C partly converts the organogold networks into covalent carbon-carbon bonded networks by reductive elimination of the organometallic Au-atom as similarly observed on Ag(111)[147] However, this conversion is accompanied by a loss of regularity. At even higher annealing temperatures of 400 °C, the blurring of the molecular networks in the STM images indicates decomposition of the molecular building blocks. (tunneling parameters and scale bars: (a) +850 mV, 100pA, 10 nm; (b) +850 mV, 100 pA, 6nm; (c) +1.0 V, 120 pA, 10 nm, all STM images were acquired at low temperatures)

5.4 Electronic Properties of the Organogold Networks

To further explore the potential of the highly stable and regular organogold networks for electronic applications, we provide a first combined theoretical and experimental assessment of their electronic structure. To this end, DFT calculations were performed on free-standing monolayers with periodic boundary conditions. Valence band and conduction band or shown in Figure 5.8a (cf. Appendix A, Figure A.6 for full band structure). The calculated electronic band structure exhibits a surprisingly small band gap of 0.71 eV (which is presumably underestimated, as is usually the case with DFT) and dispersive valence and conduction bands. These results indicate that the conjugation of the monomers extends through the organogold bonds as previously also reported for carbon-Ag-carbon bonds,[162] resulting in an overall conjugated network. The continuous electronic conjugation is already evident in the 2×2 anthra-tetrathiophene tetramer from the plots of its frontier molecular orbitals (see Appendix A, Figure A.7), which show their delocalization across the organogold bond. To experimentally underscore these theoretical results, Scanning Tunneling Spectroscopy (STS) experiments were performed with the optimized STM (cf. Chapter 4) at liquid nitrogen temperatures. The differential conductance dI/dV versus voltage V spectra shown in Figure 5.8 c were acquired above the anthra-tetrathiophene moieties and indicate an electronic band gap in the order of 1.0 eV. However, these STS experiments were conducted at liquid nitrogen temperatures, so thermal broadening cannot be neglected and fine details cannot be interpreted. Nevertheless, the data clearly indicate a comparatively small electronic band gap in accord with the DFT calculations.

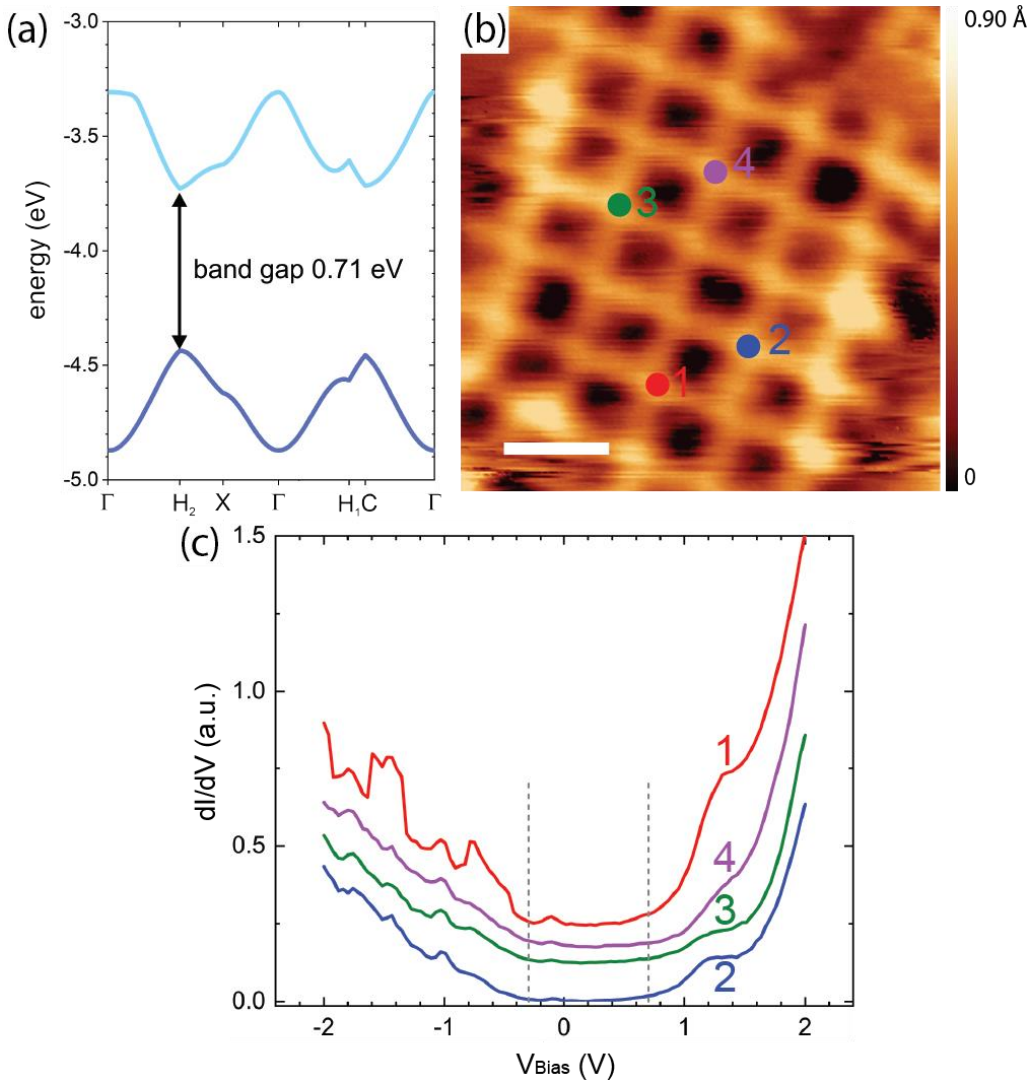

Figure 5.8 Theoretical and experimental assessment of the electronic structure of the TBATT-derived organogold networks. (a) DFT band structure calculations. Only the valence and conduction band are shown here (cf. Appendix A, Figure A.6 for a full band structure). (b) STM image showing the positions where spectra were acquired, i.e. above the anthra-tetrathiophene moieties (tunneling parameters and scale bar: +1.0 V, 120 pA, 2 nm). (c) dI/dV versus voltage curves anthra-tetrathiophene (Lock-In modulation parameters: 329 Hz, 50 mV) acquired at the positions indicated in (b). Although the spectra deviate slightly from each other, the general features are similar: onset of a pronounced feature in the unoccupied states at +0.7 V and onset of a weaker feature in the unoccupied states at -0.3 V as marked by the dashed vertical lines. In addition, all spectra consistently show a weak feature at -0.1 … -0.2 V.

5.5 Mechanistic Insights

Finally, we address the question of how the iodine monolayer might promote the formation of regular organogold networks. Two effects are conceivable: (1) Network formation on top of the iodine layer is advantageous for achieving regularity. Possible mechanisms of action are either an enhanced monomer mobility on I-Au(111) compared to bare Au(111), or registry effects that favor a uniform orientation of the monomers, hence homotacticity. (2) The presence of iodine induces reversibility of the otherwise irreversibly strong carbon-Au-carbon bonds, thereby facilitating dynamic error correction.

To further elucidate the possibility of a iodine-induced reversibility of the organogold bonds, we performed complementary experiments: TBATT was first deposited on bare Au(111), and then iodine was co-adsorbed. Two different but comparatively small iodine exposures were investigated, small enough that the iodine did not intercalate between Au(111) and TBATT, i.e. the molecules remained directly adsorbed on the metal surface. The sample was then subjected to the usual thermal treatment and heated to temperatures of 200 °C - 220 °C. The subsequently acquired STM images in Figure 5.9 a and b unveil the formation of organogold networks of intermediate quality as judged by the proportion of 76% rhombic pores (cf. Appendix A Figure A.4, 896 closed pores were counted in total). Additional STM images that were also used for the statistical assessment are shown in Figure 5.10. This is still better than the 28% rhombic pores found for synthesis on bare Au(111) without iodine, but does not reach the 92% achieved on I-Au(111). We interpret this finding as follows: On the one hand, iodine facilitates error correction during growth of organogold networks by inducing reversibility of carbon-Au-carbon bonds. This explains the improved network regularity as compared to synthesis on bare Au(111) in the absence of iodine. On the other hand, co-adsorption of iodine on Au(111) hinders network formation by reducing mobility of the molecules and imposing spatial constraints.[163] These are caused by the expansion of the molecular structure during the formation of the porous organogold networks on the iodine covered surface. This explains why the network regularity on Au(111) with co-deposited iodine falls short of those synthesized on I-Au(111).

By the same token, we attribute the high regularity of the organogold networks obtained on I-Au(111) as compared to bare Au(111) with co-deposited iodine, at least in part, to initial network formation on a more or less closed iodine layer rather than between co-adsorbed iodine atoms. However, the exact role of the iodine layer as a possible venue for formation of extended networks is less clear. First, it is not known how much iodine is already desorbed when debromination proceeds and more extended networks are formed. In addition, it remains presently unclear whether an iodine monolayer facilitates higher or lower mobility for the debrominated species, i.e. the surface-stabilized radicals.

But a further control confirmed the iodine-induced reversibility as an experimental fact: Organogold networks synthesized on I-Au(111) as in Figure 5.2d were annealed at 320 °C in a background pressure of 1×10^{-7} mbar of iodine. Afterwards, only an iodinated but otherwise empty I-Au(111) surface devoid of molecules was observed (Figure 5.11). By contrast, the networks remained stable during annealing at similar temperatures in ultra-high vacuum, i.e. in the absence of iodine (cf. Figure 5.7a and b). This pronounced difference is explained by a weakening effect of the iodine on the strength of the carbon-Au-carbon bonds. While without iodine the carbon-Au-

carbon bonds withstand the high temperatures according to their inherent strength, with iodine present these bonds can be broken, resulting in decomposition of the organogold networks and the subsequent desorption of the separated monomers.

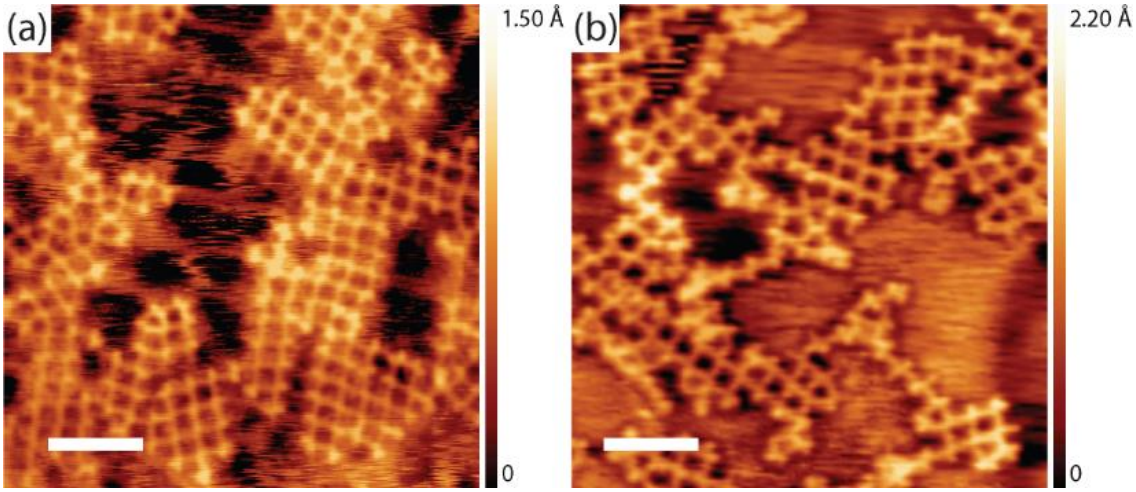

Figure 5.9 STM images of TBATT-derived organogold networks synthesized by co-deposition of TBATT and iodine on bare Au(111). After deposition of the molecules, the samples were exposed to 1×10^{-7} mbar I_2 for (a) 10 min and (b) 1 min and annealed in UHV at 200 °C for 15 min to form the networks. The presence of iodine on the surface mediates the formation of organogold networks that are with 76% rhombic pores more regular than those obtained on bare Au(111) (28% rhombic pores), but still exhibit more defects than those obtained on I-Au(111) (92% rhombic pores) by inducing reversibility in the carbon-Au-carbon bonds. Analogous to Figure 5.2, the iodine layer appears more or less closed when imaged at room temperature (b), whereas extended vacancy islands are clearly visible when imaged at low temperature (a). (tunneling parameters and scale bars: (a) +1.2 V, 120 pA, 6 nm, acquired at low temperature; (b) +1.0 V, 120 pA, 6 nm, acquired at room temperature)

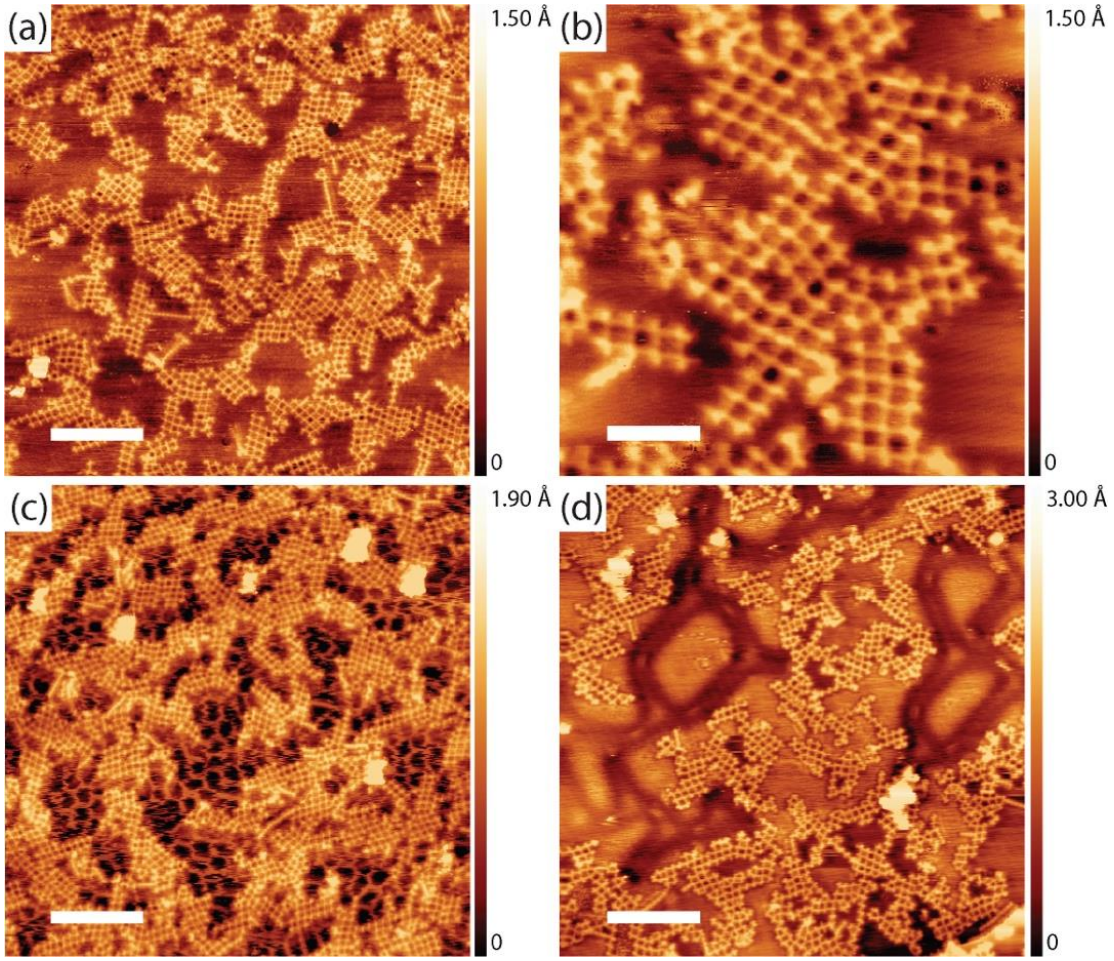

Figure 5.10 STM images of organogold networks synthesized by co-deposition of TBATT and iodine on bare Au(111). After deposition of the molecules, the samples were exposed to 1×10^{-7} mbar I_2 for (a) / (b) / (c) 10 min and (d) 1 min and annealed at 200 °C for 15 min to form the networks. At low temperature, the iodine is immobilized in a filamentous structure, which is not visible at room temperature, but gives a more realistic impression of the iodine coverage. The presence of iodine on the surface mediates the formation of organogold networks that are more regular than those obtained on bare Au(111), but still exhibit more defects than those obtained on I-Au(111) by inducing reversibility in the carbon-Au-carbon bonds. (tunneling parameters and scale bars: (a) +1.3 V, 120 pA, 20 nm; (b) +1.3 V, 120 pA, 6 nm; (c) +1.2V, 120 pA, 20 nm; (d) +1.0 V, 120 pA, 20 nm, STM images (a) / (b) / (d) were acquired at room temperature, and only image (c) was recorded at low temperature.)

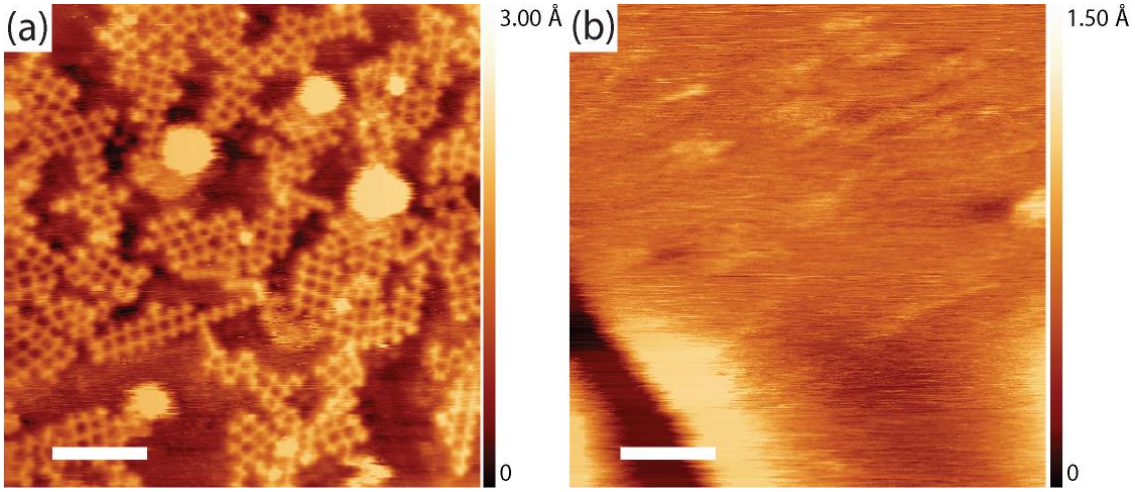

Figure 5.11 Annealing of organogold networks under reversible conditions in an iodine atmosphere. (a) STM image of the organogold networks prepared on I-Au(111) according to the established protocol. (b) STM image of the same sample acquired after annealing at 320 °C (30 min ramp time and 15 min dwell time) in a background pressure of 10^{-7} mbar iodine. The sample appears empty, from which we conclude that the networks have desorbed. This was not the case with vacuum annealing (cf. Figure 5.7) and can therefore be attributed to the presence of iodine. It weakens the organometallic carbon-Au-carbon bonds to such an extent that the networks eventually disintegrate and the individual monomers desorb at the high temperature. (tunneling parameters and scale bars: (a) +1.0 V, 120 pA, 10 nm; (b) +1.0 V, 120 pA, 10 nm; both images were acquired at room temperature)

Conclusion

In summary, we have demonstrated that I-Au(111) surfaces are viable substrates for the on-surface synthesis of 2D organogold networks by debrominative couplings. The organogold networks obtained for the TBATT precursor on I-Au(111) are highly regular with 92% rhombic pores, while those synthesized on bare Au(111) suffer from poor order with only 28% rhombic pores.

Although the domains are still comparatively small, the number of repeat units is already sufficient for the anthra-tetrathiophene network to develop an electronic band structure. This is evident from our DFT calculations, where the HOMO-LUMO gap of the isolated 2×2 anthra-tetrathiophene tetramer of 0.78 eV has almost reached the electronic band gap of 0.71 eV of the periodic monolayer. Part of the reason is topology: the electronic properties converge faster in 2D than in 1D, essentially because more intermolecular bonds are formed per monomer.[164] In this respect, the improved regularity on I-Au(111) is crucial for the emergence of defined electronic properties despite the still limited domain size.

Regarding the coupling mechanism on I-Au(111), we demonstrate that a certain permeability of the iodine passivation layer, as realized by an initially less dense packing in the iodine layer and promoted by a gradual iodine desorption during the thermal treatment, is imperative to facilitate the debromination. This makes the metal surface accessible to activate the reaction, but also to provide

the Au-atoms for the formation of organogold networks. Therefore, to facilitate on-surface synthesis on I-Au(111), it is crucial to establish a workable iodine coverage. However, once the appropriate preparation parameters are found, the protocol has proven to be highly reproducible and reliable. An unambiguous effect of the iodine monolayer for the formation of highly regular organogold networks is the iodine-induced reversibility of the strong carbon-Au-carbon bonds to facilitate dynamic error correction. This is concluded from experiments in which better organogold networks were obtained on Au(111) when iodine was co-deposited. An additional conceivable effect of the iodine monolayer is that network formation on top of the iodine layer at least initially alleviates the spatial constraints that arise when reactants and iodine are co-adsorbed on bare Au(111), but there is no strong evidence for this. There is a general consensus that higher monomer mobility favors the formation of regular structures by avoiding diffusion-limited aggregation.[165,166] But for I-Au(111) it is also unclear whether the mobility of activated, i.e. debrominated, monomers is increased or decreased compared to bare Au(111).

Although the anthra-tetrathiophene repeat units are not directly linked by carbon-carbon bonds, the organometallic carbon-Au-carbon bonds also endow the networks with all the desirable properties, that is electronic conjugation and robustness. We are optimistic that synthesis on I-Au(111) could expand the toolbox of on-surface synthesis and provide a more general approach for cases where direct reaction on bare metal surfaces does not yield the desired products.

Chapter 6

Reversible Intercalation of Organic Solvents in Graphite and its Hindrance by a Strongly Adsorbing Supramolecular Monolayer

This chapter presents solvent intercalation as the origin of the changes in graphite's ability to serve as a substrate for monolayer self-assembly at liquid-solid interfaces. The foundation for this exploration lies in the manuscript titled " Reversible Intercalation of Organic Solvents in Graphite and its Hindrance by a Strongly Adsorbing Supramolecular Monolayer," which was submitted to Advanced Materials Interfaces. This chapter is reprinted and partially adapted with the permission of Arash Badami-Behjat, Tamara Rinkovec, Pavel Procházka, Anastasiia Bazylevska, Miriam C. Rodríguez González, Hai Cao, Jan Čechal, Steven De Feyter and Markus Lackinger.

At elevated temperatures, the prototypical organic solvents used to study the self-assembly of supramolecular monolayers at liquid-solid interfaces alter a graphite substrate by intercalation. As a consequence, less strongly bound supramolecular monolayers become thermodynamically unstable. The effect can be reversed by high-temperature annealing in a vacuum. However, strongly adsorbing hydrogen-bonded monolayers of trimesic acid hinder solvent intercalation and thus protect the graphite substrate.

My contribution to this work was conducting in-situ variable-temperature STM, vacuum annealing experiments, and substrate preparation for STM, LEEM, and AFM measurements. I have done the initial AFM experiments as well as part of the initial ex-situ experiments. Additionally, I was also responsible for analyzing and interpreting the corresponding data for the manuscript preparation under the supervision of Prof. Dr. M. Lackinger who conceived and designed the study along with Prof. Dr. De Feyter. The ex-situ STM experiments were conducted by Tamara Rinkovec, who also did the confocal Raman spectroscopy with support from Miriam C. Rodríguez González. AFM experiments were supervised by Miriam C. Rodríguez González and performed by Anastasiia Bazylevska. The LEEM experiments and data analysis were conducted by Pavel Procházka and Jan Čechal, and FGC18 was synthesized by Hai Cao.

6.1 Introduction

Self-assembly of supramolecular monolayers at liquid-solid interfaces is a vibrant field of basic research that seeks to provide a solid foundation for prospective applications in surface functionalization and nano-patterning.[167] Despite three decades of intensive research, a truly quantitative understanding of the underlying thermodynamics remains the holy grail. Putting absolute numbers on the various enthalpic and entropic contributions is an indispensable prerequisite for eventually gaining predictive power over polymorph selection,[168] and will ultimately guide the design of tectons and environments to target supramolecular monolayers with desired structure and functionality. Variable-temperature studies are an important experimental key to gaining this knowledge.[169] Both contributions to free energy, enthalpy and entropy, can be extracted from the temperature and concentration dependence of thermodynamic equilibrium, i.e. which particular polymorphs are stabilized at which surface coverage. However, for such studies, reproducible conditions over extended periods of time are essential to facilitate sampling of a set of equilibrium conditions. Accordingly, any irreversible changes in solvent, solute or substrate must be safely excluded.

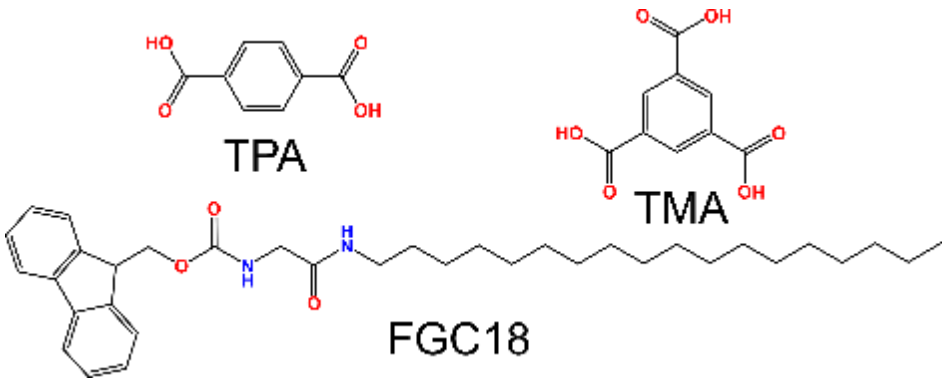

Figure 6.1 Chemical structures of the tectons: terephthalic acid (TPA), trimesic acid (TMA), (9H-fluoren-9-yl)methyl (2-(octadecylamino)-2-oxoethyl)carbamate (FGC18)

Here, we attempt such studies using a dedicated home-built Scanning Tunneling Microscope (STM) that facilitates long term experiments in liquids at elevated temperatures.[17] We have employed a well-characterized and easily measured model system consisting of terephthalic acid (TPA, benzene-1,4-dicarboxylic acid, see Figure 6.1 for chemical structure) in fatty acid solvents on Highly Oriented Pyrolytic Graphite (HOPG) substrates.[168a] In nonanoic acid (9A) solvent, the TPA monolayer remained stable up to 40 °C but was completely desorbed when the temperature was increased to 60 °C (Figure 6.2). However, the TPA monolayer was not restored after cooling to room temperature, where STM imaging showed only an apparently empty graphite surface without TPA monolayers. Analogous observations were made with heptanoic acid (7A) as a

solvent. This is obviously contraindicative of thermodynamic control,[170] where the state of the system depends only on the state variables, not on the sample's history. Similar behaviour was observed in multiple independent runs, indicating persistent changes in either the solution or the substrate, or both. The culprit was easily identified: The same previously heated solution still yielded TPA monolayers on another graphite substrate (Figure 6.3) ruling out any critical chemical changes in either the solute or the solvent. On the other hand, the same graphite substrate, when cleaved again, directly yielded TPA monolayers (Figure 6.2f). As a result, changes in the top layers of the graphite substrate can be held responsible for this.

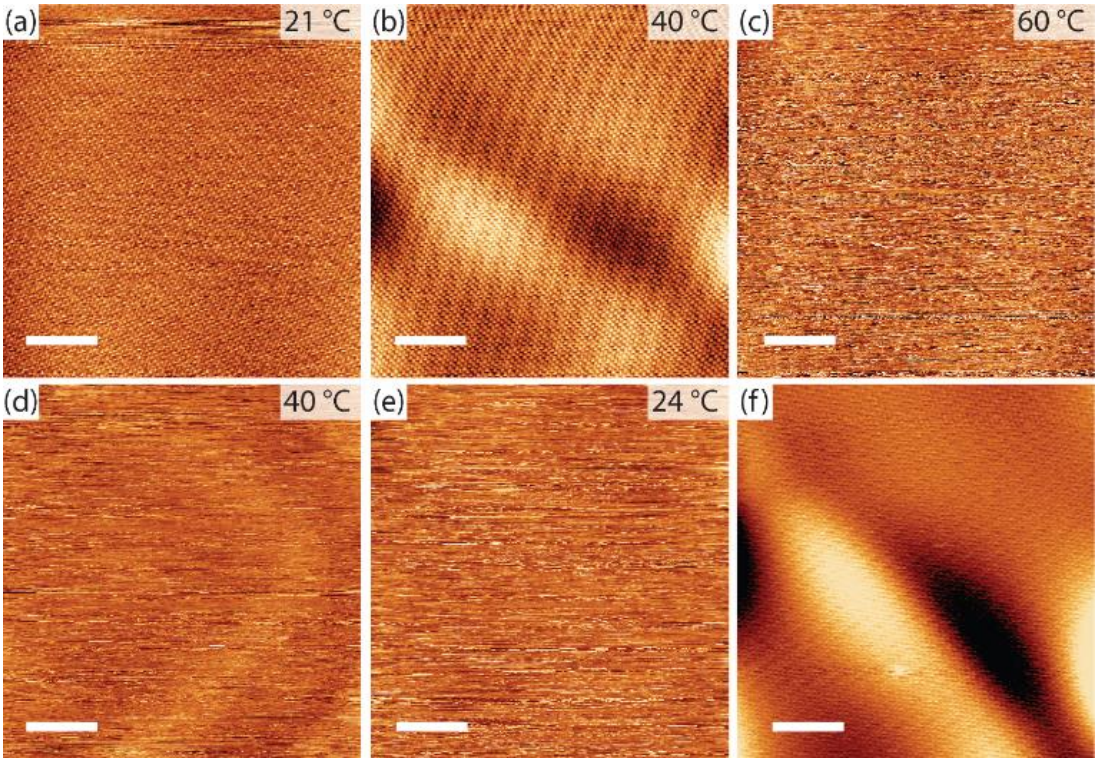

Figure 6.2 Variable-temperature STM studies of TPA monolayers at the 9A-graphite interface. Images were successively acquired in-situ from the same sample at (a) room temperature, after heating to (b) 40 °C and (c) 60 °C and after cooling down again to (d) 40 °C and further to (e) 24 °C, as also indicated in the upper right corner. TPA monolayers remain stable at 40 °C, are completely desorbed when the temperature is raised to 60°C, but are not restored after cooling to 40 °C or room temperature. (f) STM image of a TPA monolayer obtained immediately after cleaving the same graphite substrate again and applying the previously heated solution (tunneling parameters: +600 mV, 80 ... 140 pA, all scale bars are 10 nm).

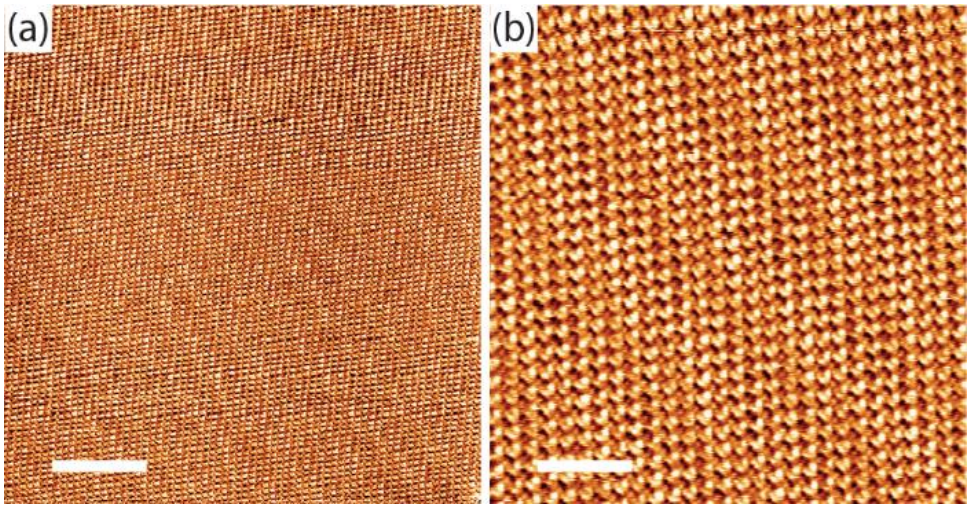

Figure 6.3 Characterization of the previously in-situ heated TPA solution. (a) Overview and (b) close-up STM images of TPA monolayers, obtained directly after application of the TPA in 9A solution that was already used for the in-situ variable temperature STM experiments (Figure 6.2) to a new and freshly cleaved graphite substrate. The observation of high quality TPA monolayers corroborates the absence of critical chemical changes in the TPA solution after heating (tunneling parameters and scale bars: (a) 500 mV, 75 pA, 10 nm; (b) 500 mV, 75 pA, 4 nm).

Analogous results have been obtained by *ex-situ* heating (see Appendix B, Materials & Methods). Therefore, a graphite sample was kept in the TPA solution at a temperature of 50 °C and taken out for STM characterization at room temperature after 1, 2, 3 and 10 days of consecutive heating. A decrease in molecular coverage was observed after 2 days, whereas no TPA monolayers were detected after 3 and 10 days of heating in solution (Figure 6.4). To further explore whether this is a solvent or solute specific phenomenon, complementary experiments were performed with (9H-fluoren-9-yl)methyl (2-(octadecylamino)-2-oxoethyl)carbamate (FGC18, see Figure 6.1 for chemical structure) dissolved in 1-phenyloctane (PO), a non-protic aromatic solvent with low affinity for graphite. Qualitatively similar results were obtained for immersing the graphite sample in 70 °C hot PO solution, with the main difference being a later onset, where FGC18 monolayers were still observed after 3 days but not after 7 days (Figure 6.5). The destabilization of supramolecular TPA and FGC18 monolayers upon prolonged exposure of the graphite to hot solution suggests that the previously measured ultra-slow desorption kinetics of 2,6-naphthalenedicarboxylic acid monolayers at the 9A-graphite interface may also be related to substrate changes.[171]

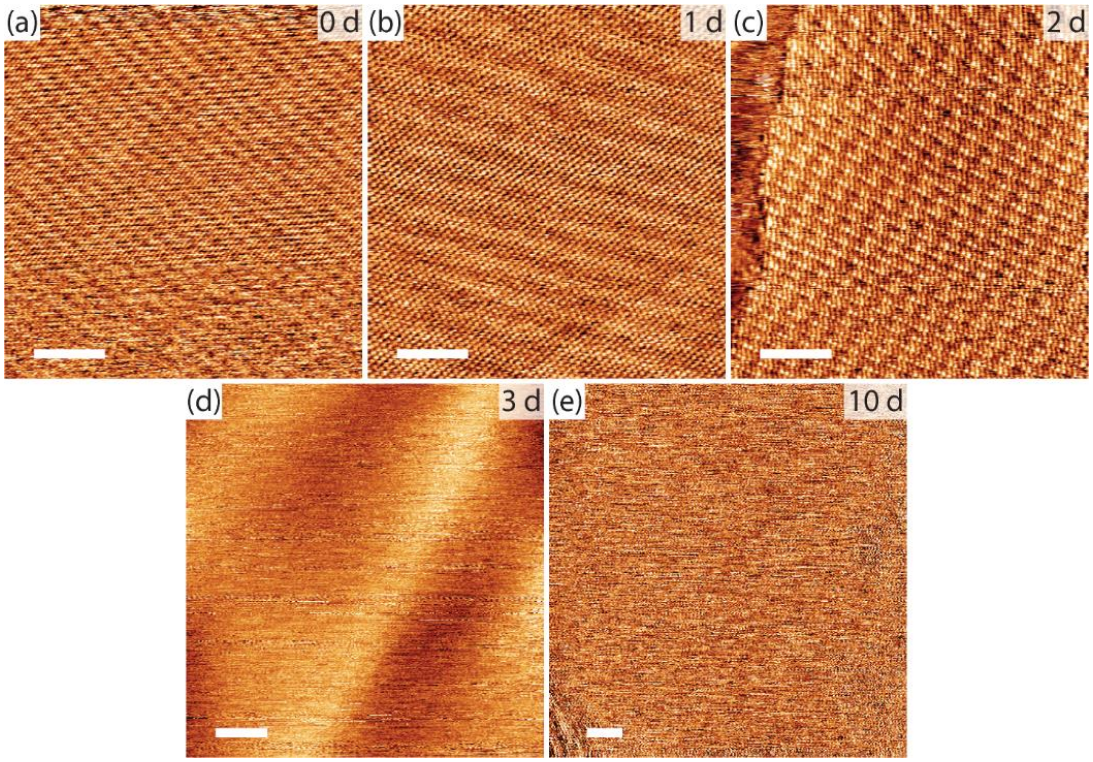

Figure 6.4 Ex-situ heating studies of TPA at the 7A-graphite interface. After (a) initial STM characterization, samples were continuously exposed to 50 °C hot TPA in 7A solution and characterized by STM imaging at room temperature after (b) 1 day, (c) 2 days, (d) 3 days and (e) 10 days. After 2 days, the surface was no longer completely covered by a TPA monolayer, as evident on the left edge of the STM image in (c). After 7 days of heating, no TPA monolayers were observed (tunneling parameters and scale bars: -800 ... -600 mV, 100 ... 200 pA, all scale bars are 10 nm).

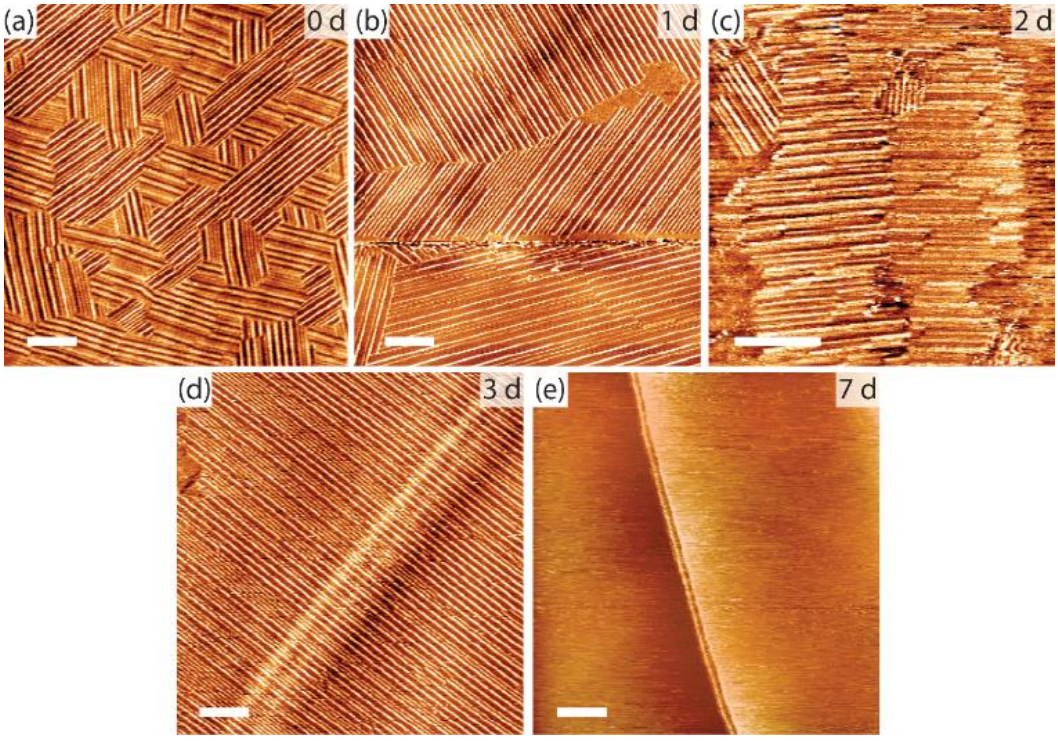

Figure 6.5 Ex-situ heating studies of FGC18 at the PO-graphite interface. After (a) initial STM characterization samples were continuously immersed in 70 °C hot PO solution and characterized by

STM imaging at room temperature after (b) 1 day, (c) 2 days, (d) 3 days and (e) 7 days. After heating for 1 day the domain size increased. But after 7 days of heating, no FGC18 monolayers were observed (tunneling parameters: -800 … -600 mV, 100 … 200 pA, all scale bars are 50 nm).

However, we did find one notable exception: Trimesic acid (TMA, 1,3,5-benzenetricarboxylic acid, see Figure 6.1 for chemical structure) monolayers were found to persist without evidence of degradation after 7 days of continuous immersion in the 7A solution at the even higher temperature of 80 °C (Figure 6.6). This remarkable result will be discussed in detail below.

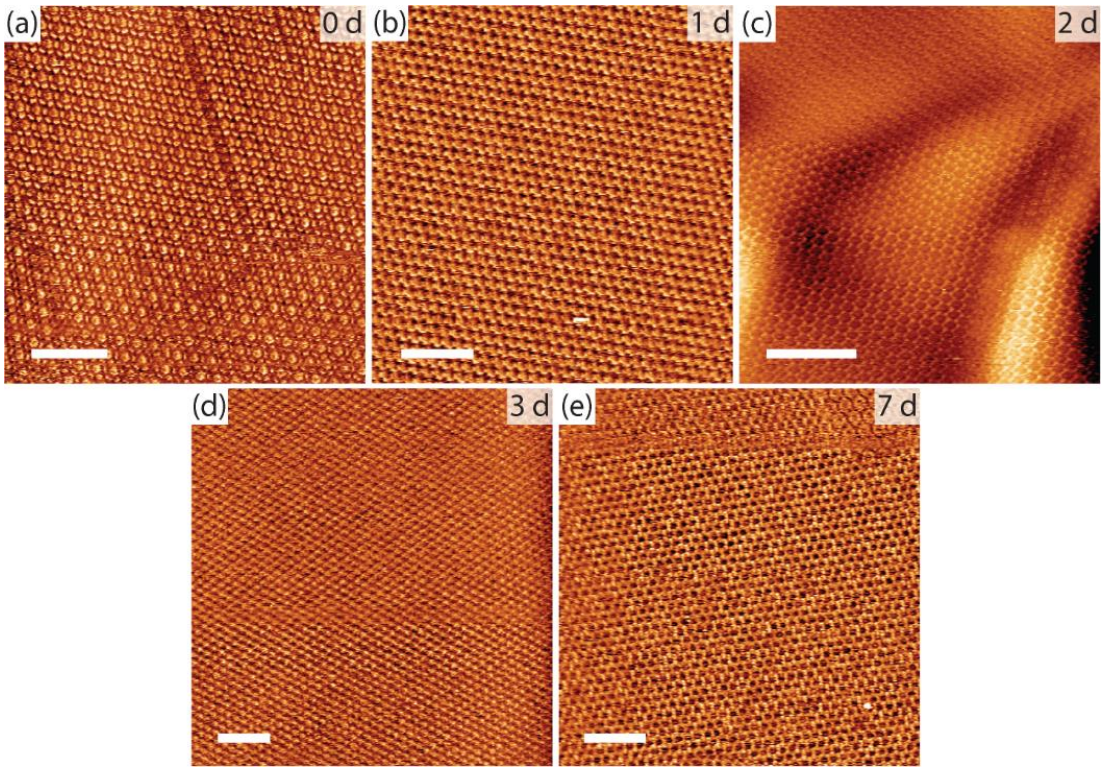

Figure 6.6 Ex-situ heating studies of TMA at the 7A-graphite interface. After (a) initial STM characterization, samples were continuously exposed to 80 °C hot TMA in 7A solution and characterized by STM imaging at room temperature after (b) 1 day, (c) 2 days, (d) 3 days and (e) 7 days. In contrast to TPA and FGC18, TMA monolayers were still observed after 7 days of continuous exposure to hot solution at an even higher temperature without any evidence of degradation. It is worth noting that in the initial characterization the TMA flower polymorph was observed, as is occasionally the case for 7A solvent,[172] but after the first heating treatment it was already converted to the TMA chicken wire polymorph, which is thermodynamically more stable in 7A[173] (tunneling parameters and scale bars: -1300 mV, 100 … 140 pA, all scale bars are 10 nm).

The next question is whether the solvent or the solute molecules are the primary cause of the changes in the graphite substrate. To this end, graphite samples were heated in pure 7A solvent at 60 °C and characterized for their ability to serve as a substrate for TPA monolayer self-assembly. Yet, the graphite substrate was no longer conducive to the self-assembly of TPA monolayers (Figure 6.7), demonstrating that the changes are mainly, if not exclusively, caused by the pure 7A solvent.

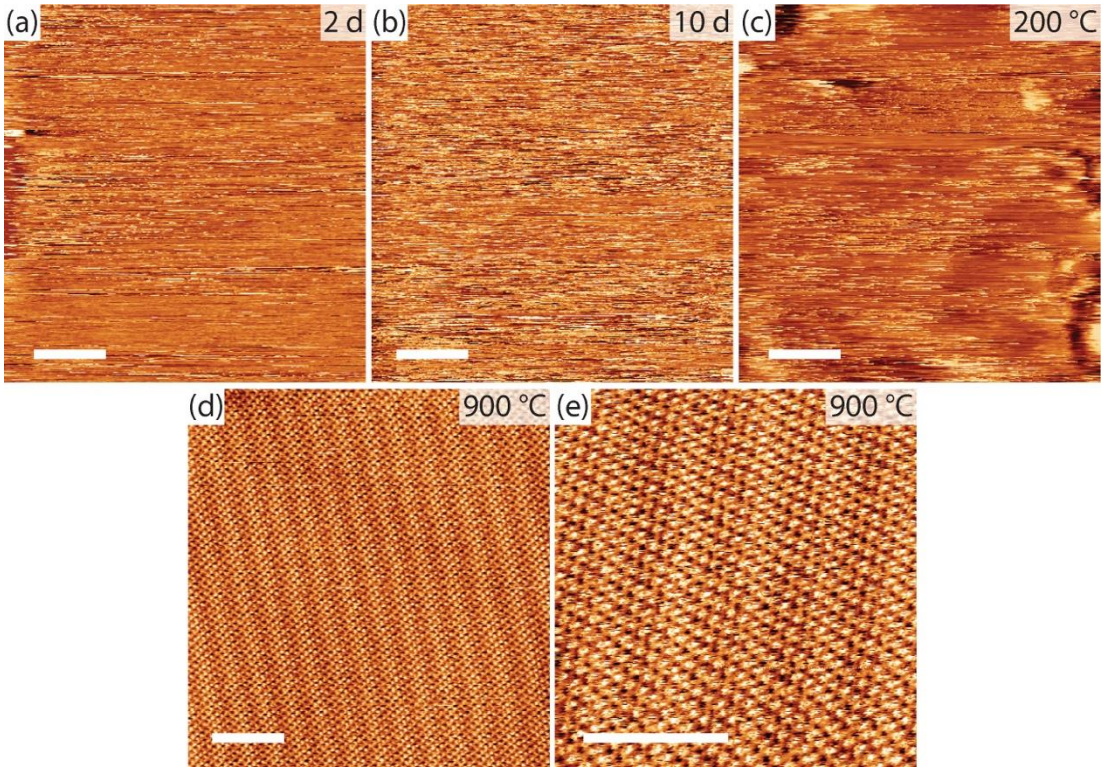

Figure 6.7 Effect of heating graphite substrates in pure 7A solvent and vacuum annealing. HOPG samples were immersed in pure 7A solvent at 60 °C for (a) 2 days and (b) 10 days and (c) 3 days and additionally vacuum annealed at 200 °C and (d) 2 days and additionally vacuum annealed at 900 °C. Vacuum annealing was performed at a pressure of ~10^{-6} mbar and a dwell time of ~1 h at the respective temperature. Subsequently, a large excess of TPA in 7A solution was applied and the samples were characterized by STM imaging at macroscopically distinct areas. (a) / (b) No TPA monolayers were observed on the solvent exposed samples without annealing, although the experiment was repeated several times. We conclude that these graphite substrates were no longer suitable for self-assembly of TPA monolayers. (c) This situation did not change after vacuum annealing at 200 °C. (d) / (e) However, after annealing at 900 °C, TPA monolayers were immediately observed with a quality indistinguishable from that of freshly cleaved HOPG. In conclusion, the changes in the graphite substrates due to intercalation are already caused by the pure 7A solvent. Moreover, they are reversible, but regeneration of the graphite samples requires vacuum annealing at relatively high temperatures on the order of 900 °C (tunneling parameters: (a) 1200 mV, 95 pA; (b) 1100 mV, 110 pA; (c) 1100 mV, 200 pA; (d) 1300 mV, 50 pA; (e) 1000 mV, 200 pA; all scale bars are 10 nm).

To further test whether the changes in the graphite substrate could be reversed, a sample previously immersed in 60 °C hot 7A for 2 days was then annealed in a vacuum (~10^{-6} mbar) at 900 °C for ~1 hour. Freshly cleaved, solvent exposed and vacuum annealed samples are visually indistinguishable (Figure 6.8). However, the application of solution on a vacuum annealed graphite immediately resulted in self-assembly of TPA monolayers with an STM appearance indistinguishable from that on freshly cleaved graphite (Figure 6.7). In summary, the changes in the graphite substrate caused by prolonged immersion in hot organic solvents are reversible. It can be regenerated by vacuum annealing, although relatively high temperatures are required.

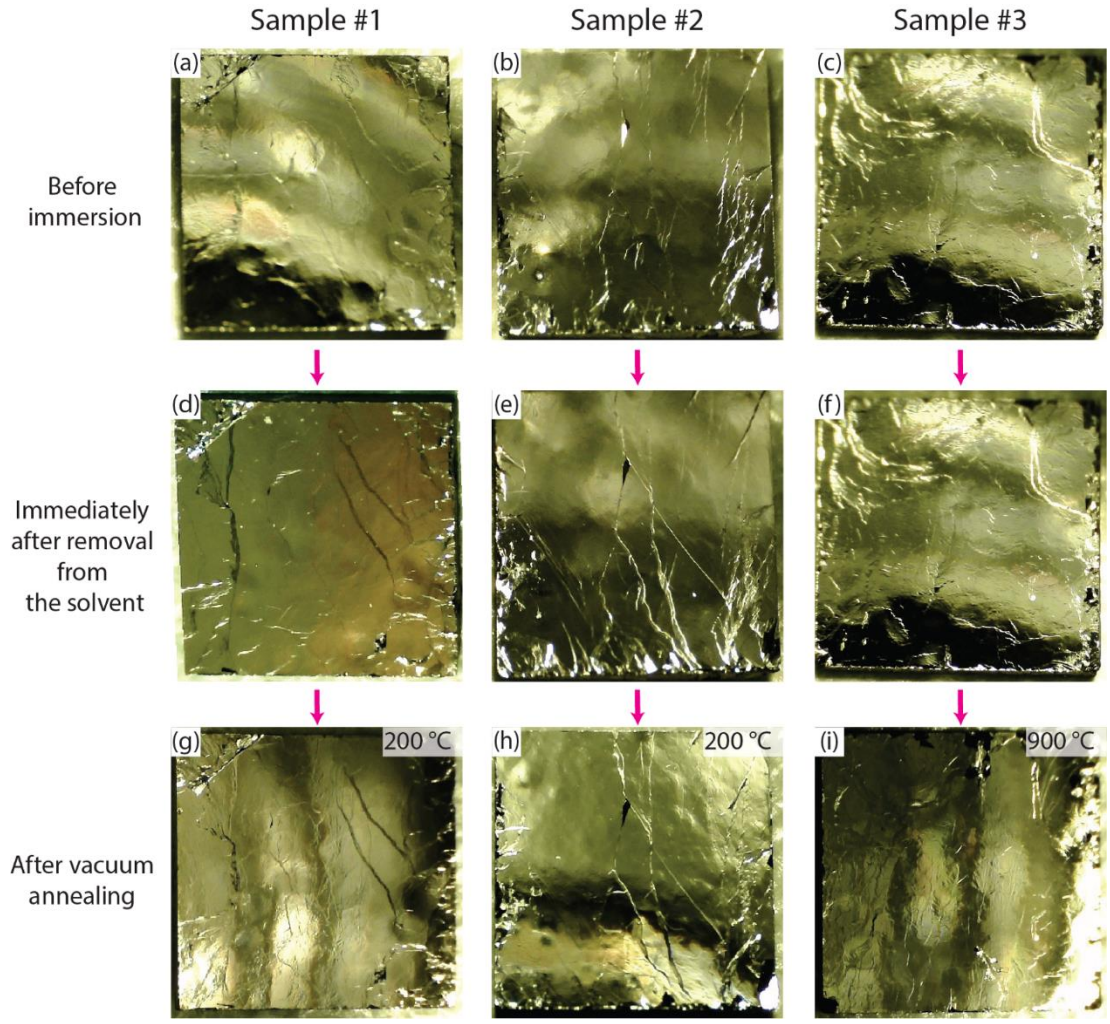

Figure 6.8 Optical characterization of solvent exposed samples. Three different HOPG samples (5×5 mm²) were immersed in pure 7A solvent at 60 °C for 3 days. Photographs were taken (a) - (c) before immersion, (d) - (f) immediately after removal of the samples from the solvent, and after vacuum annealing at (g) / (h) 200 °C and (i) 900 °C with a dwell time of ~1 h. The same samples are shown in each column. There are no obvious changes in the visual appearance between the different stages.

To evaluate possible changes in surface topography at the micron scale, solvent-exposed graphite samples were comparatively characterized by Atomic Force Microscopy (AFM). Samples taken directly from 7A and left to dry under argon show frayed surface structures (Figure 6.9). These are completely absent on freshly cleaved graphite, and their amount can be slightly reduced by rinsing with ethanol. However, ambient annealing at 200 °C removes most of these structures, except for a few persistent impurities (Figure 6.9). Note that vacuum annealing at 200 °C was not sufficient to restore the original properties of graphite (Figure 6.7). Accordingly, we attribute the structures initially observed by AFM imaging to remnants of the drying process, which are not the cause of the lack of TPA monolayer self-assembly. In conclusion, long-term exposure to hot 7A does not directly affect the surface topography of the graphite samples to a measurable extent.

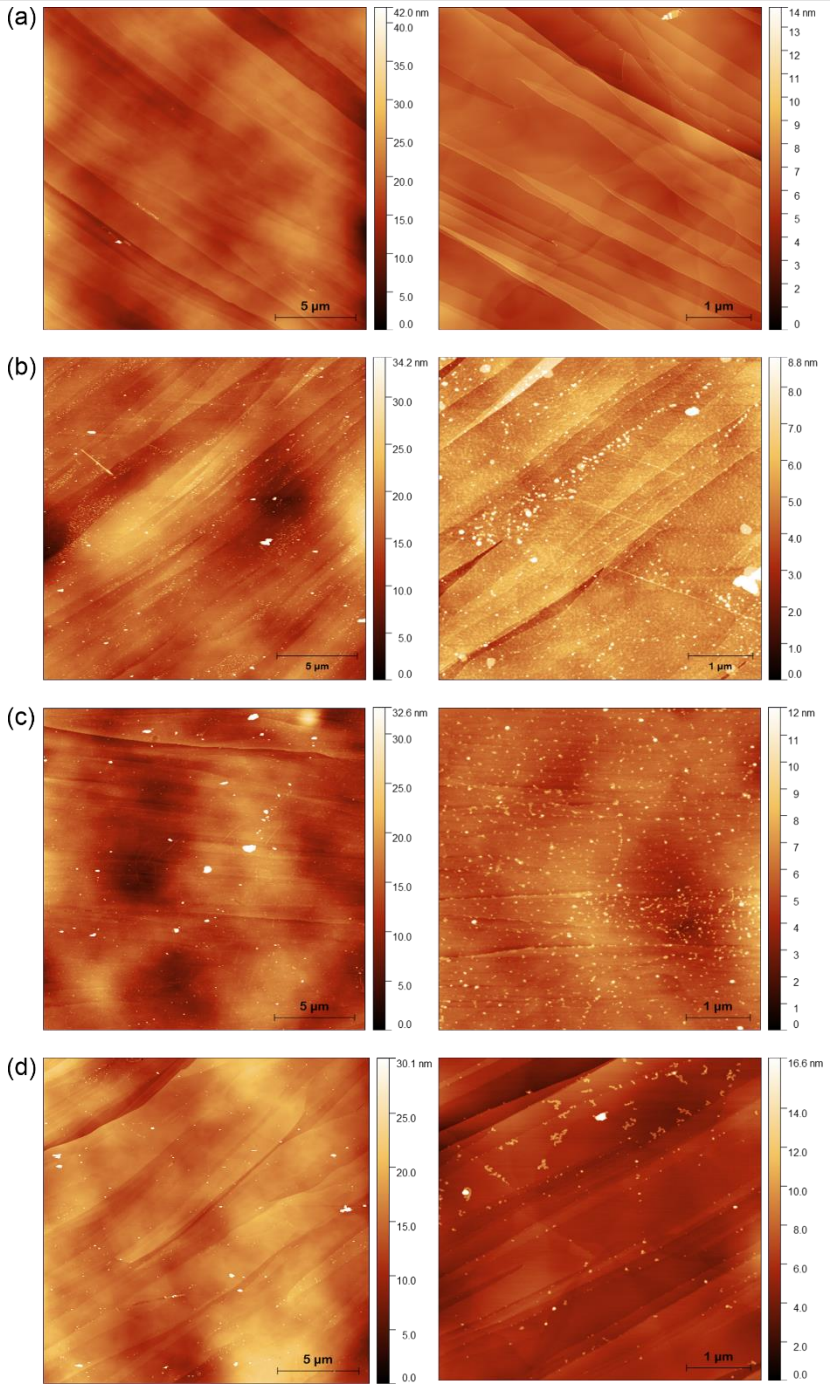

Figure 6.9 AFM characterization of solvent exposed samples. Graphite samples were immersed in pure 7A solvent at 60 °C for 3 days. AFM images with scan sizes of 20 µm (left column) and 5 µm (right column) were acquired from (a) freshly cleaved graphite, (b) immediately after removing the samples from solution and drying under argon, (c) after additional rinsing with ethanol, and (d) after additional annealing under ambient conditions at 200 °C with a dwell time of ~30 min. The frayed structures that appear after drying the samples are partially removed by rinsing in ethanol and almost completely removed by annealing. Accordingly, we interpret these as remnants of the drying process. No other obvious changes, such as surface roughness, could be detected by AFM imaging.

In the absence of evident changes on the graphite surface, the most plausible cause for the alteration in its ability as a substrate for TPA or FGC18 monolayer self-assembly is subsurface changes, i.e. intercalation of solvent molecules between graphite layers. Intercalation is commonly

observed for organic solvents and is also exploited for liquid-phase exfoliation of graphite to graphene.[174] In that respect, solvents with a high affinity for graphite are deliberately used. In contrast, solvents with a low affinity for graphite are preferred for monolayer self-assembly at liquid-solid interfaces. Based on the observed slow kinetics, we postulate a significant activation energy, allowing a non-negligible rate only at elevated temperatures. The conjecture that intercalation is responsible for the above-described changes in monolayer self-assembly is also consistent with high-temperature regeneration, which removes the intercalated solvent molecules by combined diffusion and desorption. Furthermore, we hypothesize that the effect is confined to the upper layers based on two observations: First, cleaving the solvent-exposed graphite with adhesive tape, which removes a few microns of material, is sufficient to restore the original monolayer self-assembly properties. Second, confocal Raman spectroscopy shows no obvious changes (see Appendix B, Figure B.1), although the 2D band at 2700 cm^{-1} is particularly sensitive to graphite layer stacking.[175] This is rationalized by the large optical penetration depth of the excitation and scattered light in graphite; the intensity at a wavelength of 633 nm decreases to 1/e for a thickness of the order of 42 nm, corresponding to ~120 graphite layers. Consequently, the high information depth of confocal Raman spectroscopy in graphite renders it insensitive to changes affecting only a few top atomic layers.

Accordingly, a structural characterization with sufficient surface sensitivity is required. In principle, this should be possible with X-ray diffraction, but special measurement modes and precautions are required. Alternatively, low energy electrons with kinetic energies in the range of 0 ... 100 eV can be used, which are inherently surface sensitive due to their low mean inelastic free path. Electron reflectivity measurements have proven useful for studying the layering and intercalation of graphitic materials.[176] The intensity of the specular (0,0) reflection as a function of electron energy, so-called I(V) curves, depends critically on the structure and electronic properties of the upper atomic layers, including changes in surface and interface electronic states or sample structure, e.g., layer separation.[177] Electron reflectivity can be measured with a spatial resolution down to a few nanometers by acquiring brightfield (BF) images in a Low Energy Electron Microscope (LEEM). For freshly cleaved graphite, the BF image in Figure 6.10a shows uniform intensity with only the substrate steps being highlighted by phase contrast.[178] After solvent exposure, however, a completely different picture emerges. The corresponding BF image in Figure 6.10b shows darker and brighter areas indicating lateral inhomogeneities (see Appendix B, Figure B.2). The darker regions have a dendritic appearance, which is a common hallmark of diffusion-limited growth.[179] By contrast, *ex-situ* vacuum annealing restores the original LEEM appearance as shown in Figure 6.10c. To get a deeper insight, we measured the I(V) curves for the specular (0,0) reflection in the

energy range 0 … 60 eV at the positions marked with small circles in Figure 6.10 (see Appendix B, Materials and Methods). As shown in Figure 6.10d, there are clear differences between freshly cleaved and solvent-exposed graphite, especially in the energy range 20 … 30 eV. The corresponding I(V) curve obtained after high temperature annealing again closely resembles that of freshly cleaved graphite (Figure 6.10d) except for absolute intensity, indicating reversibility of the process.

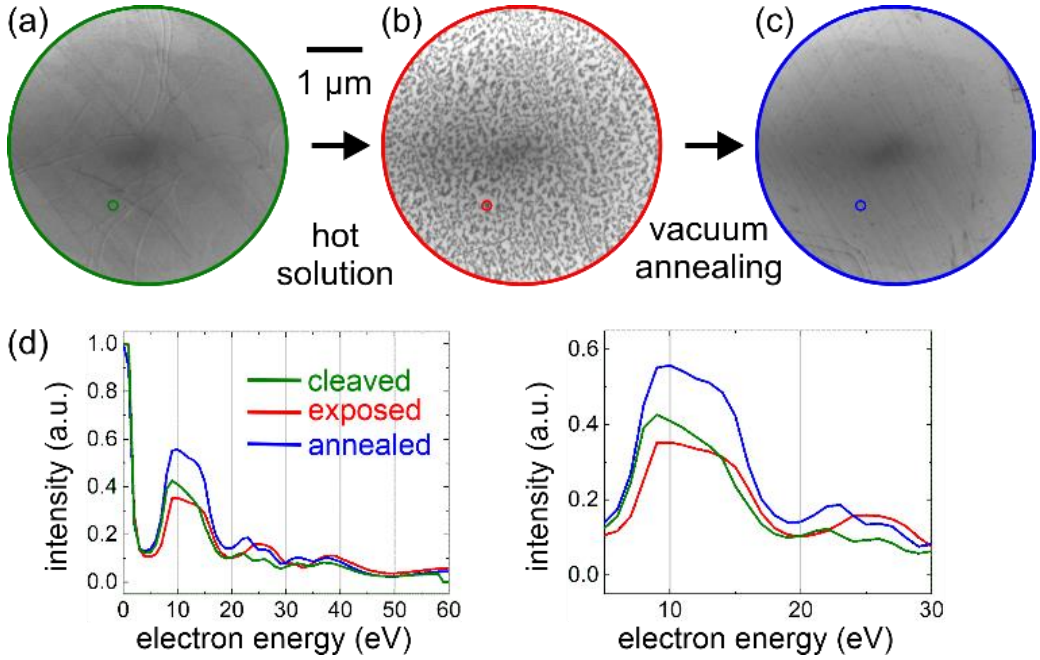

Figure 6.10 Comparative LEEM studies. BF images acquired at 12 eV of (a) freshly cleaved graphite, (b) after immersion in 60 °C hot pure 7A for 3 days and (c) after additional ex-situ vacuum annealing at 900 °C for ~1 h. (d) I(V) curves extracted from the areas marked by the circles in the BF images (colors are also matched to the borders of the corresponding LEEM images). The right hand side shows a magnification. Both BF images and I(V) curves consistently indicate changes after solvent exposure that are absent in freshly cleaved graphite and removed by vacuum annealing.

Because LEEM provides clear signatures of solvent-induced changes, we have also applied it for *in-situ* studies. Therefore, solvent-exposed samples were heated in the ultra-high vacuum chamber and characterized by LEEM at the higher temperatures. The darker regions mostly prevail even at 800 °C (see Appendix B, Figure B.3), showing only modest changes on a time scale of tens of seconds. The persistence at high temperature clearly confirms a high activation energy for deintercalation by removal of the solvent molecules. In summary, the combined experimental results, i.e., the absence of persistent changes on the graphite surface in AFM and STM images, the spatially inhomogeneous contrast with darker dendritic features in LEEM, and the need for relatively high temperatures to restore the samples, consistently point to solvent intercalation as the cause of the changes in the graphite substrates.

6.2 Self-assembly of TPA monolayers on TMA-protected graphite

Finally, we discuss the case of graphite exposure to hot TMA in 7A solution, where no changes were observed in the *ex-situ* heating experiments at even higher temperatures (Figure 6.6). To confirm the absence of crucial changes in the graphite substrate, we study a sample that was exposed to 60 °C hot TMA solution for 3 days. First, residues of the TMA solution were carefully removed with a tissue. Subsequent application of a large excess of TPA in 7A solution, directly yielded TPA monolayers as observed by STM (Figure 6.11). This indicates that the adsorbed TMA monolayer prevented or at least slowed down solvent intercalation during immersion in the hot TMA solution. The graphite substrate remained in a state that still facilitates self-assembly of TPA monolayers, which was not possible after a much shorter exposure to either pure 7A solvent or a TPA solution at the same temperature. Accordingly, dissolved TMA protects the graphite from solvent intercalation while TPA does not. The key difference is that TMA monolayers on graphite are thermodynamically much more stable than TPA monolayers. This is confirmed by variable-temperature STM experiments at the solid-liquid interface, where TMA monolayers were found to be stable even above 100 °C,[169d] while TPA monolayers were found to be already desorbed at 60 °C (Figure 6.2). This marked difference can be attributed to the two-dimensional network of strong hydrogen bonds formed by TMA, while TPA forms only hydrogen-bonded linear chains. The consequences for the binding enthalpy in the monolayer with respect to vacuum can be experimentally quantified by Temperature Programmed Desorption, which yielded desorption energies of ~140 kJ/mol[168a] and ~180 kJ/mol[169e] for TPA and TMA, respectively, in agreement with calculated values.[168a,169d] On the other hand, the (endothermic) enthalpies of solution of TPA and TMA in 7A were found to be comparatively small and similar in the order of ~10 kJ/mol,[168a,169d] suggesting that the presence of the 7A solvent has similar effects on both tectons.

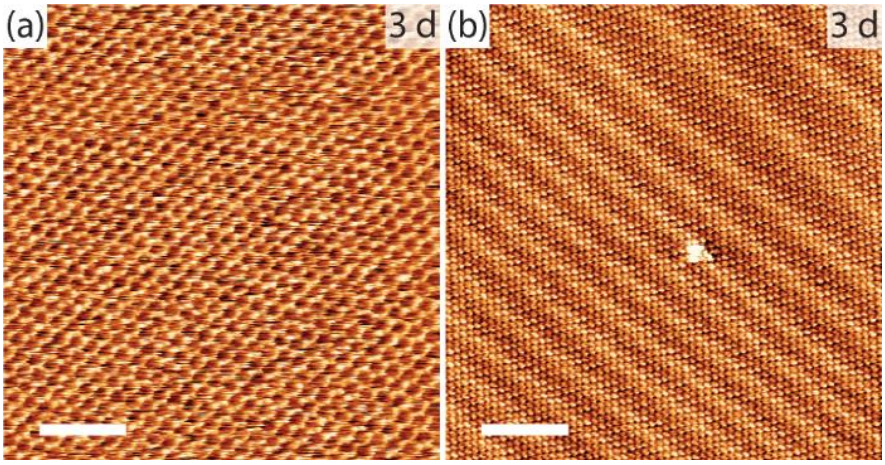

Figure 6.11 Self-assembly of TPA monolayers on TMA-protected graphite samples. Graphite substrates were exposed to 60 °C hot TMA in 7A solution for 3 days. (a) STM image of a TMA monolayer acquired immediately after removal of the sample from the solution. The TMA solution residues were then carefully removed with a tissue and a large excess of TPA in 7A solution was applied. The subsequently acquired STM image in (b) shows a pure, high quality TPA monolayer. In contrast, samples exposed to 60 °C hot pure 7A solvent for only 2 days (see Figure 6.7) were no longer conducive to TPA monolayer self-assembly. This clearly confirms that the presence of TMA in solution, and thus adsorbed TMA monolayers, protects the graphite substrate from solvent intercalation and leaves it in a state that facilitates the self-assembly of the less strongly hydrogen-bonded TPA monolayers (tunneling parameters: (a) 1000 mV, 150 pA; (b) 1000 mV, 50 pA; both scale bars are 10 nm).

6.3 Conclusions

In summary, self-assembly of TPA and FGC18 monolayers was no longer possible after the graphite substrates were immersed in their respective solutions at temperatures above the monolayer desorption threshold for durations on the order of days. Given the different nature of the two solvents being probed, i.e. aliphatic versus aromatic and protic *versus* non-protic, this appears to be a more common phenomenon. While STM and AFM showed no evidence of changes on the graphite surface, LEEM revealed spatial inhomogeneities in electron reflectivity with feature sizes on the order of tens of nanometers (Figure 6.10). Accordingly, the origin can be attributed to interlayer changes in the graphite substrate due to solvent intercalation, which can be completely reversed by vacuum annealing to relatively high temperatures of 900 °C. Apparently, this solvent intercalation weakens molecule-surface interactions to such an extent that TPA and FGC18 monolayers become thermodynamically unstable. Interestingly, solvent intercalation can be prevented by adsorption of TMA monolayers, which persist on the graphite surface during immersion in hot solvent due to their extraordinarily high thermodynamic stability.

In general, intercalation can endow graphite with intriguing properties like superconductivity.[180] Also the surface properties of graphite, such as its electrowetting behaviour, can be tuned by the more common intercalation of (an)ions.[181] Accordingly, future experiments are aimed at studying

the properties of this organic solvent-intercalated form of graphite, which is very easy to prepare and therefore widely available.

Chapter 7

Versatile Role of Molecule–Surface Interactions for Monolayer Self-Assembly at Liquid–Solid Interfaces

This chapter introduces Au (111) passivated surface with a monolayer of chemisorbed iodine (I-Au(111)) as a viable alternative substrate for fundamental studies of molecular self-assembly at liquid-solid interfaces. The foundation for this exploration lies in the published paper titled " Versatile Role of Molecule–Surface Interactions for Monolayer Self-Assembly at Liquid–Solid Interfaces: Substrate-Induced Polymorphism, Thermodynamic Stability, and New Polymorphs," which is authored by Arash Badami-Behjat, Peter S. Deimel, Francesco Allegretti, Eva Ringel, Kingsuk Mahata, Michael Schmittel, Johannes V. Barth, Wolfgang M. Heckl, and Markus Lackinger, and originally published in Chem. Mater. 2022, 34, 19, 8876–8884, Copyright © 2022 by American Chemical Society. This chapter is reprinted and partially adapted with the permission American Chemical Society.

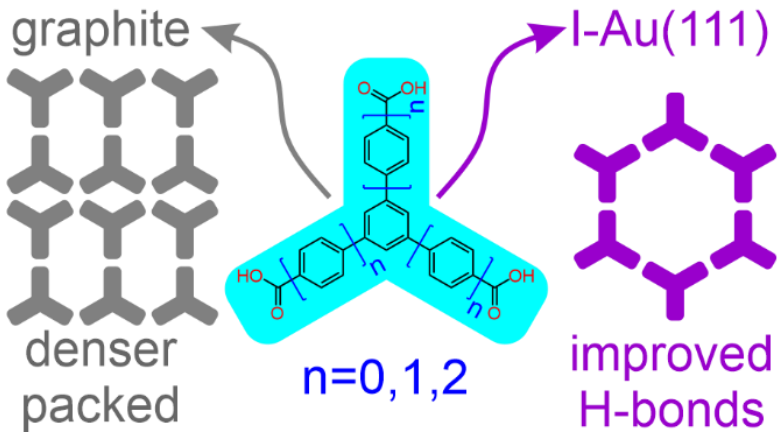

Self-assembly of supramolecular monolayers at liquid–solid interfaces has matured into an established research field. Numerous studies unveiled crucial influences of solvent, solute concentration, and temperature on the kinetics and thermodynamics of monolayer formation and their specific role for structure selection. Yet, almost all experiments are carried out on highly inert graphite surfaces that are straightforward to prepare. However, the strong focus on graphite leaves the crucial impact of the underlying surface severely underexplored. Here, we show that passivation of Au(111) with a chemisorbed monolayer of iodine atoms renders it sufficiently inert for studies at liquid– solid interfaces, even at elevated temperatures. By using aromatic homologues of benzene tricarboxylic acids as a well-explored model system and by a one-to-one comparison to graphite, we unveil that molecule–surface interactions can cause substrate-induced polymorphism, crucially affect the supramolecular monolayer's thermodynamic stability, or even result in the emergence of new polymorphs. These experiments underscore a decisive and specific thermodynamic influence of the underlying surface. We expect our study to stimulate further research on the surface influence on interfacial monolayers by employing this accessible and easy-to-prepare surface with the aim to establish a new lever for steering supramolecular self-assembly.

My contribution to this work involved enhancing variable-temperature STM. This included repairing and redesigning the scanner unit, optimizing its protection through the additional coating, and replacing various components in the STM. I also conducted experiments, which encompassed establishing substrate preparation (I-Au(111)), performing room-temperature STM experiments, and conducting concentration-dependent STM experiments. Additionally, I was responsible for analyzing and interpreting the corresponding data for the manuscript preparation under the supervision of Prof. Dr. M. Lackinger who conceived and designed the study. Moreover, TPD, LEED, and XPS experiments were conducted by Peter Deimel, with data analysis performed by Eva Ringel.

7.1 Introduction

Self-assembly of supramolecular monolayers at liquid–solid interfaces has been a thriving research field ever since the first images of adsorbed molecules were acquired by scanning tunnelling microscopy (STM) under ambient conditions.[182] This type of study has proven suitable for exploring the fundamentals of supramolecular self-assembly,[183,184,185,186] also reaching the life sciences.[187] Moreover, light was shed on various phenomena such as bilayer growth,[188] chiral induction,[189] and non-crystalline equilibrium structures.[190] Yet, this research goes beyond the determination of quasi-static structures, for instance, by exploring stimuli responsive systems[191,192,193,194,195,196] or controlled manipulation at the molecular scale.[190,197] Undoubtedly, the field also owes its rapid and ongoing development to the relative ease of real space structure determination in submolecular detail by high-resolution STM.[198] Polymorphism, which is the emergence of distinct supramolecular structures for one and the same molecular building block, is a frequently encountered phenomenon for interfacial monolayers. Initially, different polymorphs were observed depending on the applied solvent.[199,200,201,202,203] Later, also solute concentration and temperature were identified as decisive parameters for structure selection.192,[204,205,206,207,208] While the particular influence of a given solvent is hardly understood and presumably has to be evaluated on a case-by-case basis, more universal trends are delineated for both concentration and temperature: Lower concentrations and/or higher temperatures tend to yield less densely packed polymorphs on the surface.[195,204,207,208] The evident explanation is provided by the increased entropy cost per molecule ($\Delta S_{mol} < 0$) for adsorption from solution into the monolayer. This thermodynamically destabilizing contribution affects more densely packed polymorphs more severely, because for self-assembly of interfacial monolayers the free energy change per unit area ($\Delta g = \Delta G/A < 0$) is the relevant thermodynamic potential,[209,210] and its main entropy contribution scales with the area density of molecules. Consequently, less densely packed polymorphs become thermodynamically favored at higher temperatures and/or for higher negative ΔS_{mol} at lower solute concentrations. Exceptions to this rule, however, remind us that this seemingly obvious scenario can bear a hidden complexity. The counterintuitive emergence of a more densely packed row structure for 1,3,5-benzenetribenzoic acid (BTB, Figure 7.1b) as the high temperature polymorph, for instance, could be rationalized by stabilization of the porous honeycomb polymorph at lower temperatures through solvent coadsorption in its pores.[192]

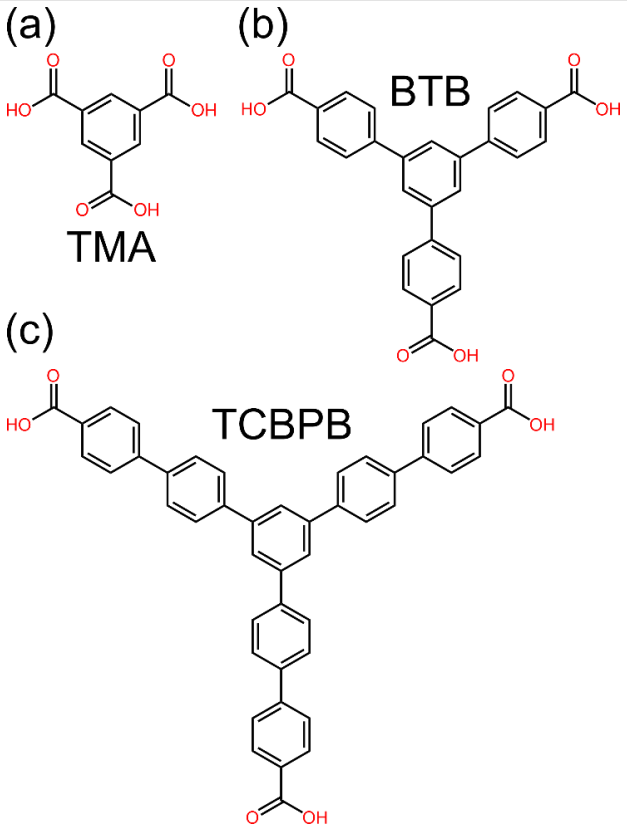

Figure 7.1 Chemical structures of aromatic tricarboxylic acids. (a) Trimesic acid (TMA), (b) 1,3,5-benzenetribenzoic acid (BTB), and (c) 1,3,5-tris[4-carboxy(1,10-biphenyl-4-yl)]benzene (TCBPB).

Moreover, the occurrence of irreversible phase transitions upon heating indicates kinetic trapping of metastable intermediates[211,212] and serves as a warning sign that thermodynamic control cannot be taken for granted. The essential and routinely implicitly assumed dynamic equilibrium between monolayer and solution may be in a frozen state, in particular for larger molecules on more strongly interacting surfaces.[213,214,215]

Despite the ever-growing body of work on polymorph selection and phase transitions for interfacial monolayers, the surface influence has not yet been systematically explored. At a first glance this appears surprising as the conventional wisdom in the field tells us that molecule–surface interactions are decisively important for structure selection.[206,209] But this apparent disinterest most plausibly has a more technical origin. STM as the prevalent analytic tool demands reasonably flat and electrically conductive surfaces. In addition, these must be sufficiently inert, not only under ambient conditions but also in solution, where corrosive fatty acids are often applied as solvents. For these reasons and also because it is available in high quality synthetic form, graphite is the almost exclusively used substrate, as opposed to molybdenite (MoS_2), which also meets the requirements but can only be obtained as a mineral. In the present study, we advocate the use of Au(111). Although at liquid–solid interfaces adsorption energies are sizably lowered by the supernatant liquid,[209,216] on pristine Au(111) they can still remain high enough to severely hamper

the dynamic equilibrium.[213,214] Accordingly, we passivated the Au(111) surfaces with a closed monolayer of chemisorbed iodine (I−Au(111)). This surface was previously introduced for studies of supramolecular self-assembly at electrified surfaces from aqueous solutions.[217,218] Adsorbates on the chemisorbed iodine monolayers become effectively decoupled from strongly interacting metal surfaces[219,220,221] through markedly increased adsorption heights in the absence of electronic interferences.[222] Moreover, we have demonstrated that iodine passivation is viable to alter the adsorption geometry of three dimensional anthracene−triptycene molecules as the starting point to steer their supramolecular self-assembly.[223] Here, we use commercially available high quality Au(111) thin films on mica instead of single crystals. The facile preparation consists of flame annealing (Figure 7.2a) and subsequent dipping into aqueous potassium iodide solution (Figure 7.2b), which readily results in complete coverage with a closed iodine monolayer (Figure 7.3b). Figure 7.3a indicates the STM image of the bare Au(111) before iodine passivation. Furthermore, Figure 7.4 demonstrates the iodine monolayer stability even at elevated temperatures. Our study comprises three different aromatic tricarboxylic acids. The direct comparison between I−Au(111) and graphite substrates reveals a pronounced surface influence on polymorph selection as well as thermodynamic stability and culminates in the observation of an unprecedented polymorph.

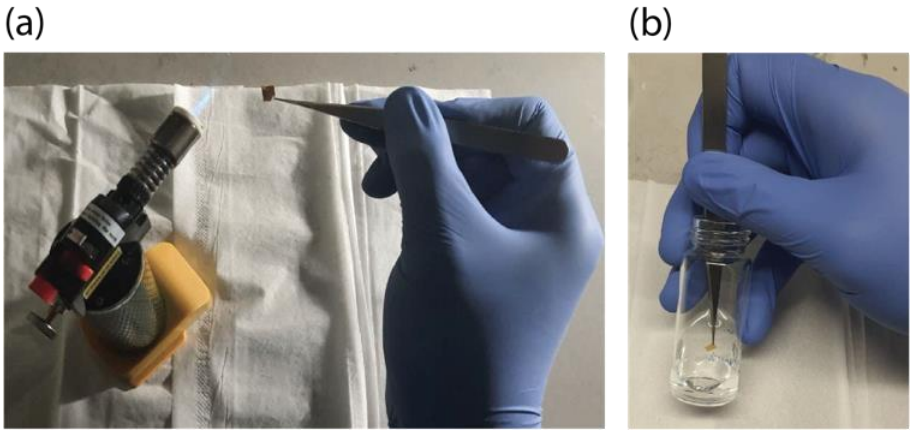

Figure 7.2 Wet chemical preparation of I-Au (111) sample. (a) Flame annealing of Au(111) samples to provide a flat and clean surface, followed by (b) dipping inside KI solution for iodine adsorption.

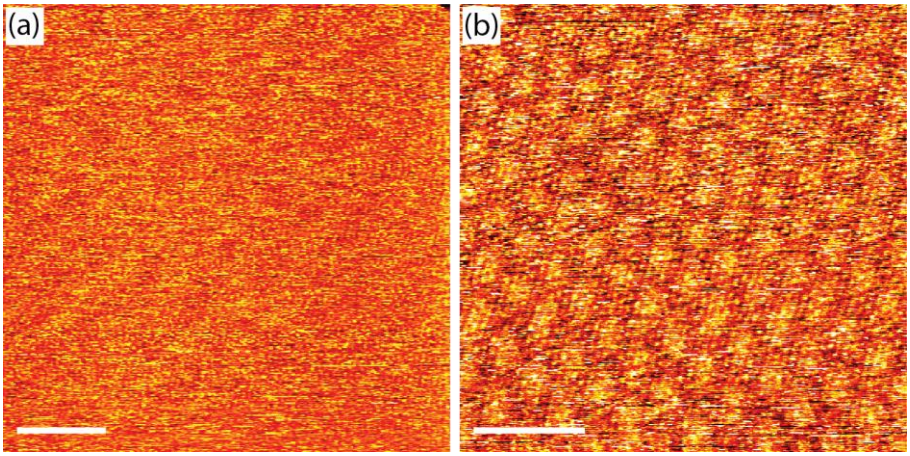

Figure 7.3 Bare I-Au(111) surface. (a) Overview and (b) atomically resolved STM images of a wet-chemically iodine-passivated Au(111) surface. Samples are atomically flat on the 500 nm scale. The close-up in (b) shows the atomic structure of the iodine layer as hexagonal dense packing of spheres with lattice parameters a=b=0.50 nm. The hexagonal Moiré pattern indicates the formation of a superstructure. (Scale bars and tunneling parameters: (a) 100 nm, 500 mV, 55 pA; (b) 5 nm, 300 mV, 55 pA)

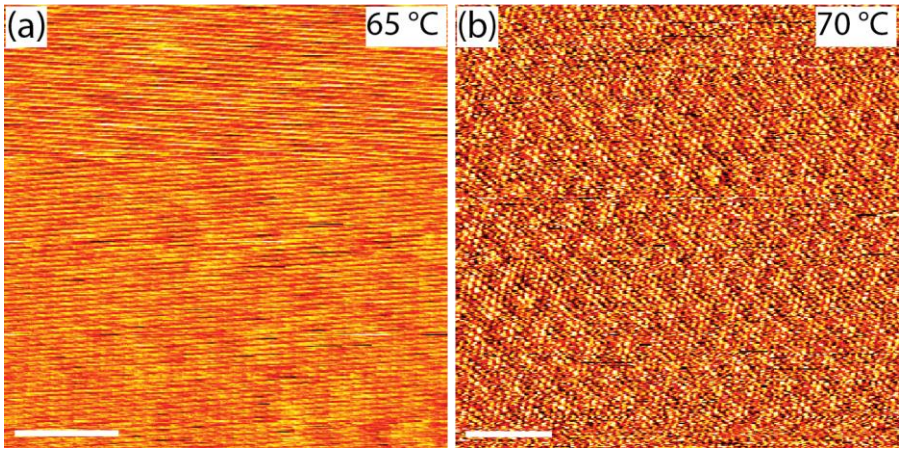

Figure 7.4 Temperature stability of the iodine passivation layer was probed in hot solvents. STM data of the bare I-Au(111) surface. The images were acquired at elevated temperatures as indicated in the upper right corners at the interface to (a) TMA in 7A solution after desorption of the TMA monolayer and (b) pure heptanoic acid solvent. In both cases, the integrity of the iodine monolayer could be confirmed at the atomic scale by STM imaging. Thereby, we demonstrate sufficient stability of I-Au(111) also for variable temperature experiments at liquid-solid interfaces. (scale bars and tunneling parameters: (a) 3 nm, 300 mV, 6 pA; (b) 5 nm, 550 mV, 65 pA)

7.2 Substrate-induced polymorphism

An intriguing research question is whether and how the underlying surface can affect polymorph selection in interfacial monolayers. To address this issue, we have chosen the aromatic homologues of benzene tricarboxylic acids shown in Figure 7.1 as a model system. All three are documented cases of solvent- and/or concentration-induced polymorphism.[199,200,206] The root cause lies in the versatility of H-bonding between carboxylic acid groups, alongside the energetic

similarities of different motifs.[224] Apart from the energetically preferred cyclic double H-bond ($R_2^2(8)$, according to graph-set notation, higher cyclic (e.g.c$R_3^3(12)$) or catemeric motifs are commonly observed.[225] Density functional theory (DFT) calculations carried out for terephthalic acid (TPA, 1,4-benzene dicarboxylic acid) yield a total binding energy of 66.9 kJ/mol for the $R_2^2(8)$cyclic dimer to be compared with 89.2 kJ/mol for the $R_3^3(12)$cyclic trimer.[226] Accordingly, the binding energy per H-bond is about 3.7 kJ/mol less in the cyclic trimer. This becomes also apparent in the DFT calculated intermolecular binding energies of the two commonly observed trimesic acid (TMA) monolayer polymorphs. The chicken wire polymorph (Figure 7.5b) that exclusively features the cyclic dimer motif results in an intermolecular binding energy of 91.9 kJ/mol per molecule, while the corresponding value amounts to 80.6 kJ/ mol for the flower polymorph (Figure 7.5a), where two-thirds of the H-bonds are within cyclic dimers and one-third are within cyclic trimers. This difference in TMA binding energy reflects the difference in H-bond binding energy.[224]Nevertheless, the energetic similarity of the various motifs in the order of thermal energy facilitates fine balancing between H-bond dominated intermolecular interactions and molecular packing.

7.3 Results and Discussion

To unambiguously isolate the substrate influence in our experiments, we applied solutions from the same batch without significant time delays and with reversed order onto both graphite and I−Au(111) surfaces. The reliably observed monolayer structures for TMA and BTB are summarized in Figure 7.5 (see Figure 7.6 for overview images). For both tricarboxylic acids, different polymorphs were observed on the two surfaces with a common trend: The structures on I−Au(111) consistently exhibit lower molecular packing densities with fewer molecules per unit area. For both TMA and BTB the chicken wire polymorphs that exclusively feature ideal $R_2^2(8)$cyclic H-bonds were found on I−Au(111). By contrast, on graphite only two-thirds (TMA) or one-third (BTB) of the carboxylic acid groups express these ideal H-bonds. The alternatively formed 3-fold cyclic $R_3^3(12)$ (TMA) or mixed catemeric H-bond and C−H···O bond motifs (BTB) are energetically inferior but facilitate higher surface packing densities.

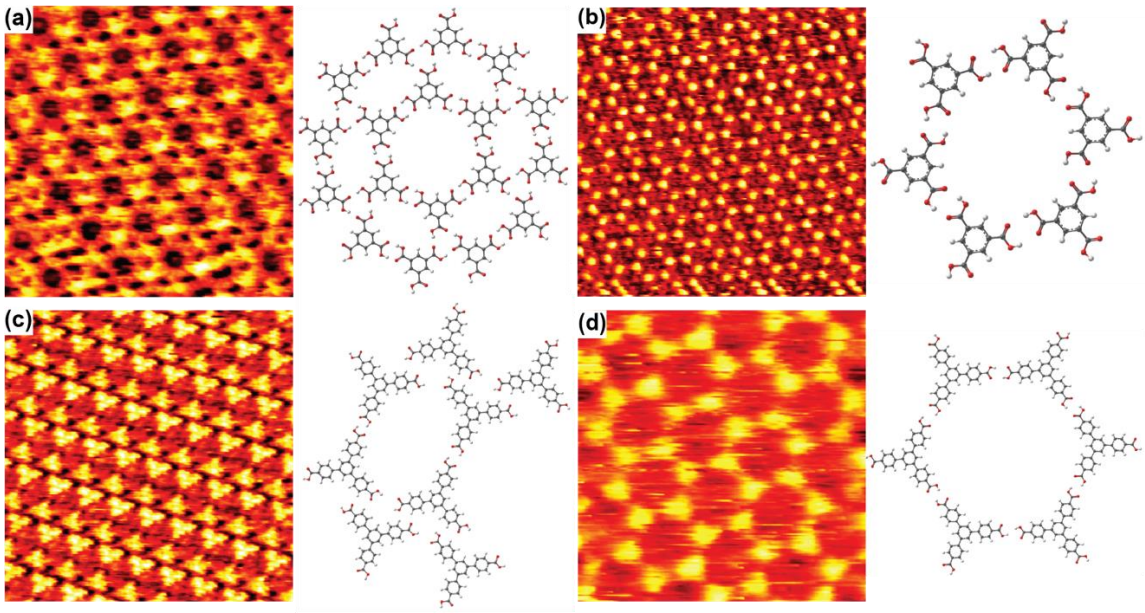

Figure 7.5 Substrate-induced polymorphism of TMA and BTB. STM images of TMA monolayers on (a) graphite and (b) I−Au(111) acquired in the same saturated hexanoic acid solution. In accord with our previous studies, TMA assembles into the flower structure on graphite,[199] while on I− Au(111) the chicken wire structure is observed. STM images of BTB monolayers on (c) graphite and (d) I−Au(111) acquired in the same saturated 7A solution. In accord with our previous studies, BTB assembles into the dimer row structure on graphite,[200] while on I− Au(111) the chicken wire structure is observed. Models of the respective structures are depicted next to each STM image. On I−Au(111) the polymorphs observed for both TMA and BTB are less densely packed but exhibit stronger H-bonding. (Atom color code: gray, carbon; red, oxygen; white, hydrogen; all STM images: 15×15 nm^2; tunneling parameters: (a) 400 mV, 55 pA; (b) 350 mV, 55 pA; (c) 300 mV, 55 pA; (d) 400 mV, 50 pA).

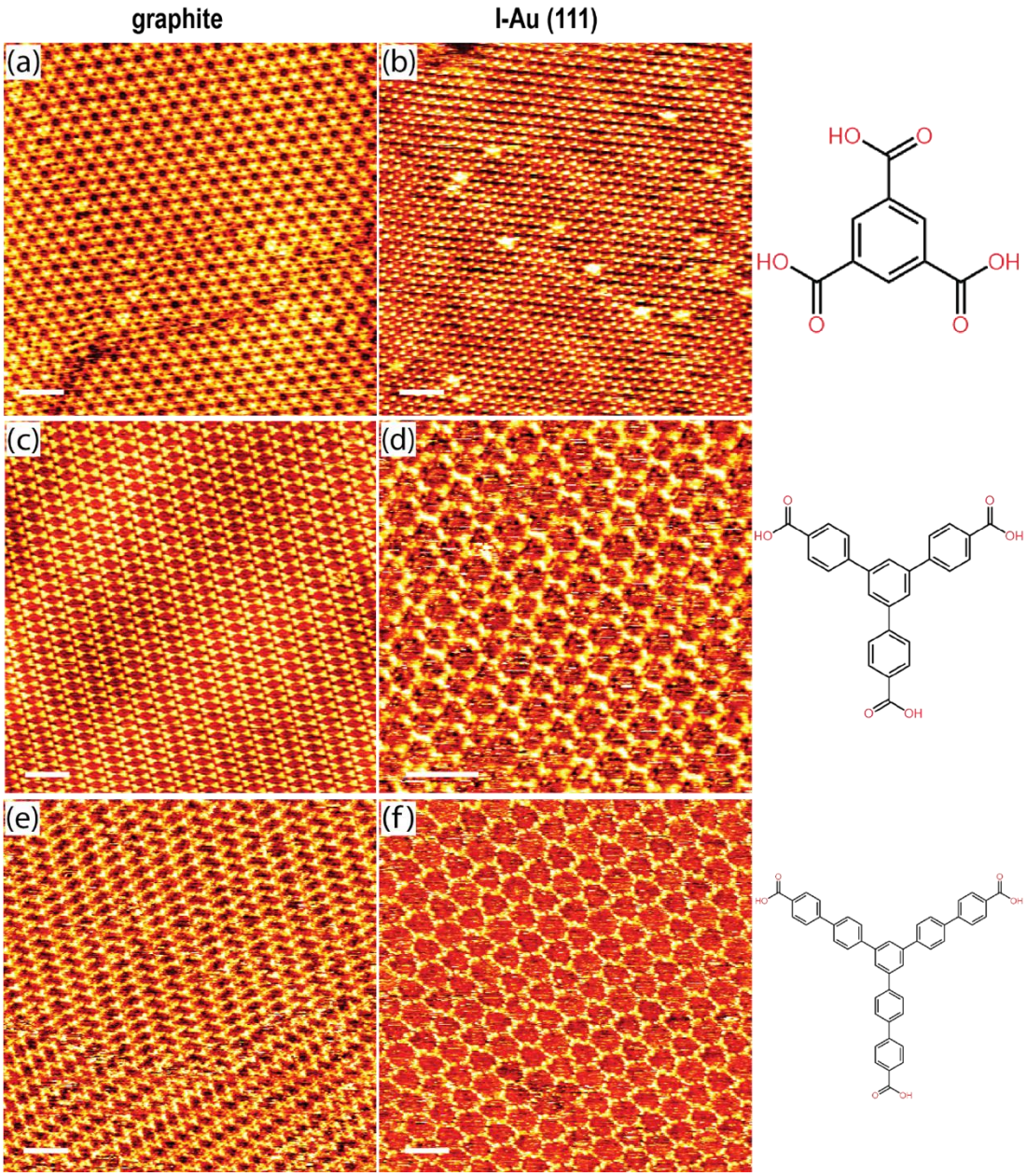

Figure 7.6 Overview STM images for the three studied tricarboxylic acids on both surfaces (left column: graphite; right column: I-Au(111)): (a) / (b) TMA; (c) / (d) BTB; (e) / (f) TCBPB; For convenience, the molecular structures of the respective tricarboxylic acids are shown on the right hand side in each row. (all scale bars: 6 nm; tunneling parameters: (a) 400 mV, 55 pA; (b) 300 mV, 55 pA; (c) 300 mV, 55 pA; (d) 300 mV, 55 pA; (e) 400 mV, 55 pA; (f) 350 mV, 55 pA)

7.4 Thermodynamical Stability

Finding less densely packed polymorphs with energetically superior H-bonds on I−Au(111) can be interpreted as an indication of weaker molecule−surface interactions. For more weakly interacting surfaces, optimizing the intermolecular binding can yield a larger negative Δg for monolayer self-assembly. Conversely, on more strongly interacting supports, the absolute value of Δg becomes larger by enhancing the contribution from molecule−surface interactions through an increased molecular area density, while accepting compromises in the intermolecular bonding. This tendency becomes more pronounced for larger building blocks, because of their higher free energy gain $\Delta G_{molecule\text{-}surface}$ for adsorption per molecule associated with molecule−surface interactions. In a first approximation the negative $\Delta H_{molecule\text{-}surface}$ increases approximately linearly with molecular size,[227] which outweighs the slower, approximately logarithmic increase of the entropy cost ΔS_{mol} for adsorption.[228] We like to point out here that it is sufficient to resort to the mean value of $\Delta H_{molecule\text{-}surface}$ for these thermodynamic considerations. Thereby, molecule-to-molecule variations of adsorption energies that can occur for inequivalent adsorption sites within a unit cell for commensurate or on an extended scale for incommensurate superstructures, respectively, are averaged out.

7.5 TPD Measurement

To experimentally test our hypothesis, we first conducted temperature-programmed desorption (TPD) experiments for TMA on both graphite and I−Au(111). Thereby, we evaluate differences in desorption energies in the absence of solvent, i.e., at the vacuum-solid interface. In TPD, desorption is induced through a linear temperature ramp and sensitively detected by a mass spectrometer.[229] Desorption spectra acquired for different heating rates are summarized in Figure 7.7. Desorption energies are normally extracted by applying suitable models.[230] This was, however, in the present case not easy to fulfill. The desorption spectra on I−Au(111) show two peaks even upon deposition of nominal submonolayer coverages, which we interpret as desorption from the second layer (low-temperature peak) prior to desorption of the directly surface-bound monolayer (high-temperature peak). Bilayer formation before completion of the first monolayer, or more generally dewetting, is a common trait of weakly interacting surfaces.[231,232] Moreover, the coexistence of different TMA polymorphs can further complicate the analysis.[233] Although the precise quantification of desorption energies was intricate, in particular for I−Au(111) (see Appendix C for a detailed analysis), the pronounced shift of the measured monolayer desorption peak maximum for $\beta = 5$ K/s of 460 K on graphite to 395 K on I−Au(111) points toward a markedly weaker adsorption of

TMA on the latter. By contrast, desorption of chemisorbed iodine from Au(111) occurs at significantly higher temperatures >670 K in a vacuum, [220,234] indicating a large safety margin for the stability of the passivation layer itself. Since intermolecular interactions are similar on both surfaces, with presumably little influence of the underlying surface on the H-bond strength,[235] the difference in desorption temperatures can readily be attributed to differences in the strengths of molecule−surface interactions. This is in accord with previous DFT calculations that inferred weak adsorption of organic adsorbates on iodine passivated Ag(111).[219,222]

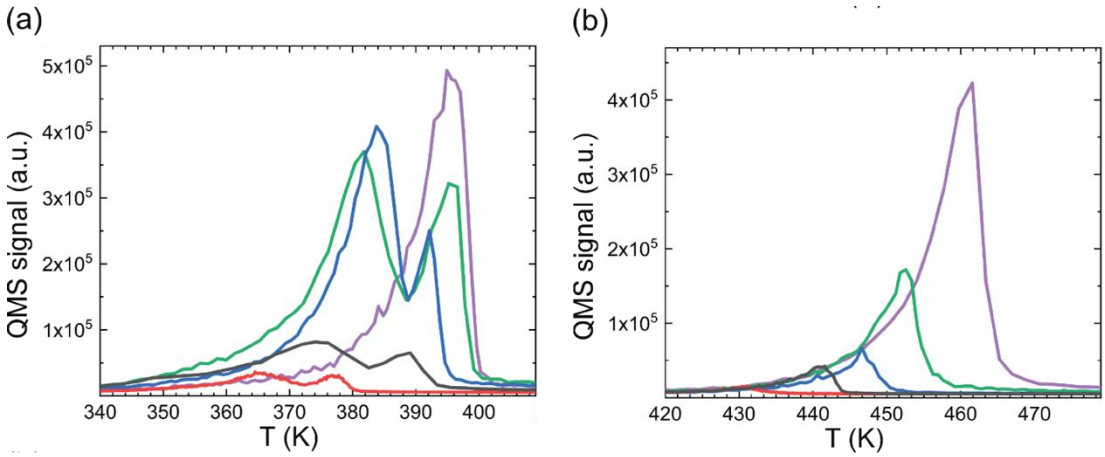

Figure 7.7 Temperature-programmed desorption of TMA from (a) I− Au(111) vs (b) graphite measured at 210 amu, i.e., the full mass of intact TMA. Desorption spectra were acquired for different heating rates β (violet, 5 K/s; green, 2 K/s; blue, 1 K/s; gray, 0.5 K/s; red, 0.15 K/s).

7.6 Immersion Scanning Tunneling Microscopy

Studies of on-surface supramolecular self-assembly are commonly conducted with a standard ambient STM, which has been integrated with a heatable sample stage for elevated temperature experiments. However, in this type of system, solvent evaporation becomes an inevitable challenge that limits the experiment duration and indicates a significant obstacle to achieving temperature stability, reducing drift, as well as investigating slow kinetics phenomena. Consequently, our group previously developed an innovative STM setup[236] with the capability to operate entirely within a solution. In this setup, the STM is hermetically sealed inside a container filled with the solution. Operating the microscope within the sealed conditions effectively prevents solvent evaporation. Consequently, the Immersion Scanning Tunnelling Microscope (I-STM) (Figure 7.8) facilitates prolonged experiments in a temperature-stable and controllable environment with a range from room temperature to 100°C.

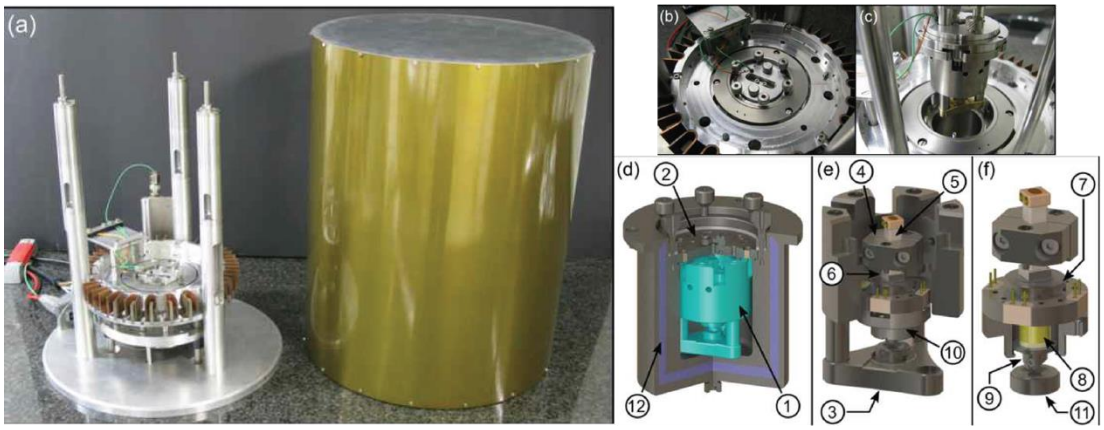

Figure 7.8 Immersion Scanning Tunnelling Microscope. (a) Complete assembly of the immersion-STM with outer shielding on the right; (b) STM lowered into the heatable container (integrated into the base plate of the vibration isolation) and sealed. (c) Retracted STM inside the lowering device (only tripod visible) standing on top of the vibration isolation, (d) CAD drawing of the STM (cyan) inside the closed heatable container, (e) enlarged section image of the STM body, and (f) moveable part of the STM with integrated nanopositioner and scan-unit. [(d)–(f)]: (1) STM, (2) lid of the heatable container, (3) sample holder stage, (4) spring loaded metal jaws, (5) ceramic axis, (6) piezo-stack actuator, (7) scan-unit base plate, (8) piezo tube, (9) tip-holder, (10) segmented metal shielding of the piezo tube, (11) sample holder, and (12) aerogel granulate. Reprinted from O. Ochs et al., Review of Scientific Instruments, 2018, 89, 053707, with the permission of AIP Publishing.

7.7 Substrate-dependent variable-temperature STM study of TMA

To corroborate the TPD results and also to explore their implications for the actual environment, where desorption energies are sizably reduced by the supernatant solution,[209,216] we have additionally studied thermal desorption at the liquid−solid interface. Therefore, we applied variable-temperature STM imaging, taking advantage of a dedicated home-built instrument that facilitates long-term experiments in solution at elevated temperatures.[236] Yet, important principal differences need to be emphasized: TPD is a kinetic experiment, where desorption energies are viewed as barriers and extracted from measured rates. On the contrary, the conceptual idea of our variable-temperature STM studies is to probe the position of the thermodynamic equilibrium as a function of temperature, albeit kinetic hindrance cannot a priori be excluded.[215,237] Observing the recession of molecular coverages and eventually full monolayer desorption indicates that a critical temperature is reached, where the interfacial monolayers become thermodynamically unstable.

For these experiments we have likewise chosen TMA. But to evaluate the surface influence on the thermodynamic stability of monolayers, it is more expedient to compare the same polymorph. Therefore, we used heptanoic acid as the solvent, because it affords the TMA chicken wire structure on both graphite and I−Au(111). The experiments on the different substrates were carried out back-to-back using the same solution. On graphite, the chicken wire polymorph could still be stably imaged up to 100 °C (Figure 7.9), which is the limit of our setup. By contrast, on I−Au(111) we could still image the TMA chicken wire polymorph at 60 °C, while it vanished completely when

the temperature was increased to 65 °C (Figure 7.10). Upon cooling, we observed reemergence of the chicken wire polymorph but often only at lower temperatures in the range of 50−55 °C. The origin of this hysteresis remains presently unclear. Notably, we have reproduced these results multiple times to ensure that disappearance of the TMA chicken wire structure is an experimental fact and not an artifact due to the loss of STM resolution. Moreover, we have experimentally corroborated the stability and integrity of the iodine monolayer on Au(111) by acquiring atomically resolved STM images at 70 °C in pure heptanoic acid solvent (see Figure 7.4). This is important to rule out any influences from changes or deterioration of the passivation layer.

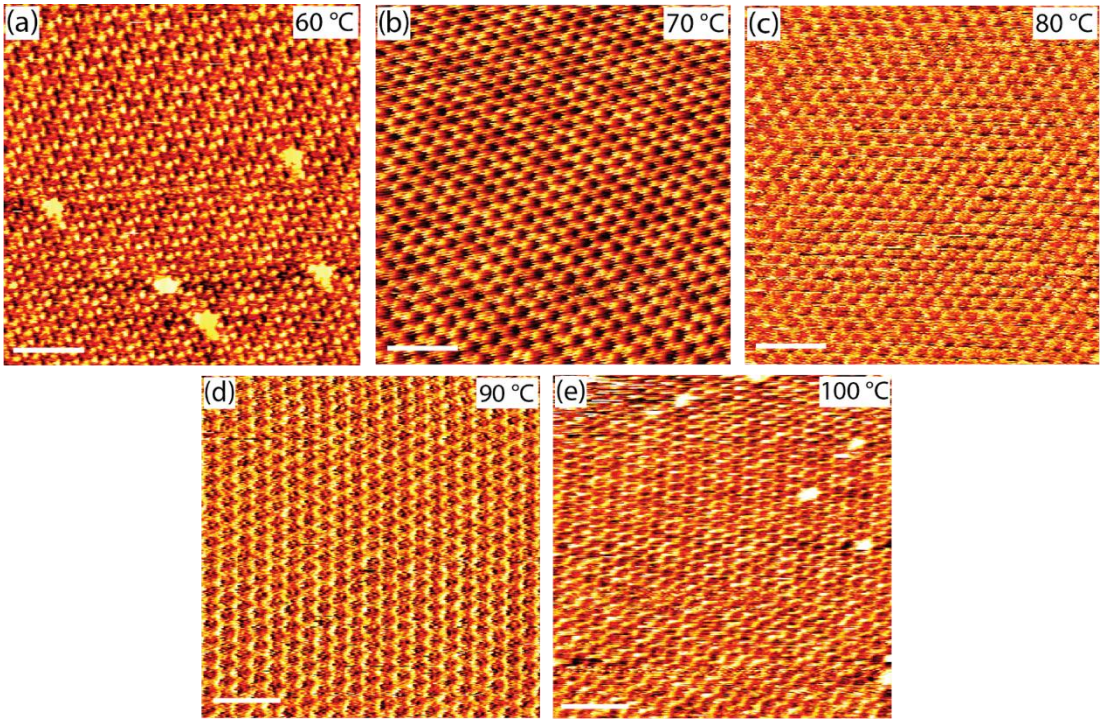

Figure 7.9 Variable-temperature STM studies of TMA on graphite. Images were acquired in saturated heptanoic acid solution at temperatures as indicated: (a) 60 °C; (b) 70 °C; (c) 80 °C; (d) 90 °C and (e) 100 °C, i.e. the upper temperature limit of our setup; All images consistently show the TMA chicken wire polymorph. This corroborates its high thermodynamic stability gained from the combined strength of molecule-molecule and molecule-surface interactions. These images were acquired in different experimental runs. (all scale bars: 5 nm; tunneling parameters: (a) 600 mV, 65 pA; (b) 600 mV, 60 pA; (c) 650 mV, 65 pA; (d) 600 mV, 65 pA; (e) 650 mV, 65 pA).

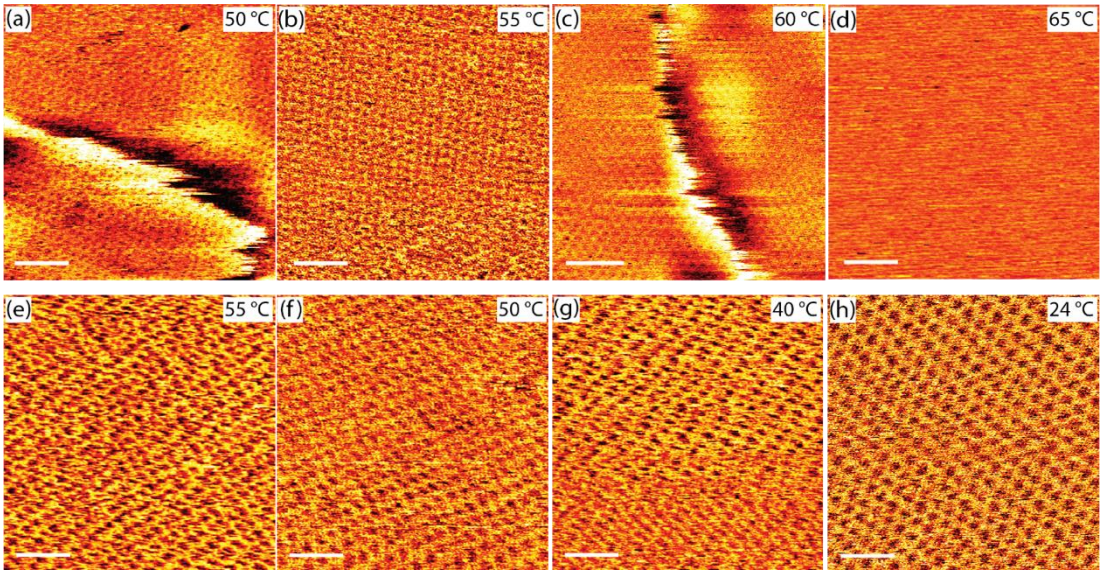

Figure 7.10 Variable-temperature STM studies of TMA on I-Au(111). Images in the upper row were acquired in the same saturated heptanoic acid solution as used for the STM experiments presented in Figure 7.9 at increasing temperatures as indicated: (a) 50 °C; (b) 55 °C ; (c) 60 °C; (d) 65 °C; Images in the lower row were acquired after heating to 65 °C where the TMA monolayers were fully desorbed and subsequently cooling to the temperatures as indicated: (e) 55 °C; (f) 50 °C ; (g) 40 °C; (h) 24 °C; In contrast to graphite, the TMA chicken wire polymorphs is no longer thermodynamically stable at temperatures >65 °C as inferred from disappearance of any discernible TMA structure in (d). Since the molecular structure, hence the intermolecular bonds, are similar on both graphite and I-Au(111), the inferior stability on I-Au(111) as compared to graphite can be attributed to the relative weakness of molecule surface interactions on I-Au(111). Reemergence of the chickenwire polymorph upon cooling down ((e)-(h)) indicates that both solution and surface do not suffer from chemical changes. (all scale bars: 5 nm; tunneling parameters: (a) 280 mV, 5 pA ; (b) 280 mV, 5 pA; (c) 300 mV, 7 pA; (d) 300 mV, 6 pA; (e) 500 mV, 7 pA; (f) 350 mV, 6 pA; (g) 350 mV, 6 pA; (h) 350 mV, 5.5 pA)

At this point, we would also like to point out that acquiring STM images on I−Au(111) is considerably more difficult than on graphite. In summary, the variable-temperature STM experiments at the liquid−solid interface provide strong evidence for inferior thermodynamic stability of the TMA chicken wire polymorph on I−Au(111) as compared to graphite. Because solvent, TMA concentration, and intermolecular binding were identical for both substrates, the most obvious explanation is provided by weaker molecule−surface interactions on I−Au(111). This is in accord with our TPD experiments, which, however, evaluated desorption energies with respect to vacuum, i.e., without the pronounced influence of a supernatant liquid. But the solvent influence is considered to be comparable for both surfaces, at least in terms of solvation enthalpies, and less so in the wetting of the surface. Nevertheless, we propose that the TPD results qualitatively hold true also for liquid−solid interfaces.

7.8 Novel Polymorphs

The pronounced substrate influence on polymorph selection ascertained for TMA and BTB prompted an additional intriguing question: Could new polymorphs emerge on I−Au(111) that had

not been observed on graphite before? In this regard, TCBPB (Figure 7.1c) is a promising candidate. On graphite, we previously found the common traits of concentration-induced polymorphism, i.e., less densely packed structures for lower solute concentrations.[204] Yet, for diluted solutions, only the so-called displaced chicken wire structure was observed, in which all carboxy-biphenyl entities were not bound head-to-head through cyclic $R_2^2(8)$H-bonds but associated sideways through C−H···O bonds analogous to the displaced dimer row structure (Figure 7.11c). The C−H···O bonds are commonly interpreted as weak H-bonds, but the origin of their binding strength lies in an attractive interaction between the H-bond acceptor and the aromatic system.[238] The packing density of the displaced chicken wire structure is the lowest, as observed experimentally for all TCBPB polymorphs on graphite, but it still exceeds that of the hypothetical TCBPB chicken wire polymorph. The search for a chicken wire polymorph isostructural to that of BTB and TMA on graphite by further diluting solutions was not crowned with success for TCBPB. It merely resulted in prohibitively low concentrations for thermodynamically stable TCBPB monolayers, as experimentally manifested by STM.

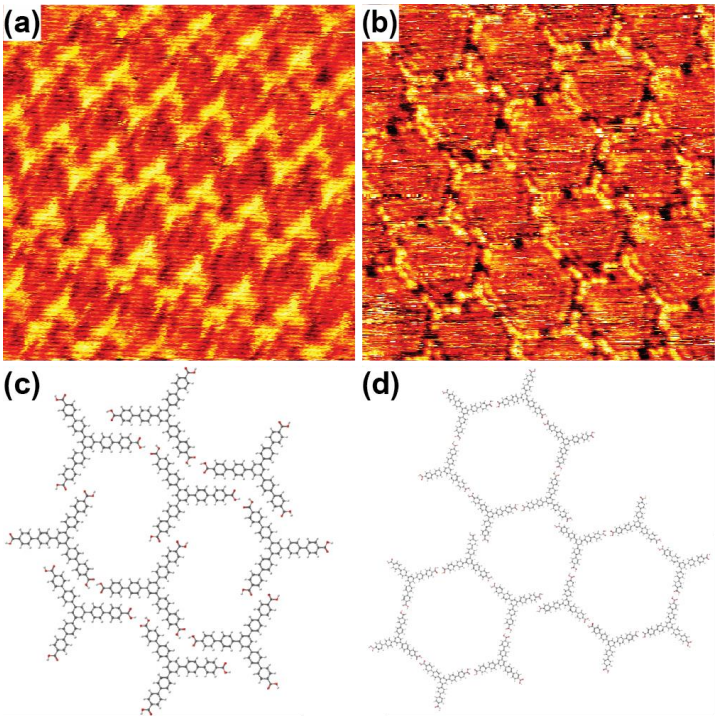

Figure 7.11 Substrate-induced polymorphism for TCBPB. STM images of TCBPB monolayers on (a) graphite and (b) I−Au(111) were acquired in the same saturated heptanoic acid solution. In accord with previous studies, TCBPB assembles into the known displaced dimer row structure on graphite,[206] while on I−Au(111) an unprecedented structure was observed that can be viewed as intermediate between the displaced and the actual chickenwire structure. (c, d) Models of the respective structures are shown below each STM image. (Atom color code as in Figure 7.5; both STM images: 15×15 nm^2; tunnelling parameters: (a) 600 mV, 55 pA; (b) 310 mV, 55 pA).

The established trend for self-assembly of polymorphs with lower packing density and superior H-bonding on I−Au(111) motivated us to resume our TCBPB studies on this more weakly interacting surface. STM images of the structures acquired on both graphite and I−Au(111) for the same saturated solution are depicted in Figure 7.11(cf. Figure 7.6 for overview images). On graphite, we observed the known more densely packed displaced dimer row polymorph,[206] where the TCBPB dimers are bonded sideways. By contrast, the TCBPB structure observed on I−Au(111) is unprecedented. It could be viewed as intermediate between the actual and the displaced chicken wire polymorph with reduced symmetry: Six TCBPB molecules form cyclic hexamers, where two-thirds of the carboxylic acid groups bind via ideal $R_2^2(8)$ H-bonds. Yet, these hexamers are interconnected via the displaced arrangement between the remaining third of the carboxylic acid groups Figure 7.11d). Thereby, the packing density is reduced from 0.15 molecules/nm^2 for the displaced chicken wire to 0.12 molecules/nm^2 for this new polymorph. Yet, similarly on I−Au(111) further dilution did not eventually yield the actual chicken wire polymorph which would exhibit an even lower packing density of 0.10 molecules/ nm^2 but again resulted in the absence of monolayer self-assembly. Nevertheless, the weaker molecule−surface interactions on I−Au(111) could still evoke a less densely packed TCBPB polymorph that had not been observed on graphite before.

7.9 Discussion and Summary

We collected multiple pieces of evidence that the facile-to-prepare I−Au(111) surface exerts a pronounced influence on monolayer self-assembly at the liquid−solid interface through attenuated molecule−surface interactions. By applying identical solutions to both graphite and I−Au(111), we present three unambiguous cases of substrate-induced polymorphism for the aromatic homologues of benzene tricarboxylic acids. For TMA and BTB the renowned chicken wire polymorphs were found on I−Au(111), while the intermediate chicken wire structure observed for TCBPB is unprecedented. All polymorphs on I−Au(111) consistently exhibit lower packing densities but energetically superior H-bonding as compared to those found on graphite. This is to be expected for more weakly interacting substrates with a diminished contribution from molecule−surface interactions to Δg. Our guiding hypothesis of weaker adsorption on I−Au(111) is corroborated by desorption experiments either in a vacuum using established TPD or in a solution using "desorption microscopy".

Albeit lower adsorption energies of the molecular building blocks plausibly explain our main experimental findings, additional, possibly substrate-dependent effects must be considered. In this respect, solvent coadsorption can play a crucial role. Analogous to bulk crystals, two cases can be

distinguished: (1) "solvate monolayers", that is, cocrystals of solute and solvent molecules with a solvent specific structure that cannot be adopted by the solute molecules alone,[211,212,239] and (2) mere solvent coadsorption within the pores of porous polymorphs, where the pristine surface is exposed to the solvent. The respective pore area fractions can be substantial, already amounting to ~39% for the TMA and increasing to ~62% for the BTB chicken wire polymorph, respectively. Even though this kind of solvent coadsorption appears more subtle because it has no discernible influence on the supramolecular monolayers in terms of molecular arrangements or lattice parameters, it can nevertheless give rise to a decisive contribution to Δg.[208,240,241] A special case arises when pore sizes and shapes become comparable to solvent molecules, and then steric matching may determine the polymorph.[224] But often solvent coadsorption cannot unequivocally be inferred from STM imaging, because larger pores accommodate several solvent molecules that dynamically adsorb and desorb at experimentally inaccessible time scales.

We argue, however, that solvent coadsorption does not play a relevant role for the here discussed cases of substrate-induced polymorphism. All structures observed on I−Au(111) are less densely packed compared to those on graphite and, hence, expose a larger area fraction of the bare surface to the solvent. This implies a larger possible contribution from solvent coadsorption to Δg on I−Au(111) from a structural point of view. However, also solvent coadsorption is weaker on I−Au(111) than on graphite, analogous to the actual molecular building blocks. We have tested this hypothesis by studying self-assembly of stearic acid (SA) as a model compound for fatty acid solvents, whose monolayers gain thermodynamic stability from the extended alkane tail. Interestingly, we could observe ordered SA monolayers at room temperature on both graphite and I−Au(111) (Figure 7.12). Yet, variable-temperature STM experiments revealed their inferior stability on I−Au(111): While on graphite, SA monolayers were still stable at 40 °C, they were already desorbed on I−Au(111). Consequently, we infer that the fatty acid solvent molecules also adsorb more strongly on graphite than on I−Au(111), in line with the notorious high affinity of alkanes to graphitic surfaces. Accordingly, the additional stabilization due to solvent coadsorption should also be stronger on graphite. In other words, solvent coadsorption would thermodynamically promote more porous polymorphs on graphite, which stands in contrast to their experimental observation on I−Au(111). To conclude, if there should be any solvent coadsorption on I−Au(111), for which we do not have credible STM evidence, its stabilizing contribution is surpassed by the weakness of molecule−surface interactions.

Registry effects between the lattices of a specific polymorph and crystalline surfaces constitute a further substrate influence worthy of discussion. Formation of commensurate superstructures is commonly interpreted as indication for a pronounced surface influence that maximizes molecule−

surface interactions, possibly in conjunction with structural adaptations at the expense of molecule−molecule interactions. On the contrary, on graphite, incommensurate supramolecular structures are common that optimize molecule−molecule interactions, while overriding the site dependence of molecule−surface interactions. These can be directly recognized in large scale STM images by periodic modulations of the apparent height known as Moiré patterns.[242] On the other hand, the I−Au(111) surface and consequently its potential energy landscape are highly corrugated. This became evident in our previous study of an anthracene−triptycene derivate, where we inferred a strong site dependence of the adsorption energy.[223] So in principle registry effects have the potential to selectively enhance $\Delta H_{molecule\text{-}surface}$ for specific lattice-matched polymorphs on the generally more weakly interacting I−Au(111) surface. Yet, for the here studied tricarboxylic acids, we did not encounter such an intriguing exception to the rule that polymorphs with lower packing density but energetically superior H-bonding emerge on more weakly interacting surfaces.

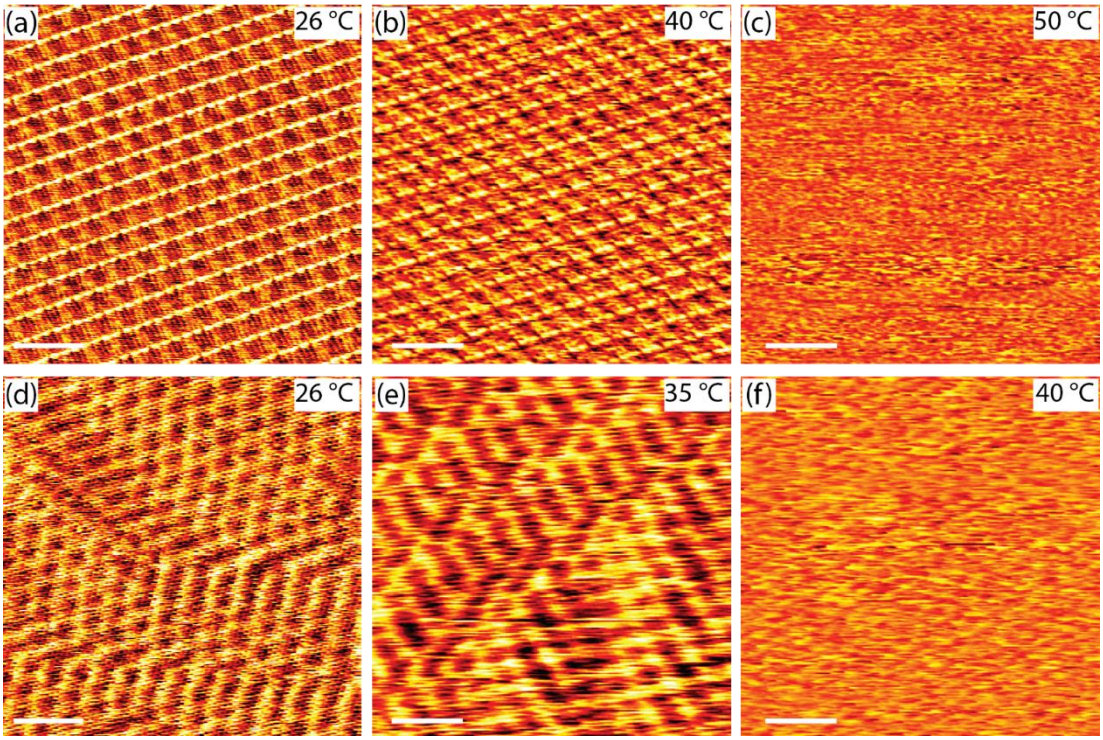

Figure 7.12 Self-assembly of stearic acid (SA). STM images of stearic SA monolayers on (a) / (b) / (c) graphite and (d) / (e) / (f) I-Au(111) acquired in the same phenyl octane solution with a concentration of ~10 mmol/L at the temperatures as indicated. On graphite the well-known lamellar structure emerges comprised of hydrogen bonded SA dimers. On I-Au(111) a comparable lamellar structure with similar spacing as in (a) is observed, but the contrast shows an additional hexagonal modulation due to the underlying iodine monolayer. Even though the SA molecules are not individually resolved on I-Au(111), the STM data indicate formation of a similar lamellar structure as on graphite with an additional signature of the hexagonal iodine monolayer. More importantly, alkane molecules can likewise form thermodynamically stable self-assembled monolayers on I-Au(111) at room temperature despite the absence of stabilization through a network of H-bonds as for the tricarboxylic acids. These variable-temperature STM experiments also indicate an inferior stability of the SA monolayer on I-Au(111) as compared to graphite: While the SA monolayer were still stable on graphite at a temperature of 40 °C (cf. (b)), they were already desorbed at the same temperature on I-Au(111) (cf. (f)) (all scale bars: 5 nm;

tunneling parameters: (a) 600 mV, 80 pA; (b) 550 mV, 65 pA; (c) 550 mV, 65 pA; (d) 300 mV, 65 pA; (e) 600 mV, 60 pA; (f) 600 mV, 60 pA)

The newly explored substrate-induced polymorphism exhibits some parallels to the established concentration-induced polymorphism. For instance, the BTB chicken wire structure is observed not only for saturated solutions on I–Au(111) but also upon dilution on graphite.[192] This does not hold true for TMA or TCBPB. The TMA flower polymorph is observed with hexanoic acid solutions on graphite (Figure 7.5), but we were not successful in obtaining the chicken wire polymorph just by dilution when using this solvent.[224] For TCPBP, dilution resulted in the displaced chicken wire polymorph on graphite,[206] but the intermediate chicken wire polymorph observed on I–Au(111) (Figure 7.11b) could not be obtained by further dilution. Albeit diluting solutions and weakening molecule–surface interactions both thermodynamically stabilize less densely packed polymorphs with stronger H-bonding, the structures observed in each case are not necessarily equal, and sometimes can only be obtained by either means.

In summary, the facile passivation of Au(111) by an iodine monolayer affords a new type of surface for studies of monolayer self-assembly at liquid–solid interfaces with a specific thermodynamic influence. Yet, on I–Au(111), molecule–surface interactions can already be too weak to thermodynamically stabilize supramolecular monolayers at the liquid–solid interface. For instance, TPA self-assembles on graphite into stable and easy-to-image monolayers comprised of one-dimensionally H-bonded chains flocked together.[216] By contrast, we did not observe any supramolecular TPA structure on I–Au(111). Accordingly, strong intermolecular interactions appear mandatory for the thermodynamic stability of supramolecular monolayers at the interface between solution and particularly weakly interacting supports as I–Au(111). On the other hand, SA self-assembled into stable monolayers also on I–Au(111), although SA molecules only form H-bonded dimers but no networks. This indicates a stabilizing influence of extended alkane tails also on I–Au(111) that should be further explored. We thus envisage I–Au(111) to complement the portfolio of suitable substrates at solid–liquid interfaces for further fundamental studies on the thermodynamics and kinetics of supramolecular self-assembly, polymorph selection, and stimuli responsive monolayers. Lastly, I–Au(111) can readily be exploited for crystal engineering in two dimensions.

Chapter 8

Conclusion and Outlook

Surface-supported nanostructures are typically classified into two main categories of supramolecular self-assembly and on-surface synthesis. Considering potential applications and remarkable mechanical, thermal, and chemical stability, on-surface synthesis of organometallic and covalently bonded networks offers significant advantages over self-assembled structures. Therefore, this study primarily focuses on exploring the on-surface synthesis of debromination on iodine-passivated Au(111) (I-Au(111)) to determine whether this surface type maintains reactivity and potentially provides advantages compared to using bare metals.

As STM measurements were a fundamental technique for this study, an approach was undertaken to enhance an existing UHV low-temperature Scanning Tunneling Microscope (STM) for conducting Scanning Tunneling Spectroscopy (STS) measurement. This enhancement aimed to investigate the electronic properties of 2D networks.

Accordingly, chapter 4 focuses on enhancing the temperature and drift stability of an existing STM. Therefore, this chapter delved into the temperature stability across the STM, which eventually allowed the stabilizing of the tunneling gap without feedback control. As a result, the instrument became sufficiently stable for STS experiments at liquid nitrogen temperatures using a flow cryostat. In the first stage, comprehensive strategies have been employed to minimize temperature gradients across the microscope. These strategies included material substitutions, mechanical modifications, and thermal anchoring of signal and control wires. Material substitutions involve replacing components with low thermal conductivity materials with alternatives such as Shapal or Sapphire, known for their superior thermal properties. Ceramic pillars were also replaced by molybdenum as a sample mounting stage. Besides, connectors made from materials with higher thermal conductivity, such as Shapal, were employed to improve heat dissipation.

Additional modifications focused on redesigning special parts for thermal anchoring wires. Copper heat bridges were added to the STM core to enhance thermal equilibration and maintain uniform temperature. A copper screw with an enlarged head was designed and fastened to the cryostat cold tip. This screw, which holds the STM inner housing, provided connection points for additional cooling wires. These cooling wires were placed on the STM body to optimize thermal equilibrium

and reduce temperature drift by providing adequate cooling power to sustain the STM at a consistently low temperature, even when unclamped for measurements. Moreover, mechanical shutters and optical windows were installed to minimize the influence of infrared (IR) radiation from the surroundings.

In addition to enhancing thermal equilibration through the STM, the focus remained on enabling the system to image with low pA tunneling currents. Therefore, to achieve this objective, a stage has been specifically designed for thermally anchoring uninterrupted co-axial signal wires from OFHC copper to preserve signal integrity. This design aimed to prevent additional noise generated by the thermovoltage effect. These modifications led to a significant improvement in the STM's temperature stability, achieving high stability after 10 hours of equilibration time, with temperature variations of less than 10 mK per hour, resulting in reduced vertical drift. Consequently, the system operated in both STM and STS modes, maintaining tunneling gap stability after feedback deactivation for at least 5 minutes, with current changes remaining below 5%.

The enhanced STM provided an opportunity to explore dehalogenative couplings as employed for the on-surface synthesis of organometallic and covalent nanostructures. These reactions are typically performed on bare coinage metal surfaces, which chemical activity lowers the activation temperature, so that the dehalogenation reaction occurs before the reactants thermally desorb. In Chapter 5, the dehalogenative coupling of a tetra-bromine-substituted thiophene-rich monomer on the bare and iodine-passivated Au(111) substrate has been studied. However, metal surfaces can be detrimental to subsequent coupling because the strong interactions hinder monomer mobility and can also lead to unwanted side reactions. Therefore, the conceptual idea was to tune the reactivity of metal surfaces so that they were still sufficiently reactive to promote dehalogenation but passivated enough to mitigate the detrimental side effects imposed by the strong interactions. This was achieved by the chemisorption of an iodine monolayer from the vapor phase. The study indicated that (1) iodine-passivated Au(111) could still be reactive for debromination; (2) the reactivity could be tuned by varying the iodine exposure used for passivation; (3) the two-dimensional organogold networks synthesized on iodine-passivated Au(111), exhibited a higher regularity, with 76% rhombic pores compared to those synthesized directly on bare Au(111) which had a proportion of 28% rhombic pores. The thermal stability of the 2D organogold networks has also been examined through annealing at progressively higher temperatures at 320°C and above. Despite some organometallic C-Au-C bonds were converted into covalent carbon-carbon bonds, the networks exhibited remarkable thermal stability. The thermal stability attributed to strong organogold bonds facilitated by high

electronic π-conjugation in the thiophene-containing scaffold, as shown by DFT calculations and confirmed by STS. It is also unambiguously demonstrated that the presence of iodine, induced reversibility of the exceptionally strong organogold bonds and facilitated dynamic error correction, leading to higher structure quality.

Self-assembly of supramolecular monolayers at liquid-solid interfaces is also a vibrant field of basic research with application prospects in surface functionalization and nano-patterning. The vast majority of studies use graphite as an inert, easily prepared, and weakly interacting surface. In fact, the significant emphasis on graphite overlooks the critical influence of the substrate underneath. Chapter 6 indicated the course of variable-temperature experimental studies on graphite. In the course of this study, it has been noticed that after heating to temperatures where the supramolecular monolayers were desorbed and cooling back to room temperature, the monolayers were not restored as expected from a thermodynamic point of view. After ruling out irreversible chemical changes in either the solute or the solvent, the graphite substrate was further examined, but any obvious changes using STM and AFM imaging or confocal Raman spectroscopy could not be found. However, the effect could be reversed by vacuum annealing the graphite substrate at relatively high temperatures of 900 °C, after which the graphite substrate was again conducive to monolayer self-assembly. Finally, by using electron reflectivity as an utmost surface-sensitive probe, changes in the graphite substrate were revealed after immersion in a hot solvent. Spatial resolution was attained by Low-Energy Electron Microscopy (LEEM), which also revealed dendritic patterns and their remarkable stability up to 800 °C. The applied multi-technique approach consistently pointed to solvent intercalation as the origin of the changes in graphite's ability to serve as a substrate for monolayer self-assembly. Interestingly, the graphite substrate retained its properties when protected with a strongly adsorbing hydrogen-bonded trimesic acid monolayer, suggesting that an adsorbed monolayer was able to inhibit solvent intercalation.

Variable temperature studies at liquid-solid interfaces are an important key to a fundamental understanding of kinetics and thermodynamics. In Chapter 7, a study of the supramolecular self-assembly at liquid-solid interfaces has been pursued, with a focus on understanding the influence of substrate on polymorphism and thermodynamic stability. Therefore, a novel approach has been introduced by passivating the Au(111) surface with a chemisorbed monolayer of iodine atoms. Since I-Au(111) remained stable even at elevated temperatures, the thermal stability of specific monolayers could be directly compared to that on a graphite substrate. The experimental setup involved using aromatic tricarboxylic acids as a model system and utilizing the Immersion Scanning Tunneling Microscope (I-STM), which allowed conducting experiments for extended periods of time without solvent evaporation, even at temperatures up to 100°C. The results

demonstrated that molecule-surface interactions can lead to substrate-induced polymorphism, affecting the supramolecular monolayer's thermodynamic stability and even resulting in the emergence of new polymorphs. The study revealed that different polymorphs emerge on two substrates, graphite and I-Au(111), with a common trend of lower molecular packing densities but stronger hydrogen bonding on I-Au(111). For both TMA and BTB, the chicken wire polymorphs that exclusively feature ideal cyclic H-bonds were found on I−Au(111). By contrast, on graphite, only two-thirds (TMA) or one-third (BTB) of the carboxylic acid groups expressed these ideal H-bonds. The alternatively formed 3-fold cyclic (TMA) or mixed catemeric H-bond and C−H···O bond motifs (BTB) were energetically inferior but facilitated higher surface packing densities. Therefore, substrate-induced polymorphism was attributed to weaker molecule-surface interactions on I−Au(111). Additionally, TPD experiments supported the hypothesis and confirmed the weaker adsorption of molecules on I−Au(111).

In this thesis, a novel approach for the synthesis of 2D nanostructures on iodine-passivated Au(111) has been discussed. Although the domains were still comparatively small, the order and number of repeat units were already sufficient for the anthra-tetrathiophene network to develop an electronic band structure. Therefore, these 2D conjugated networks are of interest for study using STS due to their electronic properties. The reduced adsorption strength of nanostructures on iodine-passivated metal surfaces facilitates their transfer to other technologically relevant surfaces using techniques such as stamping. Additionally, further experiments indicate the potential for enhancing the domain size of 2D networks, possibly through network synthesis under a specific pressure range. Consequently, this opens up opportunities for technological application by enabling their separation from the metal surfaces essential for their synthesis.

Moreover, studying molecular self-assembly is important for the further advancement of nanoscience. I−Au(111) is a suitable substrate at solid−liquid interfaces for further fundamental studies on the thermodynamics and kinetics of supramolecular self-assembly and polymorph selection. I-Au(111) serves as a viable alternative substrate for variable temperature studies due to its stability in intercalation. On the other hand, solvent-intercalated graphite presents another potential substrate option. Additional investigations revealed that TMA molecules form monolayers, whereas TPA does not. This observation suggested weaker molecule-surface interactions. Consequently, this substrate may emerge as a new platform for monolayer self-assembly at liquid-solid interfaces.

Appendix A

Iodine Passivation Facilitates On-Surface Synthesis of Robust Regular Conjugated Two-Dimensional Organogold Networks on Au (111)

A.1 Materials and Methods

A.1.1 Sample preparation

Au(111) single crystal substrates were prepared by the usual cycles of Ar^+-ion-sputtering (850 eV, 1×10^{-5} mbar, 10 min) and annealing (490 °C, 15 min), and their cleanliness was verified by STM imaging.

Iodine passivation was achieved by exposing freshly prepared Au(111) to I_2 vapor in a separate preparation chamber to avoid contamination of the main chamber. The reactive I-Au(111) surfaces (Chapter 5, Figure 5.2 and Figure 5.3) were prepared by exposing the sample to 5×10^{-7} mbar of I_2 for 10 min. To desorb excess iodine and for equilibration, the samples were then annealed in UHV in the main chamber with a 20-minute temperature ramp to 180 °C and a 15-minute hold time. This procedure results in a surface where the iodine layer still has areas that are not densely packed (see Chapter 5, Figure 5.3 and Figure 5.5). In contrast, fully closed, densely packed iodine monolayers were obtained by a 20-fold increased iodine exposure, i.e. 5×10^{-6} mbar I_2 for 20 min followed by annealing at 190 °C for 15 min. These samples were found to be unreactive for debromination (see Chapter 5, Figure 5.4).

The 2,5,9,12-tetrabromoanthra[1,2-b:4,3-b':5,6-b":8,7-b"']tetrathiophene (TBATT) precursor molecules were synthesized according to a procedure reported by Perepichka et al.[243] Before deposition from a home-built Knudsen cell,[244] TBATT was thoroughly outgassed at 300 °C for an extended period of time. Deposition was performed with a crucible temperature of 290 °C. To account for the different sticking coefficients of pristine and iodine-passivated Au(111), different

deposition times were used, that is 3-4 min for pristine Au(111) and 10 min for I-Au(111).

A.2 STM and STS experiments

A home-built low-temperature STM controlled by a Nanonis BP 4 electronics was used, operating in Ultra-High Vacuum (UHV) at a base pressure of 1×10^{-10} mbar. Unless otherwise noted, the STM experiments were performed at low temperatures. The instrument is cooled by a flow cryostat with liquid nitrogen, resulting in sample temperatures of ~80 K (cf. chapter 4 for a detailed description of the instrument and how it was optimized) Electrochemically etched tungsten tips were used and in-situ conditioned by Ar^+-ion sputtering with an applied counter voltage.[245] The bias voltage was applied to the STM tip, but stated bias polarities refer to the sample. The WSxM software was used for image processing comprised of plane correction and line-by-line levelling.[246]

STS experiments were also performed at low temperature after an extended stabilization period of typically >24 h. The dI/dV spectra were acquired with the Lock-In technique using a modulation frequency of 329 Hz and a modulation amplitude of 30 mV with a voltage slew rate of 100 V s^{-1}, a setting time of 300 ms and an integration time of 300 ms for each data point.

A.3 DFT calculations

Orca 4.2.0[247] was used for DFT calculations of organogold aggregates (cf. Figure A.6) with the B3LYP functional[248] and the def2-SVP basis set.[249]

The Quantum Espresso 6.5[250] code was used for band structure calculations of the periodic organogold networks, employing a plane-wave basis set, the Perdew-Burke-Ernzerhof (PBE) functional,[251] and norm-conserving Martins-Troullier pseudopotentials.[252] A kinetic energy cutoff of 60 Ry and a charge density cutoff of 240 Ry were used. An additional SCF step was performed on the optimized structure with a finer k-point mesh of 8×8×1 points prior to the band structure calculation. The vacuum along the z-direction perpendicular to the structure was >10 Å in order to suppress interaction between layers.

A.4 Additional DFT results

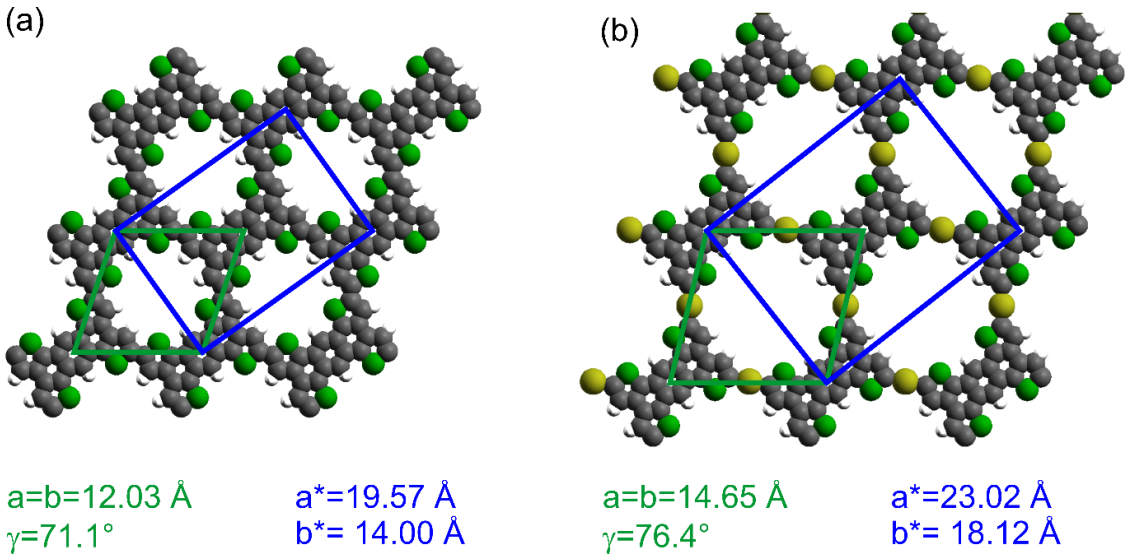

Figure A. 1 Structures and lattice parameters of DFT-calculated free-standing periodic monolayers (C: grey; H: white; S: green; Au: yellow). (a) covalent and (b) organogold networks, in which the anthra-tetrathiophene repeat units are linked by either (a) direct carbon-carbon or (b) organometallic carbon-Au-carbon bonds, respectively. Calculations were performed for the primitive unit cell (green rhombus) with optimized parameters indicated on the lower left (also in green). In this case, the lattice parameter directly represents the center-to-center distance between bonded monomers, which is 2.6 Å shorter in the covalent network. This difference can be unambiguously measured within the experimental error of the STM experiment (0.05 nm - 0.10 nm). Thereby the intermolecular carbon-carbon bond measures 1.44 Å, while the bond length of the carbon-Au-carbon bond is 4.03 Å. Crystallographically, the structures are described by a centered rectangular unit cell (blue rectangle) with the lattice parameters (also in blue, marked with asterisks) shown on the lower right.

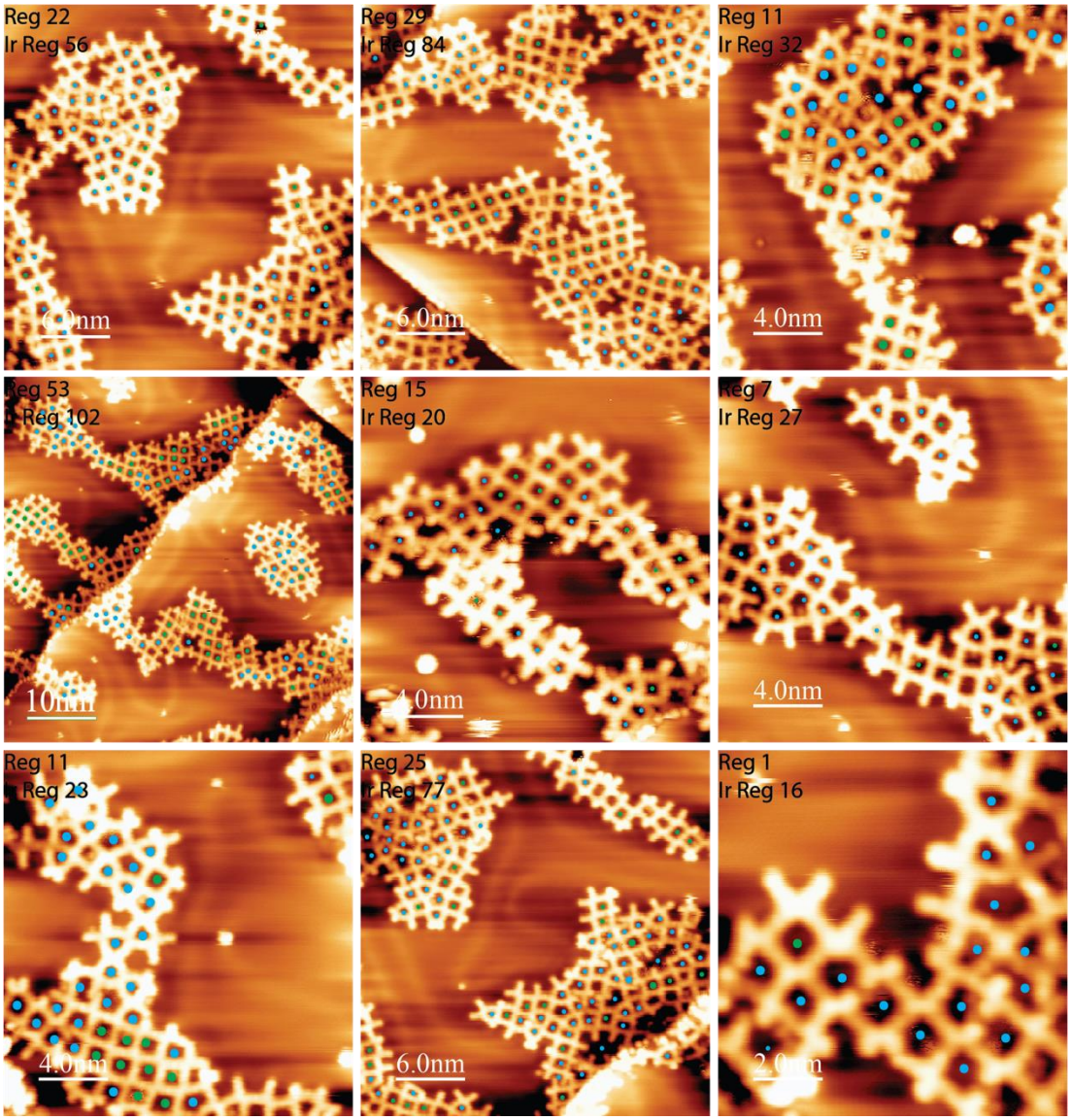

Figure A.2 Statistical analysis of the pore shapes of organogold networks synthesized on bare Au(111) surface, resulting in a proportion of 28% rhombic pores (624 closed pores were counted in total)

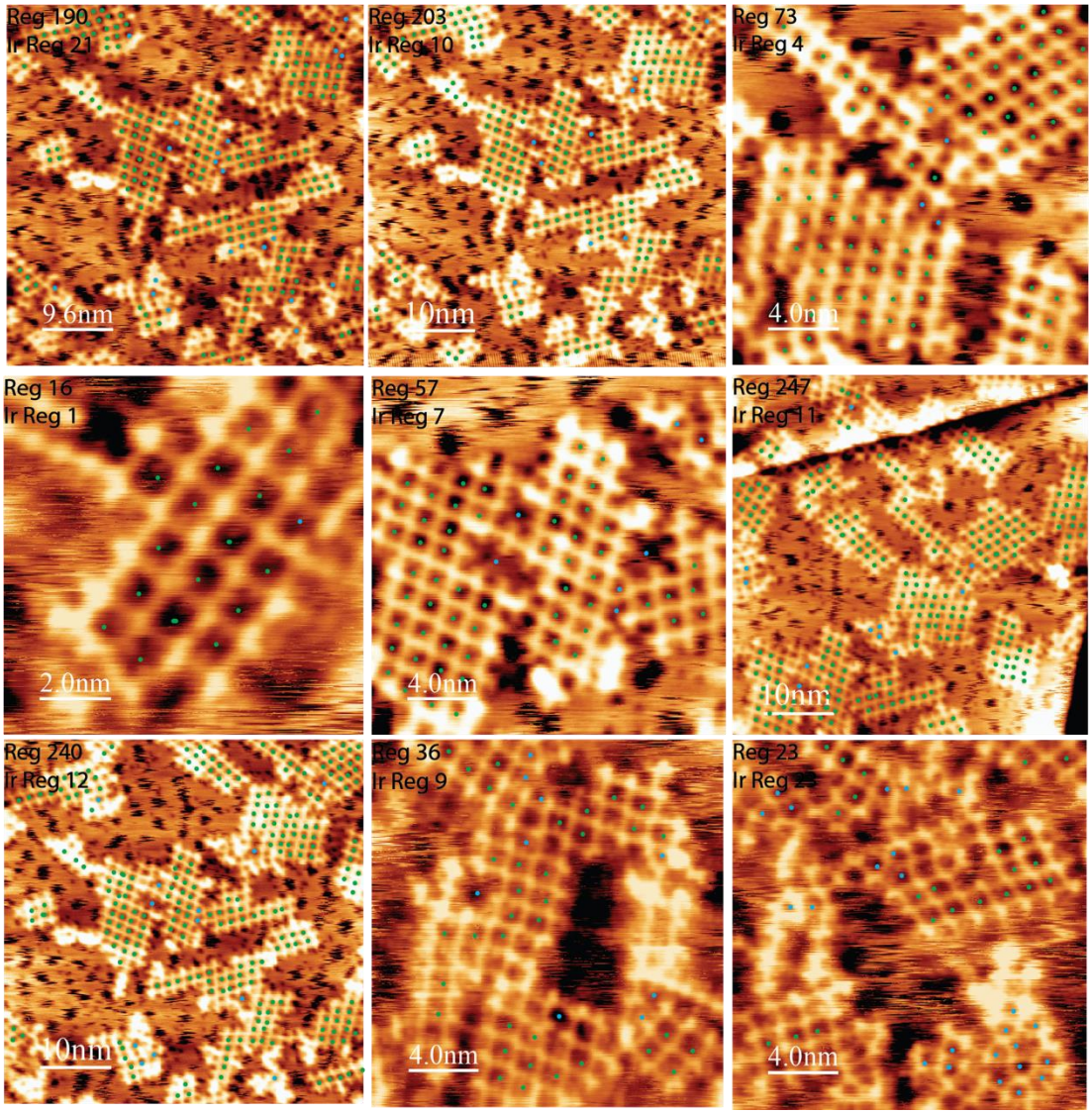

Figure A.3 Statistical analysis of the pore shapes of organogold networks synthesized on iodine-passivated Au(111) surface. The networks are highly regular, resulting in a proportion of 92% of the ideal rhombic pores (1174 closed pores were counted in total).

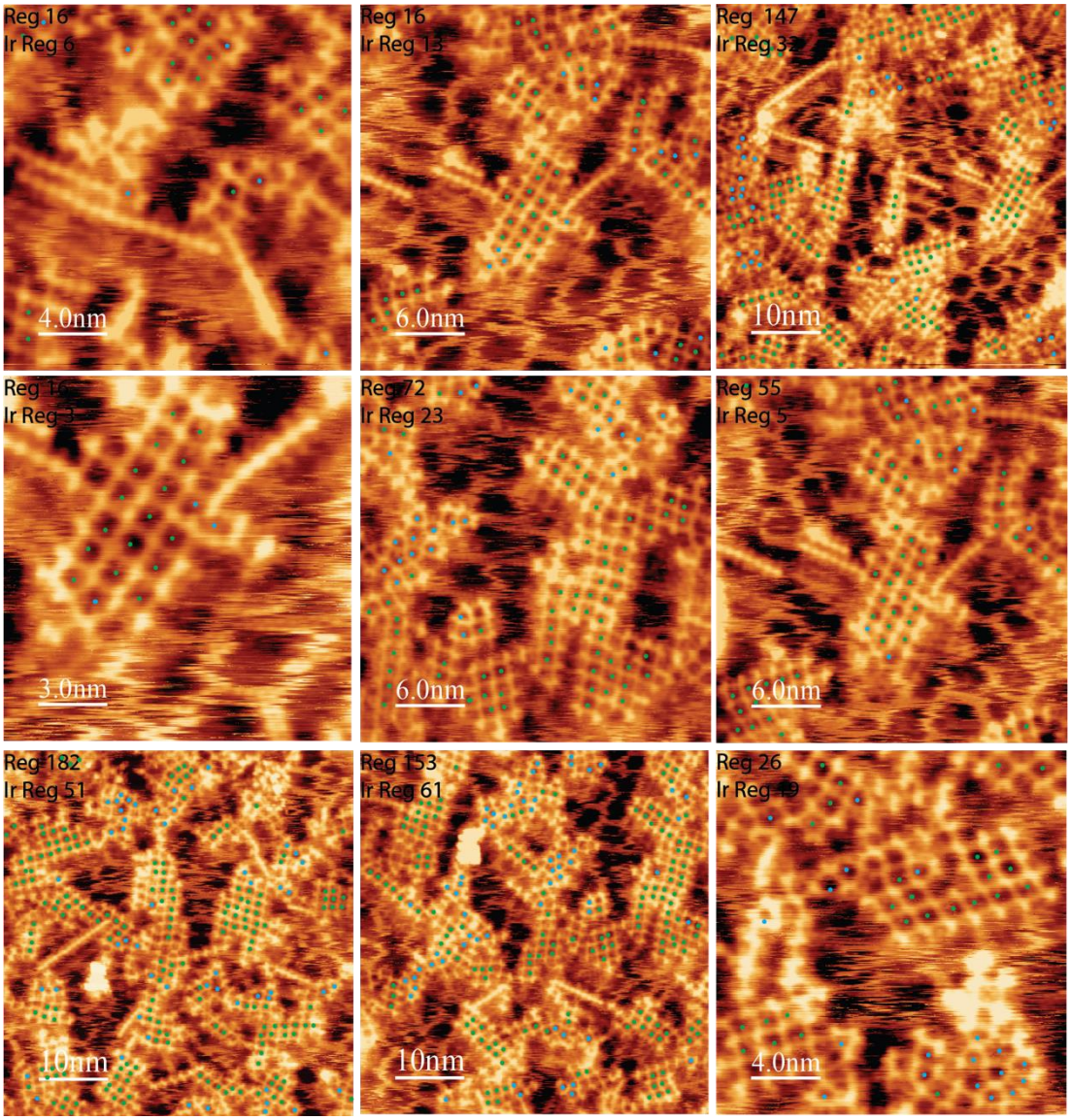

Figure A.4 Statistical analysis of the pore shapes of organogold networks synthesized on bare Au(111) surface with small amounts of co-deposited iodine. The network quality is intermediate as judged by the proportion of 76% rhombic pores. (896 closed pores were counted in total)

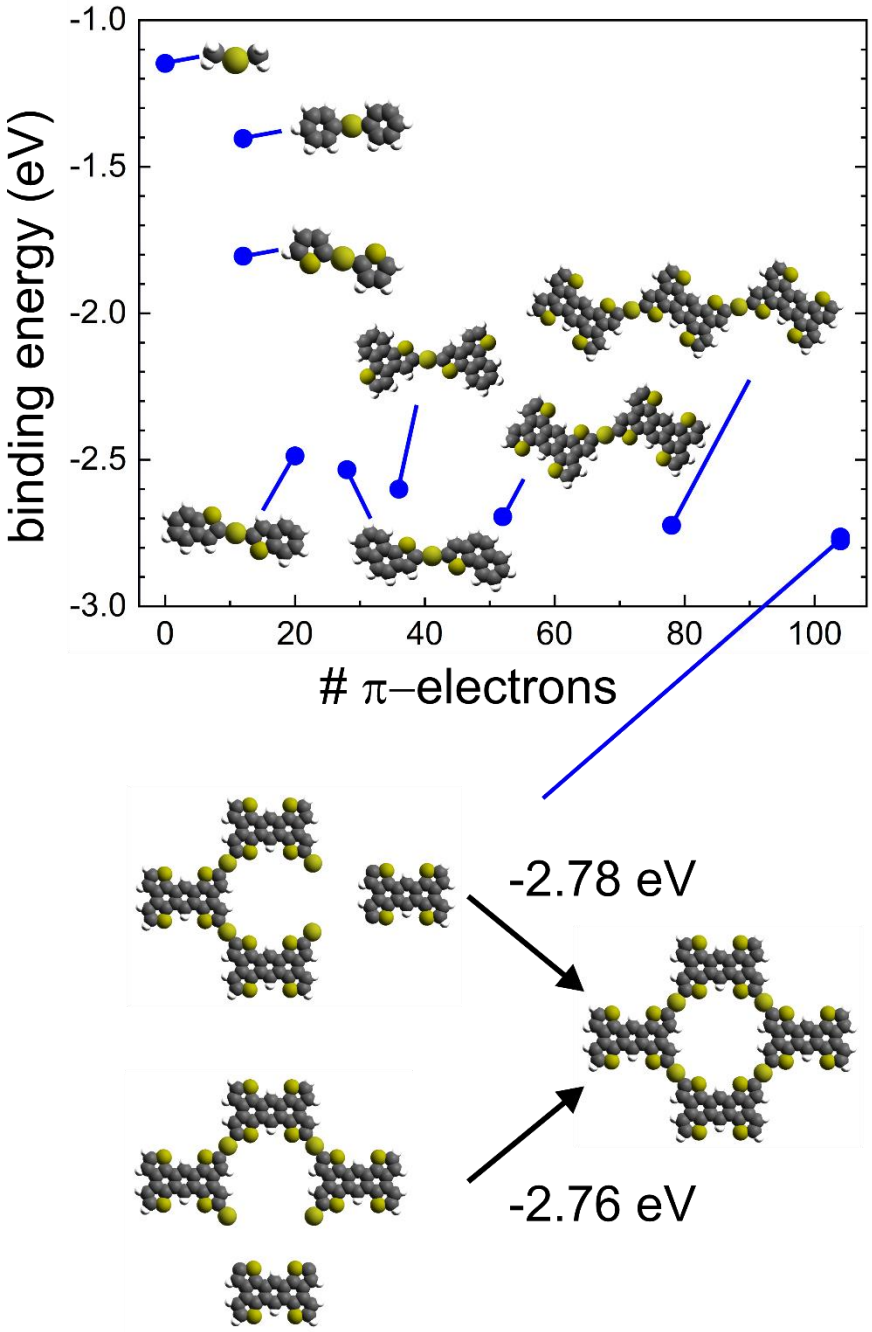

Figure A.5 DFT calculations of the binding energies (BE) of carbon-Au-carbon bonds as a function of the size of the organogold aggregates, here represented by the number of π electrons. The corresponding bonded structures are shown for all data points, and the BE values given refer to the formation of a single covalent bond between an organometallic Au-atom and a carbon-centered radical: R-C-Au + •C-R → R-C-Au-C-R. While the BE of the smallest calculated aggregate (methyl-Au-methyl) is only -1.15 eV, it increases sharply with increasing size of the aromatic system and plateaus at -2.69 eV for 52 π electrons, corresponding to the organogold anthra-tetrathiophene dimer. In the largest calculated aggregate, the 2×2 anthra-tetrathiophene tetramer, the BE increases moderately to -2.76 eV / -2.78 eV. For the 2×2 tetramer, there are two non-equivalent binding pathways, as shown below, that, however, result in nearly similar BE. Notably, although the thiophene-Au-thiophene and the phenyl-Au-phenyl dimers both have 12 π electrons, the thiophene has a significantly larger BE of -1.81 eV compared to -1.41 for the phenyl. This highlights the bond-strengthening influence of sulfur-containing heterocycles on organogold structures. In summary, the large BE for the aromatic thiophene-containing organogold aggregates reflects the experimentally found high thermal stability.

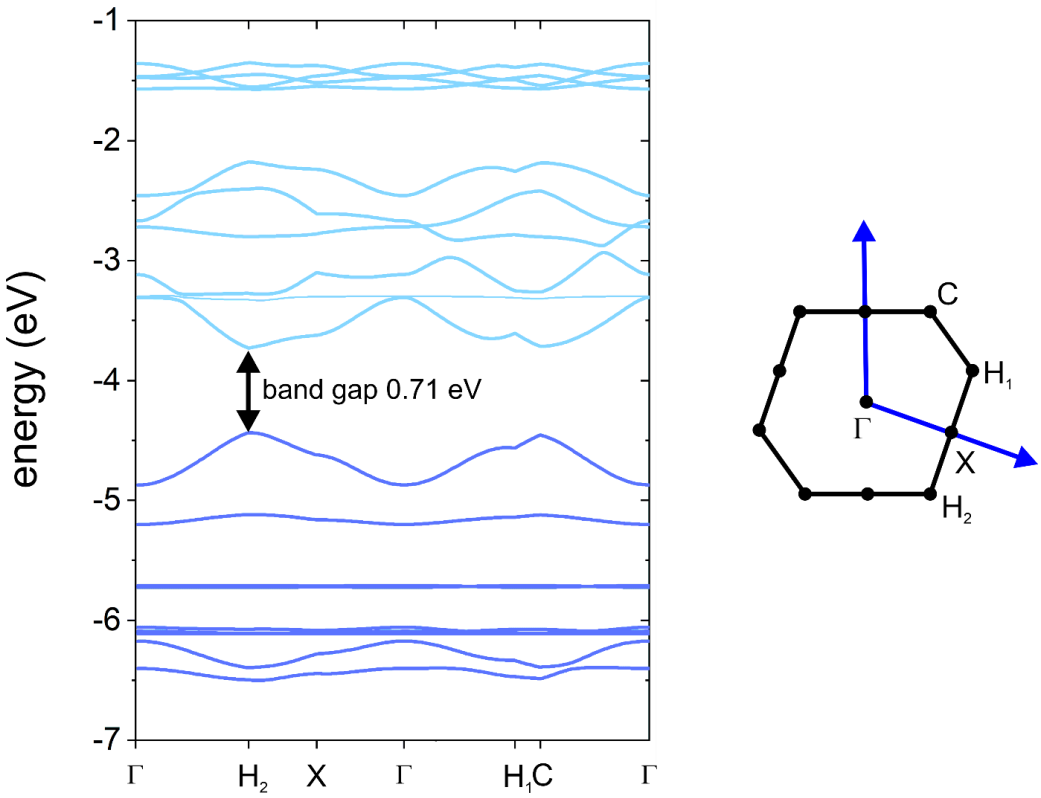

Figure A.6 DFT calculated electronic band structure of the organogold network shown for the primitive unit cell (see Figure A. 1b). The corresponding first Brillouin zone is shown on the right hand side. The calculated electronic band gap as indicated amounts to 0.71 eV. The obvious dispersion of the bands indicates π-electron conjugation through the carbon-Au-carbon linkages as also indicated by the spatial distribution of frontier molecular orbitals (cf. Figure A.7).

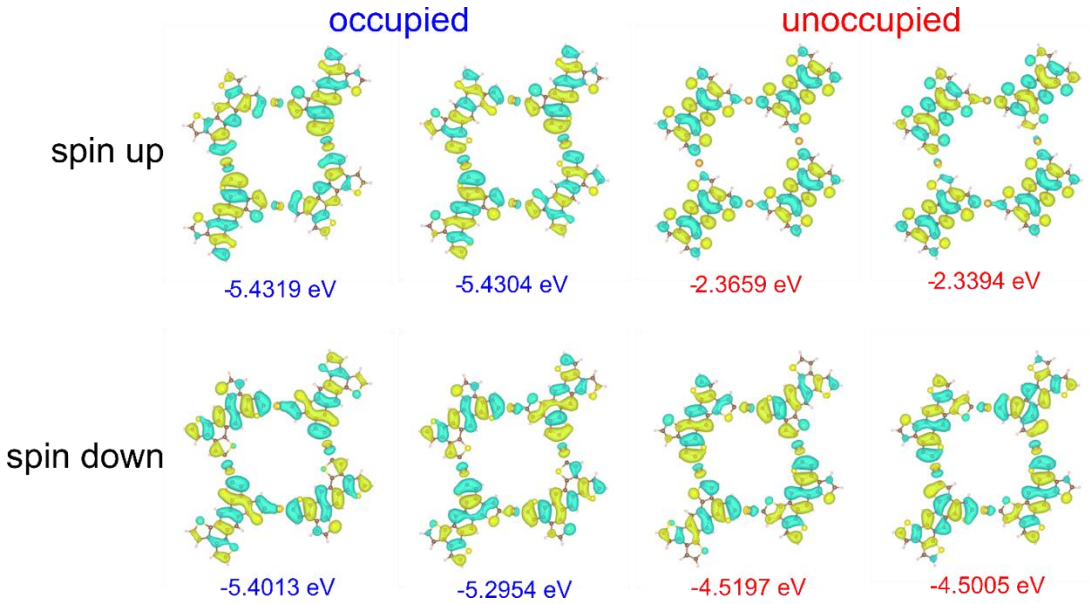

Figure A.7 DFT-calculated spatial distribution of the frontier molecular orbitals of the 2×2 organogold tetramer (structure shown in the background). Orbitals for spin up (down) are depicted in the upper (lower) row. The two columns on the left (right) depict occupied (unoccupied) molecular orbitals. Respective energies are indicated below in blue (red) for the occupied (unoccupied) molecular orbitals. These orbitals indicate conjugation through the carbon-Au-carbon bonds.

Appendix B

Reversible Intercalation of Organic Solvents in Graphite and its Hindrance by a Strongly Adsorbing Supramolecular Monolayer

B.1 Materials and Methods

B.1.1 Sample preparation

Highly Oriented Pyrolytic Graphite (HOPG) samples grade ZYB from Optigraph GmbH (Berlin, Germany) and Advanced Ceramics Inc. (Cleveland, OH, USA) were used for all experiments and comparative measurements were conducted with samples from the same batch. For the *ex-situ* heating experiments the HOPG samples were first cleaved with adhesive tape. Then they were placed into an inert 100 mL Duran lab flask filled with ~20 mL of pure solvent or saturated solution (without sediment), respectively, with the freshly cleaved side facing up. The closed flask was heated at the respective temperature for the indicated duration in a standard temperature-controlled lab oven. For the *ex-situ* heating experiments (Chapter 6, Figure 6.4, Figure 6.5 and Figure 6.6) the samples were removed after the specified duration for STM characterization at room temperature and then put back into the lab flask to continue the heating.

B.2 Characterization

B2.2 Scanning Tunneling Microscopy (STM)

For room temperature ambient STM experiments either a PicoLE (Keysight) STM system or a home-built instrument operated with an SPM 100 controller from RHK were used. Mechanically cut tips from a Pt/Ir wire were used as probes. Images were acquired in the constant-current mode at the liquid-solid interface with the STM tips immersed in the supernatant liquid film. Imaging parameters are indicated in the figure captions.

Variable-temperature *in-situ* heating experiments were carried out with a dedicated home-built instrument that is described in detail elsewhere.[17] Here, the entire STM is immersed in a hermetically sealed, temperature-controlled container, allowing STM imaging at temperatures up to 100 °C for extended periods of time without solvent evaporation.

B2.3 Atomic Force Microscopy (AFM)

AFM experiments were performed on a Multimode 8 (Bruker) with a Nanoscope V controller in tapping mode in air in ambient conditions. Olympus AC160TS probes (26 N/m) were used with a 300 kHz resonance frequency. All AFM image processing was performed using the software Gwyddion.[253] Median of differences and polynomial methods were applied for image levelling.

B2.4 Raman Spectroscopy

Raman spectra were collected with a confocal Raman microscope (Monovista CRS+, S&I GmbH) using a 632.8 nm He-Ne laser directed on the surface through an objective (OLYMPUS, BX43 100x, N.A. 0.7) with an optical density at the sample surface of about 590 kW/cm^2. The Raman scattered light was collected using the same objective and guided to a Raman spectrograph (S&I GmbH) equipped with a cooled-charge coupled device (CCD) camera operated at -100 °C (Andor Technology, DU920P-BX2DD). Raman spectra were taken in at least 25 different positions on the sample. All measurements were carried out under ambient conditions at room temperature. The acquisition time for all spectra was 6 s.

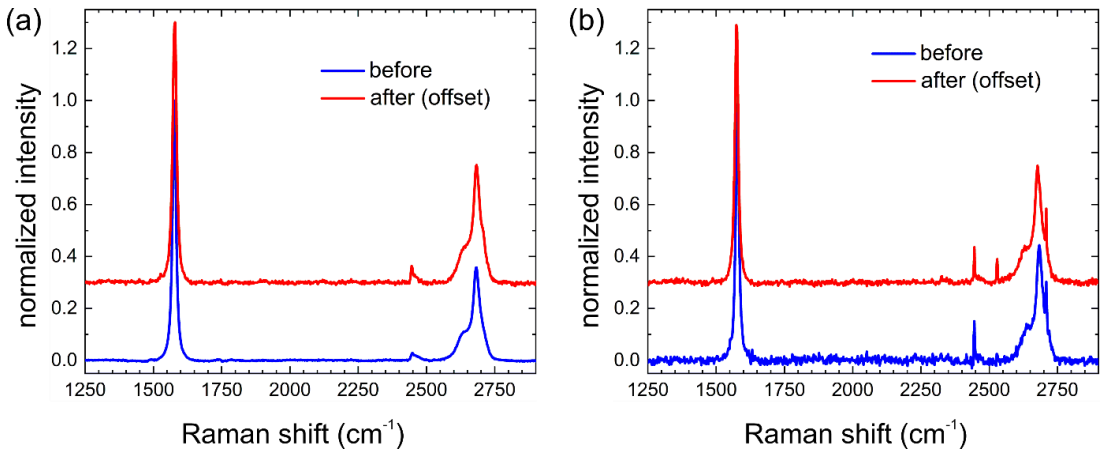

Figure B.1 Comparative confocal Raman spectroscopy on freshly cleaved and solvent-exposed graphite. Samples were exposed to (a) pure 1-PO solvent at 70 °C for 7 days and (b) pure 7A solvent at 50 °C for 10 days. Raman spectra were recorded before the graphite samples were immersed (blue curves) and after the samples were removed and rinsed with ethanol (red curves, offset for clarity). Note that without rinsing, different spectral features were observed that could be attributed to residual solvent. The Raman spectra before and after prolonged immersion in hot solvent are essentially similar. Our interpretation is that the changes induced by solvent intercalation are localized to a few upper graphite layers and that confocal Raman is not surface sensitive enough to detect them due to a large background from the bulk.

B2.5 Low-Energy Electron Microscopy (LEEM)

LEEM experiments were conducted using a Specs FE-LEEM P90 instrument, which maintained a base pressure of 2×10^{-10} mbar. Bright-field (BF) images and I(V) curves were measured by collecting electrons from the central (0,0) diffracted beam. For acquisition of the I(V) curves, a series of BF images were measured for kinetic energies ranging from 0 … 60 eV with increments of 1 eV. The I(V) curves were extracted by integrating the intensity of the respective area (marked by small circles in Chapter 6, Figure 6.10).

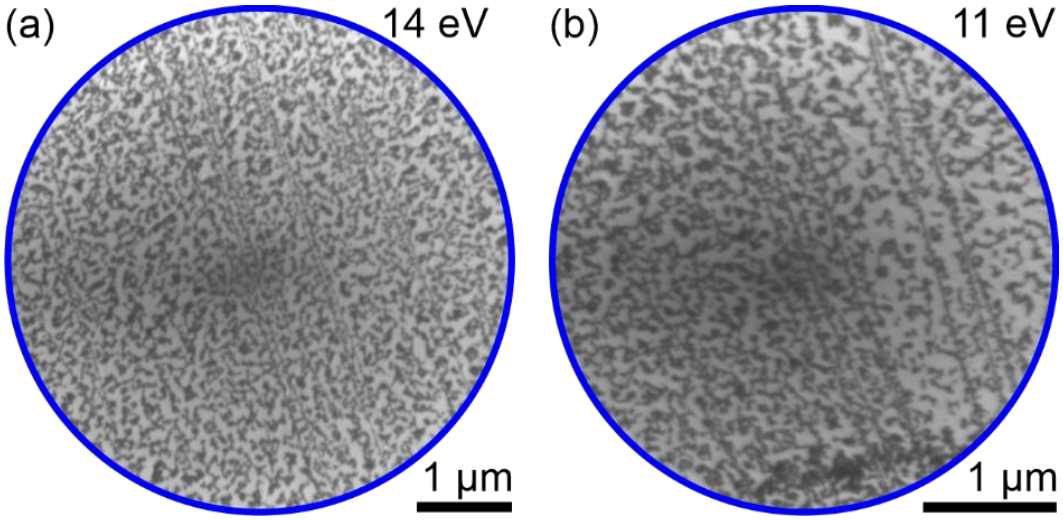

Figure B.2 Additional LEEM images of solvent-exposed samples. BF images acquired at (a) 14 eV and (b) 11 eV of a graphite sample that was immersed in 60 °C hot pure 7A solvent for 3 days. To remove solvent residues, the sample was outgassed in UHV at a temperature of 100 °C for ~ 20 min. The dendritic pattern formed by the brighter and darker areas was observed only for solvent-exposed samples.

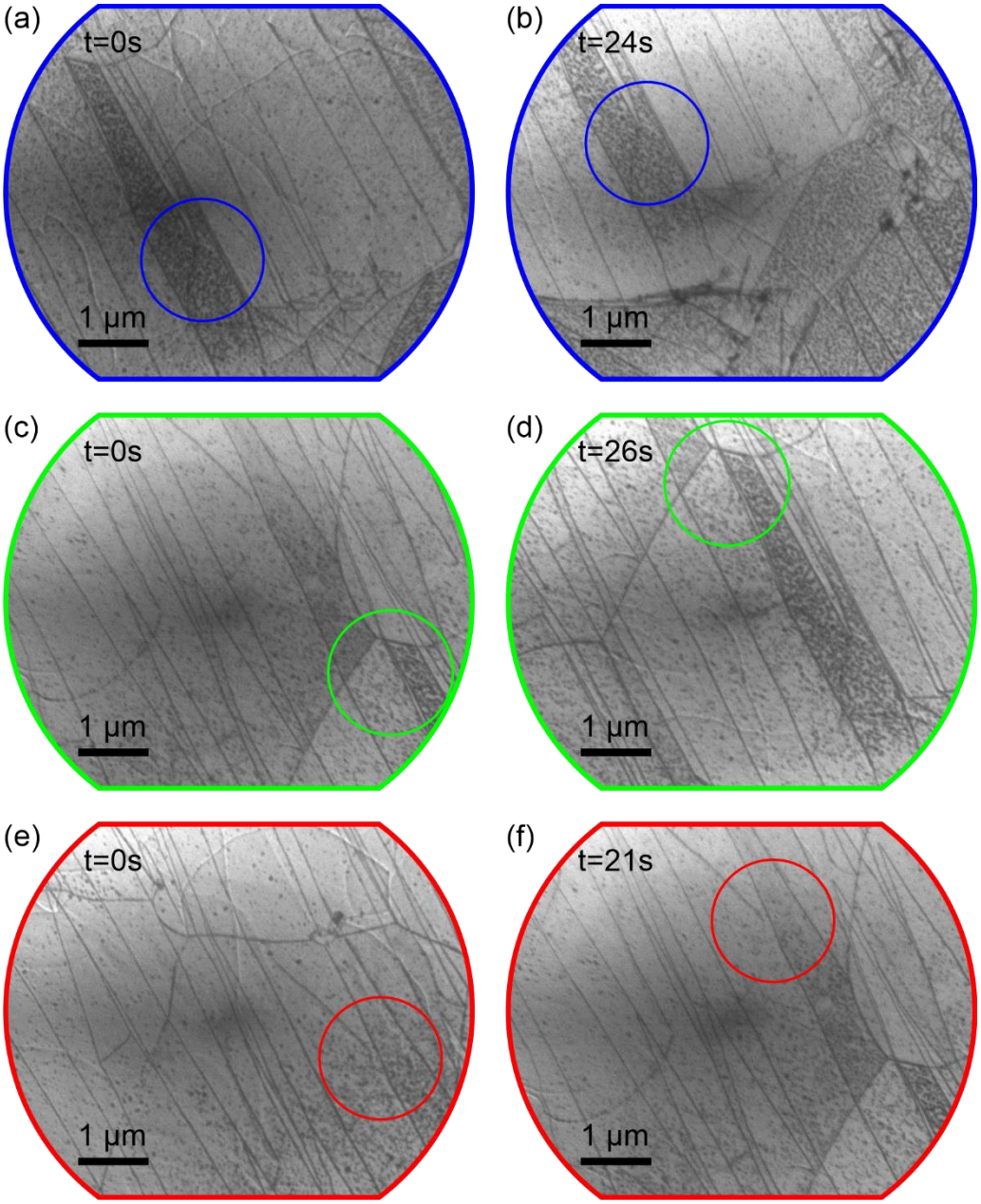

Figure B.3 High-Temperature LEEM study of solvent-exposed samples. BF images were acquired of graphite samples that were immersed in 60 °C hot 7A for 3 days at a temperature of 800 °C with an electron energy of 50 eV. Thermal drift is substantial at this temperature, but reasonably large overlapping areas can still be identified in BF image pairs with a time lapse on the order of 20 s. (a) / (b) and (c) / (d) and (e) / (f) show pairs of BF images where similar areas are marked with circles and the respective time differences are indicated in the upper left corner. At 800 °C, the solvent-exposed graphite samples still show the patterns of darker and brighter areas, indicating that solvent molecules remain mostly intercalated. For BF image pairs (a) / (b) and (c) / (d) the patterns largely persist, whereas for BF image pair (e) / (f) the extent of the darker areas is reduced, indicating the onset of deintercalation

Appendix C

Versatile Role of Molecule–Surface Interactions for Monolayer Self-Assembly at Liquid-Solid Interfaces

C.1 Materials and Methods

Sample Preparation. TMA (98%), stearic acid (99%), heptanoic acid (97%), nonanoic acid (99%), phenyl octane (98%), and potassium iodide (99%) were purchased from Sigma-Aldrich and used as received (purities stated in parentheses). BTB and TCBPB were synthesized according to previously described procedures.[200,206] Highly oriented pyrolytic graphite (HOPG) samples (grade ZYB, Optigraph GmbH) were prepared in the usual way by cleaving with adhesive tape prior to experiments. For the TPD studies, the preparation of HOPG samples included an additional annealing step in ultrahigh-vacuum (UHV) conditions. I−Au(111) samples were prepared from well-oriented Au(111) films on mica (Georg-Albert- PVD) under ambient conditions in a two-staged protocol. First, Au(111) was cleaned by flame annealing using a butane torch. (cf. Chapter 7, Figure 7.2) Then, the samples were directly immersed in 8 mmol/L aqueous potassium iodide (KI) solutions prepared with ultrapure medical-grade water for 30 s. Afterward, the samples were placed on a tissue for drying. Alternatively, we have prepared I−Au(111) samples in UHV as described for the TPD experiments, i.e., by cleaning Au(111) through cycles of sputtering and annealing followed by in situ exposure to $\sim 10^{-6}$ mbar I_2 vapor. However, we did not find any differences to wet-chemically prepared I−Au(111) samples with regard to our self-assembly studies.

C.2 Experimental Details TPD

All Temperature Programmed Desorption (TPD) experiments (cf. Chapter 7, Figure 7.7) were performed in a home built UHV chamber at a base pressure below 2×10^{-10} mbar. HOPG samples were ex-situ cleaved and cleaned in-situ by annealing to 800-900 K for 30 min. I-Au(111) samples were prepared by sputtering a Au(111) single crystal with Ne^+ ions (1×10^{-5} mbar, 0.8 kV) at room temperature for 10 minutes, followed by annealing to 730 K for 15 minutes (heating rate: 2 K s^{-1}; cooling rate: −1 K s^{-1}). The iodine monolayer was prepared by exposing the freshly cleaned Au(111) sample to 5×10^{-6} mbar I_2 for 15 min followed by annealing to 500 K for 15 min in UHV. Successful preparation of a well ordered densely packed iodine monolayer was confirmed by Low Energy Electron Diffraction (LEED) using a BDL800IR-LMX-ISH apparatus (OCI Vacuum Microengineering Inc.). Its purity was assessed by X-ray Photoelectron Spectroscopy (XPS) using a SPECS Phoibos 100 CCD hemispherical analyzer and a conventional dual-anode X-ray tube. Radiative heating was carried out with a tungsten filament in close proximity behind the samples. Temperatures were measured with a type K thermocouple directly attached to the samples. Linear temperature ramps were realized by a PID controller (HS 130, Schlichting Physikalische Instrumente). TMA was deposited from a home-built Knudsen cell with a quartz glass crucible held at a temperature of 160 °C. Deposition times for the different experimental runs are summarized in the Table C.1. Comparable deposition times for graphite and I-Au(111) resulted in similar coverages, indicating akin sticking coefficients for both surfaces. TPD spectra were acquired with a quadrupole mass spectrometer (QMS) enclosed within a copper cap. Samples were positioned within a millimeter from the cap aperture. For the desorption measurement, the inner surface of the liquid nitrogen cooled copper cap additionally pumped the enclosed volume via a freshly deposited titanium getter film and cryo trapping. Furthermore, the background pressure in the UHV system was minimized during the experiments by liquid nitrogen cooled freshly deposited titanium getter films. Additional details regarding the experimental setup can be found elsewhere.[254] The QMS signal at m/z = 210 amu/elementary charge was monitored, corresponding to the full mass of intact TMA.

Table C.1 Summary of deposition times (in min) for the variable heating rate TPD experiments with TMA on graphite and I-Au(111).

	$0.15\ \frac{K}{s}$	$0.50\ \frac{K}{s}$	$1.0\ \frac{K}{s}$	$2.0\ \frac{K}{s}$	$5.0\ \frac{K}{s}$
graphite	12	7	7	12	12
I-Au(111)	14	12	12	14	7

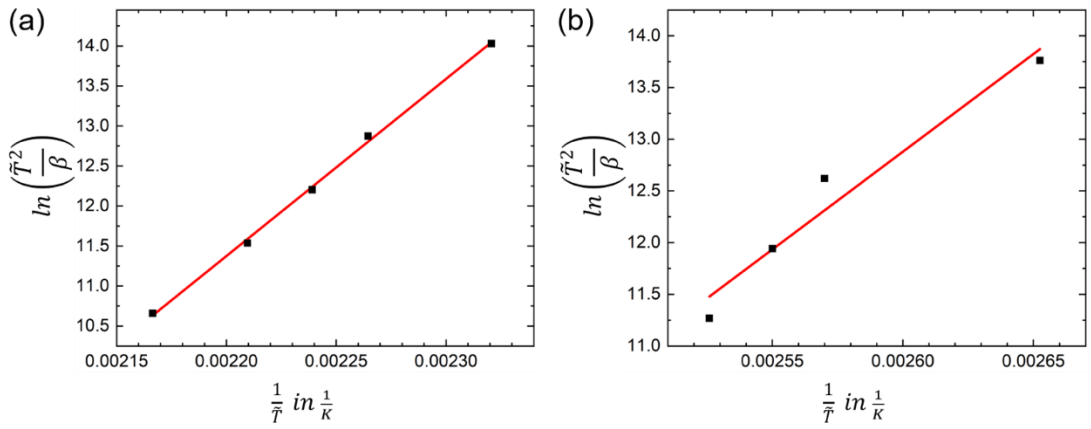

Figure C.1 Analysis of TPD data acquired for TMA. Plots of $ln\left(\frac{\tilde{T}^2}{\beta}\right)$ *intensity vs.* $\frac{1}{\tilde{T}}$ *for (a) graphite and (b) I-Au(111).* $\tilde{T}$ *corresponds to the temperature of the peak maximum observed for a heating rate* β*; the red lines are linear fits. Their slopes correspond to the desorption energy* E_{des} *under the assumption that the order of the desorption process is* $n = 1$ *and that both* E_{des} *and the pre-exponential factor of the rate constant are independent of molecular coverage. For graphite, this analysis yields a desorption energy of* $E_{des,graphite} = 183\ \frac{kJ}{mol}$*. This value is in excellent agreement with previous Density Functional Theory studies from our group, resulting in a calculated binding energy of* $180.3\ \frac{kJ}{mol}$ *for the TMA chickenwire polymorph on graphite*[224] *and with other reported theoretical estimates.*[255,256,257] *This agreement and the quality of the fit provide us with confidence that the underlying assumptions of this analysis are valid. For I-Au(111) the data point for* $\beta = 5\frac{K}{s}$ *has been omitted, because for this heating rate the second and first layer desorption peaks already overlapped (Figure 7.7). From the linear fit we obtain* $E_{des,I-Au(111)} = 157\frac{kJ}{mol}$*. As expected, the desorption energy on I-Au(111) is notably smaller as compared to graphite, however the quality of the linear fit is also inferior. This is likely related to a larger site variability of* E_{des} *on this more inhomogeneous surface.*

C.3 Scanning Tunnelling Microscopy (STM)

All STM experiments were performed using home-built instruments (cf. Chapter 7, Figure 7.8) and mechanically cut PtIr tips. For ambient STM experiments 5−10 µL of solution were applied to the surfaces, and images were acquired with the STM tip directly immersed in the liquid film. Variable-temperature STM experiments were carried out with the dedicated Immersion-STM.[17] In this setup, the entire microscope is placed in a hermetically sealed, heatable, and precisely temperature controlled container. The sample is fully immersed into a comparatively large volume (~10 mL) of solution. Thereby, solvent evaporation and associated concentration changes are virtually suppressed. This facilitates prolonged experiments at elevated temperatures and, hence, allows for long equilibration times. Accordingly, variable-temperature STM experiments in liquids with minimal drift become feasible up to temperatures of ~100 °C.

C.4 LEED and XPS of UHV prepared I-Au(111)

(a) (b)

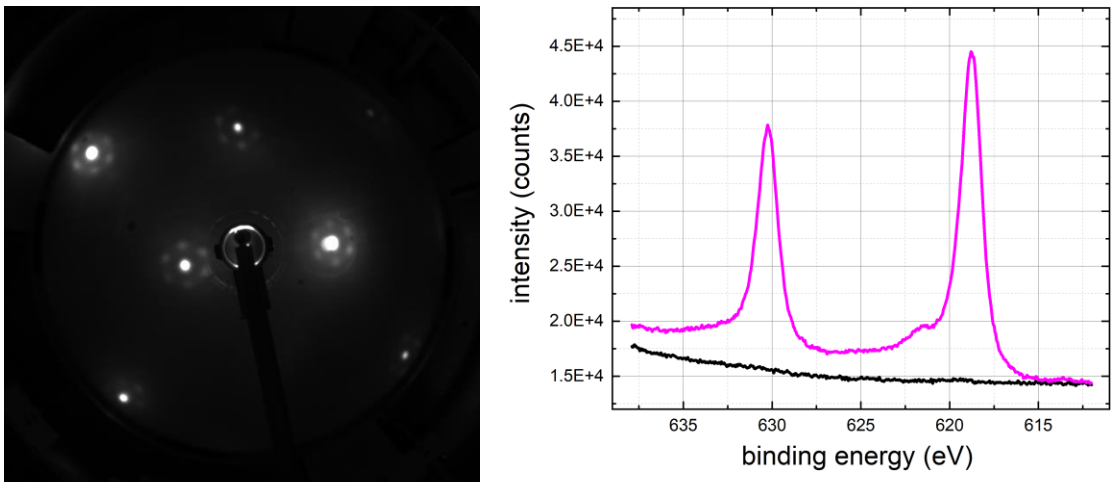

Figure C.2 Characterization of the I-Au(111) sample prepared in UHV for the TPD experiments. (a) LEED pattern acquired at a sample temperature of 90 K at an incidence angle of 7° of the electron beam with respect to the surface normal, using an electron energy of 30 eV. The LEED pattern indicates formation of a well ordered iodine superstructure. (b) XP spectrum of I 3d core levels (pink line), acquired with Mg K_α radiation and normal emission detection of photoelectrons. The high intensity and low full width at half maximum of the I 3d doublet confirms formation of a pure monolayer of chemisorbed iodine. The spectrum acquired of the clean Au(111) surface before iodine exposure (black line) indicates the absence of iodine contaminations.

References

[1] J. Sakamoto, J. van Heijst, O. Lukin, and A.D. Schlüter, Angew. Chem. Int. Ed., 2009, 48, 1030-1069.

[2] Nacci, C., Hecht, S., & Grill, L. (2016). The emergence of covalent on-surface polymerization. In On-Surface Synthesis: Proceedings of the International Workshop On-Surface Synthesis, École des Houches, Les Houches 25-30 May 2014 (pp. 1-21). Springer International Publishing.

[3] C. J. Chen, Introduction to Scanning Tunneling Microscopy (Oxford University Press, New York, 2008).

[4] Colson, J., Dichtel, W. Rationally synthesized two-dimensional polymers. *Nature Chem* 5, 453–465 (2013).

[5] Whitesides, G. M.; Mathias, J. P.; Seto, C. T. Molecular self-assembly and nanochemistry: a chemical strategy for the synthesis of nanostructures. Science 1991, 254, 13121319.

[6] Whitesides, G. M.; Grzybowski, B. Self-Assembly at All Scales. Science 2002, 295, 24182421.

[7] Mendes, A. C.; Baran, E. T.; Reis, R. L.; Azevedo, H. S. Self-assembly in nature: using the principles of nature to create complex nanobiomaterials. WIREs Nanomed. Nanobiotechnol. 2013, 5, 582612.

[8] Hemsley, A. R.; Collinson, M. E.; Kovach, W. L.; Vincent, B.; Williams, T. The role of self-assembly in biological systems: evidence from iridescent colloidal sporopollenin in Selaginella megaspore walls. Phil. Trans. R. Soc. Lond. B, Biol. Sci. 1994, 345, 163173

[9] Whitesides, G. M.; Kriebel, J. K.; Mayers, B. T. In Nanoscale Assembly: Chemical Techniques. Self-Assembly and Nanostructured Materials; Huck, W.T. S., Ed.; Springer US: Boston, MA, 2005; pp 217239.

[10] Thiruvengadathan, R.; Korampally, V.; Ghosh, A.; Chanda, N.; Gangopadhyay,K.; Gangopadhyay, S. Nanomaterial processing using self-assemblybottom-up chemical and biological approaches. Rep. Prog. Phys. 2013, 76, 066501.

[11] A. Gourdon. On-surface covalent coupling in ultrahigh vacuum. Angew. Chem. Int. Ed., 47:69506953, 2008

[12] M. Lackinger and W. M. Heckl. A STM perspective on covalent intermolecular coupling reactions on surfaces. J. Phys. D: Appl. Phys., 44:464011, 2011.

[13] R. Lindner and A. Kühnle. On-surface reactions. ChemPhysChem, 16(8):15821592, 2015.

[14] F. Klappenberger, Y. Q. Zhang, J. Björk, S. Klyatskaya, M. Ruben, and J. V. Barth. On-surface synthesis of carbon-based scaolds and nanomaterials using terminal alkynes. Acc. Chem. Res., 48:21402150, 2015.

[15] Baughman, R. H., Zakhidov, A. A., & De Heer, W. A. (2002). Carbon nanotubes--the route toward applications. science, 297(5582), 787-792.

[16] Grill, L., Dyer, M., Lafferentz, L., Persson, M., Peters, M. V., & Hecht, S. (2007). Nano-architectures by covalent assembly of molecular building blocks. *Nature nanotechnology*, 2(11), 687-691

[17] Ochs, O., Heckl, W. M., & Lackinger, M. (2018). Immersion-scanning-tunneling-microscope for long-term variable-temperature experiments at liquid-solid interfaces. *Review of Scientific Instruments*, *89*(5).

[18] Eigler, D. M., & Schweizer, E. K. (1990). Positioning single atoms with a scanning tunnelling microscope. Nature, 344(6266), 524-526.

[19] Binnig, G.; Rohrer, H. Scanning Tunneling Microscopy from Birth to Adolescence (Nobel Lecture). Angew. Chem. Int. Ed. Engl. 1986, 26, 606614.

[20] Binnig, G.; Rohrer, H.; Gerber, C.; Weibel, E. Surface Studies by Scanning Tunneling Microscopy. Phys. Rev. Lett. 1982, 49, 5761.

[21]]Binnig, G.; Rohrer, H. Scanning tunneling microscopy. Surface Science 1983, 126, 236244.

[22] M. Lackinger and W. M. Heckl. A STM perspective on covalent intermolecular coupling reactions on surfaces. J. Phys. D: Appl. Phys., 44:464011, 2011.

[23] L. Grill, M. Dyer, L. Laerentz, M. Persson, M. V. Peters, and S. Hecht. Nano-architectures by covalent assembly of molecular building blocks. Nat. Nanotechnol., 2:687691, 2007.

[24] J. V. Barth. Molecular architectonic on metal surfaces. Annu. Rev. Phys. Chem., 58:375407, 2007.

[25] Miranda, R.; García, N.; Baró, A. M.; García, R.; Peña, J. L.; Rohrer, H. Technological applications of scanning tunneling microscopy at atmospheric pressure. Appl. Phys. Lett. 1985, 47, 367369.

[26] Fritton, M.; Duncan, D. A.; Deimel, P. S.; Rastgoo-Lahrood, A.; Allegretti, F.; Barth, J. V.; Heckl, W. M.; Björk, J.; Lackinger, M. The Role of Kinetics versus Thermodynamics in Surface-Assisted Ullmann Coupling on Gold and Silver Surfaces. J. Am. Chem. Soc. 2019, 141, 48244832.

[27] McIntyre, B. J.; Salmeron, M. B.; Somorjai, G. A. A scanning tunneling microscope that operates at high pressures and high temperatures (430 K) and during catalytic reactions. Catal. Letters 1992, 14, 263269.

[28] Zhu, Z.; Tao, F. F.; Zheng, F.; Chang, R.; Li, Y.; Heinke, L.; Liu, Z.;Salmeron, M.; Somorjai, G. A. Formation of Nanometer-Sized Surface Platinum Oxide Clusters on a Stepped Pt(557) Single Crystal Surface Induced by Oxygen: A High-Pressure STM and Ambient-Pressure XPS Study. Nano Lett. 2012, 12, 14911497.

[29] De Feyter, S.; De Schryver, F. C. Self-Assembly at the Liquid/Solid Interface: STM Reveals. J. Phys. Chem. B 2005, 109, 42904302.

[30] Meyer, G. A simple low-temperature ultrahigh-vacuum scanning tunneling microscope capable of atomic manipulation. Rev. Sci. Instrum. 1996, 67, 2960 2965.

[31] Hoshino, T.; Kokubun, K.; Kumamoto, K.; Ishimaru, T.; Ohdomari, I. High-Temperature Scanning Tunneling Microscopy (STM) Observation of Metastable Structures on Quenched Si(111) Surfaces. Jpn. J. Appl. Phys. 1995, 34, 33463350.

[32] Blanco, J. M.; Flores, F.; Pérez, R., STM-theory: Image potential, chemistry and surface relaxation. Prog. Surf. Sci. 2006, 81 (10), 403-443.

[33] Gottlieb, A. D. & Wesoloski, L. Bardeen's tunnelling theory as applied to scanning tunnelling microscopy: a technical guide to the traditional interpretation. Nanotechnology 17, R57–R65 (2006).

[34] Scanning Probe Microscopy: Atomic Force Microscopy and Scanning Tunneling Microscopy Bert Voigtländer. *MRS Bulletin* 41, 165–166 (2016). https://doi.org/10.1557/mrs.2016.18

[35] J. Bardeen. Tunnelling from a many-particle point of view. Phys. Rev. Lett., 6:57_59, Jan 1961.

[36] Tersoff, J. & Hamann, D. R. Theory and application for the scanning tunneling microscope. Phys. Rev. Lett. 50, 1998–2001 (1983).

[37] Tersoff, J. & Hamann, D. R. Theory of the scanning tunneling microscope. Phys. Rev. B 31, 805–813 (1985).

[38] Pan, P., Yang, F., Wang, Z., Zhong, B., Sun, L., & Ru, C. (2016). A review of stick–slip nanopositioning actuators. *Nanopositioning Technologies: Fundamentals and Applications*, 1-32.

[39] Badami Behjat, A. (2019). *Ultra-high-resolution low-temperature magnetic force microscopy* [Thesis (M.S.) -- Graduate School of Natural and Applied Sciences. Physics.]. Middle East Technical University.

[40]. Chen, W., Yi, P., Wang, D., Huang, J., & Liu, J. (2015). On-surface synthesis of single-layered two-dimensional covalent organic frameworks via solid-vapor interface reactions. Scientific Reports, 5, 12310.

[41]. de Oteyza, D. G., et al. (2013). Direct imaging of covalent bond structure in single-molecule chemical reactions. Science, 340(6139), 1434-1437

[42] Sanz, S., et al. (2018). On-surface synthesis of bicomponent two-dimensional covalent organic structures: 1, 3, and 6. Journal of the American Chemical Society, 140(39), 12361-12366.

[43] Kory, M. J., et al. (2015). Covalent functionalization and passivation of exfoliated black phosphorus via aryl diazonium chemistry. Nature Chemistry, 7(11), 826-832.

[44] Yu, Y., Lin, J., Wang, Y., Zeng, Q. & Lei, S. Room temperature on-surface synthesis of two-dimensional imine polymers at the solid/liquid interface: Concentration takes control. Chem. Commun. 52, 6609{6612 (2016).

[45] Liu, X.-H. et al. On-surface synthesis of single-layered two-dimensional covalent organic frameworks via solid{vapor interface reactions. J. Am. Chem. Soc. 135, 10470{10474 (2013).

[46] Dai, J. et al. The role of the substrate structure in the on-surface synthesis of organometallic and covalent oligophenylene chains. Phys. Chem. Chem. Phys. 18, 20627{20634 (2016).

[47] Su, J., Wu, X., Song, S., Telychko, M. & Lu, J. Substrate induced strain for on-surface transformation and synthesis. Nanoscale 12, 7500{7508 (2020).

[48] Moreno, C. et al. Critical role of phenyl substitution and catalytic substrate in the surface assisted polymerization of dibromobianthracene derivatives. Chem. Mater. 31, 331{341 (2019).

[49] Simonov, K. A. et al. From graphene nanoribbons on Cu(111) to nanographene on Cu(110): Critical role of substrate structure in the bottom-up fabrication strategy. ACS Nano 9, 8997{9011 (2015).

[50] Fritton, M. et al. The role of kinetics versus thermodynamics in surface-assisted Ullmann coupling on gold and silver surfaces. J. Am. Chem. Soc. 141, 4824-4832 (2019).
[51] Fritton, M. et al. The influence of ortho-methyl substitution in organometallic self-assembly a comparative study on Cu(111) vs. Ag(111). Chem. Commun. 54, 9745-9748 (2018).
[52] Dong, L. et al. Transition metals trigger on-surface Ullmann coupling reaction: Intermediate, catalyst and template. In Gourdon, A. (ed.) On-Surface Synthesis, 23-42 (Springer International Publishing, Cham, 2016).
[53] Sun, K., Fang, Y. & Chi, L. On-surface synthesis on nonmetallic substrates. ACS Mater. Lett. 3, 56{63 (2020).
[54] Kittelmann, M., Lindner, R. & Kühnle, A. On-surfaces synthesis on insulating substrates. In Gourdon, A. (ed.) On-Surface Synthesis, 181-197 (Springer International Publishing, Cham, 2016).
[55] D.S. Lawrence, T. Jiang, and M. Levett. Self-assembling supramolecular complexes. Chem. Rev., 95:22292260, 1995
[56] L.F. Lindoy and I.M. Atkinson. Self assembly in supramolecular systems. The Royal Society of Chemistry, 2000.
[57] Desiraju, G. R., & Krishnamohan Sharma, C. V. (1996). Crystal engineering and molecular recognition. Twin facets of supramolecular chemistry. The Crystal as a Supramolecular Entity, 31-61.
[58] P Espinet, M. A. Esteruelas, L. A. Oro, J. L. Serrano, and E. Sola. Transition-metal liquid-crystals - advanced materials within the reach of the coordination chemist. Coord. Chem. Rev., 117:215274, 1992.
[59] R. Bissell and N. Boden. Liquid-crystals display new potential. Chem. Br., 31:3841, 1995.
[60] J. P. Collin, P. Gavina, V. Heitz, and J.-P. Sauvage. Construction of onedimensional multicomponent molecular arrays: Control of electronic and molecular motions. Eur. J. Inorg. Chem.,, pages 114, 1998.
[61] C. J. Jones. Transition metals as structural components in the construction of molecular container. Chem. Soc. Rev., 27:289299, 1998.
[62] c. D. Bain and s. D. Evans. Laying it on thin. Chem. Br., 31:4648, 1995
[63] Kudernac, T., Lei, S., Elemans, J. A., & De Feyter, S. (2009). Two-dimensional supramolecular self-assembly: nanoporous networks on surfaces. Chemical Society Reviews, 38(2), 402-421.

[64] AR. Otero, J. M. Gallego, A. L. Vázquez de Parga, N. Martin, and R. Miranda. Molecular self-assembly at solid surfaces. Adv. Mater., 23:51485176, 2011.

[65] Kolasinski, K. W. (2012). Surface science: foundations of catalysis and nanoscience. John Wiley & Sons.

[66] A.D. Buckingham, A.C. Legon, and S.M. Robers, editors. Principles of Molecular Recognition.

[67] G.C. Maitland, M. Rigby, E.B. Smith, and W.A. Wakeham. Intermolecular Forces: Their Origin and Determination. Oxford University Press, 1981.

[68] N.W. Alcock. Bonding and Structure. Ellis-Horwood, 1990.

[69] C. A. Hunter and J. K. M. Sanders. The nature of π-π interactions. J. Am. Chem. Soc., 112:5525, 1990.

[70] Arras, E., Seitsonen, A. P., Klappenberger, F., & Barth, J. V. (2012). Nature of the attractive interaction between proton acceptors and organic ring systems. Physical Chemistry Chemical Physics, 14(46), 15995-16001.

[71] P. Messina, A. Dmitriev, N. Lin, H. Spillmann, M. Abel, J. V. Barth, and K. Kern. Direct observation of chiral metal-organic complexes assembled on a Cu(100) surface. J. Am. Chem. Soc., 124:1400014001, 2002.

[72] H. Walch, J. Dienstmaier, G. Eder, R. Gutzler, S. Schlögl, T. Sirtl, K. Das, M. Schmittel, and M. Lackinger. Extended two-dimensional metal-organic frameworks based on thiolate-copper coordination bonds. J. Am. Chem. Soc., 133:79097915, 2011

[73] N. Lin, S. Stepanow, F. Vidal, K. Kern, M. S. Alam, S. Strömsdörfer, V. Dremov, P. Müller, A. Landa, and M. Ruben. Surface-assisted coordination chemistry and self-assembly. Dalton Trans., 0:27942800, 2006.

[74] U. Schlickum, F. Klappenberger, R. Decker, G. Zoppellaro, S. Klyatskaya, M. Ruben, K. Kern, H. Brune, and J. V. Barth. Surface-conned metal-organic nanostructures from co-directed assembly of linear terphenyldicarbonitrile linkers on Ag(111). J. Phys Chem. C, 114:1560215606, 2010.

[75] T. Sirtl, S. Schlögl, A. Rastgoo-Lahrood, J. Jelic, S. Neogi, M. Schmittel, W. M. Heckl, K. Reuter, and M. Lackinger. Control of intermolecular bonds by deposition rates at room temperature: hydrogen bonds versus metal coordination in trinitrile monolayers. J. Am. Chem. Soc., 135:691 695, 2013.

[76] N. N. Greenwood and A. Earnshaw. Chemistry of the elements. Pergamon Press, Oxford Oxfordshire; New York, 1984.

[77] Desiraju, G. R. Hydrogen Bridges in Crystal Engineering: Interactions without Borders. Acc. Chem. Res. 2002, 35, 565573.

[78] Desiraju, G. R. Chemistry beyond the molecule. Nature 2001, 412, 397400.

[79] Aakeröy, C. B., & Seddon, K. R. (1993). The hydrogen bond and crystal engineering. Chemical Society Reviews, 22(6), 397-407.

[80] G.R. Desiraju, Acc. Chem. Res., 1991, 24, 291; G.R. Desiraju and T. Steiner, The Weak Hydrogen Bond in Structural Chemistry and Biology, Oxford University Press, Oxford, 1999.

[81] Subramanian, S., & Zaworotko, M. J. (1994). Exploitation of the hydrogen bond: recent developments in the context of crystal engineering. Coordination Chemistry Reviews, 137, 357-401.

[82] Scheiner, S. (1997). Hydrogen bonding: a theoretical perspective (Vol. 7). Oxford University Press, USA.

[83] Jerey, G. A.; Saenger, W. Hydrogen Bonding in Biological Structures Springer Berlin Heidelberg, 1991.

[84] Steiner, T. (2002). The hydrogen bond in the solid state. Angewandte Chemie International Edition, 41(1), 48-76.

[85] Lackinger, M.; Heckl, W. M. Carboxylic Acids: Versatile Building Blocks and Mediators for Two-Dimensional Supramolecular Self-Assembly. Langmuir 2009, 25, 1130711321.

[86] Badami-Behjat, A., Deimel, P. S., Allegretti, F., Ringel, E., Mahata, K., Schmittel, M., & Lackinger, M. (2022). Versatile Role of Molecule–Surface Interactions for Monolayer Self-Assembly at Liquid–Solid Interfaces: Substrate-Induced Polymorphism, Thermodynamic Stability, and New Polymorphs. Chemistry of Materials, 34(19), 8876-8884.

[87] Leiserowitz, L. (1976). Molecular packing modes. Carboxylic acids. Acta Crystallographica Section B: Structural Crystallography and Crystal Chemistry, 32(3), 775-802.

[88] Lackinger, M.; Heckl, W. M. Carboxylic Acids: Versatile Building Blocks and Mediators for Two-Dimensional Supramolecular Self-Assembly. Langmuir 2009, 25, 11307-11321.

[89] Crabtree, R. H. (2009). The organometallic chemistry of the transition metals. John Wiley & Sons.

[90] Grill, L., & Hecht, S. (2020). Covalent on-surface polymerization. Nature Chemistry, 12(2), 115-130.

[91] Fan, Q.; Zhu, J.; Gottfried, J. M., On-Surface Ullmann Reaction for the Synthesis of Polymers and Macrocycles. In On-Surface Synthesis II, Springer: 2018; pp 83-112. 177

[92] Wang, W., Shi, X., Wang, S., VanHove, M. A. & Lin, N. Single-molecule resolution of an organometallic intermediate in a surface-supported Ullmann coupling reaction. J. Am. Chem. Soc. 133, 13264–13267 (2011).

[93] Eichhorn, J.; Nieckarz, D.; Ochs, O.; Samanta, D.; Schmittel, M.; Szabelski, P. J.; Lackinger, M., On-Surface Ullmann Coupling: The Influence of Kinetic Reaction Parameters on the Morphology and Quality of Covalent Networks. Acs Nano 2014, 8 (8), 7880-7889.

[94] Zhang, S., Fabrication of novel biomaterials through molecular self-assembly. Nat. Biotechnol. 2003, 21, 1171.

[95] Perepichka, D. F.; Rosei, F., Chemistry. Extending polymer conjugation into the second dimension. Science 2009, 323 (5911), 216-217.

[96] Di Giovannantonio, M.; Contini, G., Reversibility and intermediate steps as key tools for the growth of extended ordered polymers via on-surface synthesis. J. Phys. Condens. Matter 2018, 30 (9), 093001.

[97] Lafferentz, L.; Eberhardt, V.; Dri, C.; Africh, C.; Comelli, G.; Esch, F.; Hecht, S.; Grill, L., Controlling on-surface polymerization by hierarchical and substrate-directed growth. Nat. Chem. 2012, 4 (3), 215-220.

[98] Xi, M., Bent, B.E.: Iodobenzene on Cu(111): formation and coupling of adsorbed phenyl groups. Surf. Sci. 278, 19–32 (1992)

[99] Xi, M., Bent, B.E.: Mechanisms of the Ullmann coupling reaction in adsorbed monolayers. J. Am. Chem. Soc. 115, 7426–7433 (1993)

[100] S. Behler, M. K. Rose, J. C. Dunphy, D. F. Ogletree, M. Salmeron, and C. Chapelier, Rev. Sci. Instrum. 68, 2479 (1997).

[101] Stipe, B. C., Rezaei, M. A., & Ho, W. (1999). A variable-temperature scanning tunneling microscope capable of single-molecule vibrational spectroscopy. *Review of Scientific Instruments*, *70*(1), 137-143.

[102] Foley, E. T., Yoder, N. L., Guisinger, N. P., & Hersam, M. C. (2004). Cryogenic variable temperature ultrahigh vacuum scanning tunneling microscope for single molecule studies on silicon surfaces. *Review of scientific instruments*, *75*(12), 5280-5287.

[103] Meyer, G. (1996). A simple low-temperature ultrahigh-vacuum scanning tunneling microscope capable of atomic manipulation. *Review of Scientific Instruments*, *67*(8), 2960-2965.

[104] Pan, S. H., Hudson, E. W., & Davis, J. C. (1999). He 3 refrigerator based very low temperature scanning tunneling microscope. *Review of scientific instruments*, *70*(2), 1459-1463.

[105] Albers, B. J., Liebmann, M., Schwendemann, T. C., Baykara, M. Z., Heyde, M., Salmeron, M., ... & Schwarz, U. D. (2008). Combined low-temperature scanning tunneling/atomic force microscope for atomic resolution imaging and site-specific force spectroscopy. *Review of Scientific Instruments*, *79*(3).

[106] Kloft, S. (2020). *Entwicklung eines Raster-Sonden-Mikroskops (SPM) für die Analyse oberflächenadsorbierter und selbstassemblierter Nanostrukturen* (Doctoral dissertation, lmu).

[107] Woodcraft, A. L., & Gray, A. (2009, December). A low-temperature thermal conductivity database. In *Aip conference proceedings* (Vol. 1185, No. 1, pp. 681-684). American Institute of Physics.

[108] Schulz, B. (1994). Thermophysical properties of sapphire, AlN and MgAl2O4 down to 70 K. *Journal of nuclear materials*, *212*, 1065-1068.

[109] https://rayotek.com/PDF/Sapphire-Optical-and-Thermal-Properties-Graph.pdf

[110] Yarlagadda, S., Chan, M. H., Lee, H., Lesieutre, G. A., Jensen, D. W., & Messer, R. S. (1995). Low-temperature thermal conductivity, heat capacity, and heat generation of PZT. *Journal of intelligent material systems and structures*, *6*(6), 757-764.

[111] Gladun, A., Gladun, C., & Vinzelberg, H. (1980). Thermal conductivity of high-purity molybdenum. *physica status solidi (a)*, *58*(2), 409-413.

[112] https://www.panacol.com/panacol/datasheets/elecolit/elecolit-3655-english-tds-panacol-adhesive.pdf

[113] Nadig, D. S., Ramakrishnan, V., Sampathkumaran, P., & Prashanth, C. S. (2012, June). Effect of cryogenic treatment on thermal conductivity properties of copper. In *AIP Conference Proceedings* (Vol. 1435, No. 1, pp. 133-139). American Institute of Physics.

[114]https://www.osti.gov/servlets/purl/5066461#:~:text=Measurements%20were%20mad20on%20the,a%20resistivity%20ratio%20of%2017.

[115] Shi, Y., Chen, X., Sun, C., & Xia, X. L. (2023). Temperature-Dependent Thermal Conductivity and Absorption Coefficient Identification of Quartz Window up to 1100 K. *Journal of Thermal Science*, *32*(1), 44-58.

[116] Lackinger, M. Surface-Assisted Ullmann Coupling. *Chem. Commun.* **2017**, *53*, 7872-7885.

[117] Clair, S.; de Oteyza, D. G. Controlling a Chemical Coupling Reaction on a Surface: Tools and Strategies for on-Surface Synthesis. *Chem. Rev.* **2019**, *119*, 4717-4776.

[118] Cai, J. M.; Ruffieux, P.; Jaafar, R.; Bieri, M.; Braun, T.; Blankenburg, S.; Muoth, M.; Seitsonen, A. P.; Saleh, M.; Feng, X. L.; Müllen, K.; Fasel, R. Atomically Precise Bottom-up Fabrication of Graphene Nanoribbons. *Nature* **2010**, *466*, 470-473.

[119] Ruffieux, P.; Wang, S. Y.; Yang, B.; Sanchez-Sanchez, C.; Liu, J.; Dienel, T.; Talirz, L.; Shinde, P.; Pignedoli, C. A.; Passerone, D.; Dumslaff, T.; Feng, X. L.; Müllen, K.; Fasel, R. On-Surface Synthesis of Graphene Nanoribbons with Zigzag Edge Topology. *Nature* **2016**, *531*, 489-492.

[120] Dienstmaier, J. F.; Gigler, A. M.; Goetz, A. J.; Knochel, P.; Bein, T.; Lyapin, A.; Reichlmaier, S.; Heckl, W. M.; Lackinger, M. Synthesis of Well-Ordered Cof Monolayers: Surface Growth of Nanocrystalline Precursors Vs. Direct on-Surface Polycondensation. *ACS Nano* **2011**, *5*, 9737-9745.

[121] Tanoue, R.; Higuchi, R.; Enoki, N.; Miyasato, Y.; Uemura, S.; Kimizuka, N.; Stieg, A. Z.; Gimzewski, J. K.; Kunitake, M. Thermodynamically Controlled Self-Assembly of Covalent Nanoarchitectures in Aqueous Solution. *ACS Nano* **2011**, *5*, 3923-3929.

[122] Guan, C. Z.; Wang, D.; Wan, L. J. Construction and Repair of Highly Ordered 2d Covalent Networks by Chemical Equilibrium Regulation. *Chem. Comm.* **2012**, *48*, 2943-2945.

[123] Dienstmaier, J. F.; Medina, D.; Dogru, M.; Knochel, P.; Bein, T.; Heckl, W. M.; Lackinger, M. Isoreticular Two-Dimensional Covalent Organic Frameworks Synthesized by on-Surface Condensation of Diboronic Acids. *ACS Nano* **2012**, *6*, 7234–7242.

[124] Liu, X. H.; Guan, C. Z.; Ding, S. Y.; Wang, W.; Yan, H. J.; Wang, D.; Wan, L. J. On-Surface Synthesis of Single-Layered Two-Dimensional Covalent Organic Frameworks Via Solid-Vapor Interface Reactions. *J. Am. Chem. Soc.* **2013**, *135*, 10470-10474.

[125] Bieri, M.; Treiera, M.; Caia, J.; Aït-Mansoura, K.; Ruffieuxa, P.; Gröninga, O.; Gröninga, P.; Kastlerb, M.; Riegerb, R.; Fengb, X.; Müllen, K.; Fasel, R. Porous Graphenes: Two-Dimensional Polymer Synthesis with Atomic Precision. *Chem. Commun.* **2009**, 6919-6921.

[126] Eichhorn, J.; Strunskus, T.; Rastgoo-Lahrood, A.; Samanta, D.; Schmittel, M.; Lackinger, M. On-Surface Ullmann Polymerization Via Intermediate Organometallic Networks on Ag(111). *Chem. Commun.* **2014**, *50*, 7680-7682.

[127] Lafferentz, L.; Eberhardt, V.; Dri, C.; Africh, C.; Comelli, G.; Esch, F.; Hecht, S.; Grill, L. Controlling on-Surface Polymerization by Hierarchical and Substrate-Directed Growth. *Nat. Chem.* **2012**, *4*, 215-220.

[128] Steiner, C.; Gebhardt, J.; Ammon, M.; Yang, Z. C.; Heidenreich, A.; Hammer, N.; Görling, A.; Kivala, M.; Maier, S. Hierarchical on-Surface Synthesis and Electronic Structure of Carbonyl-Functionalized One- and Two-Dimensional Covalent Nanoarchitectures. *Nat. Commun.* **2017**, *8*, 14765.

[129] Moreno, C.; Vilas-Varela, M.; Kretz, B.; Garcia-Lekue, A.; Costache, M. V.; Paradinas, M.; Panighel, M.; Ceballos, G.; Valenzuela, S. O.; Pena, D.; Mugarza, A. Bottom-up Synthesis of Multifunctional Nanoporous Graphene. *Science* **2018**, *360*, 199-203.

[130] Fan, Q. T.; Yan, L. H.; Tripp, M. W.; Krejci, O.; Dimosthenous, S.; Kachel, S. R.; Chen, M. Y.; Foster, A. S.; Koert, U.; Liljeroth, P.; Gottfried, J. M. Biphenylene Network: A Nonbenzenoid Carbon Allotrope. *Science* **2021**, *372*, 852

[131] Galeotti, G.; De Marchi, F.; Hamzehpoor, E.; MacLean, O.; Rao, M. R.; Chen, Y.; Besteiro, L. V.; Dettmann, D.; Ferrari, L.; Frezza, F.; Sheverdyaeva, P. M.; Liu, R.; Kundu, A. K.; Moras, P.; Ebrahimi, M.; Gallagher, M. C.; Rosei, F.; Perepichka, D. F.; Contini, G. Synthesis of Mesoscale Ordered Two-Dimensional Pi-Conjugated Polymers with Semiconducting Properties. *Nat. Mater.* **2020**, *19*, 874-880.

[132] Grossmann, L.; King, B. T.; Reichlmaier, S.; Hartmann, N.; Rosen, J.; Heckl, W. M.; Björk, J.; Lackinger, M. On-Surface Photopolymerization of Two-Dimensional Polymers Ordered on the Mesoscale. *Nat. Chem.* **2021**, *13*, 730-736.

[133] Lackinger, M. Synthesis on Inert Surfaces. *Dalton Trans.* **2021**, *50*, 10020-10027.

[134] Lackinger, M. On-Surface Synthesis - There Will Be Light. *Trends. Chem.* **2022**, *4*, 471-474.

[135] Brusso, J. L.; Hirst, O. D.; Dadvand, A.; Ganesan, S.; Cicoira, F.; Robertson, C. M.; Oakley, R. T.; Rosei, F.; Perepichkat, D. F. Two-Dimensional Structural Motif in Thienoacene Semiconductors: Synthesis, Structure, and Properties of Tetrathienoanthracene Isomers. *Chem. Mater.* **2008**, *20*, 2484-2494.

[136] Gutzler, R.; Cardenas, L.; Lipton-Duffin, J.; El Garah, M.; Dinca, L. E.; Szakacs, C. E.; Fu, C.; Gallagher, M.; Vondracek, M.; Rybachuk, M.; Perepichka, D. F.; Rosei, F. Ullmann-Type Coupling of Brominated Tetrathienoanthracene on Copper and Silver. *Nanoscale* **2014**, *6*, 2660-2668.

[137] Galeotti, G.; De Marchi, F.; Taerum, T.; Besteiro, L. V.; El Garah, M.; Lipton-Duffin, J.; Ebrahimi, M.; Perepichka, D. F.; Rosei, F. Surface-Mediated Assembly, Polymerization and Degradation of Thiophene-Based Monomers. *Chem. Sci.* **2019**, *10*, 5167-5175.

[138] Morchutt, C.; Björk, J.; Krotzky, S.; Gutzler, R.; Kern, K. Covalent Coupling Via Dehalogenation on Ni(111) Supported Boron Nitride and Graphene. *Chem. Commun.* **2015**, *51*, 2440-2443.

[139] Zhao, W.; Dong, L.; Huang, C.; Win, Z. M.; Lin, N. A. Cu- and Pd-Catalyzed Ullmann Reaction on a Hexagonal Boron Nitride Layer. *Chem. Commun.* **2016**, *52*, 13225-13228.

[140] Rastgoo-Lahrood, A.; Björk, J.; Lischka, M.; Eichhorn, J.; Kloft, S.; Fritton, M.; Strunskus, T.; Samanta, D.; Schmittel, M.; Heckl, W. M.; Lackinger, M. Post-Synthetic Decoupling of on-Surface-Synthesized Covalent Nanostructures from Ag(111). *Angew. Chem. Int. Ed.* **2016**, *55*, 7650-7654.

[141] Rastgoo-Lahrood, A.; Lischka, M.; Eichhorn, J.; Samanta, D.; Schmittel, M.; Heckl, W. M.; Lackinger, M. Reversible Intercalation of Iodine Monolayers between on-Surface Synthesised Covalent Polyphenylene Networks and Au(111). *Nanoscale* **2017**, *9*, 4995-5001.

[142] Grossmann, L.; Duncan, D. A.; Jarvis, S. P.; Jones, R. G.; De, S.; Rosen, J.; Schmittel, M.; Heckl, W. M.; Björk, J.; Lackinger, M. Evolution of Adsorption Heights in the on-Surface Synthesis and Decoupling of Covalent Organic Networks on Ag(111) by Normal-Incidence X-Ray Standing Wave. *Nanoscale Horiz.* **2021**, *7*, 51-62.

[143] Badami-Behjat, A.; Deimel, P. S.; Allegretti, F.; Ringel, E.; Mahata, K.; Schmittel, M.; Barth, J. V.; Heckl, W. M.; Lackinger, M. Versatile Role of Molecule-Surface Interactions for Monolayer Self- Assembly at Liquid-Solid Interfaces: Substrate-Induced Polymorphism, Thermodynamic Stability, and New Polymorphs. *Chem. Mater.* **2022**.

[144] Grossmann, L.; Ringel, E.; Rastgoo-Lahrood, A.; King, B. T.; Rosen, J.; Heckl, W. M.; Opris, D.; Björk, J.; Lackinger, M. Steering Self-Assembly of Three-Dimensional Iptycenes on Au(111) by Tuning Molecule-Surface Interactions. *Angew. Chem. Int. Ed.* **2022**, *61*, e202201044.

[145] Bravo, B. G.; Michelhaugh, S. L.; Soriaga, M. P.; Villegas, I.; Suggs, D. W.; Stickney, J. L. Anodic Underpotential Deposition and Cathodic Stripping of Iodine at Polycrystalline and Single-Crystal Gold - Studies by Leed, Aes, Xps, and Electrochemistry. *J. Phys. Chem.* **1991**, *95*, 5245-5249.

[146] Gao, X. P.; Weaver, M. J. Probing Redox-Induced Molecular-Transformations by Atomic-Resolution Scanning Tunneling Microscopy - Iodide Adsorption and Electrooxidation on Au(111) in Aqueous-Solution. *J. Am. Chem. Soc.* **1992**, *114*, 8544-8551.

[147] Cardenas, L.; Gutzler, R.; Lipton-Duffin, J.; Fu, C. Y.; Brusso, J. L.; Dinca, L. E.; Vondracak, M.; Fagot-Revurat, Y.; Malterre, D.; Rosei, F.; Perepichka, D. F. Synthesis and Electronic Structure of a Two Dimensional Π-Conjugated Polythiophene. *Chem. Sci.* **2013**, *4*, 3263-3268.

[148] Rastgoo Lahrood, A.; Björk, J.; Heckl, W. M.; Lackinger, M. 1,3-Diiodobenzene on Cu(111) - an Exceptional Case of on-Surface Ullmann Coupling. *Chem. Commun.* **2015**, *51*, 13301-13304.

[149] Gutzler, R.; Fu, C. Y.; Dadvand, A.; Hua, Y.; MacLeod, J. M.; Rosei, F.; Perepichka, D. F. Halogen Bonds in 2d Supramolecular Self-Assembly of Organic Semiconductors. *Nanoscale* **2012**, *4*, 5965-5971.

[150] Song, W.; Martsinovich, N.; Heckl, W. M.; Lackinger, M. Thermodynamics of Halogen Bonded Monolayer Self-Assembly at the Liquid-Solid Interface. *Chem. Commun.* **2014**, *50*, 13465-13468.

[151] Saywell, A.; Greń, W.; Franc, G.; Gourdon, A.; Bouju, X.; Grill, L. Manipulating the Conformation of Single Organometallic Chains on Au(111). *J. Phys. Chem. C* **2013**, *118*, 1719-1728.

[152] Zhang, H. M.; Franke, J. H.; Zhong, D. Y.; Li, Y.; Timmer, A.; Arado, O. D.; Mönig, H.; Wang, H.; Chi, L. F.; Wang, Z. H.; Müllen, K.; Fuchs, H. Surface Supported Gold-Organic Hybrids: On-Surface Synthesis and Surface Directed Orientation. *Small* **2014**, *10*, 1361-1368.

[153] Zhang, H. M.; Lin, H. P.; Sun, K. W.; Chen, L.; Zagranyarski, Y.; Aghdassi, N.; Duhm, S.; Li, Q.; Zhong, D. Y.; Li, Y. Y.; Müllen, K.; Fuchs, H.; Chi, L. F. On-Surface Synthesis of Rylene-Type Graphene Nanoribbons. *J. Am. Chem. Soc.* **2015**, *137*, 4022-4025.

[154] Rastgoo-Lahrood, A.; Martsinovich, N.; Lischka, M.; Eichhorn, J.; Szabelski, P.; Nieckarz, D.; Strunskus, T.; Das, K.; Schmittel, M.; Heckl, W. M.; Lackinger, M. From Au-Thiolate Chains to Thioether Sierpinski Triangles: The Versatile Surface Chemistry of 1,3,5-Tris(4-Mercaptophenyl)Benzene on Au(111). *ACS Nano* **2016**, *10*, 10901-10911.

[155] Sun, Q.; Cai, L.; Ma, H.; Yuan, C.; Xu, W. Dehalogenative Homocoupling of Terminal Alkynyl Bromides on Au(111): Incorporation of Acetylenic Scaffolding into Surface Nanostructures. *ACS Nano* **2016**, *10*, 7023-7030.

[156] Liu, M. Z.; Liu, M. X.; She, L. M.; Zha, Z. Q.; Pan, J. L.; Li, S. C.; Li, T.; He, Y. Y.; Cai, Z. Y.; Wang, J. B.; Zheng, Y.; Qiu, X. H.; Zhong, D. Y. Graphene-Like Nanoribbons Periodically Embedded with Four- and Eight-Membered Rings. *Nat. Commun.* **2017**, *8*.

[157] Achilli, S.; Tumino, F.; Rabia, A.; Biroli, A. O.; Li Bassi, A.; Bossi, A.; Manini, N.; Onida, G.; Fratesi, G.; Casari, C. S. Steric Hindrance in the on-Surface Synthesis of Diethynyl-Linked Anthracene Polymers. *Phys. Chem. Chem. Phys.* **2022**, *24*, 13616-13624.

[158] Gutzler, R.; Walch, H.; Eder, G.; Kloft, S.; Heckl, W. M.; Lackinger, M. Surface Mediated Synthesis of 2d Covalent Organic Frameworks: 1,3,5-Tris(4-Bromophenyl)Benzene on Graphite(001), Cu(111), and Ag(110). *Chem. Commun.* **2009**, 4456-4458.

[159] Lischka, M.; Fritton, M.; Eichhorn, J.; Vyas, V. S.; Strunskus, T.; Lotsch, B. V.; Bjork, J.; Heckl, W. M.; Lackinger, M. On-Surface Polymerization of 1,6-Dibromo-3,8-Diiodpyrene-a Comparative Study on Au(111) Versus Ag(111) by Stm, Xps, and Nexafs. *Journal of Physical Chemistry C* **2018**, *122*, 5967-5977.

[160] Zhong, Q. G.; Niu, K. F.; Chen, L.; Zhang, H. M.; Ebeling, D.; Björk, J.; Müllen, K.; Schirmeisen, A.; Chi, L. F. Substrate-Modulated Synthesis of Metal-Organic Hybrids by Tunable Multiple Aryl-Metal Bonds. *J. Am. Chem. Soc.* **2022**, *144*, 8214-8222.

[161] Zuzak, R.; Jancarík, A.; Gourdon, A.; Szymonski, M.; Godlewski, S. On-Surface Synthesis with Atomic Hydrogen. *ACS Nano* **2020**, *14*, 13316-13323.

[162] Yang, Z. C.; Gebhardt, J.; Schaub, T. A.; Sander, T.; Schonamsgruber, J.; Soni, H.; Gorling, A.; Kivala, M.; Maier, S. Two-Dimensional Delocalized States in Organometallic Bis-Acetylide Networks on Ag(111). *Nanoscale* **2018**, *10*, 3769-3776.

[163] Schlögl, S.; Heckl, W. M.; Lackinger, M. On-Surface Radical Addition of Triply Iodinated Monomers on Au(111)—the Influence of Monomer Size and Thermal Post-Processing. *Surf. Sci.* **2012**, *606*, 999-1004.

[164] Gutzler, R.; Perepichka, D. F. Pi-Electron Conjugation in Two Dimensions. *J. Am. Chem. Soc.* **2013**, *135*, 16585-16594.

[165] Bieri, M.; Nguyen, M. T.; Groning, O.; Cai, J. M.; Treier, M.; Ait-Mansour, K.; Ruffieux, P.; Pignedoli, C. A.; Passerone, D.; Kastler, M.; Müllen, K.; Fasel, R. Two-Dimensional Polymer Formation on Surfaces: Insight into the Roles of Precursor Mobility and Reactivity. *J. Am. Chem. Soc.* **2010**, *132*, 16669-16676.

[166] Eichhorn, J.; Nieckarz, D.; Ochs, O.; Samanta, D.; Schmittel, M.; Szabelski, P. J.; Lackinger, M. On-Surface Ullmann Coupling: The Influence of Kinetic Reaction Parameters on the Morphology and Quality of Covalent Networks. *ACS Nano* **2014**, *8*, 7880-7889

[167] a) S. De Feyter, S. Furukawa, *Top. Curr. Chem.* **2009**, *287*, 87-133; b) M. Lackinger, W.M. Heckl, *Langmuir* **2009**, *25*, 11307-11321; c) S.B. Lei, K. Tahara, J. Adisoejoso, T. Balandina, Y. Tobe, S. De Feyter, *Crystengcomm* **2010**, *12*, 3369-3381; d) S. Uemura, R. Tanoue, N. Yilmaz, A. Ohira, M. Kunitake, *Materials* **2010**, *3*, 4252-4276;

e) Y. Tobe, *J. Syn. Org. Chem. Jpn.* **2012**, *70*, 1255-1266; f) X.M. Zhang, Q.D. Zeng, C. Wang, *RSC Adv.* **2013**, *3*, 11351-11366; g) J. Teyssandier, S. De Feyter, K.S. Mali, *Chem. Commun.* **2016**, *52*, 11465-11487; h) K.S. Mali, N. Pearce, S. De Feyter, N.R. Champness, *Chem. Soc. Rev.* **2017**, *46*, 2520-2542.

[168] a) W.T. Song, N. Martsinovich, W.M. Heckl, M. Lackinger, *J. Am. Chem. Soc.* **2013**, *135*, 14854-14862; b) W. Song, N. Martsinovich, W.M. Heckl, M. Lackinger, *Phys. Chem. Chem. Phys.* **2014**, *16*, 13239-13247;

c) W. Song, N. Martsinovich, W.M. Heckl, M. Lackinger, *Chem. Commun.* **2014**, *50*, 13465-13468;
d) J.R. Reimers, D. Panduwinata, J. Visser, Y. Chin, C.G. Tang, L. Goerigk, M.J. Ford, M. Sintic, T.J. Sum, M.J.J. Coenen, B.L.M. Hendriksen, J.A.A.W. Elemans, N.S. Hush, M.J. Crossley, *P. Natl. Acad. Sci. USA* **2015**, *112*, E6101-E6110; e) S. Conti, M. Cecchini, *Phys. Chem. Chem. Phys.* **2016**, *18*, 31480-31493.
[169] a) R. Gutzler, T. Sirtl, J.F. Dienstmaier, K. Mahata, W.M. Heckl, M. Schmittel, M. Lackinger, *J. Am. Chem. Soc.* **2010**, *132*, 5084-5090; b) J. Saiz-Poseu, J. Faraudo, A. Figueras, R. Alibes, F. Busqué, D. Ruiz-Molina, *Chem.-Eur. J.* **2012**, *18*, 3056-3063; c) M.O. Blunt, J. Adisoejoso, K. Tahara, K. Katayama, M. Van der Auweraer, Y. Tobe, S. De Feyter, *J. Am. Chem. Soc.* **2013**, *135*, 12068-12075; d) O. Ochs, M. Hocke, S. Spitzer, W.M. Heckl, N. Martsinovich, M. Lackinger, *Chem. Mater.* **2020**, *32*, 5057-5065; e) A. Badami-Behjat, P.S. Deimel, F. Allegretti, E. Ringel, K. Mahata, M. Schmittel, J.V. Barth, W.M. Heckl, M. Lackinger, *Chem. Mater.* **2022**.
[170] U. Mazur, K.W. Hipps, *Chem. Commun.* **2015**, *51*, 4737-4749.
[171] O. Ochs, N. Martsinovich, W.M. Heckl, M. Lackinger, *J. Phys. Chem. Lett.* **2020**, *11*, 7320-7326.
[172] M. Lackinger, S. Griessl, W.M. Heckl, M. Hietschold, G.W. Flynn, *Langmuir* **2005**, *21*, 4984-4988.
[173] O. Ochs, M. Hocke, S. Spitzer, W.M. Heckl, N. Martsinovich, M. Lackinger, *Chem. Mater.* **2020**, *32*, 5057-5065.
[174] a) A. Ciesielski, P. Samorì, *Chem. Soc. Rev.* **2014**, *43*, 381-398; b) D.W. Johnson, B.P. Dobson, K.S. Coleman, *Curr. Opin. Colloid. In.* **2015**, *20*, 367-382.
[175] A.C. Ferrari, D.M. Basko, *Nat. Nanotechnol.* **2013**, *8*, 235-246.
[176] a) K.V. Emtsev, A.A. Zakharov, C. Coletti, S. Forti, U. Starke, *Phys. Rev. B* **2011**, *84*; b) K.L. Man, M.S. Altman, *J. Phys.-Condens. Mat.* **2012**, *24*; c) M. Petrovic, I.S. Rakic, S. Runte, C. Busse, J.T. Sadowski, P. Lazic, I. Pletikosic, Z.H. Pan, M. Milun, P. Pervan, N. Atodiresei, R. Brako, D. Sokcevic, T. Valla, T. Michely, M. Kralj, *Nat. Commun.* **2013**, *4*.
[177] a) H. Hibino, H. Kageshima, F. Maeda, M. Nagase, Y. Kobayashi, H. Yamaguchi, *Phys. Rev. B* **2008**, *77*; b) R.M. Feenstra, N. Srivastava, Q. Gao, M. Widom, B. Diaconescu, T. Ohta, G.L. Kellogg, J.T. Robinson, I.V. Vlassiouk, *Phys. Rev. B* **2013**, *87*.

[178] M.S. Altman, W.F. Chung, C.H. Liu, *Surf. Rev. Lett.* **1998**, *5*, 1129-1141.

[179] R.Q. Hwang, J. Schröder, C. Günther, R.J. Behm, *Phys. Rev. Lett.* **1991**, *67*, 3279-3282.

[180] T.E. Weller, M. Ellerby, S.S. Saxena, R.P. Smith, N.T. Skipper, *Nat. Phys.* **2005**, *1*, 39-41.

[181] A.A. Papaderakis, A. Ejigu, J. Yang, A. Elgendy, B. Radha, A. Keerthi, A. Juel, R.A.W. Dryfe, *J. Am. Chem. Soc.* **2023**, *145*, 8007-8020.

[182] Rabe, J. P.; Buchholz, S. Commensurability and Mobility in 2-Dimensional Molecular-Patterns on Graphite. Science 1991, 253 (5018), 424−427.

[183] Mali, K. S.; Pearce, N.; De Feyter, S.; Champness, N. R. Frontiers of supramolecular chemistry at solid surfaces. Chem. Soc. Rev. 2017, 46 (9), 2520−2542.

[184] Furukawa, S.; De Feyter, S. Two-Dimensional Crystal Engineering at the Liquid-Solid Interface. Top. Curr. Chem. 2008, 287, 87− 133.

[185] Mali, K. S.; Adisoejoso, J.; Ghijsens, E.; De Cat, I.; De Feyter, S. Exploring the complexity of supramolecular interactions for patterning at the liquid-solid interface. Acc. Chem. Res. 2012, 45 (8), 1309−1320.

[186] Ciesielski, A.; Palma, C. A.; Bonini, M.; Samori, P. Towards Supramolecular Engineering of Functional Nanomaterials: Pre- Programming Multi-Component 2D Self-Assembly at Solid-Liquid Interfaces. Adv. Mater. 2010, 22 (32), 3506−3520.

[187] Mao, X. B.; Wang, C. X.; Wu, X. K.; Ma, X. J.; Liu, L.; Zhang, L.; Niu, L.; Guo, Y. Y.; Li, D. H.; Yang, Y. L.; et al. Beta structure motifs of islet amyloid polypeptides identified through surface-mediated assemblies. P. Natl. Acad. Sci. USA 2011, 108 (49), 19605−19610.

[188] Blunt, M. O.; Russell, J. C.; Gimenez-Lopez, M. D.; Taleb, N.; Lin, X. L.; Schr.der, M.; Champness, N. R.; Beton, P. H. Guestinduced growth of a surface-based supramolecular bilayer. Nat. Chem. 2011, 3 (1), 74−78.

[189] Fang, Y.; Ghijsens, E.; Ivasenko, O.; Cao, H.; Noguchi, A.; Mali, K. S.; Tahara, K.; Tobe, Y.; De Feyter, S. Dynamic control over supramolecular handedness by selecting chiral induction pathways at the solution-solid interface. Nat. Chem. 2016, 8 (7), 711−717.

[190] Blunt, M. O.; Russell, J. C.; Gimenez-Lopez, M. D.; Garrahan, J. P.; Lin, X.; Schr.der, M.; Champness, N. R.; Beton, P. H. Random Tiling and Topological Defects in a Two-Dimensional Molecular Network. Science 2008, 322 (5904), 1077−1081.

[191] Cometto, F. P.; Kern, K.; Lingenfelder, M. Local Conformational Switching of Supramolecular Networks at the Solid/Liquid Interface. ACS Nano 2015, 9 (5), 5544−5550.

[192] Gutzler, R.; Sirtl, T.; Dienstmaier, J. F.; Mahata, K.; Heckl, W. M.; Schmittel, M.; Lackinger, M. Reversible Phase Transitions in Self- Assembled Monolayers at the Liquid-Solid Interface: Temperature- Controlled Opening and Closing of Nanopores. J. Am. Chem. Soc. 2010, 132 (14), 5084−5090.

[193] Ubink, J.; Enache, M.; Stohr, M. Bias-induced conformational switching of supramolecular networks of trimesic acid at the solidliquid interface. J. Chem. Phys. 2018, 148 (17), 174703.

[194] Lee, S. L.; Fang, Y.; Velpula, G.; Cometto, F. R.; Lingenfelder, M.; Müllen, K.; Mali, K. S.; De Feyter, S. Reversible Local and Global Switching in Multicomponent Supramolecular Networks: Controlled

Guest Release and Capture at the Solution/Solid Interface. ACS Nano 2015, 9 (12), 11608−11617.

[195] Blunt, M. O.; Adisoejoso, J.; Tahara, K.; Katayama, K.; Van der Auweraer, M.; Tobe, Y.; De Feyter, S. Temperature-Induced Structural Phase Transitions in a Two-Dimensional Self-Assembled Network. J. Am. Chem. Soc. 2013, 135 (32), 12068−12075.

[196] Frath, D.; Yokoyama, S.; Hirose, T.; Matsuda, K. Photoresponsive supramolecular self-assemblies at the liquid/solid interface. J. Photoch. Photobio. C 2018, 34, 29−40.

[197] Greenwood, J.; Phan, T. H.; Fujita, Y.; Li, Z.; Ivasenko, O.; Vanderlinden, W.; Van Gorp, H.; Frederickx, W.; Lu, G.; Tahara, K.;et al. Covalent Modification of Graphene and Graphite Using Diazonium Chemistry: Tunable Grafting and Nanomanipulation. ACS Nano 2015, 9 (5), 5520−5535.

[198] De Feyter, S.; De Schryver, F. C. Self-assembly at the liquid/solid interface: STM reveals. J. Phys. Chem. B 2005, 109 (10), 4290− 4302.

[199] Lackinger, M.; Griessl, S.; Heckl, W. M.; Hietschold, M.; Flynn, G. W. Self-assembly of trimesic acid at the liquid-solid interface – a study of solvent-induced polymorphism. Langmuir 2005, 21 (11), 4984−4988.

[200] Kampschulte, L.; Lackinger, M.; Maier, A. K.; Kishore, R. S. K.; Griessl, S.; Schmittel, M.; Heckl, W. M. Solvent induced polymorphism in supramolecular 1,3,5-benzenetribenzoic acid monolayers. J. Phys. Chem. B 2006, 110 (22), 10829−10836.

[201] Takami, T.; Mazur, U.; Hipps, K. W. Solvent-Induced Variations in Surface Structure of a 2,9,16,23-Tetratert-butylphthalocyanine on Graphite. J. Phys. Chem. C 2009, 113 (40),17479−17483.

[202] Mamdouh, W.; Uji-i, H.; Ladislaw, J. S.; Dulcey, A. E.; Percec,V.; De Schryver, F. C.; De Feyter, S. Solvent controlled self-assembly at the liquid-solid interface revealed by STM. J. Am. Chem. Soc. 2006,128 (1), 317−325.

[203] Yang, Y.; Wang, C. Solvent effects on two-dimensional molecular self-assmblies investigated by using scanning tunnelling microscopy. Curr. Opin. Colloid In 2009, 14 (2), 135−147.

[204] Lei, S.; Tahara, K.; De Schryver, F. C.; Van der Auweraer, M.;Tobe, Y.; De Feyter, S. One Building Block, Two Different Supramolecular Surface-Confined Patterns: Concentration in Control at the Solid−Liquid Interface. Angew. Chem. Int. Ed 2008, 47, 2964−2968.

[205] Coenen, M. J. J.; den Boer, D.; van den Bruele, F. J.; Habets, T.;Timmers, K. A. A. M.; van der Maas, M.; Khoury, T.; Panduwinata, D.; Crossley, M. J.; Reimers, J. R.; et al. Polymorphism in porphyrin monolayers: the relation between adsorption configuration and molecular conformation. Phys. Chem. Chem. Phys. 2013, 15 (30), 12451−12458.

[206] Dienstmaier, J. F.; Mahata, K.; Walch, H.; Heckl, W. M.; Schmittel, M.; Lackinger, M. On the Scalability of Supramolecular Networks - High Packing Density vs. Optimized Hydrogen Bonds in Tricarboxylic Acid Monolayers. Langmuir 2010, 26 (13), 10708−10716.

[207] Ciesielski, A.; Szabelski, P. J.; Rzysko, W.; Cadeddu, A.; Cook, T. R.; Stang, P. J.; Samori, P. Concentration-Dependent Supramolecular Engineering of Hydrogen-Bonded Nanostructures at Surfaces: Predicting Self-Assembly in 2D. J. Am. Chem. Soc. 2013, 135 (18), 6942−6950.

[208] Tahara, K.; Okuhata, S.; Adisoejoso, J.; Lei, S. B.; Fujita, T.; De Feyter, S.; Tobe, Y. 2D Networks of Rhombic-Shaped Fused Dehydrobenzo[12]annulenes: Structural Variations under Concentration Control. J. Am. Chem. Soc. 2009, 131 (48), 17583−17590.

[209] Reimers, J. R.; Panduwinata, D.; Visser, J.; Chin, Y.; Tang, C. G.; Goerigk, L.; Ford, M. J.; Sintic, M.; Sum, T. J.; Coenen, M. J. J.; et al. A priori calculations of the free energy of formation from solution of polymorphic self-assembled monolayers. P. Natl. Acad. Sci. USA 2015, 112 (45), E6101−E6110.

[210] Conti, S.; Cecchini, M. Predicting molecular self-assembly at surfaces: a statistical thermodynamics and modeling approach. Phys. Chem. Chem. Phys. 2016, 18 (46), 31480−31493.

[211] Sirtl, T.; Song, W.; Eder, G.; Neogi, S.; Schmittel, M.; Heckl, W. M.; Lackinger, M. Solvent-Dependent Stabilization of Metastable Monolayer Polymorphs at the Liquid−Solid Interface. ACS Nano 2013, 7 (8), 6711−6718.

[212] Marie, C.; Silly, F.; Tortech, L.; Müllen, K.; Fichou, D. Tuning the Packing Density of 2D Supramolecular Self-Assemblies at the Solid-Liquid Interface Using Variable Temperature. ACS Nano 2010, 4 (3), 1288−1292.

[213] Bhattarai, A.; Mazur, U.; Hipps, K. W. A Single Molecule Level Study of the Temperature-Dependent Kinetics for the Formation of Metal Porphyrin Monolayers on Au(111) from Solution. J. Am. Chem. Soc. 2014, 136 (5), 2142−2148.

[214] Jahanbekam, A.; Chilukuri, B.; Mazur, U.; Hipps, K. W. Kinetically Trapped Two-Component Self-Assembled Adlayer. J. Phys. Chem. C 2015, 119 (45), 25364−25376.

[215] Ochs, O.; Martsinovich, N.; Heckl, W. M.; Lackinger, M. Quantifying the Ultraslow Desorption Kinetics of 2,6-Naphthalenedicarboxylic Acid Monolayers at Liquid-Solid Interfaces. J. Phys. Chem. Lett. 2020, 11 (17), 7320−7326

[216] Song, W. T.; Martsinovich, N.; Heckl, W. M.; Lackinger, M. Born-Haber Cycle for Monolayer Self-Assembly at the Liquid-Solid Interface: Assessing the Enthalpic Driving Force. J. Am. Chem. Soc. 2013, 135 (39), 14854−14862.

[217] Kunitake, M.; Batina, N.; Itaya, K. Self-Organized Porphyrin Array on Iodine-Modified Au(111) in Electrolyte-Solutions - in-Situ Scanning-Tunneling-Microscopy Study. Langmuir 1995, 11 (7), 2337−2340.

[218] Ogaki, K.; Batina, N.; Kunitake, M.; Itaya, K. In situ scanning tunneling microscopy of ordering processes of adsorbed porphyrin on iodine-modified Ag(111). J. Phys. Chem. 1996, 100 (17), 7185−7190.

[219] Rastgoo-Lahrood, A.; Bj.rk, J.; Lischka, M.; Eichhorn, J.; Kloft, S.; Fritton, M.; Strunskus, T.; Samanta, D.; Schmittel, M.; Heckl, W. M.; et al. Post-Synthetic Decoupling of On-Surface-Synthesized Covalent Nanostructures from Ag(111). Angew. Chem. Int. Ed 2016, 55 (27), 7650−7654.

[220] Rastgoo-Lahrood, A.; Lischka, M.; Eichhorn, J.; Samanta, D.; Schmittel, M.; Heckl, W. M.; Lackinger, M. Reversible intercalation of iodine monolayers between on-surface synthesised covalent polyphenylene networks and Au(111). Nanoscale 2017, 9, 4995−5001.

[221] Yokota, Y.; Wong, R. A.; Hong, M. S.; Hayazawa, N.; Kim, Y. Monatomic Iodine Dielectric Layer for Multimodal Optical Spectroscopy of Dye Molecules on Metal Surfaces. J. Am. Chem. Soc. 2021, 143 (37), 15205−15214.

[222] Grossmann, L.; Duncan, D. A.; Jarvis, S. P.; Jones, R. G.; De, S.; Rosen, J.; Schmittel, M.; Heckl, W. M.; Bj.rk, J.; Lackinger, M.Evolution of adsorption heights in the on-surface synthesis and decoupling of covalent organic networks on Ag(111) by normalincidence X-ray standing wave. Nanoscale Horiz 2021, 7 (1), 51−62.

[223] Grossmann, L.; Ringel, E.; Rastgoo-Lahrood, A.; King, B. T.; Rosen, J.; Heckl, W. M.; Opris, D.; Bj.rk, J.; Lackinger, M. Steering Self-Assembly of Three-Dimensional Iptycenes on Au(111) by Tuning Molecule-Surface Interactions. Angew. Chem. Int. Ed 2022, 61 (25), No. e202201044.

[224] Ochs, O.; Hocke, M.; Spitzer, S.; Heckl, W. M.; Martsinovich, N.; Lackinger, M. Origin of Solvent-Induced Polymorphism in Self- Assembly of Trimesic Acid Monolayers at Solid-Liquid Interfaces. Chem. Mater. 2020, 32 (12), 5057−5065.

[225] Lackinger, M.; Heckl, W. M. Carboxylic Acids: Versatile Building Blocks and Mediators for Two Dimensional Supramolecular Self-Assembly. Langmuir 2009, 25 (19), 11307−11321.

[226] Martsinovich, N.; Troisi, A. Modeling the Self-Assembly of Benzenedicarboxylic Acids Using Monte Carlo and Molecular Dynamics Simulations. J. Phys. Chem. C 2010, 114 (10), 4376−4388.

[227] Müller, T.; Flynn, G. W.; Mathauser, A. T.; Teplyakov, A. V. Temperature-programmed desorption studies of n-alkane derivatives on graphite: Desorption energetics and the influence of functional groups on adsorbate self-assembly. Langmuir 2003, 19 (7), 2812−2821.

[228] Mammen, M.; Shakhnovich, E. I.; Deutch, J. M.; Whitesides, G.M. Estimating the entropic cost of self-assembly of multiparticle hydrogen-bonded aggregates based on the cyanuric acid center dot melamine lattice. J. Org. Chem. 1998, 63 (12), 3821−3830.

[229] King, D. A. Thermal Desorption from Metal-Surfaces. Surf. Sci.1975, 47 (1), 384−402.

[230] Dejong, A. M.; Niemantsverdriet, J. W. Thermal-Desorption Analysis - Comparative Test of 10 Commonly Applied Procedures. Surf. Sci. 1990, 233 (3), 355−365.

[231] Burke, S. A.; Topple, J. M.; Grutter, P. Molecular dewetting on insulators. J. Phys.-Condens. Mat 2009, 21 (42), 423101.

[232] Rahe, P.; Kittelmann, M.; Neff, J. L.; Nimmrich, M.; Reichling, M.; Maass, P.; Kühnle, A. Tuning Molecular Self-Assembly on Bulk Insulator Surfaces by Anchoring of the Organic Building Blocks. Adv. Mater. 2013, 25 (29), 3948−3956.

[233] Griessl, S.; Lackinger, M.; Edelwirth, M.; Hietschold, M.; Heckl, W. M. Self-Assembled Two-Dimensional Molecular Host-Guest Architectures From Trimesic Acid. Single Mol. 2002, 3 (1), 25−31.

[234] Syomin, D.; Koel, B. E. Adsorption of iodobenzene (C6H5I) on Au(111) surfaces and production of biphenyl (C6H5-C6H5). Surf. Sci. 2001, 490 (3), 265−273.

[235] Pawin, G.; Solanki, U.; Kwon, K. Y.; Wong, K. L.; Lin, X.; Jiao, T.; Bartels, L. A quantitative approach to hydrogen bonding at a metal surface. J. Am. Chem. Soc. 2007, 129 (40), 12056.

[236] Ochs, O.; Heckl, W. M.; Lackinger, M. Immersion-scanningtunneling-microscope for long-term variable-temperature experiments at liquid-solid interfaces. Rev. Sci. Instrum. 2018, 89 (5), 053707

[237] Mazur, U.; Hipps, K. W. Kinetic and thermodynamic processes of organic species at the solution-solid interface: the view through an STM. Chem. Commun. 2015, 51 (23), 4737−4749.

[238] Arras, E.; Seitsonen, A. P.; Klappenberger, F.; Barth, J. V. Nature of the attractive interaction between proton acceptors and organic ring systems. Phys. Chem. Chem. Phys. 2012, 14 (46), 15995−16001.

[239] English, W. A.; Hipps, K. W. Stability of a surface adlayer at elevated temperature: Coronene and heptanoic acid on Au(111). J.Phys. Chem. C 2008, 112 (6), 2026−2031.

[240] Kampschulte, L.; Werblowsky, T. L.; Kishore, R. S. K.;Schmittel, M.; Heckl, W. M.; Lackinger, M. Thermodynamical equilibrium of binary supramolecular networks at the liquid-solid interface. J. Am. Chem. Soc. 2008, 130 (26), 8502−8507.

[241] Kudernac, T.; Lei, S. B.; Elemans, J. A. A. W.; De Feyter, S.Two-dimensional supramolecular self-assembly: nanoporous networks on surfaces. Chem. Soc. Rev. 2009, 38 (2), 402−421.

[242] Spitzer, S.; Helmle, O.; Ochs, O.; Horsley, J.; Martsinovich, N.; Heckl, W. M.; Lackinger, M. What can be inferred from moire patterns? A case study of trimesic acid monolayers on graphite. Faraday Discuss. 2017, 204, 331−348.

[243] Brusso, J. L.; Hirst, O. D.; Dadvand, A.; Ganesan, S.; Cicoira, F.; Robertson, C. M.; Oakley, R. T.; Rosei, F.; Perepichkat, D. F. Two-Dimensional Structural Motif in Thienoacene Semiconductors: Synthesis, Structure, and Properties of Tetrathienoanthracene Isomers. *Chem. Mater.* **2008**, *20*, 2484-2494.

[244] Gutzler, R.; Heckl, W. M.; Lackinger, M. Combination of a Knudsen Effusion Cell with a Quartz Crystal Microbalance: In-Situ Measurement of Molecular Evaporation Rates with a Fully Functional Deposition Source. *Rev. Sci. Instrum.* **2009**, *81*, 015108.

[245] Schmucker, S. W.; Kumar, N.; Abelson, J. R.; Daly, S. R.; Girolami, G. S.; Bischof, M. R.; Jaeger, D. L.; Reidy, R. F.; Gorman, B. P.; Alexander, J.; Ballard, J. B.; Randall, J. N.; Lyding, J. W. Field-Directed Sputter Sharpening for Tailored Probe Materials and Atomic-Scale Lithography. *Nat. Commun.* **2012**, *3*.

[246] Horcas, I.; Fernandez, R.; Gomez-Rodriguez, J. M.; Colchero, J.; Gomez-Herrero, J.; Baro, A. M. Wsxm: A Software for Scanning Probe Microscopy and a Tool for Nanotechnology. *Rev. Sci. Instrum.* **2007**, *78*, 013705.

[247] Neese, F. The Orca Program System. *Wires. Comput. Mol. Sci.* **2012**, *2*, 73-78.

[248] Stephens, P. J.; Devlin, F. J.; Ashvar, C. S.; Chabalowski, C. F.; Frisch, M. J. Theoretical Calculation of Vibrational Circular-Dichroism Spectra. *Faraday Discuss.* **1994**, *99*, 103-119.

[249] Weigend, F.; Ahlrichs, R. Balanced Basis Sets of Split Valence, Triple Zeta Valence and Quadruple Zeta Valence Quality for H to Rn: Design and Assessment of Accuracy. *Phys. Chem. Chem. Phys.* **2005**, *7*, 3297-3305.

[250] Giannozzi, P.; Baroni, S.; Bonini, N.; Calandra, M.; Car, R.; Cavazzoni, C.; Ceresoli, D.; Chiarotti, G. L.; Cococcioni, M.; Dabo, I.; Dal Corso, A.; de Gironcoli, S.; Fabris, S.; Fratesi, G.; Gebauer, R.; Gerstmann, U.; Gougoussis, C.; Kokalj, A.; Lazzeri, M.; Martin-Samos, L.; et al. Quantum Espresso: A Modular and Open-Source Software Project for Quantum Simulations of Materials. *J. Phys.-Condens. Mat.* **2009**, *21*.

[251] Perdew, J. P.; Burke, K.; Ernzerhof, M. Generalized Gradient Approximation Made Simple. *Phys. Rev. Lett.* **1996**, *77*, 3865-3868.

[252] Troullier, N.; Martins, J. L. Efficient Pseudopotentials for Plane-Wave Calculations. *Phys. Rev. B* **1991**, *43*, 1993-2006.

[253] D. Nečas, P. Klapetek, *Cent. Eur. J. Phys.* **2012**, *10*, 181–188.

[254] Deimel, P. S.; Feulner, P.; Barth, J. V.; Allegretti, F. Spatial decoupling of macrocyclic metal-organic complexes from a metal support: a 4-fluorothiophenol self-assembled monolayer as a thermally removable spacer. Phys. Chem. Chem. Phys. 2019, 21 (21), 10992-11003.

[255] MacLeod, J. M.; Lipton-Duffin, J. A.; Cui, D.; De Feyter, S.; Rosei, F. Substrate Effects in the Supramolecular Assembly of 1,3,5-Benzene Tricarboxylic Acid on Graphite and Graphene. Langmuir 2015, 31 (25), 7016-7024.

[256] Conti, S.; Cecchini, M. Predicting molecular self-assembly at surfaces: a statistical thermodynamics and modeling approach. Phys. Chem. Chem. Phys. 2016, 18 (46), 31480 31493.

[257] Shayeganfar, F.; Rochefort, A. Electronic Properties of Self-Assembled Trimesic Acid Monolayer on Graphene. Langmuir 2014, 30 (32), 9707-9716.